# PLASMONS IN ASSEMBLED METAL NANOSTRUCTURES:

# RADIATIVE AND NONRADIATIVE PROPERTIES, NEAR-FIELD

# COUPLING AND ITS UNIVERSAL SCALING BEHAVIOR

A Dissertation
Presented to
The Academic Faculty

by

Prashant K. Jain

In Partial Fulfillment
of the Requirements for the Degree
Doctor of Philosophy in the
School of Chemistry and Biochemistry

Georgia Institute of Technology
April 2008

# PLASMONS IN ASSEMBLED METAL NANOSTRUCTURES:

# RADIATIVE AND NONRADIATIVE PROPERTIES, NEAR-FIELD

# COUPLING AND ITS UNIVERSAL SCALING BEHAVIOR

Approved by:

Dr. Mostafa A. El-Sayed, Advisor
School of Chemistry and Biochemistry
*Georgia Institute of Technology*

Dr. L. Andrew Lyon
School of Chemistry and Biochemistry
*Georgia Institute of Technology*

Dr. C. David Sherrill
School of Chemistry and Biochemistry
*Georgia Institute of Technology*

Dr. Robert Whetten
School of Chemistry and Biochemistry
*Georgia Institute of Technology*

Dr. Zhong Lin Wang
School of Materials Science and
Engineering
*Georgia Institute of Technology*

Date Approved:  January 04, 2008

Dedicated to my parents and to Prof. M. A. El-Sayed, on his 75<sup>th</sup> birthday

# ACKNOWLEDGEMENTS

# TABLE OF CONTENTS

# LIST OF TABLES

# LIST OF FIGURES

solution and the gold nanoparticle colloid at the pump wavelength 400 nm, were adjusted to be similar to ensure that both samples reach a similar hot electron temperatures by optical pumping at 90 nJ/pulse, allowing direct comparison of the electron relaxation dynamics. Plot of (b) measured hot electron lifetimes $\tau_d$ (ps) and (c) calculated electron-phonon coupling constants G $(Wm^{-3}K^{-1})/10^{16}$, against varying degree of aggregation, as characterized by the probe wavelength (nm). The vertical error bars in b indicate the standard deviation of the time constant's exponential fit. The black curves in b and c are guides for the eye.

# LIST OF ABBREVIATIONS

| | |
|---|---|
| 1-D | one-dimensional |
| 2-D | two-dimensional |
| 3-D | three-dimensional |
| a.u. | arbitrary units |
| AR | aspect ratio |
| av | average |
| BDAC | benzyldimethylammonioum chloride hydrate |
| CTAB | cetyl trimethyl ammonium bromide |
| cw | continuous wave |
| DDA | discrete dipole approximation |
| DNA | deoxyribonucleic acid |
| ds-DNA | double stranded DNA |
| EBL | Electron-beam lithography |
| EGFR | epidermal growth factor receptor |
| EM | electromagnetic |
| EOPRD | electron oscillation-phonon resonance detuning |
| e-e | electron-electron |
| e-ph | electron-phonon |
| eq | equation |
| FRET | fluorescence resonance energy transfer |
| fs | femtosecond |

| | |
|---|---|
| fwhm | full-width-at-half-maximum |
| FWM | four-wave mixing |
| IgG | Immunoglobulin |
| LDR | lattice dispersion relation |
| LSPR | localized surface plasmon resonance |
| MW | molecular weight |
| NIR | near-infrared |
| ph-ph | phonon-phonon |
| PMMA | poly(methyl methacrylate) |
| PVP | poly(vinyl pyrrolidone) |
| ref | reference |
| RI | refractive index |
| RIU | refractive index unit |
| rpm | rotations per minute |
| SAM | self-assembled monolayer |
| SEM | scanning electron microscopy |
| SERS | surface-enhanced Raman scattering |
| SPR | surface plasmon resonance |
| ss-DNA | single stranded DNA |
| STM | scanning tunneling microscopy |
| TEM | transmission electron microscopy |
| TPA | two-photon absorption |
| TTM | two-temperature model |
| UV | ultraviolet |
| UV-vis | ultraviolet-visible |

# LIST OF SYMBOLS

| | |
|---|---|
| V | volume |
| $r_{eff}$ | Effective radius |
| $Q_{abs}$ | Absorption efficiency |
| $Q_{sca}$ | Scattering efficiency |
| $Q_{ext}$ | Extinction efficiency |
| $C_{abs}$ | Absorption cross-section |
| $C_{sca}$ | Scattering cross-section |
| $C_{ext}$ | Extinction cross-section |
| $n_m$ | medium refractive index |
| $\varepsilon_m$ | medium dielectric constant |
| $\varepsilon_o$ | permittivity of free space |
| $\varepsilon_r$ | real part of the metal dielectric function |
| $\varepsilon_i$ | imaginary part of the metal dielectric function |
| $\varepsilon_\infty$ | high frequency part of metal dielectric function due to interband and core transitions |
| $\kappa$ | shape factor |
| $\lambda$ | wavelength |
| $\lambda_{max}$ | wavelength maximum |
| $\lambda_{sp}$ | surface plasmon resonance wavelength maximum |
| $\lambda_p$ | bulk plasma wavelength |
| $\alpha$ | polarizability |
| $\mu$ | dipole moment |
| $l$ | angular momentum quantum number |
| U | Interaction energy |

| | |
|---|---|
| $\eta$ | efficiency |
| $\omega$ | frequency |
| $\rho$ | density |
| $G$ | electron-phonon coupling constant |
| $m_e$ | effective mass of electron |
| $v_f$ | Fermi velocity |
| $\varphi_f$ | work function |
| $N_A$ | Avogadro number |
| $e$ | electronic charge |
| $c$ | speed of light |
| $E_d$ | Energy of activation for dissociation process |
| $\Delta H_d$ | Enthalpy change of dissociation process |
| $\Delta S_d$ | Entropy change of dissociation process |
| $c_e$ | electronic heat capacity |
| $k_b$ | Boltzmann constant |
| $T_e$ | hot electron temperature |
| $T_l$ | lattice temperature |
| $\tau_d$ | hot electron lifetime |

# SUMMARY

Noble metal particles possess unique optical attributes due to their plasmon resonance, which is the collective coherent oscillation of the nanoparticle free electrons (with respect to the positive metallic background) in resonance with an electromagnetic wave. The plasmon oscillation could be considered essentially as a photon strongly confined to the nanoscale size of the metal particle. The plasmon resonance results in a large enhancement of the electromagnetic field around the nanoparticle, resulting in strong light absorption and scattering by the nanoparticle at the plasmon resonance frequency, which has found uses in several optical and medical applications. While past research has established the effect of the nanoparticle size, shape, composition, and environment on the plasmon resonance frequency and the plasmonic enhancement, this thesis describes how inter-particle interactions influence the optical radiative and non-radiative properties of assembled plasmonic nanostructures. We have aimed to develop a systematic fundamental understanding of the interactions between plasmonic nanoparticles, especially their electromagnetic coupling, and how these can be used to tune the plasmon resonance frequency and its enhancement. These investigations employed experimental optical spectroscopy of colloidal metal nanosphere and nanorod assemblies and lithographic nanoparticle arrays, in conjunction with electrodynamic studies using Mie theory for spherical shapes, the discrete-dipole approximation method for nanostructures of other geometries, and quasistatic dipolar models. Electron dynamics in assembled gold nanostructures has also been studied using ultrafast pump-probe transient absorption spectroscopy.

When metal nanospheres assemble, the plasmon oscillations or fields of neighboring particles couple favorably with each other, because of which the surface plasmon oscillation frequency red-shifts. We have studied the plasmon coupling between colloidal gold nanorods, giving us insight into the role of particle shape and inter-particle orientation in determining the nature of the near-field coupling. The colloidal assembly of gold nanorods along their sides results in a blue-shift of the long-axis plasmon resonance mode, which is in contrast to the red-shift resulting from their end-to-end assembly. These results supported by electrodynamic simulations show us that plasmon coupling can be of "bonding" or "anti-bonding" type depending on the relative orientation of the interacting plasmon oscillations. Plasmons, which are polarized along the inter-particle axis, favorably bond with each other (red-shift), enhancing the field at the inter-particle junction. On the other hand, when the polarization is perpendicular to the inter-particle axis, an anti-bonding interaction (blue-shift) results.

The distance dependence of the plasmon coupling is elucidated by the plasmon resonance spectra of nanodisc pairs fabricated (by Wenyu Huang, another group member) with systematically varying inter-particle separations using electron-beam lithography. With decreasing inter-particle separation, the plasmon resonance red-shifts near-exponentially, as observed previously. These results along with detailed electrodynamic simulations show us also that the plasmon coupling strength, as reflected by the fractional plasmon shift, decays near-exponentially over a separation, which is roughly 0.2 in units of the particle size universally independent of the nanoparticle size, shape, the metal type, or the medium. This origin of this universal scaling behavior is fundamentally related to the strength of the inter-particle interaction relative to the single particle polarizability.

Using this universal scaling model, we obtain a simulated "plasmon ruler equation" that is able to calculate the inter-particle separation between two interacting gold nanospheres from their observed plasmon shift, as tested by the agreement of our calculated separations with experimentally known values for particle pairs assembled by DNA linkers of varying number of base pairs. The plasmon ruler equation is potentially useful for determining inter-site distances in biological systems using Alivisatos and Liphardt's strategy based on metal nanoparticle pairs. The universal scaling model also shows that the distance range of the particle-pair plasmon ruler can be directly increased by increasing the nanoparticle size, a conceptual advantage over the short-distance range of inter-molecular interactions.

Electrodynamic simulations show that the universal size scaling of plasmon coupling also applies in the case of complex nanostructure geometries. For example, in pairs of elongated nanoparticles assembled head-to-tail, the plasmon coupling decays with the same universal behavior when the long-axis dimension (which is the dimension in the direction of coupling) is used to scale the inter-particle separation. An increase in the nanoparticle aspect ratio and/or curvature results in an increase in the coupling-induced plasmon shifts, without affecting the universal size-scaling behavior. The universal size-scaling also applies to a trimer of nanospheres, which is a first step in extending this model to chains/ arrays/assemblies with multiple particles.

The universal size scaling is found also to apply in the metal nanoshell structure, as seen from Mie theory simulations. The nanoshell resonance red-shifts exponentially with decreasing metal shell thickness in units of the core size, with a universal trend independent of nanoshell size, type of metal, core dielectric, or surrounding medium.

Thus, we show a simple analogy between the particle-pair and the metal nanoshell, in which case the net plasmon resonance is a result of coupling between plasmons on the inner and outer shell surfaces, consistent with the model of Prodan, Halas and Nordlander. The universal scaling model also incorporates in a simple manner the dependence of the nanoshell plasmon resonance frequency on both the shell thickness and the total size, making it useful in the tuning of nanoshell resonances for nano-optical and nanomedicinal applications.

The increase in plasmon coupling strength also results in the enhancement of the sensitivity of the plasmon resonance to the environment, useful for refractive index-sensing of chemical and biomolecular analytes. This is observed in the metal nanoshell, where a decrease in the shell thickness relative to the core size results in an exponential increase in the plasmon sensitivity, also in accordance with the universal scaling law. This gives us a physical basis for plasmon sensitivity, which states that nanostructures, in which electrons can be polarized by light to the metal-medium interface with great ease, provide enhanced medium sensitivity. These include nanostructures with high aspect ratio, sharp curvatures/tips, or narrow inter-particle junctions.

The coupling between gold nanoparticles in colloidal aggregates also has an effect on the non-radiative hot electron relaxation rate. While the heterogeneous aggregate solution has a broad plasmon absorption band due to contributions from assemblies with different inter-particle spacings or number of particles, an optical probe of a specific wavelength selectively interrogates only those aggregate subsets that absorb at the probe wavelength. As we move to longer wavelengths, we probe aggregates with progressively stronger coupling, observing an increase in the electron relaxation rate. These results

suggest the importance of inter-colloid electronic coupling and interfacial electronic scattering in nanoparticle assemblies.

Study of the non-radiative electron cooling dynamics in gold nanoparticles conjugated to self-assembled monolayers of thiolated DNA shows that the energy of the photoexcited electrons can channel on the electron-phonon relaxation time scale into the surface-thiol bonds resulting in their surface desorption.

We also provide a detailed study of the calculated absorption and scattering cross-sections of important nanostructures: gold nanospheres, gold nanorods, and silica-gold nanoshells. We see that in all three nanostructures, the relative contribution of the scattering (radiative) to the absorption (non-radiative) part of the plasmon relaxation can be increased by increasing the nanostructure size. This is potentially important for the design of nanostructures complementarily for imaging or photothermal applications.

The studies described in this work provide fundamental guidelines (e.g., polarization "selection rules" and universal scaling model of plasmon coupling, physical basis of plasmon sensitivity, size tunability of scattering-to-absorption) that will potentially be useful to other researchers in designing assembled noble metal nanostructures optimized for applications in nanophotonic devices, biological imaging and sensing, surface-enhanced Raman scattering, single-molecule enhancement, and nanoscale distance measurement.

# CHAPTER 1

# INTRODUCTION

Noble metal nanoparticles have attracted interest since historical times due to their bright intense colors that are distinct from metallic luster at the bulk scale and unique to the small size of the particles.[1,2] The decorative pigments in some historical artworks like the Roman Lycurgus cup[1] from the IV century and Renaissance pottery (e.g. plate from Gubbio, Italy) from the XVI century, are now known to be composed of nanosized particles of gold, silver, and copper and their alloys.[3] Due to the work of Faraday[4] among others, who was the first to point out that the colors originated from colloidal metallic particles, the interest in noble metals has evolved from artistic and empirical to scientific and technological. In this chapter, we introduce the status of scientific understanding of the optical radiative and non-radiative properties of noble metals nanostructures and their nanotechnological applications. We place especial emphasis on the tunability of the properties by change in the size, shape, composition, and environment of the nanostructure. This is followed by an overview of the recent research on inter-particle coupling in noble metal nanostructures, which has been realized as another unique way to tune the properties, thus setting the motivation for the work described in this thesis.

## 1.1 Radiative Properties of Noble Metal Nanoparticles

### 1.1.1 Plasmon Resonance in Noble Metal Nanoparticles

The size, shape, composition, and environment dependent optical properties of noble metal nanoparticles are due to their unique interaction with light.[2,5-9] This interaction can be understood from the work of Gustav Mie, who solved Maxwell's electrodynamic equations for a homogeneous sphere in 1908.[10] The solution consisted of electromagnetic waves on the surface of the sphere of different orders ranging from the lowest dipolar to higher order multipoles, depending on the size of the nanoparticle relative to the wavelength of light. In the case of particles of size much smaller than the wavelength of light, (i.e. radius $r \ll \lambda$), only the dipole mode contributes considerably to the light-nanoparticle interaction.[5,8]

For a nanoparticle in the size range of few tens of nm, it is sufficient to consider only the dipolar mode of interaction (dipole approximation) and to assume that the electric field of light is constant (quasistatic approximation).[8] In the dipolar quasistatic limit, the polarizability of a spherical particle of volume V is given by the Clausius-Mossotti relation:[8,11]

$$\alpha = 3\varepsilon_0 V \left( \frac{\varepsilon - \varepsilon_m}{\varepsilon + 2\varepsilon_m} \right) \quad (1)$$

where $\varepsilon_0$ is the permittivity of vacuum and $\varepsilon_m$ is the dielectric constant of the surrounding medium. $\varepsilon$ is the dielectric function of the metal which is complex and frequency-dependent, expressed as $\varepsilon(\omega) = \varepsilon_r(\omega) + i\varepsilon_i(\omega)$, where $\varepsilon_r$ is the real part of the dielectric function and $\varepsilon_i$ is the imaginary part.

From eq 1, we see that the polarizability has a strong maximum when the following relation is satisfied.

$$\varepsilon_r = -2\varepsilon_m \qquad (2)$$

It is assumed here that $\varepsilon_i$ is small and/or weakly dependent on frequency.[7,12] For eq 2 to be satisified, it is required that the real part $\varepsilon_r$ be negative, which is possible for some metals at optical frequencies. At the light frequency $\omega_{sp}$ where the condition in eq 2 is satisfied, the metal nanoparticle interacts very strongly with the light, resulting in the collective coherent oscillation of the conduction electrons (with respect to the positive metallic lattice) in resonance with the electromagnetic field of the light. This oscillation is known as the surface plasmon resonance (SPR). The surface plasmon resonance occurs in the visible frequency region for the noble metal (gold, silver, and copper)[1,2] nanoparticles, making them optically interesting metals.

Because of the plasmon resonance, the electromagnetic fields are strongly enhanced around the nanoparticle. We could consider the nanoparticle to be essentially a nanosized lens, and the plasmon oscillation to be a photon confined very strongly to the nanoscale size of the particle. Conventionally, the confinement of light to a size smaller than its wavelength is not allowed due to the diffraction limit, however the plasmon resonance gives the opportunity to confine the electromagnetic field of the light to a nanosized volume. The potential for achieving interesting optical effects using these strongly confined photons is tremendous, the most important being the large enhancement of light scattering and absorption cross-sections of the nanoparticle (see Figure 1.1).[8,13]
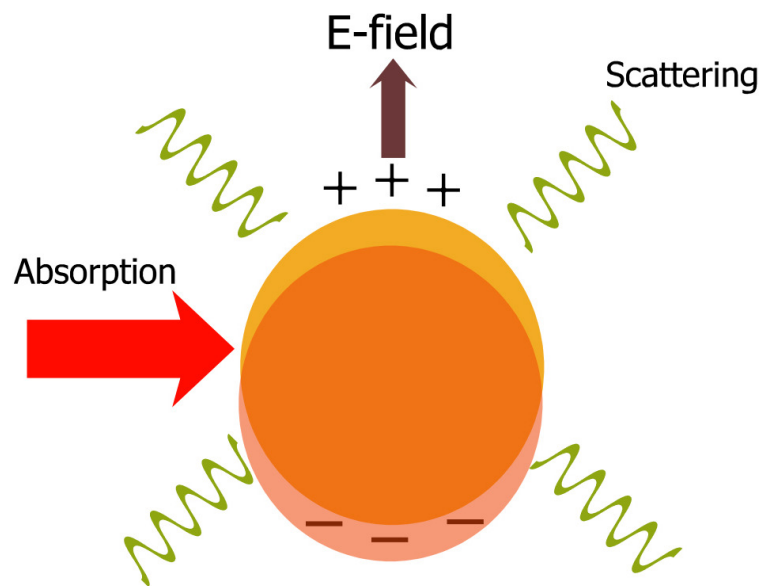
Figure 1.1: Surface plasmon resonance oscillation of electrons of a noble metal nanoparticle, resulting in the strong enhancement of the electric field, and the light scattering and absorption cross-sections.

Scattering of light results from the plasmon oscillations decaying by radiating their energy.[14] On the other hand, the oscillating electrons suffer collisions with other electrons resulting in the excitation of inter-band and intra-band excitations in the metal. Additional damping and dephasing processes include collisions with the lattice phonons, the nanoparticle surface, defects, and surface ligands.[2] These non-radiative pathways result in the generation of heat, and constitute light absorption by the particle.[2] Absorption and scattering together constitute the light extinction of the particle. The scattering and absorption processes are strongly enhanced at the surface plasmon resonance frequency. For instance, colloidal gold nanoparticles in the 10-nm size range have a strong UV-vis extinction band around 520 nm due to the plasmon resonance.[12]

The extinction and scattering cross-sections, $C_{ext}$ and $C_{sca}$ are given in the terms of the dipolar polarizability as:[8]

$$C_{ext} = k \, \text{Im}(\alpha) \quad (3)$$

$$C_{sca} = \frac{k^4}{6\pi} |\alpha|^2 \quad (4)$$

where Im denotes the imaginary part and k is the wave vector:

$$k = \frac{2\pi \varepsilon_m^{1/2}}{\lambda} \quad (5)$$

For very small particles, r $<<$ $\lambda$, the scattering cross-section is negligible and the extinction cross-section, mainly dominated by absorption is given as:[5,6,9]

$$C_{ext} = \frac{24\pi^2 r^3 \varepsilon_m^{3/2}}{\lambda} \frac{\varepsilon_i}{(\varepsilon_r + 2\varepsilon_m)^2 + \varepsilon_i^2} \quad (6)$$

**1.1.2 Tunability of the Surface Plasmon Resonance Properties**

The unique property of the surface plasmon resonance is its dependence on the metal (i.e. composition),[6] the nanoparticle size,[8,12] shape/geometry,[15-17] and the medium or environment.[18,19] Variation in these parameters allows tunability of both the plasmon resonance frequency (the color) as well as the strength of the plasmonic enhancement (the intensity).

1.1.2.1 Dependence on the Metal

Eq 1 incorporates the dependence of the surface plasmon resonance on the dielectric function of the metal, a measurable bulk quantity. This approach is much simpler than using the electronic structure of the metal to model the surface plasmon

resonance.[8] The real part of the dielectric function determines the frequency/wavelength position of the surface plasmon resonance as per eq 2. If we assume a free electron behavior for the metal (i.e., the conduction electrons can move freely independent from the ionic background and the ions only act as scattering centers)[2], the real part is given as a function of the frequency by the Drude model:[5]

$$\varepsilon_r = 1 - \frac{\omega_p^2}{\omega^2 + \gamma^2} \qquad (7)$$

where $\omega_p$ is the frequency of bulk plasma oscillations in the metal and $\gamma$ is the electron collision frequency. Since $\gamma \ll \omega$, eq 7 becomes simpler

$$\varepsilon_r = 1 - \frac{\omega_p^2}{\omega^2} \qquad (8)$$

We see that $\varepsilon_r$ becomes more negative with decreasing frequency $\omega$. The bulk plasma frequency $\omega_p$ is expressed in terms of the free electron density N of the metal, the electron charge e, and effective mass of the electron $m_e$:[12,20]

$$\omega_p = \sqrt{\frac{Ne^2}{\varepsilon_0 m_e}} \qquad (9)$$

Gold and silver have similar bulk plasma frequencies (in the UV) due to their similar electronic densities, i.e. $N = 5.90 \times 10^{22}$ and $5.86 \times 10^{22}$ /cm$^3$ respectively.[20] However, the surface plasmon absorption band for a silver nanoparticle colloid is around 390 nm as compared to 520 nm for gold.[21] This difference is because real metals have considerable deviations from free electron behavior, except at low frequencies. There is a significant effect of core electrons (relativistic effects), inter-band and intra-band transitions on the electronic properties of the metal.[22] To include these effects, a high frequency part of the

dielectric function $\varepsilon_\infty$ that depends on the metal electronic structure (e.g. response of 5d electrons)[22] is added such that:

$$\varepsilon_r = \varepsilon_\infty - \frac{\omega_p^2}{\omega^2} \qquad (10)$$

The bulk dielectric function for gold gives a value of 11 for $\varepsilon_\infty$. Combining eq 9 and eq 10 and the plasmon resonance condition eq 2, we get the surface plasmon resonance frequency:

$$\omega_{sp} = \sqrt{\frac{Ne^2}{m_e \varepsilon_0 (\varepsilon_\infty + 2\varepsilon_m)}} \qquad (11)$$

While the real part of the dielectric function determines the frequency position of the plasmon resonance as seen above, the imaginary part incorporates the plasmon dephasing and damping processes that determine the absorption contribution and homogeneous linewidth (broadening) of the plasmon resonance band.[22]

$$\varepsilon_i \approx \frac{\gamma \omega_p^2}{\omega^3} \qquad (12)$$

The collision frequency, $\gamma$, also known as the damping constant, is closely related to the resistivity of the metal and it incorporates collisions of electron-electron, electron-phonon, and electron-defect type.[12] $\gamma$ is thus expressed as a sum of the relaxation rates for each of these processes:[12]

$$\gamma = \frac{1}{\tau_{e-e}} + \frac{1}{\tau_{e-ph}} + \frac{1}{\tau_{e-d}} \qquad (13)$$

For nanoparticles much smaller compared to the electronic mean free path of the metal (ca. 40 nm for gold), scattering of the electrons with the nanoparticle surface/boundaries also becomes important.[12] Therefore, an additional term $Av_f/r$ for electron-surface scattering is added to the bulk damping frequency, where $v_f$ is the Fermi velocity of the electrons and A incorporates the nature of the surface scattering processes (0 for elastic, ¾ for diffusive, and 1 for isotropic).[22] Because of this surface correction, particles smaller than 10 nm have a resonance that is significantly broadened in inverse proportion to the nanoparticle size r.[12] Note that for much smaller particles (< 2-3 nm), quantum size effects become important, for which the above treatment is no longer valid.[22]

The linewidth of the metal nanoparticle plasmon resonance is given by: [20]

$$\Delta\omega_{1/2} \approx \frac{2\varepsilon_i\big|_{sp}}{(d\varepsilon_r/d\omega)\big|_{sp}} \tag{14}$$

where $|_{sp}$ indicates values at the surface plasmon maximum condition. Eq 14 indicates that a smaller imaginary dielectric function of the metal and a steeper gradient of the real part with frequency would give a narrower bandwidth.[20] While the slope of $\varepsilon_r$ with respect to $\omega$ is similar for both silver and gold, silver has a much lower $\varepsilon_i$ as compared to gold, because of which it possesses a narrower plasmon linewidth as well as a higher scattering-to-absorption ratio.[20] The imaginary part of the dielectric function thus represents a metal-dependent "loss factor". The effect of the real part and imaginary part of the dielectric function on the plasmon resonance can be combined together in the concept of "plasmonic quality" which is specified by the energy position of the plasmon resonance divided by its linewidth. Silver has a much higher plasmon quality as compared to gold, due to which much stronger plasmon fields are produced in silver.[23]

The plasmonic fields are relatively damped in gold nanoparticles due to the proximity of the plasmon resonance energy to the inter-band absorption edge.

However, from the practical standpoint gold is much more resistant to oxidation as compared to silver which makes it the metal of choice in many cases. Copper is rarely used due to its high susceptibility to oxygen.

1.1.2.2 Dependence on the Nanoparticle Size

As the nanoparticle size is increased, the number of electrons increases in direct proportion to the volume, because of which the extinction of the particle increases with volume as per eq 6. While this is strictly valid in the dipolar limit, as the size of the nanoparticle approaches the wavelength of light, an additional effect is observed. The nanoparticle can no longer be homogeneously polarized by the light, resulting in the excitation of higher-order oscillation modes.[8] Higher-order oscillations have a resonance at progressively higher resonance frequencies, i.e. lower wavelengths. The general resonance condition for a mode of order l is given as:[8]

$$\varepsilon_r = -\left(\frac{l+1}{l}\right)\varepsilon_m \qquad (15)$$

For the dipolar mode l=1, eq 15 is same as eq 2. Higher-order modes significantly broaden the plasmon resonance due to a reduction in the phase coherence.[12] In addition, as the particle size increases, there is increased radiative damping, i.e. emission of radiation by the plasmon oscillations, which results in an increase in the scattering contribution, but also reduces the plasmon lifetime (increased plasmon linewidth).[8] Another effect comes from electromagnetic retardation which results from the depolarization of the light field across the particle surface resulting in both the red-shift

and broadening of the plasmon resonance band.[12] This can be seen in Figure 1.2, which shows UV-vis extinction spectra of gold nanoparticle colloids synthesized with different size ranging from 9 to 99 nm.[12]

Experimentally, since the plasmon resonance depends on the particle size due to these factors, the plasmon band is also inhomogeneously broadened due to the size dispersion of the colloidal nanoparticles. Gold nanoparticles have an advantage in this regard due to their easy synthesis using the sodium citrate reduction technique[12,24] with good size control in the 10-60 nm range and low size dispersion. However, it must be noted that the size tunability possible due to the retardation-induced red-shift of the nanosphere plasmon resonance is very limited.[13]
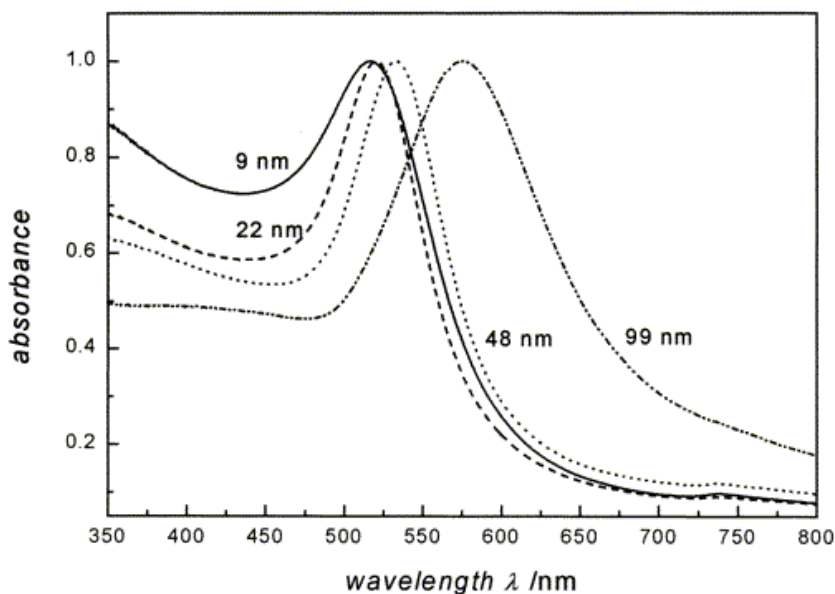


Figure 1.2: UV-vis extinction spectra of Au nanospheres of different size ranging from 9-99 nm. (Reprinted with permission from S. Link, M. A. El-Sayed, *J. Phys. Chem. B* **1999**, *103*, 4212. Copyright 1999 American Chemical Society)[12]

1.1.2.3 Dependence on the Nanoparticle Shape or Geometry

The surface plasmon oscillation essentially involves a displacement of the conduction electron cloud with respect to the positive metallic lattice by the light field. The cationic lattice applies a restoring force in response to this polarization, the magnitude of which depends on the shape of the electron cloud[8] and the polarization of the light. For a shape with a sharper surface curvature (e.g. nanotriangles or nanorods) along the light polarization direction as compared to a sphere, the Coulombic restoring force on the electron cloud is weaker. This results in a lower resonance frequency. Quantitatively, for any general shape the polarizability is given as:[5]

$$\alpha = \frac{\varepsilon_0 V}{L}\left( \frac{\varepsilon - \varepsilon_m}{\varepsilon + \left(\frac{1-L}{L}\right)\varepsilon_m} \right) \quad (16)$$

L is a depolarization factor, which depends on the shape. For a sphere, which is isotropic in all three dimensions, L=1/3, which reduces eq 16 to eq 1.[5] The plasmon resonance condition from eq 16 is given as:[5]

$$\varepsilon_r = -\left(\frac{1-L}{L}\right)\varepsilon_m \quad (17)$$

This condition summarizes the effect of the nanoparticle shape (through L) on the surface plasmon resonance frequency.

*1.1.2.3.1 Metal Nanorods*

As per the theory developed by Gans,[25] spheroidal particles have three values for L corresponding to each of the three axes A, B, C. Since A > B = C for the spheroid, there are two unique modes of electron oscillation giving rise to two SPR modes.[16] The

short-wavelength SPR mode is due to electron oscillation along the spheroid short-axis, corresponding to $L_{B=C}$. The second mode arises from electron oscillation along the spheroid long-axis, corresponding to $L_A$. The values of the depolarization factors depend on the spheroid aspect ratio R as follows: [16]

$$L_A = \frac{1-e^2}{e^2}\left(\frac{1}{2e}\ln\frac{1+e}{1-e}-1\right) \qquad (18)$$

$$L_{B=C} = \left(\frac{1-L_A}{2}\right) \qquad (19)$$

where $\qquad e = \sqrt{1-(1/R)^2} \qquad (20)$

$L_A$ decreases sharply with the aspect ratio R, because of which the long-axis SPR is a strong function of the aspect ratio. For Au, the negative real part of the dielectric function $\varepsilon_r$ increases with increasing wavelength almost linearly in the 500-800 nm range.[16] Thus, the long-axis SPR wavelength maximum red-shifts linearly with increasing aspect ratio, while the short-axis mode is only weakly dependent on the particle aspect ratio.[16] In other words, the increase in the spheroid aspect ratio (i.e. curvature) can be visualized to result in a reduction of the restoring force (in correlation with the reduction in the depolarization factor L) for the long-axis plasmon mode, thus lowering its resonance frequency. Link et al. used Gans model of spheroidal particles and simulated the shape tunability of the long-axis SPR of gold nanorods, which is depicted in Figure 1.3.[16]

Lee et al. showed through electrodynamic simulations (Figure 1.4)[26] that the end-cap shape of elongated nanoparticles also has an effect on the long-axis plasmon resonance position. A hemisphere-end capped rod has a longer plasmon resonance
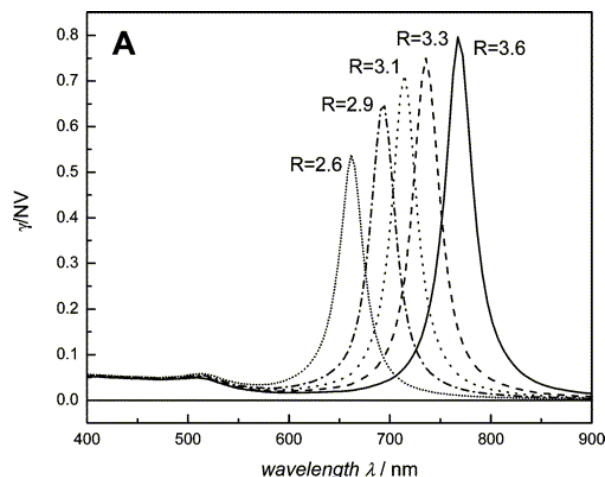
Figure 1.3: Simulated spectra of the long-axis SPR mode for gold nanorods of different aspect ratio, showing the shape tunability of the optical resonance in the visible-near-infrared region. (Reprinted with permission from S. Link, M. A. El-Sayed, *J. Phys. Chem. B* **2005**, *109*, 10531. Copyright 2005 American Chemical Society)[16]

wavelength maximum as compared to a spheroid, which can be attributed to the steeper end-curvature of the former. This effect is more pronounced at a higher aspect ratio. Similarly, triangular nanoprisms are known to have plasmon resonances, which are sensitive to the thickness of the prism, the edge length, and the nipping of the tips.[27]

The reduction in the value of L can also be seen from eq 16 to increase the dipolar polarizability. This gives a means to optimize the plasmonic enhancement without changing the size (i.e. the number of electrons) in the nanostructure. For example, the long-axis surface plasmon absorption of the nanorod has a much higher intensity as compared to the short-axis mode, increasing with increasing aspect ratio (Figure 1.3).[16,27] Similarly, nanoprisms and nanorods, due to their sharp tips support strong plasmon near-fields, calculated to be as high as ($|E|^2$ times the applied field intensity) 4500 for silver nanorods of aspect ratio 2.8 and 3500 for silver nanoprisms, compared to a value of 200

for a 20-nm silver nanosphere.[27] The field is much lower i.e. 25 for a 90 nm nanosphere, due to radiative damping effects.[27]
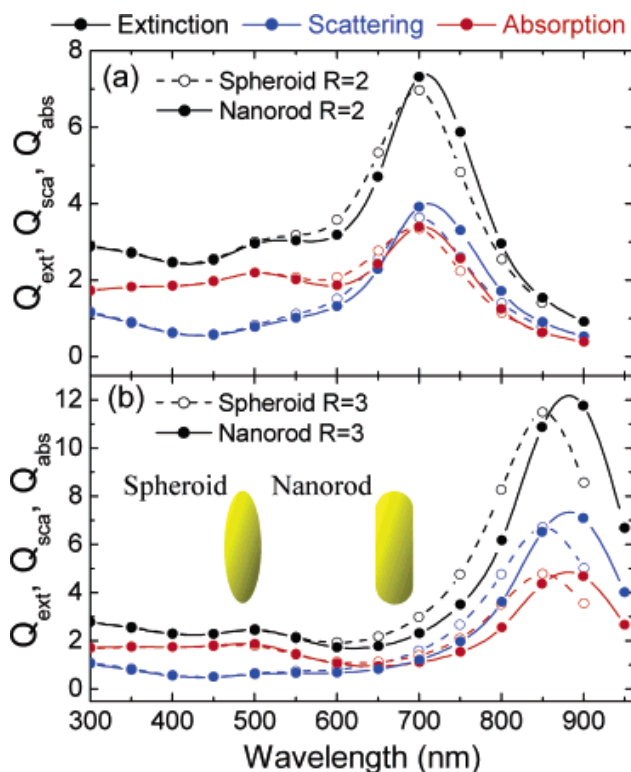


Figure 1.4: Simulated long-axis plasmon resonance extinction, scattering and absorption bands for a gold nanoparticle of spheroidal shape compared to a nanoparticle with a hemisphere end-capped rod shape, for two different aspect ratios (a) 2 and (b) 3. Note that the same volume is used for both shapes. (Reprinted with permission from K.-S. Lee, M. A. El-Sayed, *J. Phys. Chem. B* **2005**, *109*, 20331. Copyright 2005 American Chemical Society)[26]

*1.1.2.3.2. Metal Nanoshells*

Another interesting shape tunability is observed in a composite nanoparticle consisting of a dielectric (typically silica) core surrounded by a thin gold shell, developed by the Halas and Nordlander groups.[17] The thin gold shell supports two plasmons: one on the inner shell surface and another on the outer surface. As per the model of Prodan,

14

Halas and Nordlander,[28] these two modes hybridize to give a higher-energy anti-bonding mode and a lower-energy bonding mode. The resonance frequency of the low-energy plasmon resonance band can be red-shifted from the visible region up to a wavelength of 10 μm simply by decreasing the thickness of the metal shell relative to the core diameter.[17]

*1.1.2.3.3. Synthetic Tunability*

The geometric tunability of the plasmon resonance in gold nanorods and nanoshells is of great utility.[29-33] For example, *in vivo* biological/medical applications require nanoparticles that absorb or scatter in the near-infrared (NIR) region of the biological window (650-900 nm) where tissue, water and blood have the highest light transmissivity.[34] In other applications, it may be desirable to tune the plasmon resonance band according to the availability of a laser of a given wavelength or the need to enhance an optical process of a specific resonance frequency. Gold nanorods of controlled aspect ratio in the change of 2-7 can be readily made by the seeded-growth method developed by the Murphy group[35,36] and further improved by Nikoobakht and El-Sayed (see Figure 1.5).[37] The aspect ratio can be chosen according to the plasmon resonance wavelength maximum desired.

There are two synthetic methods for realizing the tunable metal nanoshell structure. One involves the growth of a thin metal shell around silica nanoparticles pre-synthesized with good size control.[17] In this method, the shell thickness can be adjusted synthetically to obtain the desired resonance frequency. Another method involves the synthesis of hollow gold nanocages and nanocubes by the galvanic replacement of silver nanoparticles with gold from a chloroauric acid source.[38] The metal wall thickness and

void size can be synthetically controlled in this method, in order to obtain the desired plasmon resonance wavelength.
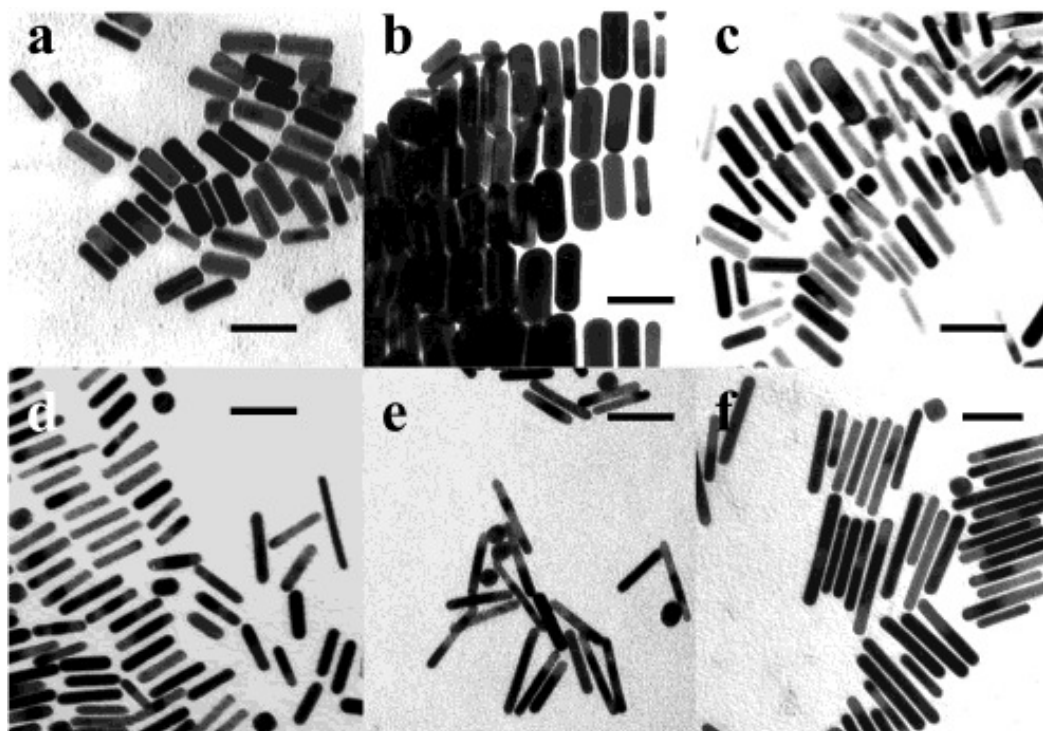


Figure 1.5: Gold nanorods of different aspect ratio synthesized by the seeded-growth method adapted by Nikoobakht and El-Sayed. TEM images (scale bar = 50 nm) show gold nanorods with long-axis plasmon absorption maximum at (a) 700, (b) 760, (c) 790, (d) 880, (e) 1130, and (f) 1250 nm. (Reprinted with permission from B. Nikoobakht, M. A. El-Sayed, *Chem. Mater.* **2003**, *15*, 1957. Copyright 2003 American Chemical Society)[38]

Triangular nanoprisms, which are highly polarizable and tunable plasmonic structures, are made by the nanosphere lithography (NSL) technique perfected by the Van Duyne group, which employs a mask consisting of close packed self-assembled monolayer of polystyrene microspheres.[39] This technique has been utilized and adapted in our group as well.[40-43]

1.1.2.4 Dependence on the Medium or Environment

The plasmon resonance frequency is highly sensitive to the dielectric properties of the medium surrounding the nanoparticle.[19] As seen from eq 2, an increase in the medium dielectric constant $\varepsilon_m$ (or refractive index $n_m = \varepsilon_m^{1/2}$) results in an increase in the negative value of $\varepsilon_r$ required to satisfy the plasmon resonance condition, thus resulting in a red-shift of the plasmon resonance wavelength position. In other words, it can be said that the increase in the medium dielectric constant results in a lowering of the Coulombic restoring force on the displaced electron cloud thus lowering the plasmon oscillation frequency. The plasmon resonance frequency is thus sensitive to any refractive index change in the local medium around the nanoparticles, including the solvent or the presence of adsorbates or surface-capping molecules.[18,19,44]

Since the increase in the medium refractive index also reduces the effective wavelength of light in the medium ($\lambda/n_m$), the size of the nanoparticle relative to the effective medium wavelength increases. This results in the increase in the electromagnetic retardation, damping and multipolar effects, and significant broadening of the plasmon resonance.

An additional effect involves the chemical interaction of the electrons with adsorbates and interfacial molecules resulting in a broadening of the plasmon resonance, also known as chemical interface damping.[45] In some cases, plasmon shifts are also observed due to the perturbation of the conduction electron density of the nanoparticle due to the adsorbate-metal interactions.[46]

**1.1.3 Applications of the Radiative Properties of Noble Metal Nanoparticles**

1.1.3.1. Light-Scattering Imaging

Due to the strongly enhanced SPR, noble metal nanoparticles scatter light very strongly at the SPR frequency.[47] A 40-nm gold nanoparticle offers a scattering cross-section that is five orders of magnitude larger than the emission from a typical dye molecule.[13] At the same time, metal nanoparticles are photostable, unlike dyes that photobleach.[47] Thus, gold nanoparticles have become very promising for optical imaging, especially biological imaging, since the small size of the nanoparticles makes it easy to incorporate them into biological systems,[48,49] while also allowing biological labeling with a high spatial resolution. Furthermore, metal nanoparticles can also be conjugated to specific targeting or recognition ligands (either small molecule or biomolecular),[50] thus giving the probing technique a molecular-specific resolution. This is highly advantageous from the point of view of molecular biology and biophysical studies.

The strongly enhanced scattering cross-sections of metal nanoparticles have been used for highly contrasted imaging using techniques such as optical coherence tomography[51] and laser reflectance confocal microscopy.[52] At the same time, the strong SPR scattering also allows for the use of the much simpler and inexpensive technique of dark-field microscopy. While most imaging techniques require sophisticated and expensive lasers, optical components and detectors, and complex image processing, dark-field imaging[14,53] using gold nanoparticles requires a simple optical microscope equipped with a dark field condenser (which ensures that the exciting light is incident at high angles such that only light scattered by the sample is collected by the microscope objective). The gold nanoparticles are excited by a broad white-light source, but only

18

light frequencies corresponding to the SPR are strongly scattered. The nanoparticles are seen as bright spots (with color corresponding to the SPR) on a dark background. In fact, due to the high scattering cross-section, individual nanoparticles can also be imaged. The dark-field microscopy technique can be utilized very effectively for the molecular-specific imaging of biomolecules by integrating the gold nanoparticles with specific targeting molecules. As an example, El-Sayed et al. diagnosed cancer (Figure 1.6) by using gold nanoparticle bioconjugates to image the cancer biomarker, epidermal growth factor receptor (EGFR), present in significantly higher amounts on cancer cells.[53]
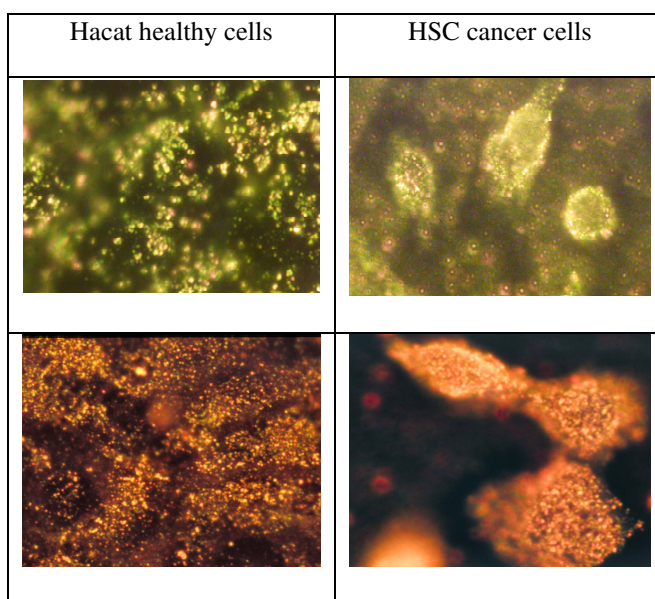


Figure 1.6: Molecular-specific imaging of cancer using gold nanoparticle/anti-EGFR conjugates. Dark-field microscopy shows (right) HSC cancer cells clearly defined by the strong SPR scattering from (top) gold nanospheres and (bottom) gold nanorods bound specifically to the cancer cells, whereas (left) HaCat healthy cells have the (top) gold nanospheres and (bottom) gold nanorods randomly dispersed without specific binding. The scattering color (SPR frequency) of the nanospheres and nanorods can be clearly distinguished. (Reprinted with permission from I. H. El-Sayed, X. Huang, M. A. El-Sayed, Nano Lett. **2005**, *5*, 829.[53] Copyright 2005 American Chemical Society and X. Huang, I. H. El-Sayed, W. Qian, M. A. El-Sayed, *J. Am. Chem. Soc.* **2006**, *128*, 2115.[32] Copyright 2006 American Chemical Society)

Gold nanospheres conjugated to anti-EGFR antibodies specifically target the cancer cells as shown by the dark-field imaging. The cancer cells showed strong Mie scattering from the gold nanoparticles bound specifically to the EGFR on the cancer cell surface. Thus, cancer cells could be easily identified from the healthy cells, in which case the gold nanoparticles were dispersed randomly due to non-specific binding. This imaging-based diagnostic approach is quite general since gold nanoparticles can be conjugated to a variety of proteins, antibodies, and small molecules.[50] The targeting ligands can be chosen depending on the disease biomarkers to be targeted.

1.1.3.2. Refractive Index Sensing

The dependence of the surface plasmon resonance frequency on the medium dielectric constant discussed earlier becomes very useful in the optical sensing of chemical and biomolecular analytes.[18,54-57] When the refractive index (dielectric constant) of the medium is increased, there is a linear red shift in the surface plasmon wavelength maximum position. By following this shift, it is possible to sense changes in the environment of the nanoparticle. For instance, the adsorption or binding of molecules to (or close to) the nanoparticle surface can cause a refractive index change and a shift in the plasmon band wavelength. There are however two fundamental requirements of such a plasmonic refractive index sensor:

In order to sense the presence of a particular chemical or biological species, only binding events specific to the target species should be allowed at the nanoparticle surface. This is achieved by the conjugation of the nanoparticle with recognition molecules, which specifically bind the target analyte.[18] The surface capping has to be designed to minimize non-specific binding. The refractive index change resulting from the binding of

the target molecules would depend on the number of molecules bound per particle, the molar mass of the molecules, their proximity to the nanoparticle surface, and the refractive index/dielectric properties of the molecules relative to the medium in which the nanoparticles are dispersed. However, the refractive index change resulting from the binding of a few molecules can be expected to very low. In order to have sensitivity down to few molecules binding per nanoparticle, the magnitude of the plasmon band shift resulting from a small refractive index change in the local medium should therefore be as high as possible.[20]

It is advantageous that the geometry of plasmonic nanostructures can be tuned to achieve enhanced plasmon sensitivity. For instance, Van Duyne and his group have explored the plasmon resonance sensing using silver nanotriangle monolayers fabricated by nanosphere lithography. The monodispersity of the particle monolayer gives very narrow plasmon bands, which aid in the plasmon resonance shift measurement. The monolayer of silver nanotriangles (with in-plane width of 100 nm and out-of-plane height of 50 nm) exhibits a sensitivity of 200 nm/refractive index unit (RIU) change in the solvent medium.[18] For alkanethiol monolayers self assembled on the nanotriangle monolayers, the plasmon band shows a shift of 3 nm for each methylene unit of the alkanethiol. Silver nanotriangle monolayers in the biotinylated form have been used to sense streptavidin molecules by specific biotin-streptavidin binding, down to pM concentrations. Similarly, the detection of Alzheimer's disease[55] has also been achieved using this strategy.

Colloidal gold nanorods constitute another nanostructure highly suited for plasmon sensing, as shown by electrodynamic simulations of Lee and El-Sayed.[20] As

discussed earlier, the change in shape from spherical to rod-shaped results in an additional longitudinal plasmon resonance, which has an enhanced optical polarizability as compared to the nanosphere resonance. The nanorod longitudinal plasmon resonance has considerably higher plasmon sensitivity as compared to the nanosphere resonance. As the nanorod aspect ratio is increased, the sensitivity increases with an almost quadratic dependence (Figure 1.7).[20] Mulvaney and coworkers showed that the long-axis of gold nanorods of aspect ratio 3 shifted almost 40 nm for a refractive index change of about 0.1 of the liquid medium, which is 6 times better than the nanosphere sensitivity.[33]
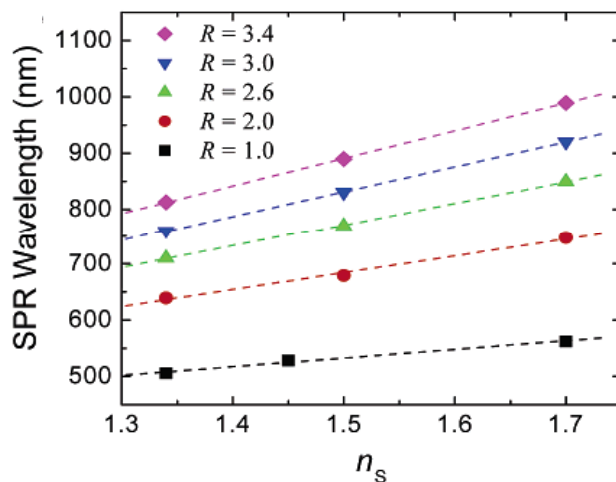


Figure 1.7: Shape tunability of the plasmonic sensitivity: By increasing the gold nanorod aspect ratio, sensitivity of the long-axis SPR to medium RI changes can be increased. (Reprinted with permission from K. S. Lee, M. A. El-Sayed, *J. Phys. Chem. B* **2006**, *110*, 19220. Copyright 2006 American Chemical Society)[20]

Yu and Irudayaraj utilized the high sensitivity of colloidal gold nanorods for effective biodetection by functionalizing the ends of the nanorods with Fab segments of

IgG molecules.[55] Anti-IgG molecules in colloidal solution could thus be recognized due to their specific binding to the functionalized gold nanorod probes and the resulting shift in the nanorod long-axis plasmon band. The shape tunability of the plasmon resonance also becomes useful for multiplexed sensing. Nanorods of significantly different aspect ratio, which exhibit well-separated longitudinal plasmon resonance maxima (or colors), can be used for simultaneous sensing of different molecules in the same solution. Yu and Irudayaraj employed a mixture of three different nanorod aspect ratios: 2.1, 4.5, and 6.3, each conjugated to a different IgG recognition unit in order to sense three different anti-IgG targets simultaneously.[55]

The metal nanoshell structure also offers highly enhanced sensitivity. The Xia group found that hollow gold metal nanoshells show 6 times higher plasmon sensitivity compared to a similar sized solid nanosphere.[56]

The plasmon shift can be simply followed by absorption spectrophotometry in the case of colloidal solutions.[55] In the case of nanoparticles deposited/fabricated on a substrate, scattering spectroscopy may be used to ensure low background noise.[57] In fact, plasmon resonance sensing has been performed on single particles by using the dark-field scattering technique, with the ability to detect zeptomolar concentrations of analytes.[57] For scattering measurements, it must be noted that silver is more suitable due to its higher scattering contribution to extinction as compared to gold for the same nanostructure size and shape.[20] This is due to the lower imaginary part of the dielectric function of silver as compared to gold. Silver also offers narrower plasmon bands compared to gold, which is an important requirement for the sensitive detection of plasmon band shifts from an experimental standpoint.[20]

1.1.3.3. Plasmon-Enhanced Raman Scattering Spectroscopy

The plasmon resonance results in a highly enhanced electric field localized on the metal nanostructure in the presence of light of frequency corresponding to the SPR. Such strongly confined near-fields have the ability to enhance spectroscopic signals from molecules in the vicinity of the nanostructure. The most common example is the plasmonic enhancement of Raman scattering.[58] Raman scattering spectroscopy can provide detailed information about molecular structure, thus offering molecular-specific signatures for chemical imaging. However, molecules typically have small Raman scattering cross-sections, resulting in weak signals. Therefore the enhancement of Raman cross-sections at the metal nanostructure surface (typically $10^5$-$10^6$ times), also known as surface enhanced Raman scattering (SERS), becomes extremely valuable.[58] While a part of this enhancement is attributed to changes in the chemical polarizability of the molecule due to interactions with the metal surface, a major part comes from the field enhancement. The electromagnetic part of the SERS enhancement is proportional to the square of the field intensity at the nanostructure,[58] and it shows an intense maximum at the plasmon resonance frequency. This plasmonic enhancement of the Raman scattering shows a strong tunability as a function of the size, shape, and composition of the nanostructure. The SERS enhancement offered by silver nanostructures is typically higher than gold due to the stronger plasmonic fields in silver.[59]

The most common example of shape tunability is the SERS observed on gold nanorods.[60] The sharper curvature of the nanorods as compared to spheres gives much stronger plasmon fields (also known as the "lightning rod effect) and hence intense SERS at the long-axis mode resonance.[27] The change in the shape from nanosphere to nanorod

also gives an effective way to tune the resonance frequency of the Raman enhancement from the visible to the NIR region by means of the nanorod aspect ratio.[61] There is significant advantage in tuning the SERS enhancement to the NIR region. Conventionally, in biomolecular studies, stronger Raman signals are obtained by using a technique known as resonance Raman scattering, in which the sample is excited with a laser of frequency resonant with an electronic transition of a chromophore in the biomolecule. However, the use of resonant UV or visible lasers frequently causes photochemical damage. In addition, interference from the fluorescence from some of the residues frequently limits the use of this technique. The use of nanorods thus allows the use of an NIR laser for achieving strong Raman signals without causing photochemical damage or interference, since biomolecules such as DNA and proteins have no absorption in the NIR region.[61]

### 1.1.3.4. Other Plasmon-Based Optical Enhancements

The "lightning rod effect"[62] also results in a million times stronger photoluminescence from gold nanorods as compared to the bulk metal.[63] The photoluminescence quantum yield is seen to increase with the square of the nanorod aspect ratio. This enhancement has been attributed to the enhanced absorption of the higher oscillator strength long-axis plasmon resonance mode of the nanorod.[64] The enhanced fluorescence of nanorods has allowed them to be used as imaging agents *in vivo* in mouse-ear blood vessels, by exciting them via a two-photon process using a femtosecond NIR laser resonant with the long-axis plasmon resonance (~820 nm). The NIR excitation provides the advantage of low absorption and auto-fluorescence from tissue and blood *in vivo*.[65] Similar to gold nanorods, metal nanoshells with their tunable

and high polarizability plasmon modes are also becoming excellent substrates for SERS,[66] surface-enhanced infrared spectroscopy, and plasmon-enhanced emission from fluorophores.[67] Other optical effects including second harmonic generation[68] have also been enhanced by utilizing the surface plasmon resonance of noble metal nanoparticles.

## 1.2 Non-radiative Properties of Noble Metal Nanoparticles

### 1.2.1 Dynamics of Non-radiative Electron Relaxation

There has been great interest in the non-radiative processes of electronic relaxation in noble metal nanoparticles since these govern the damping and dephasing of the plasmon resonance (including surface contribution to these effects which may be important in nanosized particles).[2] These processes also constitute the absorption part of the plasmon resonance. The dynamics of hot electrons is important also from the point of view of photoelectrochemical processes in noble metal nanoparticles, potentially useful for applications like solar energy conversion.[69]

The dynamics of non-radiative electron relaxation processes has been studied by femtosecond time-resolved laser techniques. Femtosecond pulses can be used to create a non-equilibrium excitation of the metal electrons following which they relax via non-radiative processes.[2,7,70] The femtosecond pump-probe transient absorption spectroscopy technique has become very useful in following the dynamics of the relaxation processes in plasmonic nanoparticles.[70] As per this technique, a femtosecond pulse (pump) excites the electrons via inter-band transitions (at a wavelength of 400 nm in the case of gold) to empty states above the Fermi level. The non-equilibrium/non-Fermi electronic distribution is thermalized via very fast electron-electron scattering processes (on the

26

timescale of 500 fs) to create a "hot" Fermi electron distribution.[2] The creation of this broadened Fermi distribution results in the broadening of the plasmon resonance, which is manifested as a transient bleach of the plasmon absorption. As the electrons subsequently cool to equilibrium, the plasmon resonance absorption is recovered. A second femtosecond pulse overlapping with the surface plasmon absorption maximum of the nanoparticles is used as a probe to follow the recovery of the plasmon resonance absorption (or decay of the transient bleach) with sub-picosecond resolution, thus yielding the kinetic trace of the hot electron relaxation (see Figure 1.8).[70] The transient bleaching of the plasmon resonance followed by its ultrafast recovery is potentially useful in ultrafast optical switching.

Pump-probe studies from our group[2,7,70-73] and others[74] have established that the electron cooling following thermalization involves a initial fast decay component, which is attributed to the exchange of the hot electron energy with the nanoparticle lattice through electron-phonon scattering. This takes place on a timescale of ~1 ps in the case of gold.[2,7,70] Following this, the hot lattice cools by transferring energy to the medium via phonon-phonon coupling processes, on a timescale of 100 ps, corresponding to a slower component of the decay.[2,7,70] Thus, the light absorbed by the electrons is converted into heat within the nanoparticle, subsequently leading to the heating of the local medium surrounding the nanoparticle.

It must be noted that the electron-phonon relaxation time is laser pump energy dependent and it increases with increasing pump energy due to the linear increase in the electronic heat capacity with increase in hot electron temperature.[2,70] The consequently slower electron-phonon relaxation also mixes with the phonon-phonon relaxation rate,

which is generally dependent on the thermal properties of the medium.[73,75,76] It is therefore necessary to carry out electron-phonon relaxation measurements at low laser fluence and extrapolate their value to zero fluence in order to get measurements that can be compared. One must also ensure that different samples being compared have the same optical density at the excitation/pump wavelength.
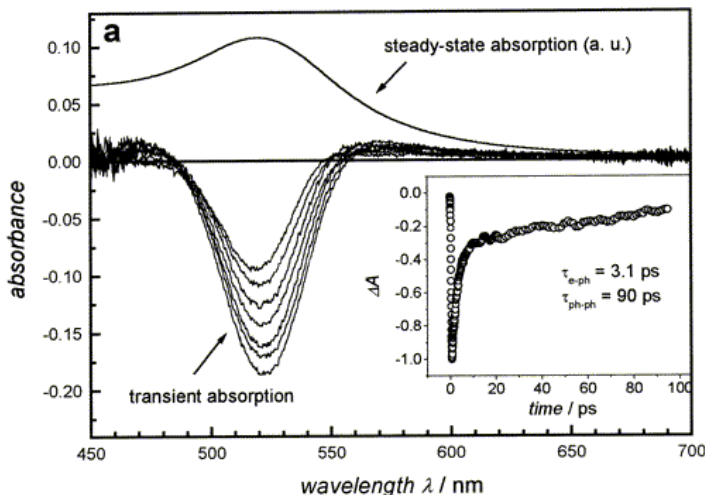
Figure 1.8: Transient absorption spectra of 15 nm gold nanospheres recorded at different delay times following their excitation at 400 nm with 100 femtosecond laser pulses. The steady-state UV-vis absorption spectrum of the colloidal gold solution is also shown for comparison. The inset shows the decay of the transient bleach when the particles are monitored at the plasmon absorption maximum at 520 nm. Fitting of the decay curve gives electron-phonon and phonon-phonon relaxation times of 3.1 and 90 ps, respectively. (Reprinted with permission from S. Link, M. A. El-Sayed, *J. Phys.Chem. B* **1999**, *103*, 8410. Copyright 1999 American Chemical Society)[70]

The electron-phonon relaxation in gold nanoparticles is found to be similar to that in the bulk and has no dependence on the particle size in the size range from 2-100 nm and the shape (nanorods of aspect ratio 2 to 5).[7,72] Thus, there seems to be negligible surface contribution to the electron-phonon relaxation in gold. Size dependence of the

electron-phonon relaxation has however been observed in tin,[77] gallium,[78] and copper

nanoparticles.[79] This difference has been proposed by Hodak et al. to depend on the metal

electron density relative to its atomic mass.[80] For heavy metals like gold, the electron-

surface collisions are not sufficient to displace the heavy nuclei, as a result of which

surface phonons are not very efficiently excited and thus they do not contribute

significantly to the electron-phonon relaxation. Metals with lighter nuclei (e.g. silver) or

more than one valence electron (e.g. copper) are expected to exhibit more efficient

surface phonon excitation in small-size nanoparticles.[80] This was found to be valid for

copper nanoparticles by Darugar et al. from our group.[79]

**1.2.2 Photothermal Applications of Noble Metal Nanoparticles**

The strong light absorption followed by rapid photothermal conversion of gold

nanoparticles has been utilized in a number of applications including laser

nanostructuring,[40,81] generating nanomotion,[82] and for biomedicine.[30-32,83-87] The

photothermal energy can be channeled effectively and selectively for a desired

application by controlling the rate of laser energy deposition relative to the rate at which

the heat is dissipated. When the rate of the energy deposition is faster than the heat

dissipation away from the nanoparticle, the nonradiative processes result in the rapid

heating of the nanoparticle, which may result in:

i) Excitation of coherent lattice phonon vibrations[42,43,88] in the nanoparticle potentially

useful in nanophotonic modulation

ii) Melting (on the timescale of 30 ps)[81] or reshaping of the nanoparticles[40]

iii) Nanoparticle atomic ablation[89] and even projectile ejection of the particle with jet-like

speeds, potentially useful in generating nanomotion[82]

At lower rates of laser energy deposition, the photothermal heating of the medium surrounding the nanoparticle can be achieved. In such a case, the metal nanoparticles serve essentially as "light-activated nanoscopic heaters" useful for biomedical applications especially the selective laser photothermolysis of cancer cells.[30-32,83,84] Gold nanoparticles conjugated to antibodies can be selectively targeted to diseased cells without significant binding to healthy cells.[90] Irradiation of the cancer cells selectively labeled with the nanoparticles, with a laser of frequency overlapping with the plasmon absorption maximum of the nanoparticles results in selective heating and destruction of cancer cells, at much lower laser powers than those required to destroy healthy cells to which the nanoparticles do not bind specifically. Gold nanoparticles (10-50 nm size range) offer 6 or more orders higher absorption coefficients compared to conventional dyes.[13] Therefore, much lower laser energies can be used to achieve cell destruction, making therapy minimally invasive.

While the use of visible light resonant gold nanospheres can be useful for external skin/surface cancer treatments, for tumors within bodily tissue, it becomes necessary to use NIR light in the biological window.[34] One method demonstrated by the El-Sayed group involves the use of gold nanorods of aspect ratio 3.9, which have a longitudinal plasmon band around 800 nm overlapping with a NIR Ti:sapphire laser.[32] NIR laser irradiation of cancer cells labeled with gold nanorod/anti-EGFR conjugates resulted in selective destruction of the cancer cells. NIR imaging/therapy has also been achieved with NIR-resonant gold nanoshells and nanocages. Recently, Huang et al. demonstrated a novel way to achieve NIR therapy using gold nanospheres by utilizing their two-photon absorption of 800-nm Ti:sapphire laser light.[91]

## 1.3 Plasmonic Nanoparticles in Assemblies

### 1.3.1 Inter-particle Coupling Effects

While the optical properties of a metal nanoparticle are determined by its surface plasmon resonance, there is dramatic change in these properties when nanoparticles come into close proximity.[27,92-98] This is due to the coupling of the plasmon oscillations of the interacting particles. The plasmon oscillation generates an enhanced electric field localized on the nanoparticle surface, decaying with distance away from the nanoparticle. The near-field of particles present in close proximity can interact with each other strongly. Thus the electric field $E^{'}$ felt by each particle is the sum of the incident light field $E$ and the perturbation due to the presence of the electric dipole present on the neighboring particle:[99]

$$E^{'} = E + \xi \frac{\mu}{4\pi\varepsilon_m\varepsilon_0 d^3} \qquad (21)$$

where $\mu$ is the dipole moment due to the particle plasmon and $\xi$ is an orientation factor. Because of the near-field coupling of the plasmons, there is a change in the frequency of the surface plasmon oscillation of the coupled nanoparticle system with respect to the isolated particle. For example, the assembly or aggregation of spherical Au nanoparticles into a close packed structure results in a red shift of the SPR wavelength from the isolated nanosphere SPR wavelength at ~520 nm to longer wavelengths.[93] The extent of the coupling-induced red shift increases with decreasing inter-particle distance and increasing number of particles in the assembly.[93,100] The shift in the surface plasmon resonance wavelength maximum resulting from the electromagnetic coupling between

the nanoparticles allows the use of far-field absorption or scattering-based measurements to probe the near-field coupling.

The coupling-induced plasmonic shift shows a polarization-dependence as governed by the orientation factor $\xi$ in eq 21. Experimentally measured plasmon resonances of pairs of 150 nm Au nanodiscs fabricated by electron-beam lithography showed that when the light polarization direction is parallel to the inter-particle axis, the plasmon resonance of the nanodisc pair is red-shifted with respect to the single particle case.[101] Conversely, when the light is polarized orthogonal to the inter-particle axis, the plasmon spectrum is relatively blue shifted with respect to the single-particle case. In the parallel polarization case, the interparticle interaction is strongly attractive ($\xi$ is positive), resulting in the plasmon red-shift; the blue-shift in the perpendicular polarization case is due to a repulsive interaction between the electronic dipoles of the particle pair partners ($\xi$ is negative). It must be noted that the situation is much more complex when the particle size becomes large enough to have severe retardation effects, such that the driving fields do not maintain the same phase across the nanoparticle.[102]

The attractive plasmon coupling between metal nanoparticles assembled in pairs or 1-D chains has been shown, mainly through simulations, to result in a huge enhancement in the electric field at the junction between the nanoparticles, especially at small gaps.[27,97,103] The field enhancement at the junction is further enhanced in the case of coupling between sharp tips (with highly concentrated fields), as found for nanotriangles interacting tip-to-tip (bowties)[27,104,105] and nanorods interacting end-to-end.[94]

The distance dependence of near-field coupling has also been studied experimentally on lithographically fabricated arrays of ellipsoidal gold nanodisc pairs with systematically varying inter-particle separations, supported by electrodynamic simulations.[95] In this study, Su et al. found that the plasmon resonance of the nanodisc pair red-shifts exponentially with the decrease in the inter-particle gap.[95] They further showed that when the inter-particle gap is normalized by the particle size, this near-exponential trend becomes independent of the particle size. The plasmon shift decays to zero over a separation of 2.5 diameters. A similar observation was made by Gunnarsson et al. in lithographically fabricated silver nanodisc pair arrays.[96] They also showed that discs that are in metallic contact, show completely new plasmon modes that have extremely large (almost abrupt) shifts relative to the single-particle resonances. In addition, higher-order modes are also seen to emerge at lower wavelengths.[99,106]

It has been found from the studies of Lamprecht et al.[107] and Haynes et al.[108] on periodic 2-D lithographic arrays, that in addition to the near-field coupling between the particles in close proximity, there is a far-field radiative coupling between the particles in a periodic array. This coupling, which is diffractive in nature, is maximum when the grating constant of the array is equal to the wavelength of the light in the medium, manifested by a plasmon band that is considerably narrower and red-shifted. As we move away from this grating constant towards smaller inter-particle separations, a blue-shift and broadening of the plasmon resonance is observed until the separations become small enough such that near-field coupling becomes important. Both far-field interactions and near-field interactions have been studied in bowtie nano-antennas.[109] Far-field coupling with its 1/d dependence is important at larger separations (on the order of the light

wavelength) along with electromagnetic retardation effects, whereas smaller inter-particle separations are dominated by near-field coupling, which decays as $1/d^3$ in the dipolar-coupling limit.[109]

The effect of inter-particle interactions in noble metal nanoparticle assemblies on non-radiative properties has also been observed.[69] Feldstein et al.[69] studied the hot electron lifetimes in thin films aggregates of 12-nm gold nanoparticles as a function of the film thickness, which was a measure of the degree of aggregation. It was found that the hot-electron lifetimes decreased with greater aggregation. The faster relaxation of the electrons in the films with greater degree of aggregation was attributed to the mobility or conduction of the electrons between the closely interacting (although not touching) nanoparticles in the aggregate.

Silver nanocrystals self-organized in face-centered cubic supracrystals show a shift of their coherent Raman-active lattice vibration frequency to lower values, attributed to the near-field coupling between the nanoparticles.[110] Similarly, the surface plasmon coupling between silver nanocolumns fabricated in an oriented assembly has been found to affect the Raman-active phonon vibration frequency of the nanostructure.[111]

## 1.3.2 Applications of Nanoparticle Assembly

The assembly of plasmonic nanoparticles thus gives a unique way to tune the optical properties such as the plasmon resonance frequency and the plasmonic field enhancement, as well as non-radiative properties. This can be useful in a range of applications as seen from the examples below.

1.3.2.1 Assembly-Based Sensing

The dependence of the nanoparticle plasmon resonance on the presence of other nanoparticles in close proximity has been utilized for the sensing of biomolecules. Mirkin and coworkers[90] first showed this by using a biomolecular event, e.g. DNA hybridization to trigger the assembly of gold nanoparticles. In this strategy, a mixture of two different flavors of gold nanoparticle-DNA oligonucleotide conjugates (NP-oligonucleotideA and NP-oligonucleotideB) assembled together into a large 3-dimensional assembly in solution by a linker DNA strand A'-B' under DNA hybridization conditions. Thus, the presence of the target DNA strand A'-B' could be easily detected (down to pM concentration and one base-pair mismatch) by the observed red-shift in the UV-visible extinction band of the solution from 520 nm to ~560 nm, resulting from the assembly. In addition, color change from red (for isolated colloidal nanoparticle solution) to purplish (for the assembled nanoparticle solution) served as a visual detection. This assembly-based sensing strategy has been extended to the detection of antibody-antigen interactions and of specific disease biomarkers (e.g. prostate cancer) by using appropriately functionalized particles that assemble in the presence of the target analyte.[48] The technique has also been extended to nanorods where the assembly of end-functionalized nanorods results in a red-shift of the nanorod long-axis plasmon absorption band, which has been utilized for the detection of cysteine and glutathione down to micromolar concentrations.[112]

1.3.2.2 Photonic Waveguiding

By means of the strong near-field coupling between metal nanoparticles, the plasmon oscillation of a nanoparticle can induce an oscillation in a neighboring particle

in close proximity.[113] This has great potential for designing plasmonic waveguides consisting of a linear chain/array of closely spaced nanoparticles. It has been theoretically shown that the near-field coupling between the nanoparticles results in coupled plasmon-polariton modes leading to the coherent transport of electromagnetic energy along the nanoparticle chain.[114] This makes possible waveguiding of photons at a lateral confinement much below the diffraction limit, which is not attainable using conventional photonics. Near-field coupling-based photonic transport has been experimentally demonstrated in a lithographically fabricated plasmonic waveguide consisting of a linear array of silver spheroids interacting along their short axes parallel to the chain axis. In this experiment, localized excitation of the waveguide was achieved by the tip of a near-field scanning optical microscope, while the photonic transport was evidenced by observation of distant (up to 500 nm) excitation of fluorophores by the transported plasmons.[113]

1.3.2.3 Plasmon Ruler

Since the coupling-induced red-shift between two interacting metal nanoparticles depends on the distance between them,[95,115] such a two-particle system becomes very attractive as a distance probe, conceptually similar to conventional Fluorescence Resonance Energy Transfer (FRET)-based distance probing.[116] FRET probing involves a pair of dyes, in which energy is transferred from the excited donor to the acceptor. The energy transfer efficiency depends on the inter-dye distance, which has been very well characterized as per the Forster's theory, because of which FRET-based dye pairs have become a very valuable tool in probing distances and dynamic distance changes in biomolecules.[116] There has been a lot of recent interest in utilizing the distance-dependent

plasmon resonance of a plasmonic particle pair as a ruler for probing nanoscale distances.[117] Metal nanoparticle rulers offer much stronger optical signals as compared to FRET dyes and also overcome the difficulty of photobleaching of dyes.[117] Alivisatos and Liphardt first demonstrated the plasmon ruler concept.[117] They showed that the formation of a gold nanoparticle pair from a nanoparticle with a single biotin functionality and another particle with a single streptavidin functionality resulted in a plasmon shift of 23 nm, as observed by the dark-field scattering spectroscopy of single particle pairs immobilized on a glass substrate. In addition to the plasmon shift, the dimerization also results in a strong increase in the scattering intensity as well as a change in the color of the light scattered. Particle pair plasmon rulers linked by ss-DNA were shown to detect DNA hybridization by means of a distance change.[117] Hybridization with a complementary DNA strand results in the stiffening of the linkage between the particle pair partners, resulting in an increase in the inter-particle distance by 2 nm and an observable blue shift. Particle pair plasmon rulers linked by ss-DNA have also shown to be able to detect DNA bending and cleavage by means of a change in the scattering intensity resulting from a distance change between the particle partners.[118]

1.3.2.4 SERS Enhancement

The assembly or aggregation of nanoparticles has been shown to result in huge SERS enhancements.[119-121] The inter-particle junctions formed by the assembly of nanoparticles are sites for electric field enhancements that are much stronger than isolated nanoparticles, due to the favorable coupling of the plasmon resonances between nanoparticles.[27] These junction electric fields can increase very sharply with decreasing inter-particle separation. In fact, some single molecule experiments have shown up to 14

orders of magnitude enhancement in SERS of R6G molecules on silver nanoparticles,[122] which has been attributed to be from the molecules at the junctions or hot spots formed from the aggregation of two or more nanoparticles.[119]

Nikoobakht and El-Sayed showed that a layer of aggregated gold nanorods exhibited a huge enhancement in the SERS of adsorbed 2-aminothiophenol (2-ATP) molecules and nanorod capping molecules, as compared to a surface with a lower coverage of nanorods and a film of aggregated nanospheres (see Figure 1.9).[120]

Strong SERS enhancement has also been observed in an array of silver nanorods standing vertically on a glass substrate.[123] The SERS enhancement has been attributed to the strong electromagnetic coupling between the adjacent nanorods and the resulting confinement of strong fields in the gaps between the nanorods, under light polarization perpendicular to the long-axis of the rods.

Very recently, Huang et al. utilized the SERS enhancement resulting from nanorod assembly for the molecular diagnosis of cancer.[32] They showed that gold nanorods conjugated with anti-EGFR antibodies assembled on the surface of cancer cells, due to the specific binding between the antibodies on the rod surface and the EGFR on the cancer cells. This assembly of nanorods on the cancer cells gave highly enhanced, sharp, and polarized SERS of the molecules in the vicinity of the nanorod surface including the nanorod capping molecules, the bridging molecules, anti-EGFR antibodies, and EGFR receptors, and other molecules on the cell surface. These strongly enhanced SERS spectra allowed the cancer cells to be distinguished from normal cells that only showed weak or no SERS signals.[32]
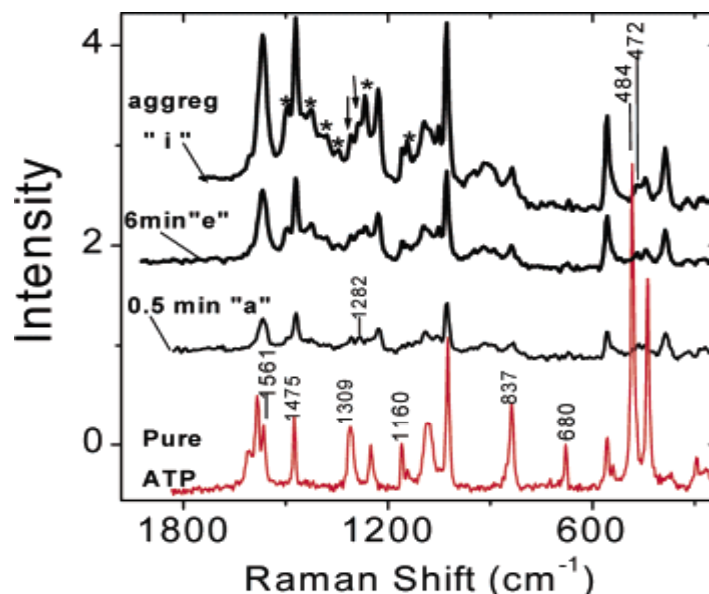
Figure 1.9 SERS of 2-Aminothiophenol (2-ATP) from (top to bottom): aggregated nanorods, 6-min nanorod deposition time, 0.5 min nanorod deposition time, and Raman spectrum of pure 2-ATP in the liquid phase. The SERS enhancement is seen to increase as the aggregation of nanorods proceeds. Peaks labeled with stars belong to the nanorod capping molecules. (Reprinted with permission from B. Nikoobakht, B.; M. A. El-Sayed, *J. Phys. Chem. A* **2003**, *107*, 3372. Copyright 2003 American Chemical Society)[120]

1.2.2.5 Nanoparticle Clusters in Biomedicine

Recently Zharov et al.[85,86] targeted gold nanoparticles to cells followed by their self- assembly directly within live cells. This assembly resulted in a shift in the plasmon absorption of the nanoparticles from 520 nm to the 700-1000 nm region, overlapping with the biological window, which provided better light penetration for performing laser photothermal diagnostics and therapy. At the same time, the close packing of the nanoparticles resulted in non-linear or synergistically amplified photothermal effects, strongly enhancing their diagnostic and therapeutic ability.

## 1.4 Outline of the Contents of the Thesis Chapters

As discussed above, there is a great deal of interest in assembled noble metal nanostructures from the point of view of nanotechnology. Most real devices are expected to be based on assemblies of nanoparticles, thus making it important to characterize the interactions between nanoparticles in their assembled state and understand their effects on the optical and non-radiative properties of the nanostructure. This is the goal of our research, as described in the remaining chapters of this thesis. Of special interest is the plasmon coupling between nanoparticles, which is not only fundamentally interesting but also important for applications such as biosensing, Raman enhancement, and plasmonic waveguiding.

Before entering into the nature of coupling between noble metal nanoparticles, we take a detailed look at isolated nanoparticles in Chapter 2. We provide a detailed comparative study of the absorption and scattering cross-sections of three important plasmonic nanostructures, viz., gold nanospheres, gold nanorods, and silica-gold nanoshells. While the radiative aspects of the plasmon resonance (e.g. scattering) are important in imaging and sensing applications, the non-radiative part (absorption) is important in photothermal applications. We show that the relative contribution of scattering versus absorption can be increased by increasing the nanostructure size in all three nanostructure types. For bio-applications where nanoparticle size is an important consideration, we present a comparison of size-normalized scattering and absorption coefficients, showing that the nanorod shape offers the most enhanced optical coefficients at small size.

We look at coupled gold nanospheres in the form of colloidal aggregates in Chapter 3, where we study their plasmon resonance using UV-vis spectroscopy and their non-radiative electron relaxation dynamics using ultrafast pump-probe transient absorption spectroscopy. The aggregate solution shows a broad plasmon absorption band due to contributions from a heterogeneous mix of assemblies (with different inter-particle spacings or number of particles). However, we are able to use an optical probe of a specific wavelength to selectively interrogate only those aggregate subsets that absorb at the probe wavelength. As we probe at longer wavelengths, we interrogate the electron-relaxation dynamics in aggregates with progressively stronger coupling, observing an increase in the measured rate of hot electron relaxation. Based on these results we propose the role of inter-colloid electronic coupling and interfacial electronic scattering in determing electron dynamics in nanoparticle assemblies.

How does the particle shape affect the nature of plasmon coupling? We address this question in Chapter 4, where we describe the assembly of anisotropic particles i.e. colloidal gold nanorods, which offer two modes by which they can be assembled. The side-by-side assembly of gold nanorods in solution results in a blue-shift of the longitudinal plasmon absorption band, which is in contrast to the end-to-end assembly of nanorods seen in the past to result in a red-shift of the longitudinal plasmon resonance mode. This orientation dependence of the assembly-induced plasmon shift is confirmed by electrodynamic simulations of nanorod dimers, based on which we conclude simple polarization "selection" rules of plasmon coupling. When the plasmon oscillations are polarized along the inter-particle interaction axis, the coupling between the plasmons is bonding in nature, resulting in a red-shift (end-to-end assembly), in contrast to the blue-

shift that results from the anti-bonding interaction when the polarization is perpendicular to the inter-particle axis (side-by-side assembly).

In Chapter 5, we study the distance dependence of the near-field plasmon coupling in gold nanodisc pairs fabricated by electron-beam lithography (by Wenyu Huang, another group member) with systematically varying inter-particle separations, accompanied by an electrodynamic study of particle pairs. In agreement with past literature, we find that the plasmon resonance wavelength maximum red-shifts almost exponentially with decreasing inter-particle separation and also that this exponential trend becomes independent of the nanodisc diameter when the inter-particle gap is normalized by the diameter. Further, we find from our simulations that the fractional shift ($\Delta\lambda/\lambda_0$) of the plasmon resonance wavelength decays over an inter-particle separation s, which is roughly 0.2 in units of the particle dimension D, independent of the particle size, the shape (nanodisc pairs or nanosphere pairs), type of metal (gold or silver), and the surrounding medium. This universal scaling behavior is expressed as $\Delta\lambda/\lambda_0 \sim a.\exp^{-s/0.2D}$, giving us a "plasmon ruler" equation which can be used to calculate the inter-particle separation in a nanoparticle pair from its plasmon resonance shift. We successfully test this with Alivisatos and coworkers' experimentally determined plasmon resonances of gold nanosphere pairs assembled by DNA linkers of varying number of base pairs, thus making our equation applicable to the determination of nanoscale distances in macro/biomolecular systems using the particle-pair plasmon ruler. A quasistatic dipolar-coupling model is used to explain the universal size-scaling behavior based on the magnitude of the (inter-particle) coupling strength relative to the (intraparticle) polarizability.

The universal scaling behavior also extends to the metal nanoshells, as described in Chapter 6. Mie theory simulations show that the plasmon resonance red-shifts near-exponentially with decreasing thickness of the metal shell in units of the core size, according to a trend universally independent of the nanoshell size, type of shell metal, the core dielectric, and surrounding medium. We are able to extend the universal size-scaling from the particle-pair system to the nanoshell, because in analogy to the particle-pair, the nanoshell plasmon resonance results from plasmons on the inner and outer shell surfaces coupling over a distance defined by the shell thickness. Our model is consistent with the plasmon hybridization model developed by Prodan, Nordlander and Halas. At the same time, it gives a simple dependence of the nanoshell plasmon resonance frequency on both the shell thickness and nanoshell size unlike earlier models and is thus very useful in estimating the resonance wavelength maximum of a nanoshell of given dimensions.

Chapter 7 describes how the plasmonic sensitivity of assembled nanostructures (e.g. metal nanoshell and particle-pair) is enhanced in correlation with increasing plasmon coupling strength. Mie theory results show that the sensitivity of a metal nanoshell increases near-exponentially with decreasing shell thickness (in units of the core size) according to the same universal scaling behavior as seen for the plasmon resonance. A general physical rule that emerges from these observations is that the plasmon sensitivity is strongly enhanced in those nanostructures, which offer a high polarizability of the electrons to the metal-medium interface. Thus, nanostructures with sharp curvatures, high aspect ratios, or narrow inter-particle junctions are most suitable for refractive index-based sensing applications.

We extend the universal scaling model to nanostructures of complex geometry in Chapter 8 by means of electrodynamic simulations. The fractional plasmon shift in a trimer of nanospheres decays with the inter-particle separation (in units of particle diameter) with the same universal scaling behavior seen in dimers. This is the first step towards extending the universal size-scaling model to 1-D, 2-D, and 3-D assemblies with large number of interacting particles. In addition, the plasmon shift in a pair of elongated nanoparticles assembled head-to-tail decays according to the universal scaling law, when the inter-particle separation is scaled by the long-axis dimension, which is the dimension in the direction of inter-particle coupling. We also see that an increase in the particle aspect ratio and end-curvature results in an increase in the coupling-induced plasmonic shifts, without affecting the universal size scaling.

In Chapter 9, we describe the investigation of the non-radiative electron relaxation dynamics in gold nanoparticles conjugated to self-assembled monolayers of thiolated DNA ligands, using femtosecond laser studies. We find that the femtosecond pulse (400 nm) excitation of the thiolated DNA-modified nanoparticles leads to desorption of the thiol ligands from the nanoparticle surface, as seen from the blue shift of the plasmon resonance, followed by nanoparticle aggregation. We attribute this to the nonradiative relaxation of the hot electron energy, on the electron-phonon relaxation timescale, into surface gold-sulfur bond vibrations leading to the surface desorption. This additional pathway for non-radiative cooling of the electrons in the conjugates is manifested in a faster rate of electron-phonon relaxation in the thiolated DNA-modified nanoparticles compared to that in unmodified nanoparticles, at progressively higher laser pulse energies.

## 1.5 References

(1)    Liz-Marzan, L. M. *Materials Today* **2004**, *7*, 26.

(2)    Link, S.; El-Sayed, M. A. *Annu. Rev. Phys. Chem.* **2003**, *54*, 331.

(3)    Padovani, S.; Sada, C.; Mazzoldi, P.; Brunetti, B.; Borgia, I.; Sgamellotti, A.; Giulivi, A.; D'Acapito, F.; Battaglin, G. *J. Appl. Phys.* **2003**, *93*, 10058.

(4)    Faraday, M. *Philos. Trans. R. Soc. London* **1857**, 147, 145.

(5)    Bohren, C. F.; Huffman, D. R. *Absorption and Scattering of Light by Small Particles*; Wiley: New York, 1983.

(6)    Kreibig, U.; Vollmer, M. *Optical Properties of Metal Clusters*; Springer: Berlin, 1995; Vol. 25.

(7)    Link, S.; El-Sayed, M. A. *Int. Rev. Phys. Chem.* **2000**, *19*, 409.

(8)    Kelly, K. L.; Coronado, E.; Zhao, L. L.; Schatz, G. C. *J. Phys. Chem. B* **2003**, *107*, 668.

(9)    Papavassiliou, G. C. *Prog. Solid State Chem.* **1980**, *12*, 185.

(10)   Mie, G. *Ann. Phys.* **1908**, *25*, 377.

(11)   Kreibig, U.; Fragstein, C. v. *Z. Physik* **1969**, *224*, 307.

(12)   Link, S.; El-Sayed, M. A. *J. Phys. Chem. B* **1999**, *103*, 4212.

(13)   Jain, P. K.; Lee, K. S.; El-Sayed, I. H.; El-Sayed, M. A. *J. Phys. Chem. B* **2006**, *110*, 7238.

(14)   Sonnichsen, C.; Franzl, T.; Wilk, T.; von Plessen, G.; Feldmann, J.; Wilson, O.; Mulvaney, P. *Phys. Rev. Lett.* **2002**, *88*, 077402.

(15)     Murphy, C. J.; Sau, T. K.; Gole, A. M.; Orendorff, C. J.; Gao, J.; Gou, L.; Hunyadi, S. E.; Li, T. *J. Phys. Chem. B* **2005**, *109*, 13857.

(16)     Link, S.; Mohamed, M. B.; El-Sayed, M. A. *J. Phys. Chem. B* **1999**, *103*, 3073 and Erratum: *J. Phys. Chem. B* **2005**, *109*, 10531.

(17)     Oldenburg, S. J.; Averitt, R. D.; Westcott, S. L.; Halas, N. J. *Chem. Phys. Lett.* **1998**, *28*, 243.

(18)     Haes, A. J.; Van Duyne, R. P. *J. Am. Chem. Soc.* **2002**, *124*, 10596.

(19)     Underwood, S.; Mulvaney, P. *Langmuir* **1994**, *10*, 3427.

(20)     Lee, K.-S.; El-Sayed, M. A. *J. Phys. Chem. B* **2006**, *110*, 19220.

(21)     Link, S.; Wang, Z. L.; El-Sayed, M. A. *J. Phys. Chem. B* **1999**, *103*, 3529.

(22)     Alvarez, M. M.; Khoury, J. T.; Schaaff, G.; Shafigullin, M. N.; Vezmar, I.; Whetten, R. L. *J. Phys. Chem. B* **1997**, *101*, 3706.

(23)     Pustovit, V. N.; Shahbazyan, T. V. *J. Opt. Soc. Am. A* **2006**, *23*, 1369.

(24)     Turkevich, J.; Stevenson, P. C.; Hillier, J. *Discuss. Faraday Soc.* **1951**, *11*, 55.

(25)     Gans, R. *Ann. Phys.* **1912**, *37*, 881.

(26)     Lee, K.-S.; El-Sayed, M. A. *J. Phys. Chem. B* **2005**, *109*, 20331.

(27)     Hao, E.; Schatz George, C. *J. Chem. Phys.* **2004**, *120*, 357.

(28)     Prodan, E.; Radloff, C.; Halas, N. J.; Nordlander, P. *Science* **2003**, *302*, 419.

(29)     Loo, C.; Lin, A.; Hirsch, L.; Lee, M.-H.; Barton, J.; Halas, N.; West, J.; Drezek, R. *Technol. Cancer Res. Treat.* **2004**, *3*, 33.

(30)     Loo, C., A.; Lowery, A.; Halas, N.; West, J.; Drezek, R. *Nano Lett.* **2005**, *5*, 709.

(31)     Hirsch, L. R.; Stafford, R. J.; Bankson, J. A.; Sershen, S. R.; Rivera, B.; Price, R. E.; Hazle, J. D.; Halas, N. J.; West, J. L. *Proc. Natl. Acad. Sci., USA* **2003**, *100*, 13549.

(32)     Huang, X.; El-Sayed, I. H.; Qian, W.; El-Sayed, M. A. *J. Am. Chem. Soc.* **2006**, *128*, 2115.

(33)     Pérez-Juste, J.; Pastoriza-Santos, I.; Liz-Marzán, L. M.; Mulvaney, P. *Coord. Chem. Rev.* **2005**, *249*, 1870.

(34)     Weissleder, R. *Nat. Biotechnol.* **2001**, *19*, 316.

(35)     Jana, N. R.; Gearheart, L.; Murphy, C. J. *Langmuir* **2001**, *17*, 6782.

(36)     Jana, N. R.; Gearheart, L.; Murphy, C. J. *Adv. Mater.* **2001**, *13*, 1389.

(37)     Nikoobakht, B.; El-Sayed, M. A. *Chem. Mater.* **2003**, *15*, 1957.

(38)     Sun, Y.; Mayers, B. T.; Xia, Y. *Nano Lett.* **2002**, *2*, 481.

(39)     Hulteen, J. C.; Van Duyne, R. P. *J. Vac. Sci. Technol. A* **1995**, *13*, 1553.

(40)     Huang, W.; Qian, W.; El-Sayed, M. A. *J. Appl. Phys.* **2005**, *98*, 114301/1.

(41)     Huang, W.; Qian, W.; El-Sayed, M. A. *Proc. SPIE-Int. Soc. Opt. Eng.* **2005**, *5927*, 592701/1.

(42)     Huang, W.; Qian, W.; El-Sayed, M. A. *J. Phys. Chem. B* **2005**, *109*, 18881.

(43)     Huang, W.; Qian, W.; El-Sayed, M. A. *Nano Lett.* **2004**, *4*, 1741.

(44)     Ghosh, S. K.; Nath, S.; Kundu, S.; Esumi, K.; Pal, T. *J. Phys. Chem. B* **2004**, *108*, 13963.

(45)    Hovel, H.; Fritz, S.; Hilger, A.; Kreibig, U. *Phys. Rev. B* **1993**, *48*, 18178.

(46)    Mulvaney, P.; Pérez-Juste, J.; Giersig, M.; Liz-Marzán, L. M.; Pecharroman, C. *Plasmonics* **2006**, *1*, 61.

(47)    Yguerabide, J.; Yguerabide, E. E. *Anal. Biochem.* **1998**, *262*, 137.

(48)    Rosi, N. L.; Mirkin, C. A. *Chem. Rev.* **2005**, *105*, 1547 and references therein.

(49)    Alivisatos, A. P. *Nat. Biotechnol.* **2004**, *22*, 47.

(50)    Katz, E.; Willner, I. *Angew. Chem. Int. Ed.* **2004**, *43*, 6042.

(51)    Chen, J.; Saeki, F.; Wiley, B. J.; Cang, H.; Cobb, M. J.; Li, Z.-Y.; Au, L.; Zhang, H.; Kimmey, M. B.; Li, X.; Xia, Y. *Nano Lett.* **2005**, *5*, 473.

(52)    Sokolov, K.; Follen, M.; Aaron, J.; Pavlova, I.; Malpica, A.; Lotan, R.; Richards-Kortum, R. *Cancer Res.* **2003**, *63*, 1999.

(53)    El-Sayed, I. H.; Huang, X.; El-Sayed, M. A. *Nano Lett.* **2005**, *5*, 829.

(54)    Haes, A. J.; Hall, W. P.; Chang, L.; Klein, W. L.; Van Duyne, R. P. *Nano Lett.* **2004**, *4*, 1029.

(55)    Yu, C.; Irudayaraj, J. *Anal. Chem.* **2007**, *79*, 572.

(56)    Sun, Y.; Xia, Y. *Anal. Chem.* **2002**, *74*, 5297.

(57)    McFarland, A. D.; Van Duyne, R. P. *Nano Lett.* **2003**, *3*, 1057.

(58)    Schatz, G. C. *Acc. Chem. Res.* **1984**, *17*, 370 and references therein.

(59)    Qiu, J.; Jiang, X.; Zhu, C.; Shirai, M.; Si, J.; Jiang, N.; Hirao, K. *Angew. Chem. Int. Ed.* **2004**, *43*, 2230.

(60)  Orendorff, C. J.; Gearheart, L.; Jana, N. R.; Murphy, C. J. *Phys. Chem. Chem. Phys.* **2006**, *8*, 165.

(61)  Huang, X.; El-Sayed, I. H.; Qian, W.; El-Sayed, M. A. *Nano Lett.* **2007**, *7*, 1591.

(62)  Boyd, G. T.; Rasing, T.; Leite, J. R. R.; Shen, Y. R. *Phys. Rev. B* **1984**, *30*, 519.

(63)  Mohamed, M. B.; Volkov, V.; Link, S.; El-Sayed, M. A. *Chem. Phys. Lett.* **2000**, *317*, 517.

(64)  Eustis, S.; El-Sayed, M. *J. Phys. Chem. B* **2005**, *109*, 16350.

(65)  Wang, H.; Huff, T. B.; Zweifel, D. A.; He, W.; Low, P. S.; Wei, A.; Cheng, J.-X. *Proc. Natl. Acad. Sci., USA* **2005**, *102*, 15752.

(66)  Jackson, J. B.; Halas, N. J. *Proc. Natl. Acad. Sci. USA* **2004**, *101*, 17930.

(67)  Tam, F.; Goodrich, G. P.; Johnson, B. R.; Halas, N. J. *Nano Lett.* **2007**, *7*, 496.

(68)  Antoine, R.; Brevet, P. F.; Girault, H. H.; Bethellb, D.; Schiffrin, D. J. *Chem. Commun.* **1997**, 1901.

(69)  Feldstein, M. J.; Keating, C. D.; Liau, Y.-H.; Natan, M. J.; Scherer, N. F. *J. Am. Chem. Soc.* **1997**, *119*, 6638.

(70)  Link, S.; El-Sayed, M. A. *J. Phys. Chem. B* **1999**, *103*, 8410.

(71)  Link, S.; Burda, C.; Wang, Z. L.; El-Sayed, M. A. *J. Chem. Phys.* **1999**, *111*, 1255.

(72)  Link, S.; Burda, C.; Mohamed, M. B.; Nikoobakht, B.; El-Sayed, M. A. *Phys. Rev. B* **2000**, *61*, 6086.

(73)  Link, S.; Furube, A.; Mohamed, M. B.; Asahi, T.; Masuhara, H.; El-Sayed, M. A. *J. Phys. Chem. B* **2002**, *106*, 945.

(74)  Hodak, J. H.; Henglein, A.; Hartland, G. V. *Pure App. Chem.* **2000**, *72*, 189.

(75)  Roberti, T. W.; Smith, B. A.; Zhang, J. Z. *J. Chem. Phys.* **1995**, *102*, 3860.

(76)  Link, S.; Hathcock, D. J.; Nikoobakht, B.; El-Sayed, M. A. *Adv. Mater.* **2003**, *15*, 393.

(77)  Stella, A.; Nisoli, M.; De Silvestri, S.; Svelto, O.; Lanzani, G.; Cheyssac, P.; Kofman, R. *Phys. Rev. B* **1996**, *53*, 15497.

(78)  Nisoli, M.; Stagira, S.; De Silvestri, S.; Stella, A.; Tognini, P.; Cheyssac, P.; Kofman, R. *Phys. Rev. Lett.* **1997**, *78*, 3575.

(79)  Darugar, Q., Qian, W.; El-Sayed, M. A.; Pileni, M.-P. *J. Phys. Chem. B* **2006**, *110*, 143.

(80)  Hodak, J. H.; Henglein, A.; Hartland, G. V. *J. Chem. Phys.* **2000**, *112*, 5942.

(81)  Link, S.; Burda, C.; Nikoobakht, B.; El-Sayed, M. A. *Chem. Phys. Lett.* **1999**, *315*, 12.

(82)  Huang, W.; Qian, W.; El-Sayed, M. A. *J. Am. Chem. Soc.* **2006**, *128*, 13330.

(83)  Huang, X.; Jain, P. K.; El-Sayed, I. H.; El-Sayed, M. A. *Photochem. Photobiol.* **2006**, *82*, 412.

(84)  El-Sayed, I. H.; Huang, X.; El-Sayed, M. A. *Cancer Lett.* **2006**, *239*, 129.

(85)  Zharov, V. P.; Galitovskaya, E. N.; Johnson, C.; Kelly, T. *Las. Surg. Med.* **2005**, *37*, 219.

(86)  Zharov, V. P.; Kim, J.-W.; Curiel, D. T.; Everts, M. *Nanomedicine* **2005**, *1*, 326.

(87)  Zharov, V. P.; Mercer, K. E.; Galitovskaya, E. N.; Smeltzer, M. S. *Biophys. J.* **2006**, *90*, 619.

(88)     Hartland, G. V. *Annu. Rev.Phys. Chem.* **2006**, *57*, 403.

(89)     Tabor, C.; Qian, W.; El-Sayed, M. A. *J. Phys. Chem. C* **2007**, *111*, 8934.

(90)     Elghanian, R.; Storhoff, J. J.; Mucic, R. C.; Letsinger, R. L.; Mirkin, C. A. *Science* **1997**, *277*, 1078.

(91)     Huang, X.; Qian, W.; El-Sayed, I. H.; El-Sayed, M. A. *Las. Surg. Med.* **2007**, *39*, 747.

(92)     Storhoff, J. J.; Lazarides, A. A.; Mucic, R. C.; Mirkin, C. A.; Letsinger, R. L.; Schatz, G. C. *J. Am. Chem. Soc.* **2000**, *122*, 4640.

(93)     Storhoff, J. J.; Elghanian, R.; Mucic, R. C.; Mirkin, C. A.; Letsinger, R. L. *J. Am. Chem. Soc.* **1998**, *120*, 1959.

(94)     Aizpurua, J.; Bryant, G. W.; Richter, L. J.; García de Abajo, F. J.; Kelley, B. K.; Mallouk, T. *Phys. Rev. B* **2005**, *71*, 235420/1.

(95)     Su, K. H.; Wei, Q.-H.; Zhang, X.; Mock, J. J.; Smith, D. R.; Schultz, S. *Nano Lett.* **2003**, *3*, 1087.

(96)     Gunnarsson, L.; Rindzevicius, T.; Prikulis, J.; Kasemo, B.; Käll, M.; Zou, S.; Schatz, G. C. *J. Phys. Chem. B* **2005**, *109*, 1079

(97)     Sweatlock, L. A.; Maier, S. A.; Atwater, H. A.; Penninkhof, J. J.; Polman, A. *Phys. Rev. B* **2005**, *71*, 235408/1.

(98)     Xiao, J. J.; Huang, J. P.; Yu, K. W. *Phys. Rev. B* **2005**, *71*, 045404/1.

(99)     Jain, P. K.; Huang, W.; El-Sayed, M. A. *Nano Lett.* **2007**, *7*, 2080.

(100)   Lazarides, A. A.; Kelly, L. K.; Jensen, T. R.; Schatz, G. C. *Theochem* **2000**, *529*, 59.

(101)   Rechberger, W.; Hohenau, A.; Leitner, A.; Krenn, J. R.; Lamprecht, B.; Aussenegg, F. R. *Opt. Commun.* **2003**, *220*, 137.

(102)  Kottmann, J. P.; Martin, O. J. F. *Opt. Lett.* **2001**, *26*, 1096.

(103)  Krenn, J. R.; Dereux, A.; Weeber, J. C.; Bourillot, E.; Lacroute, Y.; Goudonnet, J. P.; Schider, G.; Gotschy, W.; Leitner, A.; Aussenegg, F. R.; Girard, C. *Phys. Rev. Lett.* **1999**, *82*, 2590.

(104)  Sundaramurthy, A.; Crozier, K. B.; Kino, G. S.; Fromm, D. P.; Schuck, P. J.; Moerner, W. E. *Phys.Rev. B* **2005**, *72*, 165409.

(105)  Schuck, P. J.; Fromm, D. P.; Sundaramurthy, A.; Kino, G. S.; Moerner, W. E. *Phys. Rev. Lett.* **2005**, *94*, 017402.

(106)  Jain, P. K.; Eustis, S.; El-Sayed, M. A. *J. Phys. Chem. B* **2006**, *110*, 18243.

(107)  Lamprecht, B.; Schider, G.; Lechner, R. T.; Ditlbacher, H.; Krenn, J. R.; Leitner, A.; Aussenegg, F. R. *Phys. Rev. Lett.* **2000**, *84*, 4721.

(108)  Haynes, C. L.; McFarland, A. D.; Zhao, L.; Van Duyne, R. P.; Schatz, G. C.; Gunnarsson, L.; Prikulis, J.; Kasemo, B.; Kaell, M. *J. Phys. Chem. B* **2003**, *107*, 7337.

(109)  Fromm, D. P.; Sundaramurthy, A.; Schuck, P. J.; Kino, G.; Moerner, W. E. *Nano Lett.* **2004**, *4*, 957.

(110)  Courty, A.; Mermet, A.; Albouy, P. A.; Duval, E.; Pileni, M. P. *Nat. Mater.* **2005**, *4*, 395.

(111)  Margueritat, J.; Gonzalo, J.; Afonso, C. N.; Mlayah, A.; Murray, D. B.; Saviot, L. *Nano Lett.* **2006**, *6*, 2037.

(112)  Sudeep, P. K.; Joseph, S. T. S.; Thomas, K. G. *J. Am. Chem. Soc.* **2005**, *127*, 6516.

(113)  Maier, S. A.; Kik, P. G.; Atwater, H. A.; Meltzer, S.; Harel, E.; Koel, B. E.; Requicha, A. A. G. *Nat. Mater.* **2003**, *2*, 229.

(114)  Maeir, S. A.; Pieter, G. K.; Harry, A. A. *Appl. Phys. Lett.* **2002**, *81*, 1714.

(115) Reinhard, B. M.; M. Siu; Agarwal, H.; Alivisatos, A. P.; Liphardt, J. *Nano Lett.* **2005**, *5*, 2246.

(116) Deniz, A. A.; Dahan, M.; Grunwell, J. R.; Ha, T.; Faulhaber, A. E.; Chemla, D. S.; Weiss, S.; Schultz, P. G. *Proc. Nat. Acad. Sci., USA* **2007**, *96*, 3670.

(117) Sonnichsen, C.; Reinhard, B. M.; Liphardt, J.; Alivisatos, A. P. *Nat. Biotechnol.* **2005**, *23*, 741.

(118) Reinhard, B.; Sheikholeslami, S.; Mastroianni, A.; Alivisatos, A. P.; Liphardt, J. *Proc. Natl. Acad. Sci., USA* **2007**, *104*, 2667.

(119) Michaels, A. M.; Jiang, J.; Brus, L. *J. Phys. Chem. B* **2000**, *104*, 11965.

(120) Nikoobakht, B.; El-Sayed, M. A. *J. Phys. Chem. A* **2003**, *107*, 3372.

(121) Qin, L.; Zou, S.; Xue, C.; Atkinson, A.; Schatz, G. C.; Mirkin, C. A. *Proc. Nat. Acad. Sci., USA* **2006**, *103*, 13300.

(122) Nie, S.; Emory, S. R. *Science* **1997**, *275*, 1102.

(123) Zhao, Y. P.; Chaney, S. B.; Shanmukh, S.; Dluhy, R. A. *J. Phys. Chem. B* **2006**, *110*, 3153.

# CHAPTER 2

# ABSORPTION AND SCATTERING CROSS-SECTIONS OF GOLD NANOSTRUCTURES OF DIFFERENT SIZE, SHAPE, AND COMPOSITION FOR APPLICATIONS IN BIOLOGICAL IMAGING AND BIOMEDICINE

## Abstract

The selection of nanoparticles for achieving efficient contrast for biological and cell imaging applications, as well as for photothermal therapeutic applications, is based on the optical properties of the nanoparticles. We use Mie theory and discrete dipole approximation method to calculate absorption and scattering efficiencies and optical resonance wavelengths for three commonly used classes of nanoparticles: gold nanospheres, silica-gold nanoshells, and gold nanorods. The calculated spectra clearly reflect the well-known dependence of nanoparticle optical properties viz. the resonance wavelength, the extinction cross-section, and the ratio of scattering to absorption, on the nanoparticle dimensions. A systematic quantitative study of the various trends is presented. By increasing the size of gold nanospheres from 20 to 80 nm, the magnitude of extinction as well as the relative contribution of scattering to the extinction rapidly increases. Gold nanospheres in the size range commonly employed (~40 nm) show an absorption cross-section 5 orders higher than conventional absorbing dyes, while the magnitude of light scattering by 80-nm gold nanospheres is 5 orders higher than the light

emission from strongly fluorescing dyes. The variation in the plasmon wavelength maximum of nanospheres, i.e., from ~520 to 550 nm, is however too limited to be useful for in vivo applications. Gold nanoshells are found to have optical cross-sections comparable to and even higher than the nanospheres. Additionally, their optical resonances lie favorably in the near-infrared region. The resonance wavelength can be rapidly increased by either increasing the total nanoshell size or increasing the ratio of the core-to-shell radius. The total extinction of nanoshells shows a linear dependence on their total size, however, it is independent of the core/shell radius ratio. The relative scattering contribution to the extinction can be rapidly increased by increasing the nanoshell size or decreasing the ratio of the core/shell radius. Gold nanorods show optical cross-sections comparable to nanospheres and nanoshells, however, at much smaller effective size. Their optical resonance can be linearly tuned across the near-infrared region by changing either the effective size or the aspect ratio of the nanorods. The total extinction as well as the relative scattering contribution increases rapidly with the effective size, however, they are independent of the aspect ratio. To compare the effectiveness of nanoparticles of different sizes for real biomedical applications, size-normalized optical cross-sections or per micron coefficients are calculated. Gold nanorods show per micron absorption and scattering coefficients that are an order of magnitude higher than those for nanoshells and nanospheres. While nanorods with a higher aspect ratio along with a smaller effective radius are the best photoabsorbing nanoparticles, the highest scattering contrast for imaging applications is obtained from nanorods of high aspect ratio with a larger effective radius.

## 2.1 Introduction

The strongly enhanced surface plasmon resonance of noble metal nanoparticles at optical frequencies makes them excellent scatterers and absorbers of visible light.[1-3] Superior optical properties, coupled with recent advances in nanoparticle synthesis,[4] conjugation,[5] and assembly,[6] have stimulated interest in the use of plasmon-resonant nanoparticles and nanostructures for optical and photonic applications[7,8] and, more recently, for biomedical applications.[9-26] Nanoparticles composed of gold offer, in addition to their enhanced absorption and scattering, good biocompatibility, facile synthesis,[4] and conjugation to a variety of biomolecular ligands, antibodies, and other targeting moieties,[5] making them suitable for use in biochemical sensing and detection,[9-11] medical diagnostics, and therapeutic applications.[12,13] There have been several demonstrations of bioaffinity sensors based on the plasmon absorption and scattering of nanoparticles[9,10] and their assemblies.[11]

Another notable use of gold nanoparticles has been as contrast agents in cellular and biological imaging.[14-17] Contrast agents in medical and biological imaging[18] improve the sensitivity and diagnostic ability of the imaging modality by site specifically labeling tissues or cells of interest. Cellular imaging utilizing microscopy techniques and immunotargeted optical contrast agents provides anatomic details of cells and tissue architecture important for diagnosis of cancer as well as other disorders. Biomedical imaging contrast agents have been traditionally based on photoabsorbing and fluorescent dyes such as malachite green and rhodamine-6G.[19] More recently, quantum dots have been used and studied for biological and cell imaging due to their unique size-dependent fluorescence properties.[20,21] However, the potential human toxicity and cytotoxicity of the

semiconductor material are two major problems for its in vitro and in vivo application. Colloidal gold nanoparticles have become an important alternative as imaging agents due to their potential noncytotoxic, facile immunotargeting[5] as well as due to their non-susceptibility to photobleaching or chemical/thermal denaturation, a problem commonly associated with dyes.[22] Immunogold nanoparticles conjugated to antibodies have been widely used for biological labeling and staining for electron microscopy.[23] Recently, strongly absorbing nanoparticles composed of gold have been shown to offer excellent promise for cell and tissue imaging by using techniques such as multiphoton plasmon resonance microscopy[14] and photoacoustic tomography.[15] Similarly, the strong light scattering of gold nanoparticles has been exploited for real-time optical imaging of precancer by using confocal reflectance microscopy.[16] El-Sayed et al. have demonstrated differentiation of cancerous cells from noncancerous cells by dark field light-scattering imaging and absorption spectroscopy of solid ~40 nm gold nanospheres immunotargeted to epidermal growth factor receptor overexpressed on cancer cells.[17] Along with cancer imaging and diagnostic applications, the ability of gold nanoparticles to efficiently convert absorbed light into localized heat can be readily employed for therapy based on photothermal destruction of cancerous cells.[24-28] For example, Hirsch et al.[24] employed NIR absorbing silica-gold core-shell particles for photothermal destruction of human breast carcinoma cells in vitro as well as solid tumors in vivo. Recently, Loo et al.[25] reported simultaneous imaging and therapy of breast cancers in vitro using silica-gold nanoshells that were conjugated with anti-Her2 antibodies. El-Sayed et al. and Huang et al. used immunotargeted nanospheres of solid gold for imaging and selective photothermal destruction of cancer cells by Ar laser irradiation.[26,27] More recently, Huang

et al. provided an in vitro demonstration of gold nanorods conjugated to anti-EGFR antibodies as novel contrast agents for both NIR cell imaging and photothermal cancer therapy.[28]

The effectiveness of nanoparticles as biomedical imaging contrast and therapeutic agents depends on their optical properties. For instance, a high-scattering cross-section is essential for cell imaging applications based on light-scattering microscopy. On the other hand, effective photothermal therapy with minimal laser dosage requires a high nanoparticle absorption cross-section with low scattering losses. Biosensing applications based on surface plasmon resonance shifts necessitate strong resonance in the wavelength sensitivity range of the instrument as well as narrow optical resonance line widths.[29] For actual in vivo imaging and therapeutic applications, the optical resonance of the nanoparticles is strongly desired to be in the near-infrared (NIR) region of the biological water window, where the tissue transmissivity is the highest.[30] In addition, the nanoparticle size is also an important consideration for nanoparticle uptake and retention by cells and tissue.[31]

It is well-known that the plasmon resonance of metal nanoparticles is strongly sensitive to the nanoparticle size, shape, and the dielectric properties of the surrounding medium. Optical properties of gold nanoparticles can thus be readily tuned by varying their size and shape.[1,2,32-34] In addition, Halas and co-workers have shown that the use of composite nanoparticles based on a core-shell morphology (e.g., silica-gold nanoshells) allows optical tunability by variation in the composition.[35]

There have been several experimental reports[2,36] on the optical properties of metal nanoparticles, including gold nanospheres, [33,34,36-42] nanorods,[33,34,36,43] and nanoprisms,[44]

silver nanospheres,[36,37,39,45-47] nanowires,[4] and nanoprisms,[49-52] copper nanospheres, [37,45,53] aluminum nanospheres,[36] bimetallic nanoparticles, [54,55] composite nanoparticles with a core-shell structure,[35,56-60] and nanoparticle chains and assemblies.[61-63] At the same time, well-established theoretical tools based on the Mie theory[64] and the discrete dipole approximation (DDA)[65] method have been readily exploited for a quantitative study of the nanoparticle optical properties of different size, shape, composition, and aggregation state, etc.[2,36,66-73]

In the work described in this chapter, we used Mie theory and the DDA method to calculate the absorption and scattering efficiencies and optical resonance wavelengths of gold nanospheres, silica-gold nanoshells, and gold nanorods, for various nanoparticle dimensions, so as to aid the selection of nanoparticles for specific biomedical applications. The calculated optical cross-sections of all three nanoparticle classes are found to be a few orders of magnitude higher than those for conventionally used absorbing and fluorescent dyes. Besides, the optical properties of nanoparticles, i.e., the optical resonance wavelength, the extinction cross-section, and the relative contribution of scattering to the extinction, are strongly dependent on the nanoparticle dimensions, allowing tunability for specific applications. For all three nanoparticle types, the increase in the size results in an increase in the extinction as well as the relative contribution of scattering. Nanospheres offer resonance wavelengths in the visible region, however, the tunability of the wavelength with size is too limited to be useful for in vivo biomedical applications. In the case of nanoshells, the resonance wavelength can be rapidly tuned in the NIR region by either changing the total nanoshell size or the ratio of the core/shell radius. Similarly, the optical resonance of nanorods can be linearly tuned across the near-

infrared region by changing either the effective size or the aspect ratio of the nanorods. To compare the effectiveness of nanoparticles of different size for real-life biomedical applications, size normalized optical cross-sections or per micron coefficients have been calculated. Gold nanorods on account of an order of magnitude higher per micron absorption and scattering coefficients, combined with easy resonance tunability and lack of cytotoxicity, are concluded to offer the best imaging contrast as well as the highest effectiveness for photothermal therapy applications.

## 2.2 Calculation Methods

The optical properties of gold nanospheres, nanorods, and silica-gold nanoshells were quantified in terms of their calculated absorption and scattering efficiency ($Q_{abs}$ and $Q_{sca}$) and their optical resonance wavelength ($\lambda_{max}$).

### 2.2.1 Gold Nanospheres and Silica-Gold Nanoshells.

For nanospheres of gold, $Q_{abs}$ and $Q_{sca}$ were calculated on the basis of Mie theory for homogeneous spheres[64] by using MiePlot which implements the BHMIE code. The Mie total extinction and scattering efficiency $Q_{ext}$ and $Q_{sca}$ for a homogeneous sphere are expressed as infinite series:

$$Q_{ext} = \frac{2}{x^2} \sum_{n=1}^{\infty} (2n+1) \mathrm{Re}\left[a_n + b_n\right] \qquad (1)$$

$$Q_{sca} = \frac{2}{x^2} \sum_{n=1}^{\infty} (2n+1)\left[a_n^2 + b_n^2\right] \qquad (2)$$

$$Q_{abs} = Q_{ext} - Q_{sca} \qquad (3)$$

$$a_n = \frac{m \psi_n(mx) \psi_n'(x) - \psi_n(x) \psi_n'(mx)}{m \psi_n(mx) \xi_n'(x) - m \xi_n(x) \psi_n'(mx)} \qquad (4)$$

$$b_n = \frac{\psi_n(mx) \psi_n'(x) - m \psi_n(x) \psi_n'(mx)}{\psi_n(mx) \xi_n'(x) - m \xi_n(x) \psi_n'(mx)} \qquad (5)$$

where m is the ratio of refractive index of the sphere n to that of the surrounding medium $n_m$, x is the size parameter given as $2\pi n_m R / \lambda$, $\psi_n$ and $\xi_n$ are the Riccati-Bessel functions, and the prime represents first differentiation with respect to the argument in parentheses. Numerical calculations of the Mie series were performed at discrete points in the wavelength range from 300 to 800 nm.

Calculations of the optical absorption and scattering efficiency of silica-gold nanoshells were performed by using a computer code employing Mie scattering for concentric sphere geometry developed by Ivan Charamisinau.[74] The required parameters for the code were the value of the core and shell radii, $R_1$ and $R_2$ (note that due to an error in the program the correct input needed is half of these values) and the complex refractive indices for the core, shell, and the surrounding medium, $n_c$, $n_s$, and $n_m$, respectively. $n_c$ was taken to be $1.44 + 0i$ for the silica core at all wavelengths. For gold, values of the complex dielectric function at different wavelengths were obtained from Johnson and Christy[75] and corrected for nanoparticle size.[76,77] Cubic interpolation was used to calculate the complex refractive indices at intermediate wavelengths, where data was not available directly from Johnson and Christy. The embedding medium for both nanospheres and nanoshells was considered to be water with a refractive index $n_m$ of $1.33 + 0i$. The results of the Mie code for core-shell particles were checked against the Mie theory results for homogeneous spheres for three cases: vanishing shell, vanishing core,

and vanishing refractive index difference between core and shell materials. There was excellent agreement in the calculated $Q_{abs}$ and $Q_{sca}$ by the two methods, verifying the accuracy of the Mie code for core-shell particles. In the case of nanospheres, the diameter D of the particles is the only size variable. Mie theory calculations were performed for three different sizes, i.e., D = 20, 40, and 80 nm, corresponding to the size range of gold nanospheres used in earlier demonstrations of light-scattering imaging[16,17] and selective photothermal destruction of cancer cells.[26,27] Mie parameters were also evaluated for 300-nm diameter polystyrene nanospheres, so as to serve as a basis for comparison of the optical properties of the metal nanoparticles. A refractive index value of 1.56 + 0i was used for polystyrene at all wavelengths. Nanoshells, on the other hand, can be defined by two distinct variables: the total particle radius $R_2$ and the ratio of the core radius to the shell radius $R_1/R_2$. Calculations for nanoshells were performed for two different cases: first, at a fixed $R_2$ of 70 nm and $R_1$ varying as 40, 50, and 60 nm, and second, for a fixed $R_1/R_2 = 0.857$ and $R_2 = 70$, 105, and 140 nm.

## 2.2.2 Gold Nanorods

The calculation of the optical extinction, absorption, and scattering efficiency of gold nanorods was performed by another group member Kyeong-Seok Lee using the discrete dipole approximation (DDA) method,[65] which has been regarded as one of the most powerful and flexible electrodynamic methods for computing the optical properties of particles with an arbitrary geometry. For this calculation, we adopted the DDA code developed by Draine and Flatau[65] and characterized the gold nanorod case with fixed target orientation, where the propagation direction of the incident light was assumed to be perpendicular to the optic axis of the nanorod. Only two orthogonal polarizations of

incident light were considered in the calculation, one with an electric field parallel to the optic axis and another that is perpendicular to it. The gold nanorod was considered to have the geometry of a cylinder capped with two hemispheres. It is common to specify the size of a particle of an arbitrary shape and volume V in terms of an effective radius given by $r_{eff} = (3V/4\pi)^{1/3}$, which represents the radius of a sphere having a volume equal to that of the particle. Thus, $r_{eff}$ defines the volume of the nanorod. An additional defining size variable in case of nanorods is the aspect ratio (R), i.e., the ratio of the nanorod dimension along the long axis to that along the short axis. The calculations were therefore carried out for two different cases, one for nanorods with a fixed effective radius (and hence volume) $r_{eff} = 11.43$ nm but different aspect ratios of 3.1, 3.9, and 4.6 and the other for nanorods with a fixed R of 3.9 but different $r_{eff}$ of 8.74, 11.43, 17.9, and 21.86 nm. Dielectric function for gold was assumed to be the same as that of the bulk metal.[75] The refractive index of the surrounding medium was considered to be 1.34 + 0i at all wavelengths, close to that of water. Details of the DDA calculations for nanorods have been described elsewhere.[68]

## 2.3 Results and Discussion

### 2.3.1 Gold Nanospheres

Figure 2.1 shows the calculated spectra of the efficiency of absorption $Q_{abs}$, scattering $Q_{sca}$, and extinction $Q_{ext}$ for gold nanospheres (D = 20, 40, and 80 nm) and polystyrene nanospheres (D = 300 nm). The dimensionless efficiencies $Q_{abs}$, $Q_{sca}$, and $Q_{ext}$ can be converted to the corresponding cross-sections $C_{abs}$, $C_{sca}$, and $C_{ext}$ by multiplication with the cross-sectional area of the nanoparticle. $C_{abs}$, $C_{sca}$, and $C_{ext}$ have

units of $m^2$ because they represent an equivalent cross-sectional area of the particle that contributes to the absorption, scattering, and extinction of the incident light. The cross-sections can also be directly related to the molar coefficients measured by spectrophotometry. It is seen that the optical cross-sections of the gold nanospheres are typically 4-5 orders of magnitude higher compared to those of conventionally used dyes. For instance, gold nanospheres with a diameter of 40 nm, which have been successfully used by El-Sayed et al.[26] and Huang et al.[27] for laser photothermal destruction of cancer cells, have a calculated absorption cross-section of 2.93 x $10^{-15}$ $m^2$ (thus corresponding to a molar absorption coefficient $\varepsilon$ of 7.66 x $10^9$ $M^{-1}$ $cm^{-1}$)[78] at a plasmon resonance wavelength maximum $\lambda_{max}$ of 528 nm. This value is 5 orders larger than the molar extinction coefficient for indocyanine green ($\varepsilon$ = 1.08 x $10^4$ M-1 cm-1 at 778 nm),[79] a NIR dye commonly used in laser photothermal tumor therapy.[80,81] Similarly other strongly absorbing dyes such as rhodamine-6G ($\varepsilon$ = 1.16 x $10^5$ $M^{-1}$ $cm^{-1}$ at 530 nm)[82] and malachite green ($\varepsilon$ = 1.49 x $10^5$ $M^{-1}$ $cm^{-1}$ at 617 nm)[82] have 4 orders much lower absorption as compared to the nanoparticles.

In addition, the magnitude of visible light scattering by the metal nanoparticles ($C_{sca}$ = 1.23 x $10^{-14}$ $m^2$ at 560 nm for 80-nm gold nanospheres) is comparable to the scattering from the much larger 300-nm polystyrene nanospheres ($C_{sca}$ = 1.77 x $10^{-14}$ $m^2$ at 560 nm), which are commonly used in confocal imaging of cells.[83] The light emission from fluorescent molecules such as fluorescein ($\varepsilon$ = 9.23 x $10^4$ $M^{-1}$ $cm^{-1}$ with a quantum yield of 0.98 at 483 nm),[82] also commonly used in imaging is 5 orders of magnitude lower than the light scattering from the 80-nm gold nanospheres ($C_{sca}$ = 1.23 x $10^{-14}$ $m^2$ corresponding to a molar scattering coefficient of 3.22 x $10^{10}$ $M^{-1}$ $cm^{-1}$). The superior
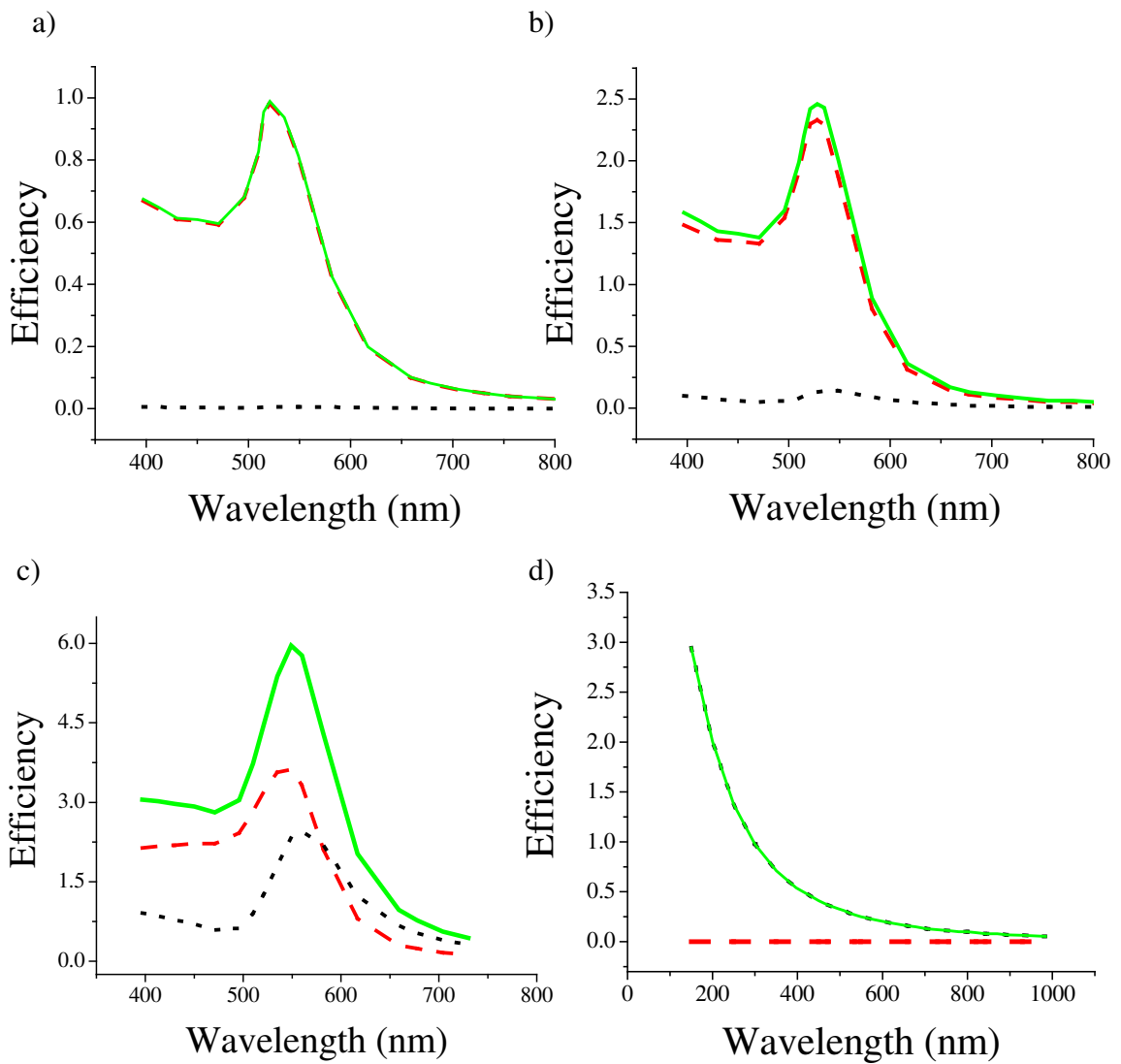
Figure 2.1: Calculated spectra of the efficiency of absorption $Q_{abs}$ (red dashed), scattering $Q_{sca}$ (black dotted) and extinction $Q_{ext}$ (green solid) for gold nanospheres (a) D = 20 nm, (b) D = 40 nm, (c) D = 80 nm, and (d) polystyrene nanospheres D = 300 nm.

scattering properties of gold nanospheres have already been exploited for the selective imaging of cancer cells by using simple dark field microscopy[17] and confocal

microscopy.[16] The strongly enhanced absorption and scattering of metal nanoparticles as compared to polystyrene nanospheres or dyes is attributable to the well-known surface plasmon oscillation of electrons of the metal nanoparticle.[2,36]

### 2.3.2 Silica-Gold Nanoshells

Calculated spectra of $Q_{abs}$, $Q_{sca}$, and $Q_{ext}$ for various dimensions of the silica-gold nanoshells (i.e., $R_1$ = 40 nm $R_2$ = 70 nm, $R_1$ = 50 nm $R_2$ = 70 nm, $R_1$ = 60 nm $R_2$ = 70 nm, $R_1$ = 90 nm $R_2$ = 105 nm, $R1$ = 120 nm $R_2$ = 140 nm, and $R_1$ = 120 nm $R_2$ = 155 nm) are shown in Figure 2.2. The nanoshells show absorption and scattering cross-sections ($C_{abs}$ = 5.09 x $10^{-14}$ m$^2$, $C_{sca}$ = 3.25 x $10^{-14}$ m$^2$ for $R_1$ = 60 nm $R_2$ = 70 nm nanoshell) that are comparable to and even higher in magnitude than those of solid gold nanospheres. Additionally, the nanoshell optical resonance lies in the NIR region ($\lambda_{max}$ = 892 nm for $R_1$ = 60 nm $R_2$ = 70 nm), where biological tissue transmissivity is the highest[30] and away from the hemoglobin visible absorption around 500-600 nm.[84] Thus the nanoshells are much more suited to in vivo imaging and therapy applications as compared to the gold nanospheres. Silica-gold nanoshells have been successfully employed in experimental demonstrations by Hirsch et al.[24] and Loo et al.[25] However, there have been concerns about the potential carcinogenicity of the silica material of the nanoshell core.[85] It would thus be highly desirable to have nanoparticles of solid gold with NIR absorption. However, as seen in Figure 2.4a, change in the nanosphere size does not provide the
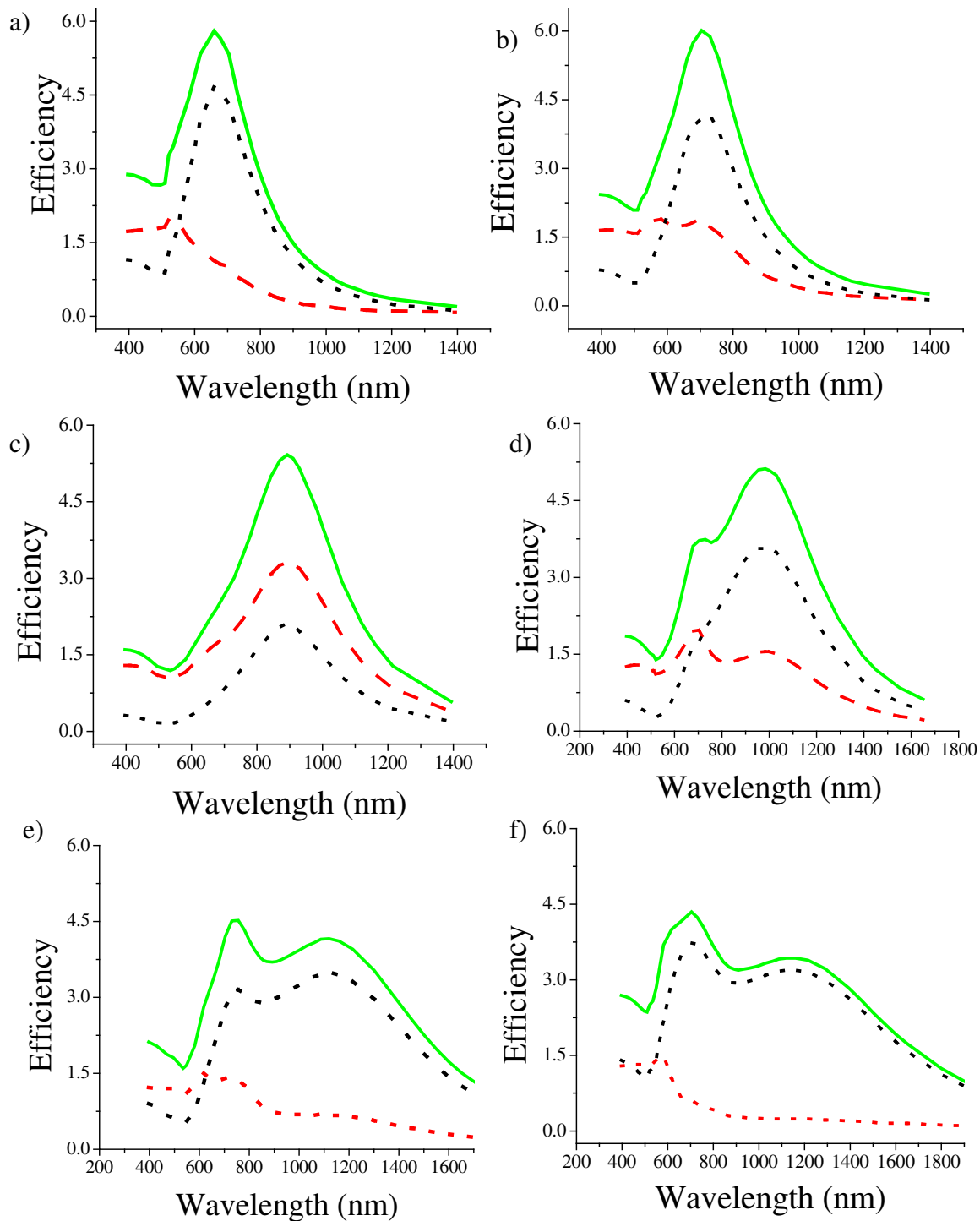
Figure 2.2: Calculated spectra of the efficiency of absorption $Q_{abs}$ (red dashed), scattering $Q_{sca}$ (black dotted) and extinction $Q_{ext}$ (green solid) for silica-gold nanoshells with dimensions (a) $R_1 = 40$ nm $R_2 = 70$ nm, (b) $R_1 = 50$ nm $R_2 = 70$ nm, (c) $R_1 = 60$ nm $R_2 = 70$ nm, (d) $R_1 = 90$ nm $R_2 = 105$ nm, (e) $R_1 = 120$ nm $R_2 = 140$ nm and (f) $R_1 = 120$ nm $R_2 = 155$ nm.

desired tunability in the optical resonance. In fact, it is known that pure gold nanospheres have resonance around 528 nm for different sizes from tens to 100 nm.[33]

### 2.3.3 Gold Nanorods

It is well-known that, by changing the shape of nanoparticles to that of elongated rods, the optical characteristics can be significantly changed.[2,33,34,36,43,73] Gold nanorods possess, in addition to the surface plasmon band around 528 nm seen in gold nanospheres, a band at longer wavelengths due to the plasmon oscillation of electrons along the long axis of the nanorods.[2,33,34,36,43,73] The calculated absorption, scattering, and extinction spectra of the surface plasmon band of gold nanorods have been shown in Figure 2.3. Figure 2.3a shows calculations for nanorods with a fixed aspect ratio R of 3.9 and effective radius $r_{eff}$ = 8.74, 11.43, 17.90, and 21.86 nm. Calculations for a fixed $r_{eff}$ (and hence volume) of 11.43 nm but with different aspect ratios R = 3.1, 3.9 and 4.6 are shown in Figure 2.3b. The figure shows that the plasmon maximum of the nanorods (corresponding to the mode with the electric field parallel to the long axis of the nanorod) lie in the desirable NIR region, thus making gold nanorods potentially useful for in vivo applications. The magnitude of their NIR absorption and scattering ($C_{abs}$ = 1.97 x $10^{-14}$ $m^2$ and $C_{sca}$ = 1.07 x $10^{-14}$ at $\lambda_{max}$ = 842 nm for nanorods with $r_{eff}$ = 21.86 nm, R = 3.9) is comparable to that of the nanospheres and nanoshells, at a much smaller size or volume.

a)
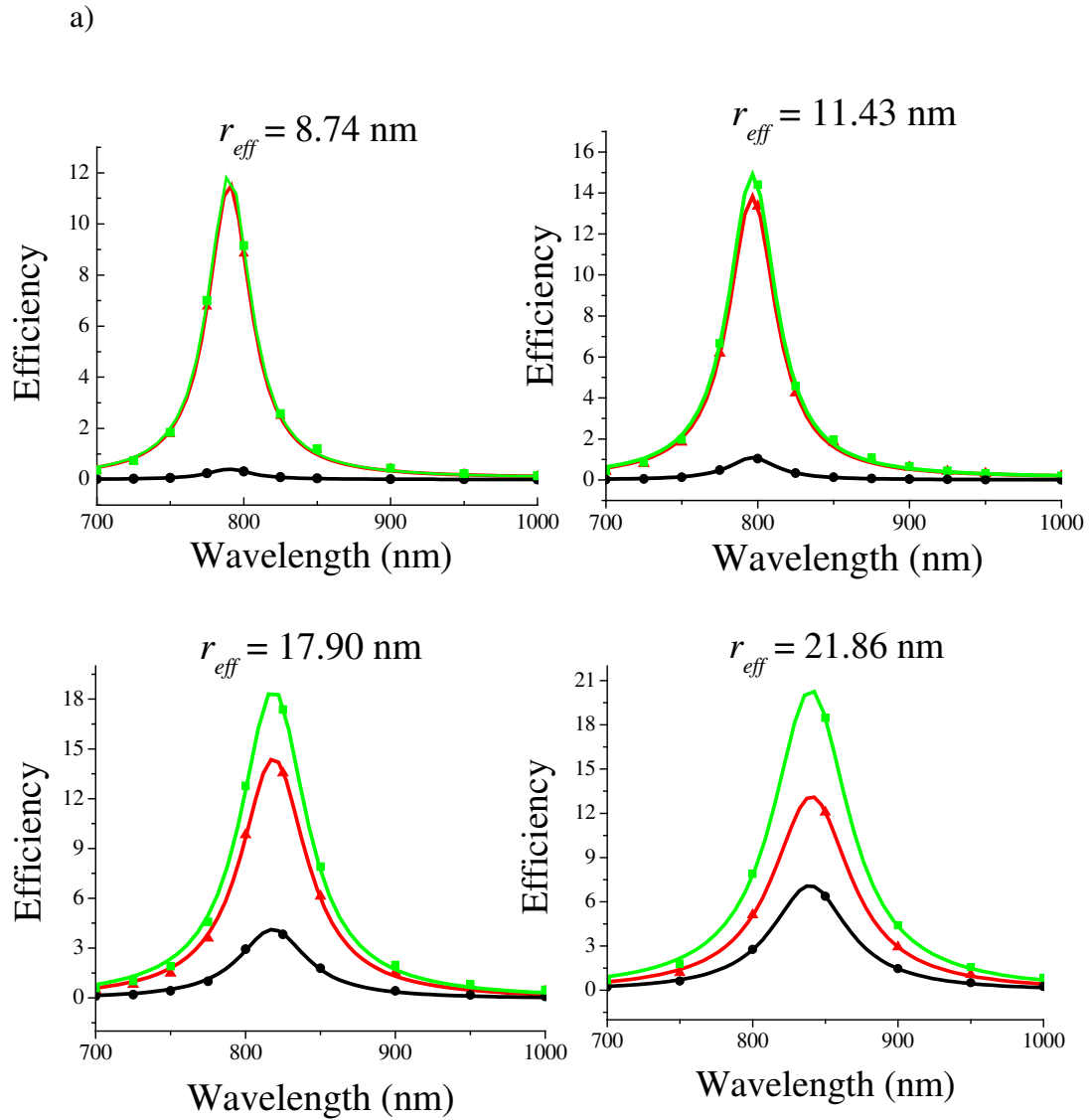


Figure 2.3: Calculated spectra of the efficiency of absorption $Q_{abs}$ (red triangles), scattering $Q_{sca}$ (black circles) and extinction $Q_{ext}$ (green squares) for gold nanorods (a) with fixed aspect ratio R = 3.9 and $r_{eff}$ = 8.74, 11.43, 17.90 and 21.86 nm and (b) with fixed effective radius $r_{eff}$ = 11.43 nm and R = 3.1, 3.9 and 4.6. Note the solid curves are Lorentzian fits to the calculated data points.

b)
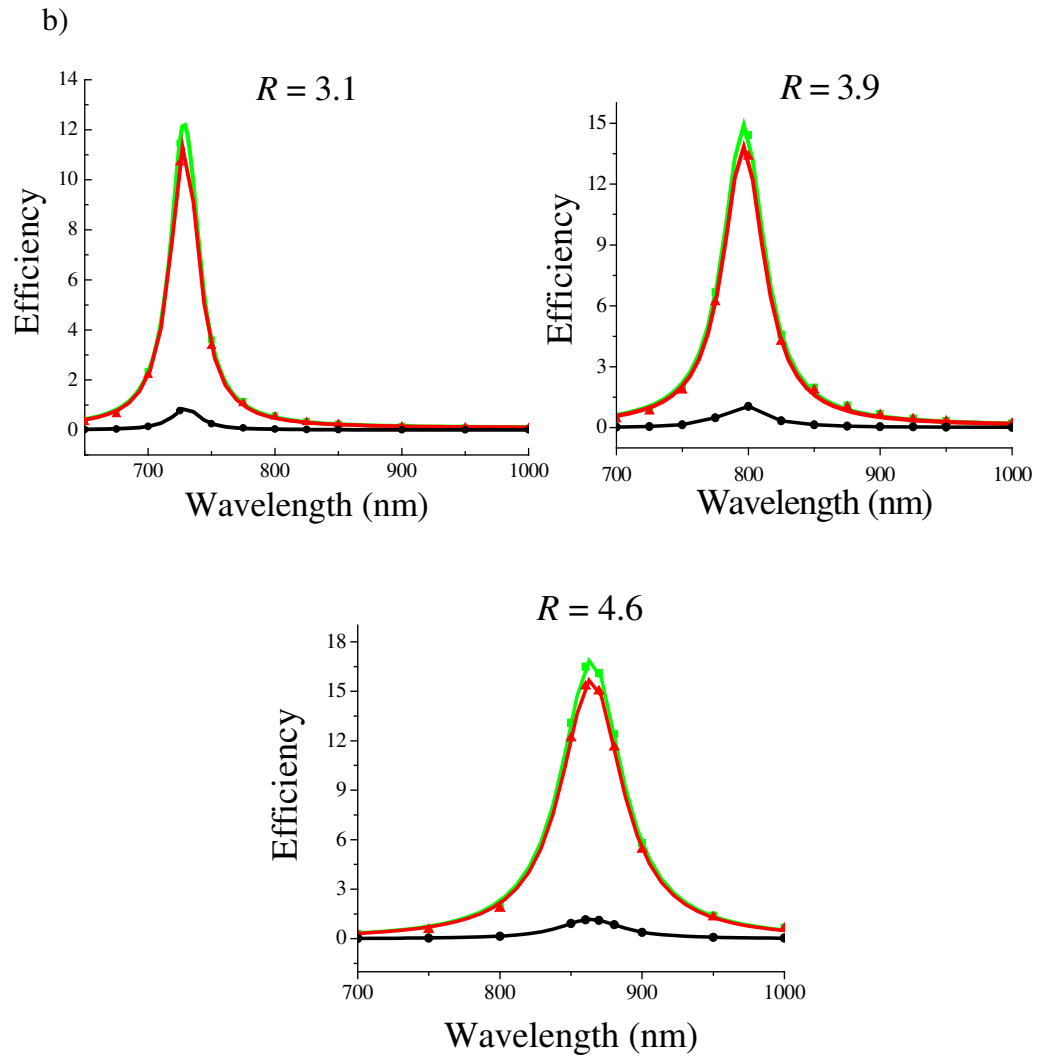


Figure 2.3 continued
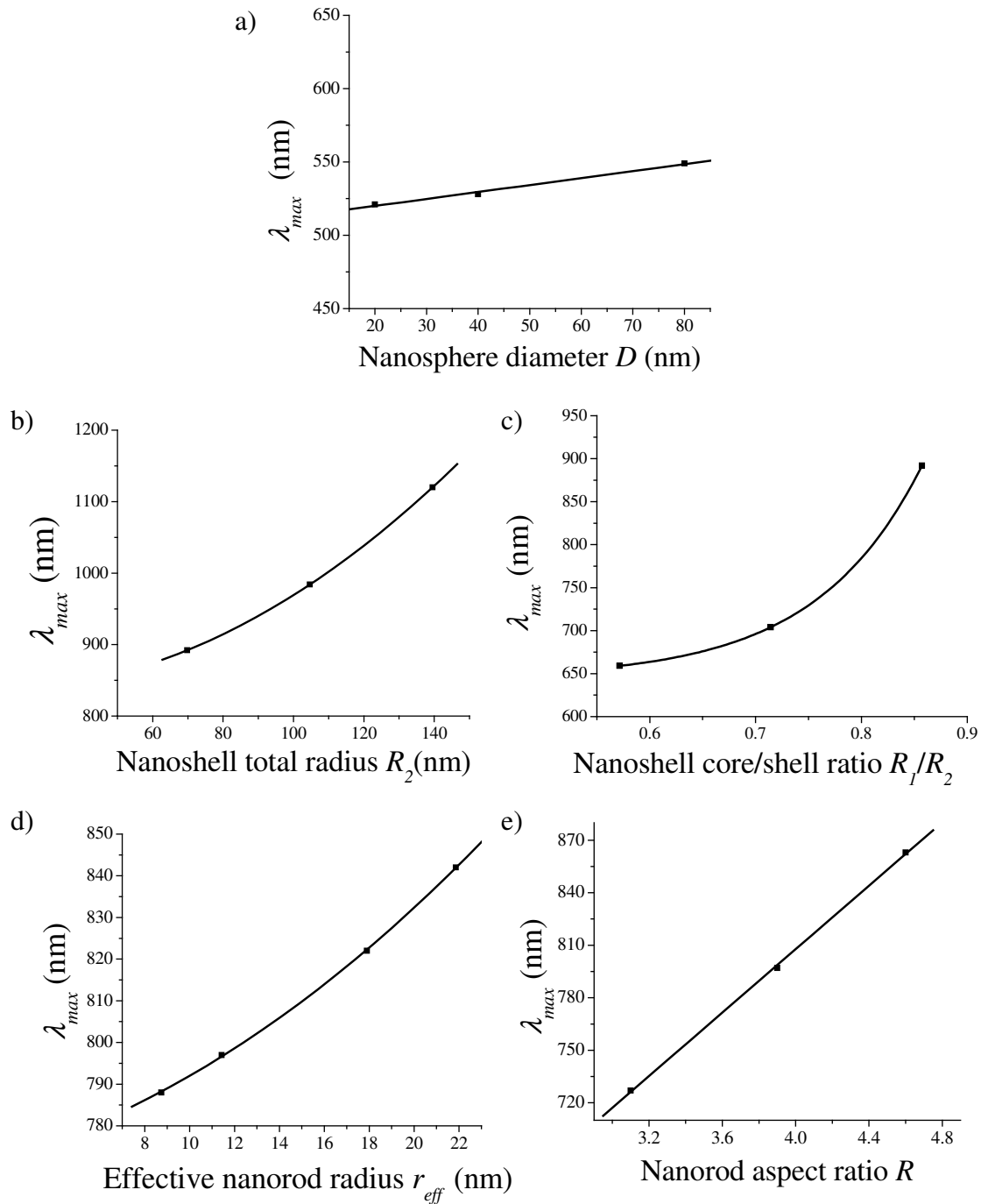
Figure 2.4: Tunability of the plasmon resonance maximum in nanoparticles. Variation of surface plasmon extinction maximum $\lambda_{max}$ with (a) nanosphere diameter D (b) nanoshell total radius $R_2$ at fixed $R_1/R_2 = 0.857$ (c) nanoshell core/shell ratio $R_1/R_2$ at fixed $R_2 = 70$ nm (d) nanorod effective radius $r_{eff}$ at fixed aspect ratio R = 3.9 (e) nanorod aspect ratio R at fixed $r_{eff}$ = 11.43 nm (and straight line fit).

**2.3.4 Optical Tunability**

The calculated spectra for different nanoparticle types clearly reflect the well-known fact[2,33,34,36] that the surface plasmon resonance wavelength as well as the extent of the plasmon enhancement is highly dependent on the size, shape, and core-shell composition of the nanoparticles, thus allowing easy optical tunability, which is lacking in the case of dyes. To aid the selection of an appropriate nanoparticle for a suitable biomedical application, a systematic quantitative discussion of the trends in the optical tunability of nanoparticles follows.

2.3.4.1 Dependence of the Plasmon Resonance Maximum on Nanoparticle Dimensions

Figure 2.4 summarizes the dependence of the nanoparticle plasmon resonance wavelength maximum $\lambda_{max}$ on the nanoparticle dimensions. Figure 2.4a shows the plot of ìmax versus the nanosphere diameter D. With increase in the nanosphere diameter from 20 to 80 nm, there is a small red-shift in the $\lambda_{max}$ from ~520 to 550 nm. Similar red-shift has been observed in the measured optical spectra of gold nanoparticles and is attributed to the effect of electromagnetic retardation in larger nanoparticles.[2,34,36,38,39,66,86] Nevertheless, changing the diameter D of the nanospheres does not offer sufficient change in the surface plasmon resonance maximum to be useful in the present applications. On the other hand, the optical resonance wavelength of nanoshells can be easily tuned by variation in their dimensions. As shown in Figure 2.4b, the nanoshell $\lambda_{max}$ can be increased by increasing the total nanoshell radius $R_2$ while keeping $R_1/R_2$ fixed. Alternatively, Figure 2.4c shows that the $\lambda_{max}$ can be tuned by changing the relative core-shell dimensions $R_1/R_2$ at a fixed total nanoshell size $R_2$. In other words, reducing the shell thickness shifts $\lambda_{max}$ to longer wavelengths. In the case of larger nanoshells, the

spectra show additional resonance peaks having strong intensity at shorter wavelengths as compared to the dipolar plasmon resonance. For example, for the nanoshell configuration with $R_1$ = 120 nm $R_2$ = 140 nm, a resonance peak can be seen around 756 nm in addition to the dipolar band at 1120 nm (Figure 2.2e). An additional resonance can also be seen in the case of $R_1$ = 120 nm $R_2$ = 155 (Figure 2.2f). These additional resonances arise from quadrupolar oscillations in the nanoshells of larger size (comparable to the light wavelength) Similar multipolar excitation has been observed in the theoretical spectra of large triangular nanoprisms of gold calculated by Shuford et al.,[69] in which case three distinct peaks corresponding to the multipole orders l = 1, 2, 3 were seen at progressively shorter wavelengths. Multipolar resonance peaks in the nanoshells serve to provide additional wavelength tunability.[57] Silica-gold nanoshells of various dimensions have been synthesized by Halas and co-workers, and such optical tunability has been experimentally demonstrated.[35,57,59] In the case of nanorods, the plasmon resonance maximum (corresponding to the mode with the electric field parallel to the nanorod axis) can be shifted by either a change in size or aspect ratio. Figure 2.4d shows the change in nanorod $\lambda_{max}$ by changing the effective radius (hence volume) of the nanorod at a fixed aspect ratio. The linear dependence of $\lambda_{max}$ on the nanorod aspect ratio R ($\lambda_{max}$ = 445.4 + 90.6R) at a fixed effective radius is shown in Figure 2.4e. Similar dependence has been seen in experiments from Mohamed et al.[87] and simulations for nanorods based on Gans theory.[73] Gold nanorods can be synthesized by wet chemical[88] as well as electrochemical methods[89] in a range of aspect ratios from 2.0 to 18.0,[90] thus allowing for experimental tunability of the optical resonance wavelength. From the point of view of imaging applications, size tunability of the resonance wavelength in gold nanoparticles would

allow multicolor labeling of different cell structures, similar to that allowed by quantum dots with size-dependent fluorescence.[20,21]

## 2.3.4.2 Dependence of Total Extinction Cross-section and Scattering/Absorption Ratio on Nanoparticle Dimensions

Two trends in the optical cross-sections with variation in nanoparticle size are uniform across different nanoparticle types. As seen in Figure 2.5a, $C_{ext}$ for nanospheres increases as the nanosphere size is increased. This trend has been commonly observed in experiments[33,34] and reflects the direct dependence of the nanosphere extinction cross-section on the sphere volume in Mie theory (when the dipole mode contributes predominantly).[2,36] At the same time, with increasing nanosphere diameter, the relative contribution of scattering to the total extinction $C_{sca}/C_{abs}$ increases as seen from Figure 2.6a. The magnitude of the extinction increases linearly with the total nanoshell size $R_2$ as seen from the plot in Figure 2.5b and rapidly with the effective radius $r_{eff}$ in the case of nanorods (Figure 2.5d). The relative scattering contribution increases with increase in the total nanoshell size $R_2$ (Figure 2.6b) and the effective radius $r_{eff}$ in the case of nanorods (Figure 2.6d). The increase in the ratio of scattering to absorption with the nanoparticle volume has been related to increased radiative damping in larger nanoparticles based on experimental scattering spectra of gold nanospheres and nanorods measured by Sönnichsen et al.[39,43] These trends suggest that larger nanoparticles would be more suitable for biological cell imaging applications based on light scattering, while those in the intermediate size range would serve as excellent photoabsorbers for laser photothermal therapy and applications based on absorption contrast. It can be seen that the change in the nanorod aspect ratio at a constant nanorod effective radius (or the

74

nanorod volume) does not result in any considerable effect on either the extinction cross-section or the ratio of scattering to absorption (Figures 2.5e and 2.6e). In the case of nanoshells, the relative core-shell dimensions do not have much effect on the magnitude of light extinction as long as the total nanoshell size (i.e., volume) is kept fixed (Figure 2.5c). However, a decrease in the core/shell ratio can be seen to be an effective handle in increasing the scattering contribution to the total extinction. For instance, a nanoshell with the configuration $R_1$ = 40 nm $R_2$ = 70 nm is dominantly scattering (Figure 2.2a), while a nanoshell with $R_1$ = 60 nm $R_2$ = 70 nm is a predominantly absorptive nanoparticle (Figure 2.2c). These trends in the nanoshell tunability have already been experimentally exploited by the Halas group for a dual cancer imaging and therapy approach.[24,25,91]

### 2.3.5 Size-Normalized Absorption and Scattering Cross-sections

The absolute magnitude of the optical cross-section does not provide a reliable measure for the optical properties of an ensemble of nanoparticles employed in real-life biomedical applications because smaller particles can be loaded in a given volume in greater numbers as compared to particles of a larger size. Therefore, a more meaningful property for comparison across a range of sizes is the size-normalized cross-section or volumetric coefficient C/V where V is the particle volume.[36] The volumetric coefficients expressed in units of $\mu m^{-1}$ give us the per micron absorption coefficient $\mu_a$ and scattering coefficient $\mu_s$ of the nanoparticles. Values of $\mu_a$ and $\mu_s$ have been tabulated (Table 2.1) for the different nanoparticle configurations. It can be seen from Table 2.1 that the nanoshell configuration used by Hirsch et al. and Loo et al. ($R_1$ = 60 nm, $R_2$ = 70 nm)[24,25] offers a combination of high $\mu_a$ (35.66 $\mu m^{-1}$) and $\mu_s$ (22.73 $\mu m^{-1}$) among all the different nanoshell
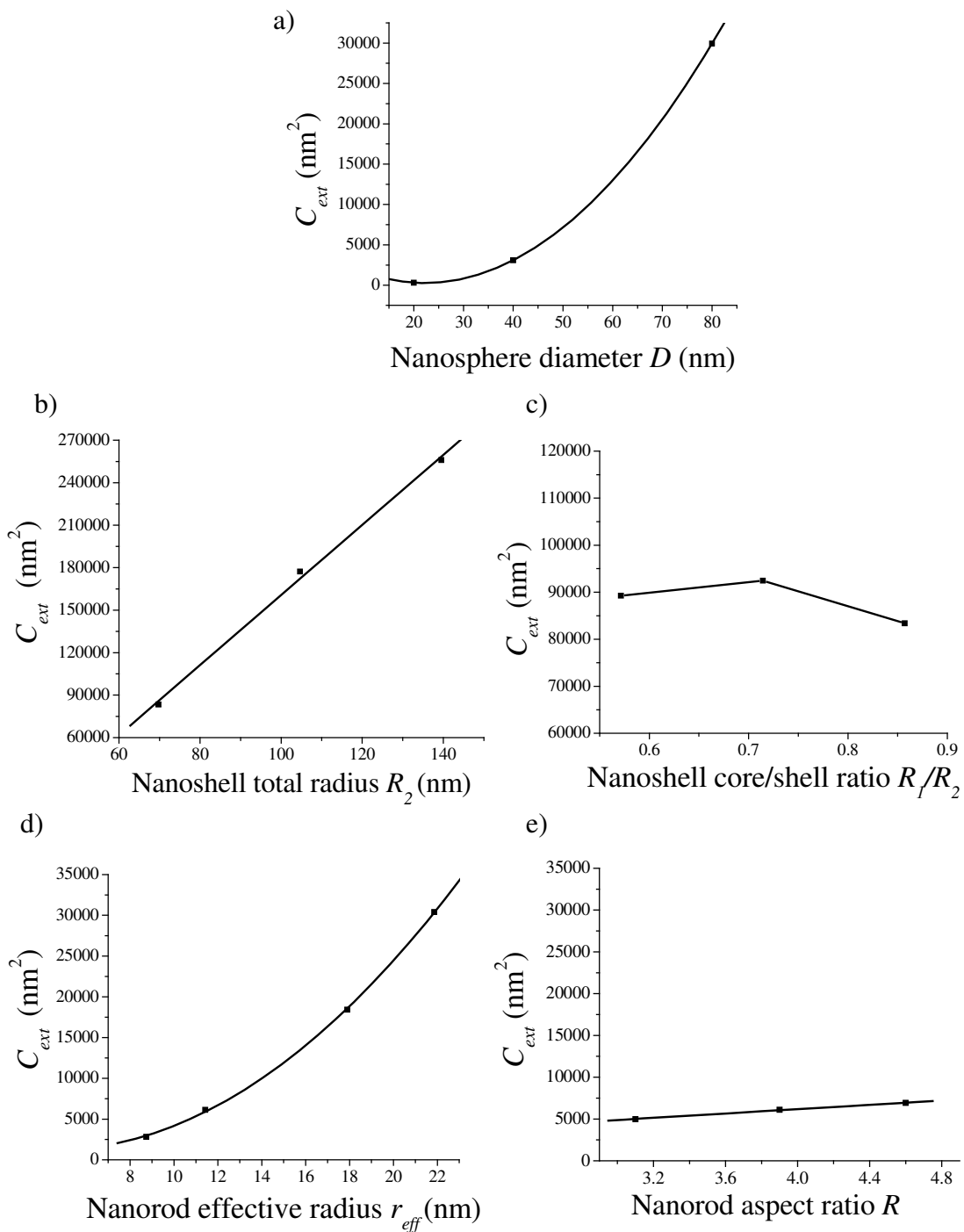
Figure 2.5: Tunability of the extinction cross-section of nanoparticles. Variation of $C_{ext}$ (in $nm^2$) with (a) nanosphere diameter D (b) nanoshell total radius $R_2$ at fixed $R_1/R_2 = 0.857$ (c) nanoshell core/shell ratio $R_1/R_2$ at fixed $R_2 = 70$ nm (d) nanorod effective radius $r_{eff}$ at fixed aspect ratio R = 3.9 (e) nanorod aspect ratio R at fixed $r_{eff} = 11.43$ nm.
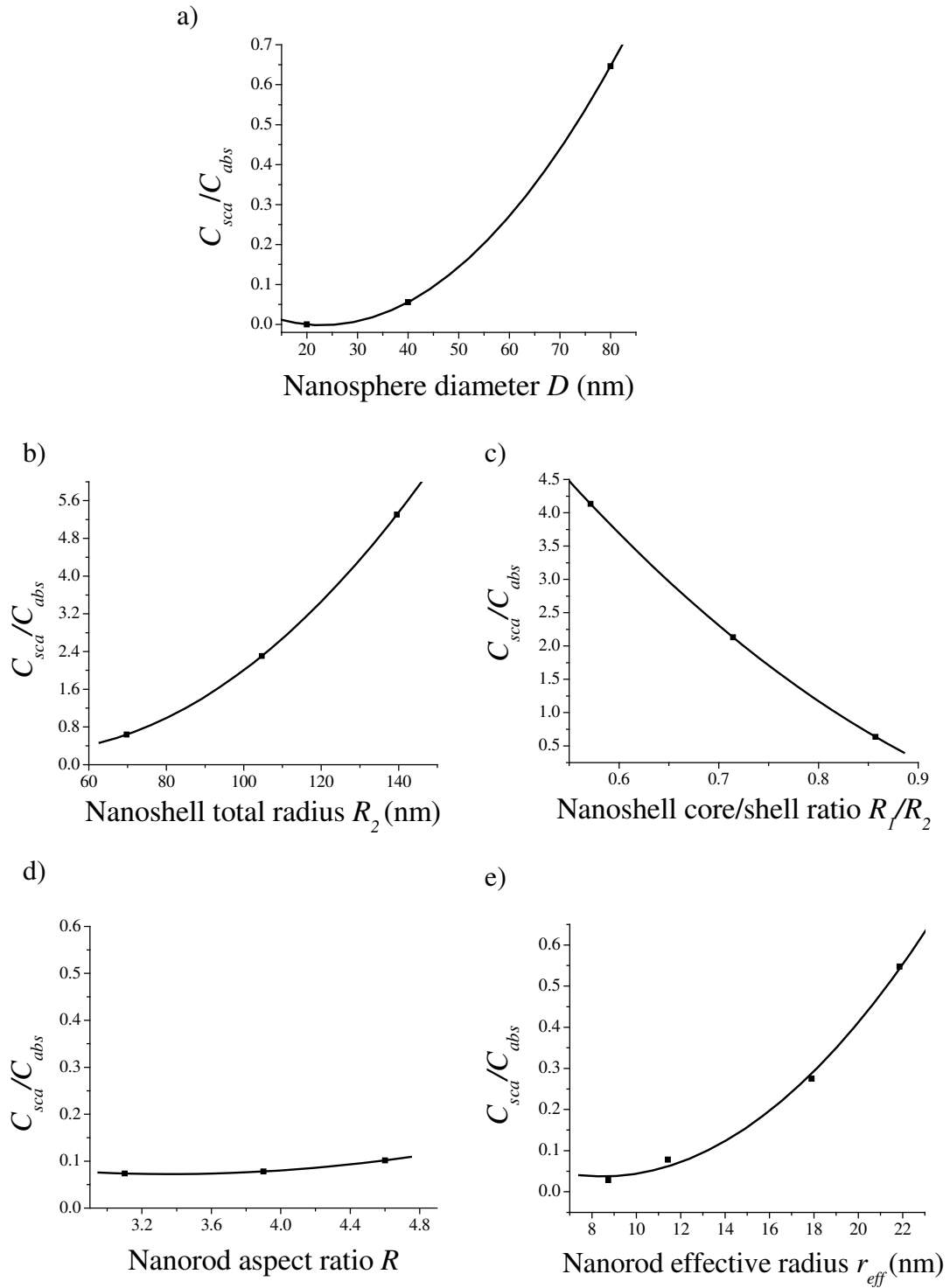
Figure 2.6: Tunability of the ratio of scattering to absorption of nanoparticles. Variation of $C_{sca}/C_{abs}$ with (a) nanosphere diameter D (b) nanoshell total radius $R_2$ at fixed $R_1/R_2 =$ 0.857 (c) nanoshell core/shell ratio $R_1/R_2$ at fixed $R_2 = 70$ nm (d) nanorod effective radius $r_{eff}$ at fixed aspect ratio R = 3.9 (e) nanorod aspect ratio R at fixed $r_{eff}$ = 11.43 nm.

configurations considered in our calculations, making them efficient agents for a dual imaging/therapy approach. The gold nanospheres have a higher $\mu_a$ than the nanoshells. Especially, the intermediate size nanospheres (D = 40 nm) employed in the earlier photothermal therapy experiments from our laboratory[26,27] offer the strongest photoabsorption with relatively low scattering among nanospheres. Larger nanospheres (e.g., D = 80 nm) offer better scattering properties. Gold nanorods have $\mu_a$ and $\mu_s$ values that are an order of magnitude higher than those of nanoshells and nanoparticles. While nanorods with a higher aspect ratio along with a smaller effective radius are the best photoabsorbers, the best scattering contrast for imaging is obtained from high-aspect ratio nanorods with a larger effective radius or volume.

## 2.4 Conclusion

To obtain a quantitative guide for selection of nanoparticles for light-scattering and absorption-based applications in biomedicine, a systematic study of the trends in the optical resonance wavelength, the extinction cross-section, and the relative contribution of scattering to the extinction with changes in the nanoparticle dimensions, was undertaken for three different classes of nanoparticles viz. silica-gold nanoshells, gold nanospheres, and gold nanorods. It was clearly evident from the calculated spectra that the optical properties of nanoparticles were highly dependent on the nanoparticle size, shape, and core-shell composition. All three nanoparticle types had optical cross-sections a few orders of magnitude higher than those of conventional dyes. For all three nanoparticle types, the increase in the size resulted in an increase in the extinction cross-

Table 2.1: Calculated Extinction Wavelength Maximum, Per Micron Absorption Coefficient, Per Micron Scattering Coefficient, and Ratio of Scattering to Absorption for Gold Nanospheres, Gold Nanorods, and Silica-Gold Nanoshells of Different Dimensions

| Nanoparticle type | Dimensions | $\lambda_{max}$ nm | $\mu_a (\lambda_a)$ $\mu m^{-1}$ (nm) | $\mu_s (\lambda_s)$ $\mu m^{-1}$ (nm) | $\mu_s / \mu_a$ |
|---|---|---|---|---|---|
| Silica-gold nanoshells | $R_1 = 36$ nm $R_2 = 40$ nm | 843 | 50.61 (843) | 4.31 (843) | 0.09 |
| Silica-gold nanoshells | $R_1 = 50$ nm $R_2 = 70$ nm | 704 | 20.57 (704) | 44.57 (730) | 2.17 |
| Silica-gold nanoshells | $R_1 = 60$ nm $R_2 = 70$ nm | 892 | 35.66 (892) | 22.73 (892) | 0.64 |
| Silica-gold nanoshells | $R_1 = 90$ nm $R_2 = 105$ nm | 984 | 11.07 (984) | 25.50 (984) | 2.33 |
| Silica-gold nanoshells | $R_1 = 120$ nm $R_2 = 140$ nm | 1120 | 7.61(730) | 18.75 (1120) | 2.44 |
| Silica-gold nanoshells | $R_1 = 120$ nm $R_2 = 155$ nm | 1160 | 7.26 (582) | 15.44 (1160) | 2.13 |
| Gold nanospheres | D = 20 nm | 521 | 73.72 (521) | 0.45 (535) | 0.01 |
| Gold nanospheres | D = 40 nm | 528 | 87.36 (528) | 5.25 (535) | 0.06 |
| Gold nanospheres | D = 80 nm | 549 | 67.88 (549) | 45.94 (560) | 0.68 |
| Gold nanorods | $R = 3.1$ $r_{eff} = 11.43$ nm | 727 | 741.86 (727) | 54.70 (727) | 0.07 |
| Gold nanorods | $R = 3.9$ $r_{eff} = 11.43$ nm | 797 | 907.09 (797) | 70.86 (797) | 0.08 |
| Gold nanorods | $R = 4.6$ $r_{eff} = 11.43$ nm | 863 | 1003.87 (863) | 102.05 (863) | 0.10 |
| Gold nanorods | $R = 3.9$ $r_{eff} = 8.74$ nm | 788 | 986.56 (792) | 34.49 (792) | 0.03 |
| Gold nanorods | $R = 3.9$ $r_{eff} = 17.90$ nm | 815 | 601.47 (817) | 172.32 (817) | 0.29 |
| Gold nanorods | $R = 3.9$ $r_{eff} = 21.86$ nm | 842 | 449.34 (842) | 242.58 (837) | 0.54 |

section as well as the relative contribution of scattering. However, nanoshells and nanorods were found more favorable for in vivo applications due to their tunable optical resonance in the NIR region. Moreover, their relative scattering to absorption contribution could be easily tuned by a change in their dimensions. For the comparison of the optical properties of nanoparticles across a range of sizes, size-normalized cross-sections were calculated. From the numerical comparison, the gold nanorods are seen to offer the most superior NIR absorption and scattering at much smaller particle sizes. Smaller sized nanorods may also offer better cell uptake[31] as compared to the larger nanoshells and nanospheres. This, in addition to the potential noncytotoxicity[92] of the gold material, easy optical tunability, and facile synthesis, makes gold nanorods the most promising nanoparticle agents for use in biomedical imaging and photothermal therapy applications.

## 2.5 References and Notes

(1)     McConnell, W. P.; Novak, J. P.; Brousseau, L. C., III; Fuierer, R. R.; Tenent, R. C.; Feldheim, D. L. *J. Phys. Chem. B* **2000**, *104*, 8925.

(2)     Kreibig, U.; Vollmer, M. *Optical Properties of Metal Clusters*; Springer: New York, 1995; and references therein.

(3)     Faraday, M. *Philos. Trans. R. Soc. London* **1857**, *147*, 145.

(4)     Burda, C.; Chen, X.; Narayanan, R.; El-Sayed, M. A. *Chem. Rev.* **2005**, *105*, 1025, and references therein.

(5)     Katz, E.; Willner, I. *Angew. Chem., Int. Ed.* **2004**, *43*, 6042 and references therein.

(6)     Mirkin, C. A. *Inorg. Chem.* **2000**, *39*, 2258.

(7)     Pendry, J. B. *Science* **1999**, *285*, 1687.

(8)     Maier, S. A.; Kik, P. G.; Atwater, H. A.; Meltzer, S.; Harel, E.; Koel, B. E.; Requicha, A. G. *Nat. Mater.* **2003**, *2*, 229-232.

(9)     Riboh, J. C.; Haes, A. J.; McFarland, A. D.; Ranjit, C.; Van Duyne, R. P. *J. Phys. Chem. B* **2003**, *107*, 1772.

(10)    Shafer-Peltier, K. E.; Haynes, C. L.; Glucksberg, M. R.; Van Duyne, R. P. *J. Am. Chem. Soc.* **2003**, *125*, 588.

(11)    Storhoff, J. J.; Elghanian, R.; Mucic, R. C.; Mirkin, C. A.; Letsinger, R. L. *J. Am. Chem. Soc*. **1998**, *120*, 1959.

(12)    Rosi, N. L.; Mirkin, C. A. *Chem. Rev.* **2005**, *105*, 1547 and references therein.

(13)    Chen, J.; Wiley, B. J.; Li, Z.-Y.; Campbell, D.; Saeki, F.; Cang, H.; Leslie, A.; Lee, J.; Li, X.; Xia, Y. *Adv. Mater.* **2005**, *17*, 2255 and references therein.

(14)    Yelin, D.; Oron, D.; Thiberge, S.; Moses, E.; Silberberg, Y. *Opt. Express* **2003**, *11*, 1385.

(15)    Wang, Y.; Xie, X.; Wang, X.; Ku, G.; Gill, K. L.; O'Neal, D. P.; Stoics, G.; Wang, L. V. *Nano Lett.* **2004**, *4*, 1689.

(16)    Sokolov, K.; Follen, M.; Aaron, J.; Pavlova, I.; Malpica, A.; Lotan, R.; Richards-Kortum, R. *Cancer Res.* **2003**, *63*, 1999.

(17)    El-Sayed, I. H.; Huang, X., El-Sayed, M. A. *Nano Lett.* **2005**, *5*, 829.

(18)    Grainger, R. G. *Br. J. Radiol.* **1982**, *55*, 1.

(19)    Bugaj, J. E.; Achilefu, S.; Dorshow, R. B.; Rajagopalan, R. *J. Biomed. Opt.* **2001**, *6*, 122.

(20)    Bruchez, M., Jr.; Moronne, M.; Gin, P.; Weiss, S.; Alivisatos, A. P. *Science* **1998**, *281*, 2013.

(21)    Chan, W. C. W.; Nie, S. *Science* **1998**, *281*, 2016.

(22)    Landsman, M. L. J.; Kwant, G.; Mook, G. A.; Zijlstra, W. G. *J. Appl. Physiol.* **1976**, *40*, 575.

(23)    Hayat, M. A. Colloidal Gold: Principles, Methods and Applications; Academic Press: San Diego, 1989; Vol. 1.

(24)    Hirsch, L. R.; Stafford, R. J.; Bankson, J. A.; Sershen, S. R.; Rivera, B.; Price, R. E.; Hazle, J. D.; Halas, N. J.; West, J. L. *Proc. Natl. Acad. Sci. U.S.A.* **2003**, *100*, 13549.

(25)    Loo, C.; Lowery, A.; Halas, N.; West, J.; Drezek, R. *Nano Lett.* **2005**, *5*, 709.

(26)    El-Sayed, I. H.; Huang, X.; El-Sayed, M. A. *Cancer Lett.* **2006**, *239*, 129.

(27)    Huang, X.; Jain, P. K.; El-Sayed, I. H.; El-Sayed, M. A. *Photochem. Photobiol.* **2006**, *82*, 412.

(28)    Huang, X.; El-Sayed, I. H.; Qian, W.; El-Sayed, M. A. *J. Am. Chem. Soc.* **2006**, *128*, 2115.

(29)    Aslan, K.; Lacowicz, J. R.; Geddes, C. R. *Curr. Opin. Chem. Biol.* **2005**, *9*, 538.

(30)    Weissleder, R. *Nat. Biotechnol.* **2001**, *19*, 316.

(31)    Zauner, W.; Farrow, N. A.; Haines, A. M. R. *J. Control. Rel.* **2001**, *71*, 39.

(32)    Underwood, S.; Mulvaney, P. *Langmuir* **1994**, *10*, 3427.

(33)    Link, S.; El-Sayed, M. A. *J. Phys. Chem. B* **1999**, *103*, 8410.

(34)    Link, S.; El-Sayed, M. A. *Int. Rev. Phys. Chem.* **2000**, *19*, 409.

(35)    Oldenburg, S. J.; Averitt, R. D.; Westcott, S. L.; Halas, N. J. *Chem. Phys. Lett.*
        **1998**, *288*, 243.

(36)    Bohren, C. F.; Huffman, D. R. *Absorption and Scattering of Light by Small
        Particles*; John Wiley: New York, 1983.

(37)    Heilmann, A.; Kreibig, U. *Eur. Phys. J.: Appl. Phys.* **2000**, *10*, 193.

(38)    Doremus, R. *J. Chem. Phys.* **1964**, *40*, 2389.

(39)    Sönnichsen, C.; Franzl, T.; Wilk, T.; von Plessen, G.; Feldmann, J. *New J. Phys.*
        **2002**, *4*, 1.

(40)    Scaffardi1, L. B.; Pellegri, N.; de Sanctis, O.; Tocho, J. O. *Nanotechnology* **2005**,
        *16*, 158.

(41)    Cini, M. *J. Opt. Soc. Am.* **1981**, *71*, 386.

(42)    Alvarez, M. M.; Khoury, J. T.; Schaaff, T. G.; Shafigullin, M. N.; Vezmer, I.;
        Whetten, R. L. *J. Phys. Chem. B* **1997**, *101*, 3706.

(43)    Sönnichsen, C.; Franzl, T.; Wilk, T.; von Plessen, G.; Feldmann, J.; Wilson, O.;
        Mulvaney, P. *Phys. Rev. Lett.* **2002**, *88*, 077402.

(44)    Millstone, J. E.; Park, S.; Shuford, K. L.; Qin, L.; Schatz, G. C.; Mirkin, C. A. *J.
        Am. Chem. Soc.* **2005**, *127*, 5312.

(45)    Kreibig, U. *J. Phys. F* **1974**, *4*, 999.

(46)    Doremus, R. *J. Chem. Phys.* **1964**, *42*, 414.

(47)    Pinchuk, A.; Hilger, A.; von Plessen, G.; Kreibig, U. *Nanotechnology* **2004**, *15*,
        1890.

(48)    Graff, A.; Wagner, D.; Ditlbacher, H.; Kreibig, U. *Eur. Phys. J. D* **2005**, *34*, 263.

(49)   Jin, R.; Cao, Y.; Mirkin, C. A.; Kelly, K. L.; Schatz, G. C.; Zheng, J. G. *Science* **2001**, *294*, 1901.

(50)   Pastoriza-Santos, I.; Marzán, L. M. *Nano Lett.* **2002**, *2*, 903.

(51)   Chen, S.; Carroll, D. L. *Nano Lett.* **2002**, *2*, 1003.

(52)   Sun, Y.; Mayers, B.; Xia, Y. *Nano Lett.* **2003**, *3*, 675.

(53)   Doremus, R.; Kao, S.; Garćıa, R. *Appl. Opt.* **1992**, *31*, 5773.

(54)   Hubenthal, F.; Ziegler, T.; Hendrich, C.; Alschinger, M.; Träger, F. *Eur. Phys. J. D* **2005**, *34*, 165.

(55)   Link, S.; Wang, Z. L.; El-Sayed, M. A. *J. Phys. Chem. B* **1999**, *103*, 3529.

(56)   Liz-Marzán, L. M.; Giersig, M.; Mulvaney, P *Langmuir* **1996**, *12*, 4329.

(57)   Oldenburg, S. J.; Hale, G. D.; Jackson, J. B.; Halas, N. J. *Appl. Phys. Lett.* **1999**, *75*, 1063.

(58)   Pastoriza-Santos, I.; Gomez, D.; Pérez-Juste, J. Liz-Marzán, L. M.; Mulvaney, P. *Phys. Chem. Chem. Phys.* **2004**, *6*, 5056.

(59)   Oldenburg, S. J.; Jackson, J. B.; Westcott, S. L.; Halas, N. J. *Appl. Phys. Lett.* **1999**, *75*, 2897.

(60)   Nehl, C. L.; Grady, N. K.; Goodrich, G. P.; Tam, F.; Halas, N. J.; Hafner, J. H. *Nano Lett.* **2004**, *4*, 2355.

(61)   Maier, S.; Kik, P. G.; Atwater, H. A. *Appl. Phys. Lett.* **2002**, *81*, 1714.

(62)   Storhoff, J. J.; Lazarides, A. A.; Mucic, R. C.; Mirkin, C.; Letsinger, R. L.; Schatz, G. C. *J. Am. Chem. Soc.* **2000**, *122*, 4640.

(63)     Félidj, N.; Truong, S. L.; Aubard, J.; Lévi, G.; Krenn, J. R.; Hohenau, A.; Leitner, A.; Aussenegg, F. R. *J. Chem. Phys.* **2004**, *120*, 7141.

(64)     Mie, G. *Ann. Phys.* **1908**, *25*, 377.

(65)     Draine, B. T.; Flatau, P. J. *J. Opt. Soc. Am. A* **1994**, *11*, 1491.

(66)     Kelly, K. L.; Coronado, E.; Zhao, L. L.; Schatz, G. C. *J. Phys. Chem. B* **2003**, *107*, 668 and references therein.

(67)     Schatz, G. C. *J. Mol. Struct.* **2001**, *573*, 73 and references therein.

(68)     Lee, K. S.; El-Sayed, M. A. *J. Phys. Chem. B* **2005**, *109*, 20331.

(69)     Shuford, K. L.; Ratner, M. A.; Schatz, G. C. *J. Chem. Phys.* **2005**, *123*, 114713.

(70)     Aden, A. L.; Kerker, M. *J. Appl. Phys.* **1951**, *22*, 1242.

(71)     Link, S.; Mohamed, M. B.; El-Sayed, M. A. *J. Phys. Chem. B* **1999**, *103*, 3073 and correction; Link, S.; El-Sayed, M. A. *J. Phys. Chem. B* **2005**, *109*, 10531.

(72)     Coronado, E. A.; Schatz, G. C. *J. Phys. Chem. B* **1999**, *119*, 3926.

(73)     Gans, R. *Ann. Phys.* **1915**, *47*, 270.

(74)     Charamisinau, I.; Happawana, G.; Evans, G.; Rosen, A.; Hsi, R. A.; Bour, D. *Appl. Opt.* **2005**, *44*, 5055.

(75)     Johnson, P. B.; Christy, R. W. *Phys. Rev. B* **1972**, *6*, 4370.

(76)     Averitt, R. D.; Sarkar, D.; Halas, N. J. *Phys. Rev. Lett.* **1997**, *78*, 4217.

(77)     Kreibig, U.; Genzel, L. *Surf. Sci.* **1985**, *156*, 678.

(78)     The relationship between the extinction cross-section ($C_{ext}$ in $m^2$) and the molar extinction coefficient ($\varepsilon$ in $M^{-1}$ $cm^{-1}$) is expressed as $C_{ext} = 0.2303\ \varepsilon/N_A$ where $N_A$ is Avogadro's number.

(79)     Urbanska, K.; Romanowska-Dixon, B.; Matuszak, Z.; Oszajca, J.; Nowak-Sliwinska, P.; Stochel, G. *Acta Biochim. Pol.* **2002**, *43*, 387.

(80)     Chen W. R.; Adams R. L.; Carubelli, R.; Nordquist, R. E. *Cancer Lett.* **1997**, *115*, 25.

(81)     Chen, W. R.; Adams R. L.; Higgins A. K.; Bartels K. E.; Nordquist, R. E. *Cancer Lett.* **1996**, *98*, 169.

(82)     Du, H.; Fuh, R. A.; Li, J.; Corkan, A.; Lindsey, J. S. *Photochem. Photobiol.* **1998**, *68*, 141.

(83)     Smithpeter, C.; Dunn, A.; Drezek, R.; Collier, T.; Richards-Kortum, R. *J. Biomed. Opt.* **1998**, *3*, 429.

(84)     Schenkman, K. A. *Crit. Care Med.* **2002**, *30*, 267.

(85)     World Health Organization International Agency for Research on Cancer, http://www-cie.iarc.fr/monoeval/grlist.html.

(86)     Aizpurua, J.; Hanarp, P.; Sutherland, D. S.; Ka¨ll, M.; Bryant, G. W.; García de Abajo, F. J. *Phys. Rev. Lett.* **2003**, *90*, 057401.

(87)     Mohamed, M. B.; Ismail, K. Z.; Link, S.; El-Sayed, M. A. *J. Phys. Chem. B* **1998**, *102*, 9370.

(88)     Murphy, C. J.; Jana, N. R. *Adv. Mater.* **2002**, *14*, 80.

(89)     Yu, Y.; Chang, S.; Lee, C.; Wang, C. R. C. *J. Phys. Chem. B* **1997**, *101*, 6661.

(90)     Jana, N. R.; Gearheart, L.; Murphy, C. J. *J. Phys. Chem. B* **2001**, *105*, 4065.

(91)    Loo, C.; Lin, A.; Hirsch, L.; Lee, M.-H.; Barton, J.; Halas, N.; West, J.; Drezek, R. *Technol. Cancer Res. Treat.* **2004**, *3*, 33.

(92)    Connor, E. E.; Mwamuka, J.; Gole, A.; Murphy, C. J.; Wyatt, M. D. *Small* **2005**, *1*, 325.

# CHAPTER 3

# COUPLING BETWEEN METAL NANOPARTICLES IN SOLUTION-PHASE AGGREGATES: EFFECT ON ELECTRON RELAXATION DYNAMICS

## Abstract

We report the effect of assembly or aggregation in gold nanoparticles on their electron-phonon relaxation dynamics measured by ultrafast femtosecond transient absorption pump-probe spectroscopy. UV-visible extinction and transient absorption of the solution-stable aggregates of gold nanoparticles show a broad absorption in the 550-700-nm region in addition to the isolated gold nanoparticle plasmon resonance. This broad red-shifted absorption can be attributed to contributions from gold nanoparticle aggregates with different sizes and/or different fractal structures. The electron-phonon relaxation, reflected as a fast decay component of the transient bleach, is found to depend on the probe wavelength, suggesting that each wavelength interrogates one particular subset of the aggregates. As the probe wavelength is changed from 520 to 635 nm across the broad aggregate absorption, the rate of electron-phonon relaxation increases. The observed trend in the hot electron lifetimes can be explained on the basis of an increased overlap of the electron oscillation frequency with the phonon spectrum and enhanced interfacial electron scattering, with increasing extent of aggregation. The experimental

results strongly suggest the presence of inter-colloid electronic coupling within the nanoparticle aggregates, besides the well-known dipolar plasmon coupling.

### 3.1 Introduction

Noble metal nanoparticles are fascinating materials with great nanotechnological potential because of their unique and strongly size-dependent electronic, chemical, and optical properties.[1,2] In the past few years there has been a strong interest in the self-assembly of nanoparticles into 1-D chains,[3] dense 2-D and 3-D superlattices,[4] and Langmuir-Blodgett films.[5] The Alivisatos and Mirkin groups have developed protocols for assembling Au nanoparticles based on site-selective DNA hybridization.[6,7] Various experiments on such assembled systems have shown the emergence of novel physical properties due to the interaction between nanoparticles.[8,9] There is a great motivation to exploit the unique properties of these assembled materials for electronic and optical device applications. A great deal of effort has been devoted to the study of the optical properties of such nanoparticle assemblies. Nanoparticle assemblies with very short interparticle separations (comparable to the nanoparticle size) show a whole new absorption band in the 600-950-nm region in addition to the nanoparticle plasmon absorption because of strong internanoparticle interaction.[10-12] Interparticle interactions regulate various linear and nonlinear optical properties, for example, surface-enhanced Raman scattering (SERS),[9,13] two-photon absorption (TPA), and four-wave mixing (FWM), of nanoparticles embedded in matrices or assembled into thin films at a high volume fraction.[14]

It has been suggested that many applications of materials assembled from metal nanoparticles might be based upon their ultrafast response to optical excitation. They have potential applications in ultrafast optical switching[15] and as hot electron sources for photoelectrochemical processes, such as solar energy conversion or organic waste reduction.[16] For applications such as these, it would be ideal to be able to tune their optical response and excitation lifetime. Tunability would be especially useful in the case of hot electron transfer to an electron acceptor where, to be effective, the electron cooling process should be slower than the time scale required for trapping and relaxation by the electron acceptor.[17] It is essential to have a detailed understanding of the electron dynamics in such nanoparticle assemblies before such applications can be realized.

Optical excitation of the conduction electrons in metal nanoparticles (without appreciable heating of the nanoparticle lattice) by means of ultrashort laser pulses has emerged as a powerful tool for probing the electron dynamics within these systems.[18,19] The energy of the photoexcited electrons is rapidly (within a few hundred femtoseconds) spread over the entire electron distribution via electron-electron scattering.[20] Comprehensive information about electron-electron scattering in conducting metals may be found in Kaveh et al.[21] and the references contained therein. The excited or "hot" Fermi electron distribution subsequently relaxes by exchanging energy with the nanoparticle lattice phonon modes (known as electron-phonon relaxation) on the time scale of few picoseconds. This is followed by phonon-phonon heat flow to the surrounding medium proceeding to equilibrium in several picoseconds, depending on the nanoparticle size and the thermal conductivity of the surrounding medium.[22-24] The electron-phonon relaxation process in colloidal gold nanoparticles has been well studied

by femtosecond pump probe spectroscopic techniques in our lab[24-26] as well as other groups[27,28] and has been found to be on the time scale of ~1 ps (at the lower limit of the excitation laser power), similar to that in bulk gold. The electron-phonon relaxation time was observed to be independent of the size or shape of the nanoparticles in these studies.[25-28] However, Del Fatti et al.,[29] Stella et al.,[30] Nisoli et al.,[31] and Perner et al.[32] observed size-dependent electron-phonon relaxation dynamics in silver, gallium, and tin nanoparticles.

Although there are numerous studies on the size dependence of electron relaxation in metal nanoparticles, the effect of aggregation or assembly of these nanoparticles on their electron phonon relaxation dynamics has not been given much attention. Spatial and electromagnetic coupling between nanoparticles in an aggregate can be expected to have a considerable effect on the electron-phonon relaxation dynamics within these structures. For instance, Scherer and co-workers[33] studied the hot electron relaxation in thin films assembled from ~12-nm gold nanoparticles and demonstrated a decrease in the hot electron lifetimes with increasing aggregation, as characterized by the thickness of the nanoparticle film. Recently, Zhang and coworkers[34] observed coherent vibrational oscillation in gold nanoparticle aggregates prepared by the addition of $Na_2S$. The period of oscillation was found to increase as the probe wavelength was increased across the broadband absorption of the aggregates.

Although the optical properties of interacting nanoparticles have been studied mostly on nanoparticle assemblies formed on a substrate,[10,12,13,33,35] in the current work, we study the optical absorption and electron-phonon relaxation dynamics of stable aggregates of ~13-nm gold nanoparticles in solution. The solution has a wide distribution

of aggregate sizes and fractal structures, as reflected in their broad absorption (550-700 nm) in addition to the characteristic plasmon absorption of the individual nanoparticles centered around 520 nm, in steady state UV-visible extinction as well as in the transient absorption spectra. The electron-phonon relaxation dynamics within the aggregates, as measured by femtosecond transient absorption spectroscopy, is found to be significantly faster than that in the case of isolated gold nanoparticles and is seen to be probe wavelength-dependent. It has been suggested that probing at a particular wavelength interrogates a particular subset of the aggregates (with a particular size and/or fractal structure), that has a maximal absorption in the probe wavelength region.[34] Consistent with this suggestion, we find that as the probe wavelength is varied from 520 to 635 nm across the broadband absorption of the aggregates, the electron-phonon relaxation becomes progressively faster. Increase in the electron-phonon relaxation rate across the broad aggregate spectrum can be correlated to an enhanced overlap of the electronic oscillation frequency with the phonon spectrum as well as increased interfacial electron scattering with increasing extent of aggregation.

## 3.2 Experimental Section

### 3.2.1 Synthesis and Controlled Aggregation of Gold Nanoparticles

Gold nanoparticles (av diameter 13.1 nm) were prepared by the citrate reduction of chloroauric acid.[36] Solution-stable nanoparticle aggregates were synthesized by the controlled addition of cationic surfactant cetyl trimethyl ammonium bromide (CTAB) (commonly used as a template in gold nanorod synthesis[37]) to the gold colloid in order to neutralize the negatively charged citrate-capped surface of the nanoparticles and thus

initiate their aggregation.[38] To prevent the formation of very large aggregates, which eventually precipitate out, polyvinyl-pyrrolidone (PVP) was added to the solution as a stabilizing agent and the solution was allowed to aggregate for several days. Typically, 4 µL of a 0.5 mM solution of CTAB was added to 1 mL of the gold colloid with a nanoparticle concentration of ~11 nM, followed by addition of PVP (av MW = 55000) to the solution, up to a final concentration of 0.01 M. The solution was stirred and further allowed to aggregate for 6 days. The synthesized sample was characterized by its UV-visible extinction (400-800 nm) on a Shimadzu UV-3101-PC spectrophotometer in transmission mode. A dilute solution of the nanoparticle aggregates was spotted on a carbon-coated copper grid and imaged by TEM (Figure 3.1).

### 3.2.2 Pump-Probe Study of Hot Electron Relaxation Dynamics in Nanoparticle Aggregates

To study electron-phonon relaxation dynamics in gold nanoparticle aggregates by femtosecond transient absorption spectroscopy,[23] a pump-probe setup was employed. A frequency-doubled Nd:vanadate laser (Coherent Verdi) was used as the pump for the Ti:sapphire laser system (Clark MXR CPA 1000), which generated laser pulses of 100-fs duration (fwhm) with energy of 1 mJ at 800 nm at a repetition rate of 1 kHz. The pump beam was chopped mechanically with a light beam chopper (HMS 221). The second harmonic of the 800-nm fundamental at 400 nm was used as the pump for the optical excitation of the nanoparticle aggregates in solution placed under constant stirring in an optical cell (path length = 2 mm). The diameter of the laser focus spot on the sample was 100 µm. The laser pump pulse energy used in the experiments was reduced to less than 250 nJ with neutral density filters. A white-light continuum generated by focusing a
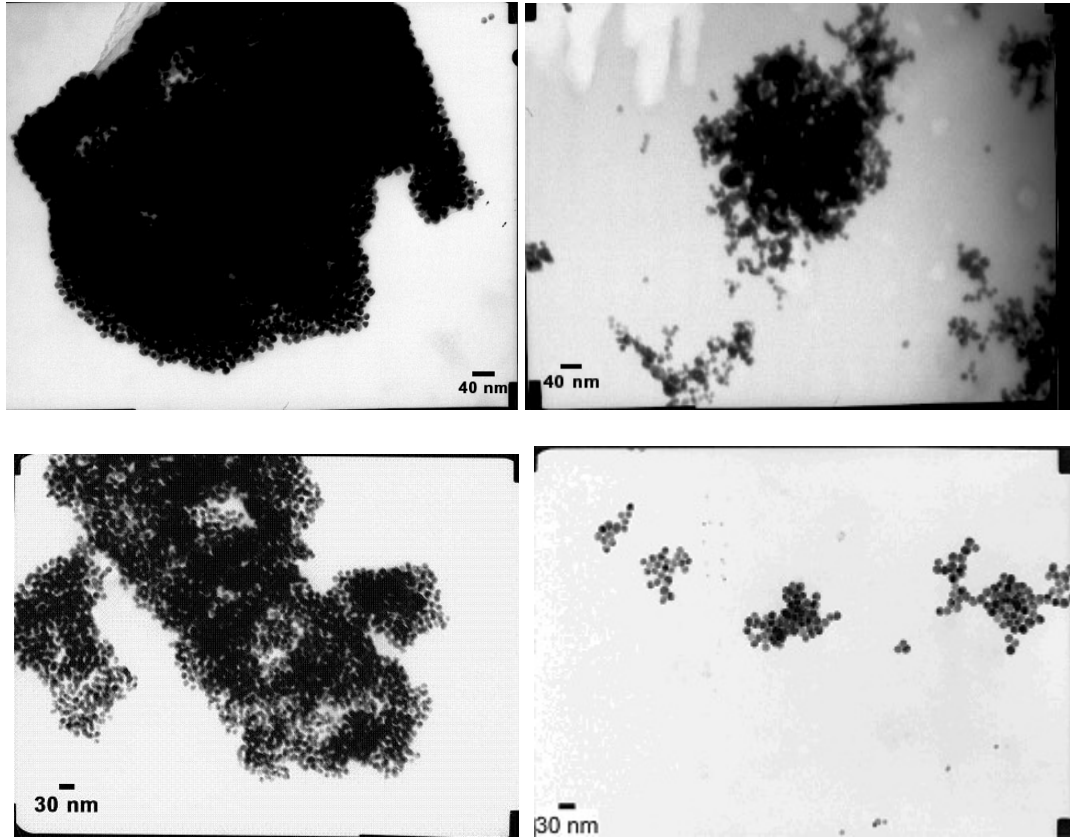
Figure 3.1: TEM images of the gold nanoparticle aggregates. Nanoparticles within the aggregate can be seen to be approximately spherical in shape rather than ellipsoidal and in close physical proximity with each other.

small portion (4%) of the 800-nm fundamental beam of the Ti:sapphire laser into a 1-mm

sapphire plate was used to probe the transient absorption of the sample at various delay

times (t). The differential transmission signal, S(t), was recorded with a pair of silicon

photodiodes (Thorlab) and a lock-in amplifier (Stanford Research Systems). The

recorded signal, S(t), can be expressed as:

$$S(\lambda, t) = \Delta T/T = (I_{\lambda,t} - I_{\lambda,0})/I_{\lambda,0} , \qquad (1)$$

where $\Delta T/T$ is the % change in the transmission of probe light, $I_{\lambda,t}$ is the intensity of the probe light at wavelength $\lambda$ after a delay time t from the pump laser heating pulse, and $I_{\lambda,0}$ is the intensity of the probe light at $\lambda$ without the pump. As a result, the recorded signal, $S(\lambda, t)$, represents a transient bleach, which results from the optical excitation of the free electron distribution within the nanoparticles. Using this setup, the transient absorption spectra (300-800 nm) of the aggregate solution at delay times of 0, 1, and 2 ps were recorded. It is known that the fast decay component of the transient bleach is a direct measure of the electron-phonon relaxation within the nanoparticle. Following this procedure, electron-phonon relaxation dynamics in the gold nanoparticle aggregates was measured in the low fluence regime and compared to the dynamics in isolated gold nanoparticles. The isolated gold nanoparticles were probed at their plasmon maximum at 520 nm, whereas the nanoparticle aggregates were probed at four different wavelengths (530, 565, 600, and 635 nm) across their broadband absorption.

## 3.3 Results and Discussion

### 3.3.1 Plasmon Absorption in Gold Nanoparticle Aggregates

Figure 3.2 shows the UV-visible extinction spectra (400-800 nm) of a solution of isolated ~13-nm gold nanoparticles (Figure 3.2a) and a solution of ~13-nm gold nanoparticle aggregates (Figure 3.2b). As compared to the gold nanoparticle colloid, the aggregate solution shows a broadened absorption at longer wavelengths (550-700 nm) with respect to the single particle surface plasmon resonance maximum at 520 nm. The observation of a red-shifted spectral structure in aggregated nanoparticles is well-known in the literature as being due to interactions between the closely spaced nanoparticles [39,40]
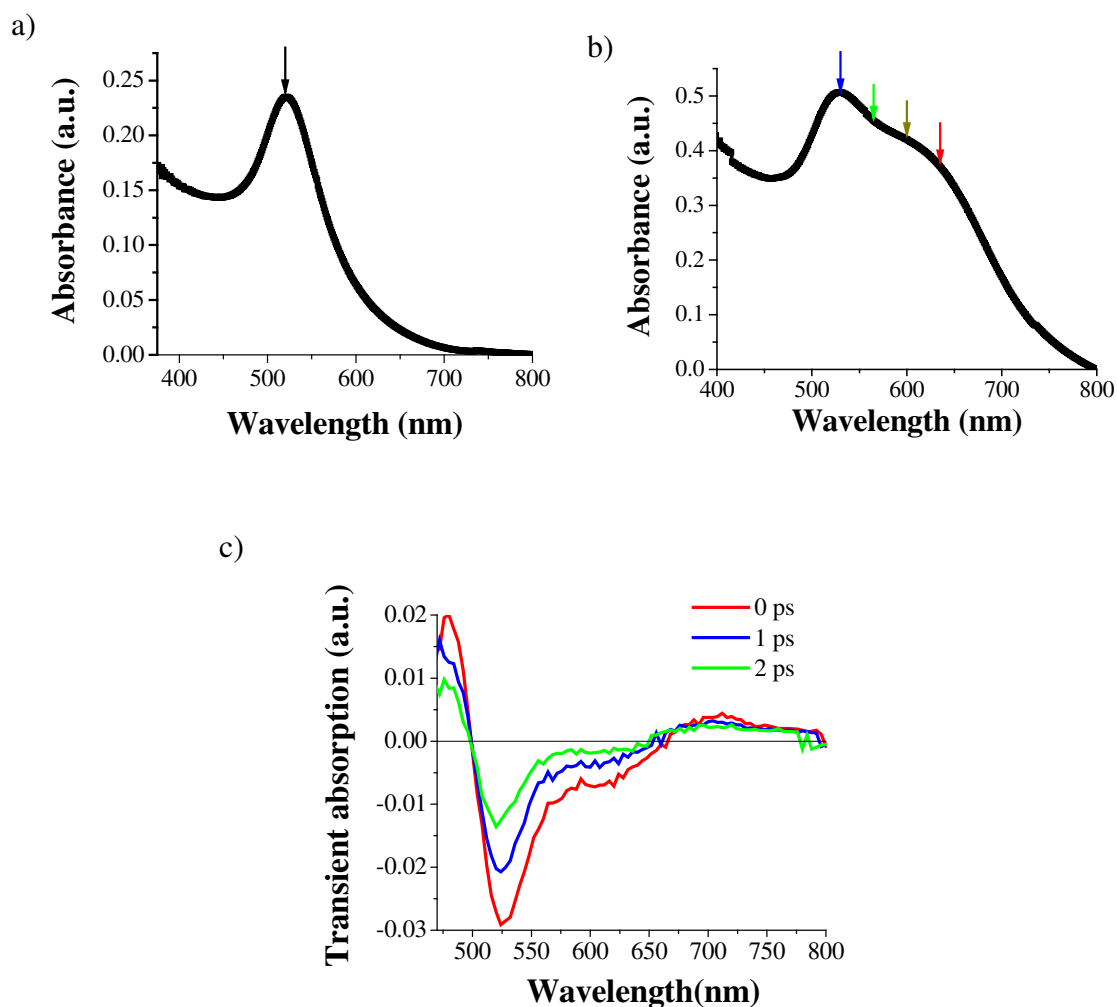
Figure 3.2: UV-visible extinction spectrum of (a) ~13 nm gold nanoparticle colloid, showing a peak absorption at 520 nm due to the surface plasmon resonance for isolated 13 nm nanoparticles (b) UV-visible extinction spectrum of a solution of ~13 nm gold nanoparticle aggregates showing a broad absorption in the region 550-700 nm, in addition to the plasmon band at 520 nm. The arrows indicate different wavelengths across the broadband absorption, at which the aggregates were probed for the femtosecond transient bleach dynamic studies (c) Transient absorption bleach spectra of gold nanoparticle aggregates recorded at delay times of 0, 1 and 2 ps after optical excitation by 400 nm 100 fs pulse. In addition to the peak in the transient bleach at 528 nm, a broad shoulder in the range 550-650 nm can be distinctly seen.

within the aggregates. The organic molecules CTAB and PVP do not have visible absorption to account for the spectral changes on aggregation. Similar spectral features are observed when aggregation is carried out by addition of an electrolyte (e.g., NaCl) to the citrate-capped nanoparticles or on addition of excess single-stranded DNA oligonucleotides that bind to the gold nanoparticle surface and link them together.[41] Previous studies have also shown very similar spectral features in closely assembled gold nanoparticle structures.[12,13] The transient absorption spectrum (Figure 3.2c) of the nanoparticle aggregates shows a peak at 528 nm due to a transient bleach resulting from the femtosecond optical excitation of the metal free electrons, similar to that seen in isolated gold nanoparticles.[23] However, an additional shoulder in the 550-650 nm range can be seen clearly in the aggregate transient absorption. The red-shifted absorption resulting from the aggregation, as confirmed by estimations of Mie extinction from nanoparticle clusters, is due to strong dipolar electromagnetic (EM) coupling between the plasmons of closely spaced nanoparticles in the aggregate (as seen in Figure 3.1), thus shifting the net plasmon resonance to lower frequencies.[42] The extent of the plasmon absorption shift depends on the degree of interparticle coupling within an individual aggregate; consequently, the plasmon resonance is at relatively longer wavelengths for larger aggregate sizes and aggregate structures with closely spaced nanoparticles.[43] The absorption of the aggregate solution is broad because of the contribution from various absorption sub-bands corresponding to different aggregate sizes and/or fractal structures, distributed in the solution. We expected relaxation dynamics of the nanoparticle aggregates to be different when probed at different wavelengths along the broad absorption band seen in their steady-state UV-vis and transient absorption spectra.

**3.3.2 Electron-Phonon Relaxation Dynamics in Gold Nanoparticle Aggregates**

Figure 3.3 shows the transient bleaching dynamics of the nanoparticle aggregates probed at 530 nm for two different pulse energies, that is, 40 nJ/pulse and 90 nJ/pulse. It is well known that the rise of the transient bleach is a result of electron-electron scattering within the gold nanoparticles on the time scale of 300-500 fs, whereas the fast decay of the transient bleach can be related directly to the dynamics of relaxation of the
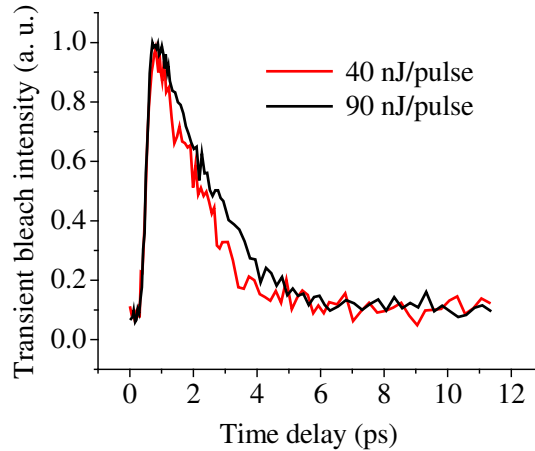


Figure 3.3: Power-dependence of transient bleach dynamics in gold nanoparticle aggregates probed at 530. 100 fs pulses at 400 nm were used as the pump, at two different pulse energies, 40 nJ/pulse (red) and 90 nJ/pulse (black). The rise and decay of the transient bleaching were fit to an exponential function of the form $(1-\exp(-t/\tau_r)).\exp(-t/\tau_d)$ so as to obtain a hot electron lifetime $\tau_d$ of $1.64 \pm 0.07$ ps at 37 nJ/pulse and $1.72 \pm 0.09$ ps at 90 nJ/pulse.

photoexcited electrons by exchanging energy with the nanoparticle phonon modes on the time-scale of ~1 ps and slower decay because of phonon-phonon coupling on longer time scales ~100 ps within the nanoparticles.[44,45] The limited time resolution of our laser pump

pulse (100 fs) does not allow us to study the much faster electron-electron scattering processes. The essential result in our experiments is thus the creation of an excited or hot electron distribution just after the pump pulse, which consequently relaxes by electron-phonon scattering. The rise and decay of the transient bleach kinetics are fit to an exponential function of the form $(1-\exp(-t/\tau_r)).\exp(-t/\tau_d)$ to obtain the rise time $\tau_r$ (ps) and the decay time (or the hot electron lifetimes) $\tau_d$ (ps). The decay time at the higher power 90 nJ/pulse ($\tau_d = 1.72 \pm 0.09$ ps) is longer than at 40 nJ/pulse ($\tau_d = 1.64 \pm 0.07$ ps). Thus, the pump-probe dynamics of the aggregates shows a power dependence similar to that seen in isolated gold nanoparticles as attributed to the linear dependence of the electronic heat capacity on the hot electron temperature.[25,27,44,45] The laser energy dependence of the electron-phonon relaxation time in the 13-nm isolated gold nanoparticles is shown separately in Figure 3.4. The extrapolated zero power limit of the electron-phonon relaxation time in the 13-nm nanoparticles is determined to be 0.68 ps, which is consistent with earlier results from our lab[44] and others.[46]

The electron-phonon relaxation dynamics within the aggregates at different probe wavelengths (530, 565, 600, and 635 nm) and that in isolated gold nanoparticles (probed at 520 nm) has been compared at a pulse energy of 90 nJ/pulse in Figure 3.5a. The figure shows a faster electron-phonon relaxation in the nanoparticle aggregates as compared to that in isolated gold nanoparticles ($\tau_d = 1.86 \pm 0.10$ ps) at the same pulse energy. This is also observed for nanoparticle aggregates prepared by other methods. In addition, the
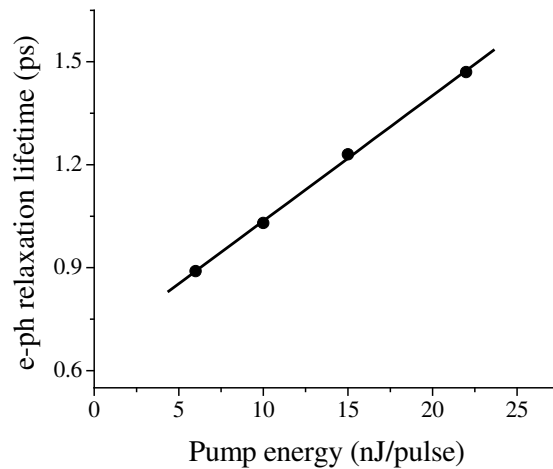
Figure 3.4: Laser pump energy (nJ/pulse) dependence of the electron-phonon relaxation time (ps) in 13 nm gold nanoparticles in the low fluence regime. 100 fs pulses at 400 nm were used as the pump while the probe wavelength was 521 nm corresponding to the plasmon absorption maximum of the nanoparticles. The black line in the plot is a straight-line fit to the data with an intercept of 0.68 ps, corresponding to the zero power limit of the electron-phonon relaxation time in the 13 nm gold nanoparticles.

electron-phonon relaxation rate in the aggregates becomes faster at progressively longer probe wavelengths. It has been widely suggested in the literature that by probing at a particular wavelength along the broad absorption band of aggregates, one can interrogate a particular size/local fractal structure of the aggregates within the inhomogeneous absorption band.[34] This suggestion has been verified by burning of spectral holes in the broad aggregate absorption by irradiating the aggregates at a particular wavelength.[34,47] Accordingly, our experimental results demonstrate that the electron relaxation dynamics can be probed independently within a subset of aggregate sizes/structures by using a
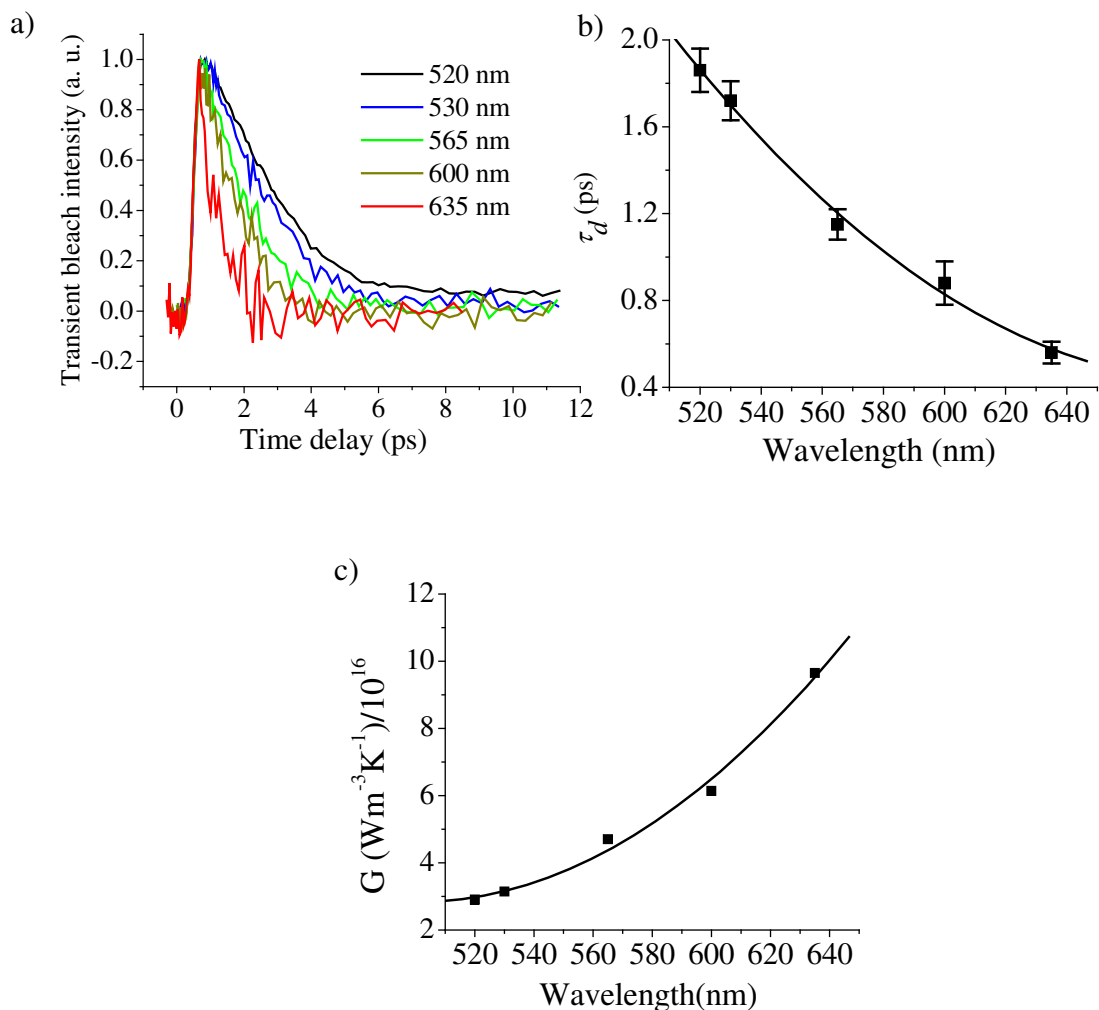
Figure 3.5: (a) Transient bleach dynamics in isolated gold nanoparticles at 520 nm (black) and that in gold nanoparticle aggregates probed at 530 (blue), 665 (green), 600 (yellow) and 635 nm (red). 100 fs pulses at 400 nm with an energy of 90 nJ/pulse were used as the pump. The rise and decay of the transient bleaching were fit to an exponential function of the form $(1-\exp(-t/\tau_r)).\exp(-t/\tau_d)$ so as to obtain the hot electron lifetime $\tau_d$ (ps) for each case. Note that the optical densities of the aggregate solution and the gold nanoparticle colloid at the pump wavelength 400 nm, were adjusted to be similar to ensure that both samples reach a similar hot electron temperatures by optical pumping at 90 nJ/pulse, allowing direct comparison of the electron relaxation dynamics. Plot of (b) measured hot electron lifetimes $\tau_d$ (ps) and (c) calculated electron-phonon coupling constants $G$ $(Wm^{-3}K^{-1})/10^{16}$, against varying degree of aggregation, as characterized by the probe wavelength (nm). The vertical error bars in b indicate the standard deviation of the time constant's exponential fit. The black curves in b and c are guides for the eye.

probe wavelength close to the absorption of that subset. The trend of the hot electron lifetimes with the probe wavelength, shown in Figure 3.5b, thus indicates that electron-phonon relaxation is relatively faster within those aggregates with greater interparticle coupling (due to either a larger aggregate size or closely spaced nanoparticles) and, hence, absorbing at longer wavelengths. This is in good agreement with the observations of Scherer and co-workers on the electron dynamics in thin films assembled from ~12-nm gold nanoparticles; electron relaxation dynamics was observed to get faster with increasing extent of nanoparticle aggregation within the films.[33] Although Scherer and co-workers characterized the extent of aggregation/inter-nanoparticle coupling by the thickness of the aggregated film, we have employed different probe wavelengths to selectively interrogate structures with varying extent of aggregation, distributed within the same solution. Similarly, Zhang and co-workers observed a variation of the coherent phonon oscillation period within gold nanoparticle aggregate structures because they probed at different wavelengths across the broad aggregate absorption; however, they did not find any variation in the electron-phonon relaxation dynamics itself.[34]

The value of the electron-phonon coupling constant, $G$ (W/m$^{-3}$K$^{-1}$), for the nanoparticle aggregates can be calculated from their hot electron lifetimes, $\tau_d$, as per the two-temperature model (TTM),[20] which considers the hot electron gas and the lattice to be two coupled subsystems and is generally valid for time scales longer than the electron-electron scattering processes. In the low fluence approximation, the TTM model gives:

$$G = c_e / \tau_d, \qquad (2)$$

where $c_e$ is the electronic heat capacity (Jm$^{-3}$K$^{-1}$). On the basis of a value of $c_e$ for gold of $2.0 \times 10^4$ Jm$^{-3}$K$^{-1}$ at room temperature and the extrapolated zero power decay time of 0.68

ps from Figure 3.4, the electron-phonon coupling constant, G, for 13-nm gold nanoparticles is estimated to be 2.90 x $10^{16}$ Wm$^{-3}$K$^{-1}$. The value of $c_e$ at the 90 nJ/pulse is calculated to be 5.4 x $10^4$ Jm$^{-3}$K$^{-1}$ from the measured hot electron lifetime $\tau_d$ = 1.86 ps for isolated 13-nm gold nanoparticles at the 90 nJ/pulse. Using this value of $c_e$ at the 90 nJ/pulse, the electron phonon coupling constants can be estimated for the aggregates for the different probe wavelength cases. Figure 3.5c shows the trend of the calculated electron-phonon coupling constant, G, for the aggregates increasing with the interrogating probe wavelength. It can be seen that the value of G for the aggregates supersedes the bulk value of ~3.0 x $10^{16}$ W/m$^{-3}$K$^{-1}$.

### 3.3.3 Dependence of Hot Electron Lifetime on the Degree of Aggregation

To explain the dependence of the hot electron lifetimes on the extent of nanoparticle aggregation, the mechanism of electron-phonon relaxation within the nanoparticles of the aggregate must be analyzed. Electron-phonon relaxation within nanoparticles has two pathways: first, scattering of the excited electron by the nanoparticle lattice phonons and, second, inelastic scattering of hot electrons at the surface of the nanoparticles. Both of these pathways contribute to the net observed electron-phonon coupling constant, G.[48] The effectiveness of electron-phonon scattering has been suggested to depend inversely on the electron oscillation frequency-phonon resonance detuning (EOPRD) within a nanostructural domain.[49] The effective oscillation frequency arises from elastic scattering of electrons from the domain boundary. The spectral overlap of the electron oscillation frequency with the phonon spectrum governs the efficient exchange of energy between the electron and phonon baths. EOPRD can be

expressed as:

$$\text{EOPRD} = \upsilon_f/d - \omega_d , \qquad (3)$$

where $\upsilon_f$ is the Fermi velocity of the electrons in gold, $\omega_d$ is the Debye frequency for gold, and d is the size of the domain or the distance over which the hot electrons are delocalized within the nanostructure. With increasing degree of aggregation, the aggregate size, d, increases, resulting in a decrease in the electron oscillation frequency and a lower EOPRD (thus, better electron-phonon spectral overlap). The e-ph coupling constants thus increase with greater extent of aggregation, starting from the value for an isolated nanoparticle toward the bulk value for gold. At the same time, hot electrons delocalized over a nanoparticle aggregate can be expected to undergo much more enhanced inelastic scattering at the interface of the particles, as compared to the case of isolated nanoparticles.[33] With a greater degree of nanoparticle aggregation, a greater extent of interfacial scattering can be expected, leading to a further increase in the electron relaxation rates, even beyond the bulk value. Such an explanation is analogous to the finding of Juhasz et al.[50] of higher electron relaxation rates in polycrystalline gold films as compared to single gold crystals, attributed to additional electron scattering at grain boundaries. Our experimental results thus suggest that the electrons in the nanoparticle aggregate are not restricted to a single colloidal particle; they are mobile over the aggregated domains, as originally suggested by Scherer and co-workers.[33] Apart from the well-known dipolar plasmon coupling, significant electronic coupling can thus be seen between closely interacting nanoparticles.

## 3.4 Conclusion

We studied the ultrafast dynamics in solution-stable aggregates of ~13-nm gold nanoparticles by femtosecond laser pump-probe spectroscopy. UV-visible extinction and transient absorption of the nanoparticle aggregates showed an extended plasmon broadband absorption in the 550-700-nm region, in addition to the isolated gold nanoparticle plasmon resonance because of absorption contributions from aggregates with different sizes and/or different fractal structures. The aggregates showed a electron-phonon relaxation rate that was faster than that in isolated gold nanoparticles and also probe-wavelength dependent. As the probe wavelength was varied from 520 to 635 nm across the broad aggregate absorption, the electron phonon relaxation became faster. Thus, each wavelength can selectively interrogate a subset of aggregate sizes/structures with an absorption around that wavelength. Our results thus support the proposition that optical excitations within the broad distribution of nanoparticle aggregates are localized in small sub-wavelength regions (also known as hot spots), a phenomenon that can be potentially useful in optical writing of data within these nanostructures.[47] We also correlated the increase in electron-phonon relaxation rate with increasing probe wavelength to an increase in electron oscillation-phonon spectral overlap and interfacial scattering with increasing extent of aggregation. Our results may be potentially useful for tuning hot electron lifetimes to fast response in nanoparticle assemblies and for optoelectronic device and photochemical applications.

## 3.5. References

(1)    Kelly, K. L.; Coronado, E.; Zhao, L. L.; Schatz, G. C. *J. Phys.Chem. B* **2003**, *107*, 668.

(2)    Kreibig, U.; Vollmer, M. *Optical Properties of Metal Clusters,* Springer, New York, 1995.

(3)    Wei, Q.-H.; Su, K.-H.; Durant, S.; Zhang, X. *Nano Lett.* **2004**, *4*, 6.

(4)    Mirkin, C. A. *Inorg. Chem.* **2000**, *39,* 2258.

(5)    Sastry, M.; Rao, M.; Ganesh, K. N. *Acc. Chem. Res.* **2000**, *35*, 847.

(6)    Alivisatos, A. P.; Johnsson, K. P.; Peng, X.; Wilson, T. E.; Loweth, C. J.; Bruchez, M. P., Jr.; Schultz, P. G. *Nature* **1996**, *382*, 609.

(7)    Mirkin, C. A.; Letsinger, R. L.; Mucic, R. C.; Storhoff, J. J. *Nature* **1996**, *382*, 607.

(8)    Collier, C. P.; Saykally, R. J.; Shiang, J. J.; Henrichs, S. E.; Heath, J. R. *Science* **1997**, *277*, 1978.

(9)    Grabar, K. C.; Freeman, R. G.; Hommer, M. B.; Natan, M. J. *Anal. Chem.* **1995**, *67*, 735.

(10)   Félidj, N.; Aubard, J.; Lévi, G.; Krenn, J. R.; Hohenau, A.; Schider, G.; Leitner, A.; Aussenegg, F. R. *App. Phys. Lett.* **2003**, *82,* 3095.

(11)   Dimon, P.; Sinha, S. K.; Weitz, D. A.; Safinya, C. R.; Smith, G. S.; Varady, W. A.; Lindsay, H. M. *Phys. Rev. Lett.* **1986**, *57*, 595.

(12)   Westcott, S. L.; Oldenburg, S. J.; Lee, T. R.; Halas, N. J. *Chem. Phys. Lett.* **1999**, *300*, 651.

(13)   Félidj, N.; Truong, S. L.; Aubard, J.; Lévi, G.; Krenn, J. R.; Hohenau, A.; Leitner, A.; Aussenegg, F. R. *J. Chem. Phys.* **2004**, *120*, 7141.

(14)     Poliakov, E.; Shalaev, V. M.; Shubin, V.; Markel, V. A. *Phys. Rev. B* **1999**, *60*, 10739.

(15)     Haus, J.; Kalyaniwalla, N.; Inguva, R.; Bloemer, M.; Bowden, C. M. *J. Opt. Soc. Am. B* **1989**, *6*, 787.

(16)     Hagfeldt, A.; Grätzel, M. *Chem. Rev.* **1995**, *95*, 49.

(17)     Cavanagh, R. R.; King, D. S.; Stephenson, J. C.; Heinz, T. F. *J. Phys. Chem.* **1993**, *97*, 786.

(18)     Heilweil, E. J.; Hochstrasser, R. M. *J. Chem. Phys.* **1985**, *82*, 4762.

(19)     Schoenlin, R. W.; Lin, W. Z.; Fujimoto, J. G.; Eesley, G. J. *Phys. Rev. Lett.* **1987**, *58*, 1680.

(20)     Sun, C.-K.; Vallee, F.; Acioli, L. H.; Ippen, E. P.; Fujimoto, J. G. *Phys. Rev. B* **1993**, *48*, 12365.

(21)     Kaveh, M.; Wiser, N. *Adv. Phys.* **1984**, *33*, 257.

(22)     Hodak, J. H.; Henglein, A.; Hartland, G. V. *J. Phys. Chem. B* **2000**, *104*, 9954.

(23)     Ahmadi, T. S.; Logunov, S. L.; El-Sayed, M. A. *J. Phys. Chem.* **1996**, *100*, 8053.

(24)     Roberti, T. W.; Smith, B. A.; Zhang, J. Z. *J. Chem. Phys.* **1995**, *102*, 3860.

(25)     Logunov, S. L.; Ahmadi, T. S.; El-Sayed, M. A.; Khoury, J. T.; Whetten, R. L. *J. Phys. Chem. B* **1997**, *101*, 3713.

(26)     Link, S.; Burda, C.; Mohamed, M. B.; Nikoobakht, B.; El-Sayed, M. A. *Phys. Rev. B* **2000**, *61*, 6086.

(27)     Hodak, J. H.; Martini, I.; Hartland, G. V. *Chem. Phys. Lett.* **1998**, *284*, 135.

(28)     Hodak, J. H.; Henglein, A.; Hartland, G. V. *J. Chem. Phys.* **1999**, *111*, 8613.

(29)    Del Fatti, N.; Flytzanis, C.; Vallee, F. *Appl*. *Phys*. B **1999**, *68*, 433.

(30)    Stella, A.; Nisoli, M.; de Silvestri, S.; Svelto, O.; Lanzani, G.; Cheyssac, P.; Kofman, R. *Phys*. *Rev*. *B* **1996**, *53*, 15497.

(31)    Nisoli, M.; Stagira, S.; de Silvestri, S.; Stella, A.; Togini, P.; Cheyssac, P.; Kofman, R. *Phys*. *Rev*. *Lett*. **1997**, *53*, 3575.

(32)    Perner, M.; Bost, P.; Plessen, G. V.; Feldmann, J.; Becker, U.; Mennig, M.; Schmidt, H. *Phys. Rev. Lett*. **1997**, *78*, 2192.

(33)    Feldstein, M. J.; Keating, C. D.; Liau, Y.-H.; Natan, M. J.; Scherer, N. F. *J. Am. Chem. Soc.* **1997**, *119*, 6638.

(34)    Grant, C. D.; Schwartzberg, A. M.; Norman, T. J., Jr.; Zhang J. Z. *J. Am. Chem. Soc.* **2003**, *125*, 549.

(35)    Eah, S.-K.; Jaeger, H. M.; Scherer, N. F.; Lin, X.-M.; Wiederrecht, G. P. *Chem. Phys. Lett.* **2004**, *386*, 390.

(36)    Turkevich, J.; Stevenson, P. C.; Hillier, J. *Discuss. Faraday Soc*. **1951**, *11*, 55.

(37)    Jana, N. R.; Gearheart, L.; Murphy, C. *J. Phys. Chem. B* **2001**, *105*, 4065.

(38)    Pal, A.; Ghosh, S. K.; Esumi, K.; Pal, T. *Langmuir* **2004**, *20*, 575.

(39)    Rechberger, W.; Hohenau, A.; Leitner, A.; Krenn, J. R.; Lamprecht, B.; Aussenegg, F. R. *Opt. Commun.* **2003**, *220*, 137.

(40)    Su, K.-H.; Wei, Q.-H. Zhang, X.; Mock, J. J.; Smith, D. R.; Schultz, S. *Nano Lett.* **2003**, *3*, 1087.

(41)    Storhoff, J. J.; Elghanian, R.; Mirkin, C. A.; Letsinger, R. L. *Langmuir* **2002**, *18,* 6666.

(42)    Quinten, M.; Kreibig, U. *Surf. Sci.* **1986**, *172*, 557.

(43)    Lazarides, A. A.; Schatz, G. C. *J. Phys. Chem. B* **2000**, *104*, 460.

(44)    Link, S.; El-Sayed, M. A. *J. Phys. Chem. B* **1999**, *103*, 8410.

(45)    Link, S.; El-Sayed, M. A. *Annu. Rev. Phys. Chem*. **2003**, *54*, 331.

(46)    Qui, T. Q.; Tien, C. L. *Int. J. Heat Mass Transfer* **1992**, *35*, 719.

(47)    Safonov, V. P.; Shalaev, V. M.; Markel, V. A.; Danilova, Y. E.; Lepeshkin, N. N.; Kim, W.; Rautian, S. G.; Armstrong, R. L. *Phys. Rev. Lett*. **1998**, *80*, 1102.

(48)    Smith, B. A.; Zhang, J. Z.; Giebel, U.; Schmid, G. *Chem. Phys. Lett*. **1997**, *270*, 139.

(49)    Gorban, S. A.; Nepijko, S. A.; Tomchuk, P. M. *Int. J. Electron*. **1991**, *70*, 485.

(50)    Juhasz, T.; Elsayed-Ali, H. E.; Smith, G. O.; Suárez, C.; Bron, W. E. *Phys. Rev. B* **1993**, *48*, 15488.

# CHAPTER 4

# PLASMON COUPLING IN COLLOIDAL NANOROD ASSEMBLIES: OPTICAL ABSORPTION AND ELECTRODYNAMIC SIMULATIONS

## Abstract

The shape anisotropy of nanorods gives rise to two distinct orientational modes by which nanorods can be assembled, i.e., end-to-end and side-by-side, analogous to the well-known H and J aggregation in organic chromophores. Optical absorption spectra of gold nanorods have earlier been observed to show a red-shift of the longitudinal plasmon band for the end-to-end linkage of nanorods, resulting from the plasmon coupling between neighboring nanoparticles, similar to the assembly of gold nanospheres. We observe, however, that side-by-side linkage of nanorods in solution shows a blue-shift of the longitudinal plasmon band and a red-shift of the transverse plasmon band. Optical spectra calculated using the discrete dipole approximation method were used to simulate plasmon coupling in assembled nanorod dimers. The longitudinal plasmon band is found to shift to lower energies for end-to-end assembly, but a shift to higher energies is found for the side-by-side orientation, in agreement with the optical absorption experiments. The strength of plasmon coupling was seen to increase with decreasing inter-nanorod distance and an increase in the number of interacting nanorods. For both side-by-side and end-to-end assemblies, the strength of the longitudinal plasmon coupling increases with

increasing nanorod aspect ratio as a result of the increasing dipole moment of the longitudinal plasmon. For both the side-by-side and end-to-end orientation, the simulation of a dimer of nanorods having dissimilar aspect ratios showed a longitudinal plasmon resonance with both a blue-shifted and a red-shifted component, as a result of symmetry breaking. A similar result is observed for a pair of similar aspect ratio nanorods assembled in a nonparallel orientation. The inter-nanorod plasmon coupling scheme concluded from the experimental results and simulations is found to be qualitatively consistent with the molecular exciton coupling theory, which has been used to describe the optical spectra of H and J aggregates of organic molecules. The coupled nanorod plasmons are also suggested to be electromagnetic analogues of molecular orbitals. Investigation of the plasmon coupling in assembled nanorods is important for the characterization of optical excitations and plasmon propagation in these nanostructures. The surface plasmon resonance shift resulting from nanorod assembly also offers a promising alternative for analyte-sensing assays.

## 4.1 Introduction

Recently, increasing amount of attention has been directed toward the assembly of metal nanoparticle building blocks into ordered structures[1-11] for biodiagnostic [1,2,8,11-16] and potential optoelectronic device applications[17-23] like photonic waveguiding[24-30] and optical switching.[31,32] The process of metal nanosphere assembly or aggregation is known to alter the optical properties of the nanostructure.[12,33-38] For instance, the nanosphere surface plasmon resonance shifts to lower energies in assembled structures, which is attributed to the electromagnetic coupling of plasmons of the individual nanospheres

interacting in the assembly.[12,38,39] The Mirkin[16] and Alivisatos[11] groups have already demonstrated biosensing schemes based on the programmed assembly of gold and silver nanospheres using proteins and nucleic acids, a more recent example being the "molecular plasmon ruler" described by Sönnichsen et al.[40] There has been a strong interest in understanding plasmon coupling in assembled metal nanostructures; detailed investigations have been carried out by past experiments and computational electromagnetic simulations of metal nanosphere dimers,[39,41-43] chains,[29,36] and 2-D[44] and 3-D assemblies/aggregates.[35,38] Besides applications in surface plasmon resonance-based biosensing, interparticle electromagnetic coupling has been proposed to result in a strong localized enhancement of the electric field in the gap between the particles,[45,46] allowing enhanced Raman scattering,[47,48] photoluminescence,[49] multiphoton excitation,[50] and other linear and nonlinear spectroscopies[51,52] of adsorbed molecules. The Atwater[25-28] and Krenn groups[24,29] have also demonstrated the utility of the near-field plasmon coupling between assembled metal nanospheres for photonic waveguiding below the diffraction limit. On account of their anisotropic structure, gold nanorods possess much more interesting optical properties as compared to nanospheres,[3,53,54] including stronger and tunable absorption (corresponding to the longitudinal plasmon oscillation),[55-59] enhanced photoluminescence,[60,61] higher surface-enhanced Raman cross-sections,[62,63] and the possibility of unidirectional plasmon propagation,[64] thus motivating interest in the controlled assembly of nanorods into functional architectures as well as for analyte-sensing applications.[3,65] The Murphy group[66,67] and Nikoobakht et al.[68] have already demonstrated self-assembly of gold nanorods. On account of their shape anisotropy, nanorods can be assembled via two orientational modes. Selective end-to-end

functionalization and 1-D assembly of gold nanorods has been achieved by the use of the streptavidin-biotin linkage,[69,70] thiolated-DNA hybridization schemes[71] and co-operative hydrogen-bonding schemes based on thiolated molecules.[72] Recently, Kamat and co-workers[72] as well as Joseph et al.[73] used thioalkyl carboxylic acid-based bifunctional molecules for end-to-end alignment of nanorods in solution. They also demonstrated by optical spectroscopy that the end-to-end assembly process leads to a red-shift in the longitudinal plasmon resonance of the nanorod spectrum, similar to the case of nanosphere assembly.

In this chapter, we explore the orientation dependence of plasmon coupling in assemblies of anisotropic plasmonic nanoparticles. We observed that the aggregation of gold nanorods in a side-by-side orientation in solution shows a blue-shift of the longitudinal nanorod plasmon band and a red-shift of the transverse band. The plasmon coupling in side-by-side vs end-to-end dimers of nanorods is systematically modeled by the discrete dipole approximation method, showing qualitative agreement with the experimental shifts in the optical resonance bands i.e., red-shift of the longitudinal plasmon band for end-to-end assembly in contrast to the blue-shift for the case of side-by-side assembly. For both end-to-end and side-by-side assembly, the strength of plasmon coupling is found to increase with decreasing inter-nanorod distance and an increase in the number of rods in the assembly. Nanorods with increasing aspect ratio show increasing strength of longitudinal plasmon coupling for both assembly orientations. Dimers of nanorods of dissimilar aspect ratio, rod-sphere pairs, as well as nanorods assembled in a nonparallel orientation are also investigated. The general scheme of plasmon coupling in assembled nanostructures as inferred from the

experimental and simulation results is found to be qualitatively consistent with the exciton coupling model.[74,75] The situation of side-by-side vs end-to-end assembly of nanorods is thus found analogous to the H and J aggregation of organic molecules.[76]

## 4.2 Methods

### 4.2.1 Experimental Methods

Colloidal gold nanorods were obtained from another group member, Susan Eustis. These were prepared by the chemical seeding technique described previously.[61] Briefly, a seed solution was generated by adding ice cold $NaBH_4$ to a solution of $HAuCl_4$ and cetyltrimethylammonium bromide (CTAB). The solution was kept at 25 °C for a few minutes before use. A brownish-yellow color was observed in all seed solutions used. The growth solution contained 5 mL of a solution of 0.20 mM CTAB and 0.25 mM benzyldimethylammonioum chloride hydrate (BDAC), which was added to 0.20 mL of 4.0 mM $AgNO_3$. Then 5.0 mL of 0.90 mM $HAuCl_4$ and 54 μL of 0.10 M ascorbic acid were added. Twelve milliliters of seed solution was then added to the solution, which was left undisturbed for 4 h for the nanorods to grow. Kinetic growth conditions determine the aspect ratio of the nanorods generated, with narrower widths in the higher aspect ratio samples. Optical extinction spectra of the synthesized nanorods were recorded on a UV-Vis-NIR scanning spectrometer. The nanorod samples were imaged on a JEOL100 transmission electron microscope (TEM). The gold nanorods have a positively charged surface due to the presence of adsorbed $CTA^+$ ions and the aggregation of nanorods in solution was induced by the addition of 0.07 M sodium citrate solution to 1 mL of the nanorod solution and monitored by UV-vis optical extinction. Resulting nanorod

aggregates were imaged by TEM by drop casting the aggregated nanorod solution onto a copper grid placed on a filter paper and allowed to dry.

### 4.2.2. Calculation Methods

To model the plasmon coupling in the assembled nanorod structures, optical spectra of isolated nanorods, nanorod dimers, and nanorod trimers were calculated by the discrete dipole approximation (DDA) method, a discretization procedure for solving the Maxwell's equations where the target particle is geometrically reproduced by a cubic array of virtual point dipoles. DDA has been demonstrated to be one of the most powerful and flexible electrodynamic methods for computing the optical spectra of particles with an arbitrary geometry. Details of the DDA method have been described elsewhere.[77] The Schatz group[78,79] has already carried out extensive studies showing that DDA is suited for optical calculations of the extinction spectrum and the local electric field distribution in metal particles with different geometries and environments. Recently, Pileni and co-workers have established the applicability of using DDA simulations to model experimental optical spectra of gold nanorods.[80] Using the DDA method, Lee and El-Sayed have investigated the systematic dependence of nanorod absorption and scattering on their aspect ratio, size, and medium refractive index.[81]

The spectra of the extinction efficiency of nanorods and assembled nanorod structures were calculated by employing the DDSCAT code developed by Draine and Flatau.[77] The nanorod shape was approximated by a cubic array (40 x 10 x 10) of point dipoles representing a prolate spheroid. In DDSCAT, the size of the nonspherical target of volume V is expressed in terms of an effective radius, $r_{eff} = (3V/4\pi)^{1/3}$, which is the radius of a sphere having a volume equal to that of the particle. The nanorod target used

for most of the calculations had $r_{eff}$ = 16 nm and aspect ratio AR (i.e., the ratio of the long

axis a to the short axis b of the particle) of 4.0, which is also equivalent to a = 80 nm and

b = 20 nm. Calculations were carried also carried out for two other values of the nanorod

aspect ratio, AR = 2.8 and 3.5 while the effective radius was kept constant. Dipole

representations of assembled nanorod dimers (corresponding $r_{eff}$ = 20 nm) and trimers

(corresponding $r_{eff}$ = 23 nm) in different orientations i.e., assembled side-by-side, end-to-

end, or with their axes mutually perpendicular were generated. The center-to-center

distance R between the interacting nanorods was also varied. Although a quasi-static

treatment of the interaction between cylindrical particles (each represented by a single

point dipole) has been undertaken earlier,[82] the DDA method does not place any dipolar

limit on the center-to-center distance between the particles because each particle is

modeled by a few thousand point-dipoles. The chief requirement for the applicability of

DDA is that the interdipole separation d be small compared to any structural dimensions

of the target and the wavelength of light $\lambda$, or, in other words, that a sufficient number of

dipoles be employed to represent the target. This criterion is quantitatively expressed as

$|n|kd < 1$, where n is the complex refractive index of the target material. Validity of this

criterion was verified by the DDSCAT program. Note that the accuracy of the DDSCAT

calculations can be increased by increasing the number of dipoles used to simulate the

target, however with a significant increase in the computational cost especially for

assembled nanostructures. The target particle in the surrounding dielectric medium is

considered by using a dielectric function of the target $\varepsilon$ relative to that of the medium $\varepsilon_m$,

which is reflected in the DDA calculation in the form of a dipole polarizability. The

dielectric function of gold was generated from the bulk experimental data of Johnson and

Christy[83] and the medium was assumed to have a refractive index $n_m$ of 1.33 corresponding to that of liquid water. Dipole polarizabilities were assigned by the lattice dispersion relation (LDR) developed by Draine and Goodman,[84] which includes a radiative reaction correction term and is suited for finite dipole arrays. The light polarization direction E with respect to the nanorod assembly was selected so as to model the longitudinal plasmon excitation mode and the transverse mode separately.

## 4.3 Results and Discussion

### 4.3.1 Optical Absorption Shifts with Assembly

The visible extinction spectrum of the gold nanorod solution shows a wavelength maximum around 520 nm corresponding to the transverse plasmon oscillation band and a higher intensity maximum around 805 nm corresponding to the longitudinal plasmon oscillation.[59] An average aspect ratio of 3.2 was obtained for the nanorod sample by fitting the experimental extinction spectrum to Gans' theory as described elsewhere.[61,85] Figure 4.1a shows the evolution of the optical spectrum of the gold nanorod solution upon the addition of increasing aliquots of 0.07 M sodium citrate solution to 1 mL of the nanorod solution. Figure 4.1b shows the optical spectrum at different time intervals following addition of 300 μL of 0.07 M sodium citrate solution to the nanorod colloid. It is clearly seen that the addition of the sodium citrate induces the blue-shift of the longitudinal plasmon band along with a smaller red-shift of the transverse band. Visible color change of the solution from red to purple (with diminished color intensity) was also observed. These absorption changes are attributable to aggregation/assembly of the nanorods in solution induced by addition of sodium citrate, as also evidenced by the

physical precipitation of metallic gold on further standing of the solution. It has been observed by Kamat and co-workers[72] and Joseph et al.[73] that the aggregation of gold nanorods induced by thiol carboxylic acid-based bifunctional linkers results in a red-shift of the longitudinal plasmon band without significant shift in the transverse plasmon band. These studies also established that thiol-based linker molecules selectively adsorb to the ends of the nanorods; further hydrogen bonding of the terminal carboxylic acid groups results in the end-to-end assembly of the nanorods. The optical band shifts in our nanorod aggregation experiments resulting from sodium citrate addition are clearly in contrast to those induced by the end-to-end assembly method. This contrast results possibly from the mechanism of nanorod assembly in our experiments, which we explore further.

**4.3.2 Mechanism of Nanorod Assembly**

A detailed study of the self-assembly of gold nanorods in the presence of carboxylate molecules has been carried out by the Murphy group.[66] In accordance with their proposed assembly mechanism, the gold nanorods in our experiments have a positively charged surface due to strongly adsorbed $CTA^+$ ions along the side surface. The resulting electrostatic repulsion between nanorods is responsible for the stability of the nanorods in solution. The colloidal assembly of nanorods most likely results from the electrostatic attraction between the positively charged nanorod surface and the negatively charged carboxylate ends of the citrate ions. The adsorbed citrate ions may either bridge between nanorods, or lead to the formation of local negatively charged regions on the nanorod that are electrostatically attracted to cationic regions on adjacent nanorods, or
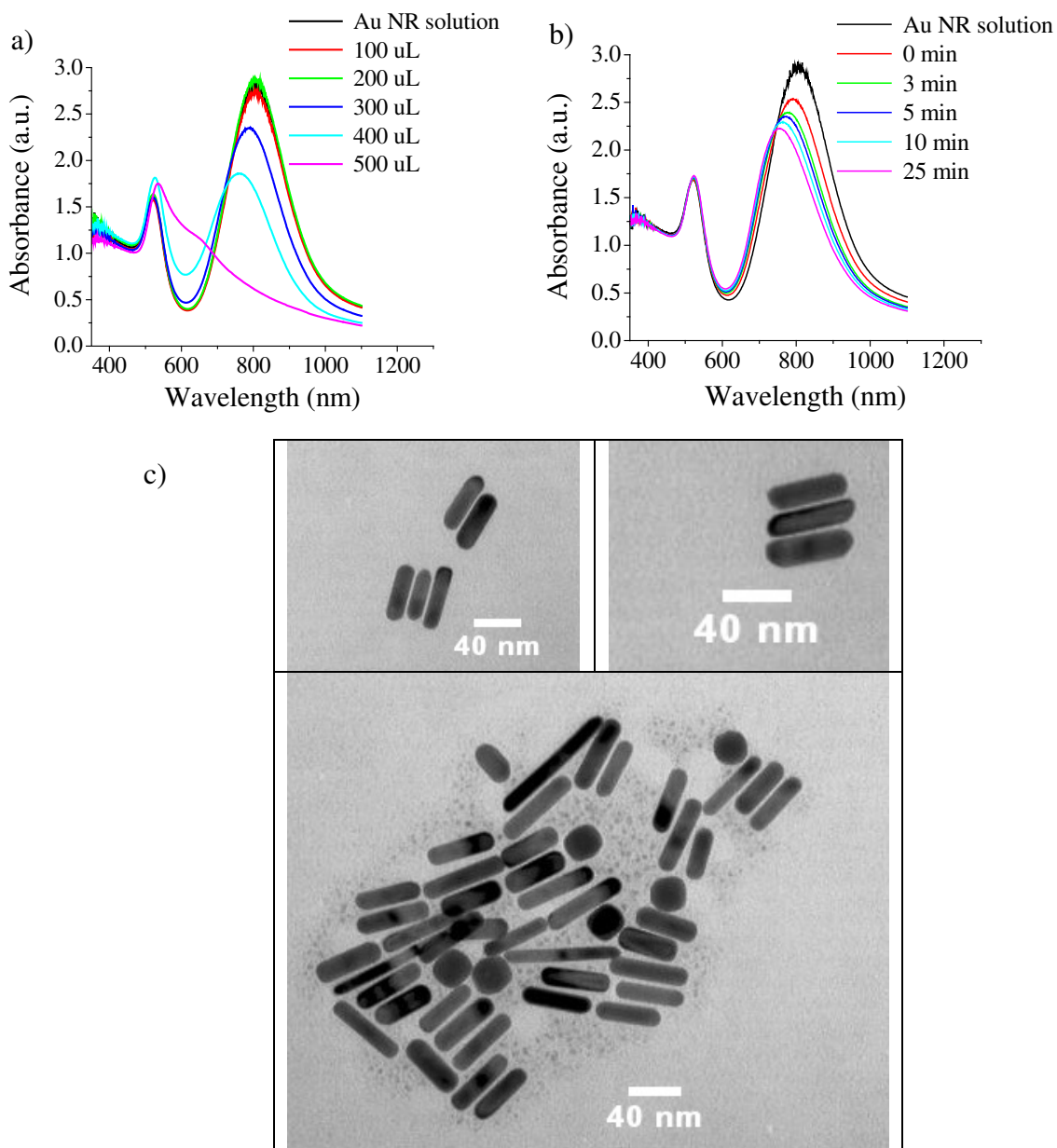
Figure 4.1: UV-visible extinction spectra of a 1-ml gold nanorod solution, shown in black, (a) on addition of increasing aliquots (100, 200, 300, 400 and 500 μL) of 0.07 M sodium citrate solution, and (b) on addition of 300 μL of 0.07 M sodium citrate solution at different time intervals (0, 3, 5, 10 and 25 min). (c) TEM images of a solution of gold nanorods aggregated by the addition of sodium citrate showing examples of nanorod aggregation in a side-by-side arrangement.

simply neutralize the electrostatic repulsion between the nanorods. Such a mechanism is expected to result predominantly in the side-by-side assembly of the gold nanorods.

Figure 4.1c shows examples of nanorods assembled side-by-side imaged by TEM. However, the TEM images are not entirely representative of the solution phase, due to the transfer of the sample to a planar solid support followed by evaporation of the solvent. The process of drying of a colloidal nanorod solution on the TEM grid itself has been studied by Nikoobakht et al.[68] and was found to result in the formation of side-by-side nanorod assemblies by the action of capillary forces. Such drying-mediated assemblies formed on the grids[86,87] cannot be distinguished from the assemblies formed in solution by the addition of the sodium citrate. Thus TEM, although a vital nanoparticle characterization tool, may not provide an accurate picture of solution phase behavior. Optical absorption measurements of the solution phase provide more definite characterization of the colloidal assembly process, especially when the interpretation of the experimental absorption results is aided by electrodynamic simulations of the optical spectra of model nanoparticle systems. We thus present electrodynamic simulations of the plasmon shift resulting from the assembly of nanorods for both side-by-side as well as end-to-end type assembly.

**4.3.3 DDA Simulation of Nanorod Assembly**

<u>4.3.3.1 Side-by-Side Assembly</u>

Figure 4.2a shows the DDA simulated optical spectra corresponding to the longitudinal plasmon excitation of a pair of gold nanorods, as they approach each other in a side-by-side orientation. The calculated longitudinal band of an isolated single nanorod (AR = 4.0) is shown for comparison as a black curve. When the nanorods are far apart (R

= 120 nm), the optical resonance maximum does not seem to be shifted in position from that of the isolated nanorod case. As the nanorods approach each other, there is a clear blue-shift of the longitudinal plasmon band, as attributable to the coupling of the plasmons of the two interacting nanorods; the strength of this coupling increases with
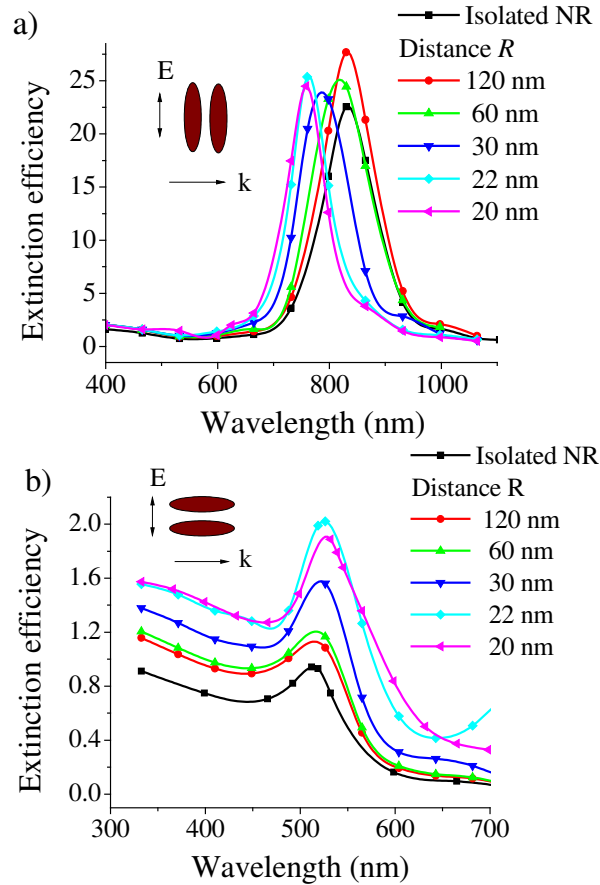


Figure 4.2: DDA-simulated extinction efficiency spectra of gold nanorods (a ~ 80 nm, b ~ 20 nm) assembled in a side-by-side orientation: (a) Longitudinal plasmon excitation and (b) transverse plasmon excitation of a pair of nanorods as a function of the inter-nanorod center-to-center distance (R = 120, 60, 30, 22 nm and finally 20 nm where nanorods touch each other). The isolated nanorod spectrum is also shown as a black curve for comparison. (c) Longitudinal plasmon excitation and (d) transverse plasmon excitation of a nanorod assembly as a function of the number of nanorods (isolated nanorod, dimer and trimer) with the inter-nanorod distance fixed at 22 nm.
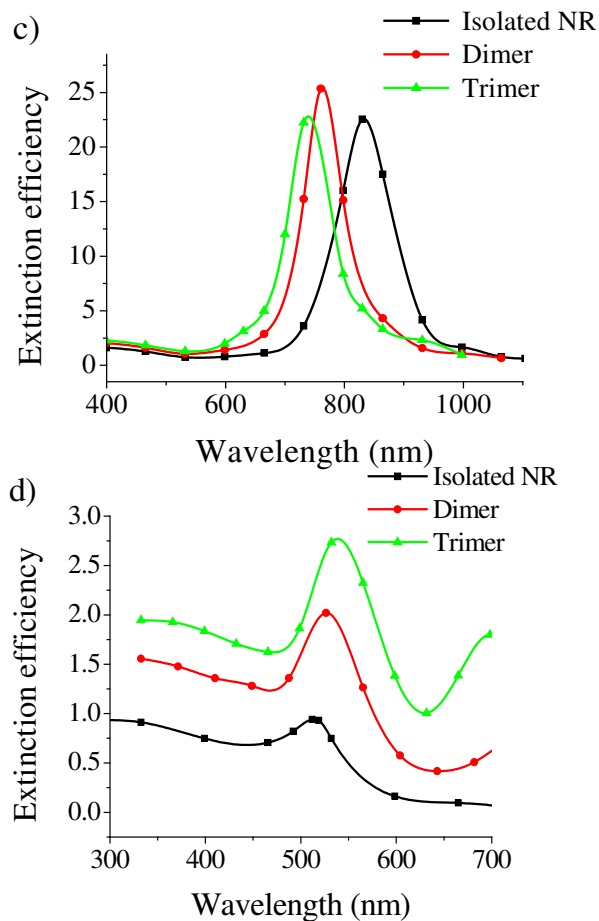
Figure 4.2 continued

decreasing inter-nanorod distance. The strength of coupling also increases with the number of nanorods interacting in an assembly. This is seen in Figure 4.2c from the larger blue-shift of the longitudinal plasmon band as we go from a nanorod dimer to a nanorod trimer. The effect of the side-by-side assembly on the transverse plasmon excitation (polarization direction along interparticle axis) has been similarly depicted in Figure 4.2b,d.

In contrast to the longitudinal plasmon oscillation, the coupling of the transverse plasmon oscillations in side-by-side assembled nanorods leads to a red-shifted resonance.

Thus, the DDA simulation of the side-by-side nanorod assembly process agrees well with the experimental optical absorption band shifts induced by solution assembly/aggregation of nanorods in our experiments (Figure 4.1), confirming the side-by-side mechanism of nanorod assembly. Although 100% of the nanorods in our experimental sample may not be assembled in a perfect side-by-side orientation, the experimental optical spectra reflect the average characteristics of the colloidal assembly process in solution.

4.3.3.2 End-to-End Assembly

The calculated optical absorption spectra corresponding to the longitudinal plasmon excitation of a pair of gold nanorods, approaching each other along their long axis (i.e., end-to-end assembly) is shown in Figure 4.3a. The calculated longitudinal band of the isolated single nanorod (AR = 4.0) is shown for comparison as a black curve. The optical resonance maximum does not seem to shift its position from that of the isolated nanorod case for a large inter-nanorod distance (R = 282 nm). As the distance decreases, the longitudinal plasmon band progressively red-shifts due to the coupling of the longitudinal plasmons. Figure 4.3c shows that as we go from a nanorod dimer to a nanorod trimer, there is a larger red-shift of the longitudinal plasmon band. Whereas the longitudinal plasmon band red-shifts, the transverse plasmon resonance does not show any appreciable shift for the end-to-end alignment (Figure 4.3b,d). These simulation results are in agreement with the experimental results of Kamat and co-workers[72] and Joseph et al.[73]

The anisotropic shape of nanorods thus allows two orientational modes of nanorod plasmon coupling, i.e., end-to-end and side-by-side. The DDA simulation results
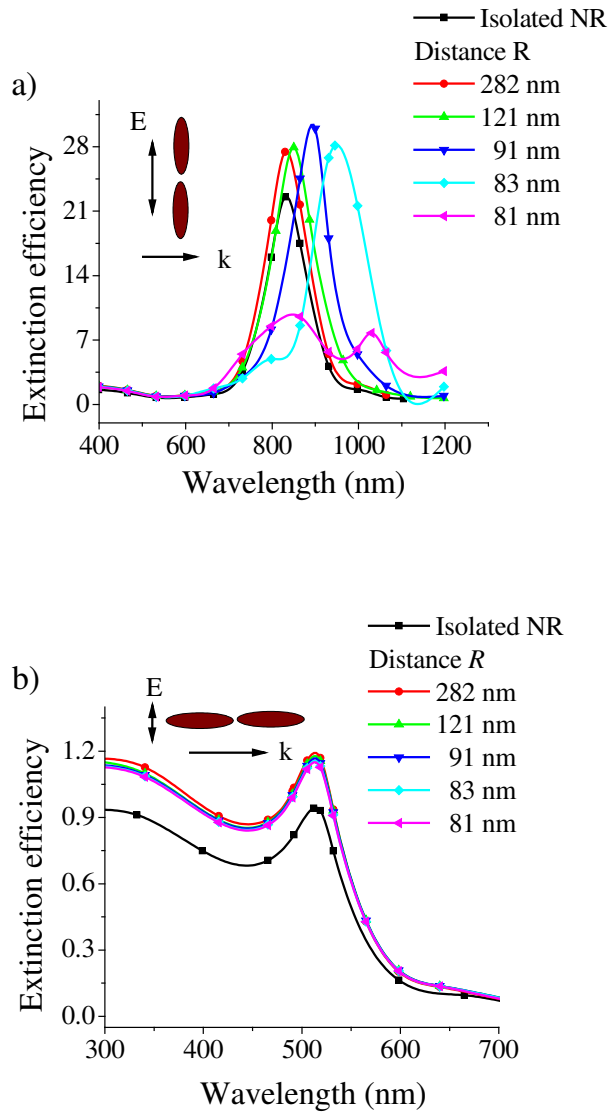
Figure 4.3: DDA-simulated extinction efficiency spectra of gold nanorods (a ~ 80 nm, b ~ 20 nm) assembled in an end-to-end orientation: (a) Longitudinal plasmon excitation and (b) transverse plasmon excitation of a pair of nanorods as a function of the inter-nanorod center-to-center distance (R = 282, 121, 91, 83 nm and finally 81 nm where nanorods touch each other). The isolated nanorod spectrum is also shown as a black curve for comparison. (c) Longitudinal plasmon excitation and (d) transverse plasmon excitation of a nanorod assembly as a function of the number of nanorods (isolated nanorod, dimer and trimer) with the inter-nanorod distance fixed at 83 nm.

c)



d)
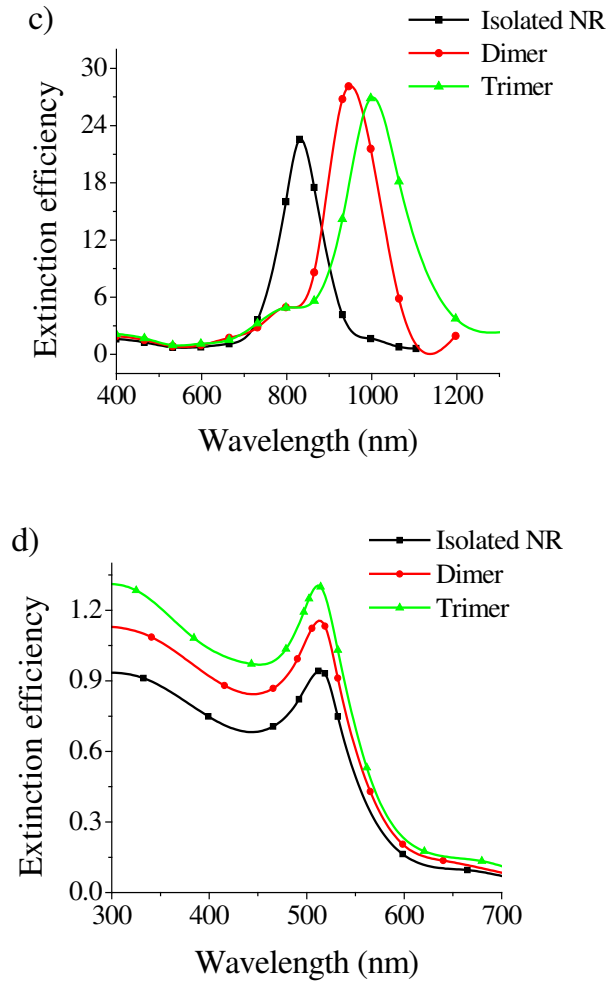


Figure 4.3 continued

confirm the experimental suggestion that these two modes of coupling result in plasmon shifts in opposite directions. These results are also consistent with earlier theoretical predictions by Gluodenis et al.[82] of the spectral shifts resulting from the dipolar interaction of a pair of cylindrical gold nanoparticles as well as a recent investigation of the optical extinction characteristics of metal nanorod arrays by Cortie et al.[88]

**4.3.4 Origin of Assembly Induced Plasmon Shift: Dipolar Exciton Coupling Model**

Dimerization and aggregation in organic molecules and its effect on their optical absorption and fluorescence is very well studied.[76] The dipole-dipole interactions between individual chromophores/fluorophores in the aggregate are generally described in the framework of the exciton coupling theory.[74,75] Exciton theory predicts that the excited-state levels of the monomer split in two levels upon dimerization, a lower energy level and a higher energy level relative to the monomer excited state corresponding respectively to two possible arrangements of the transition dipoles of the chromophores in the dimer, i.e., in-phase or symmetric and out-of-phase or anti-symmetric (see Figure 4.4). The energy splitting 2U is given by the interaction energy between the chromophores, which is approximated by the Coulombic interaction between the transition dipole moments of the monomers, the angle and the distance between the transition dipoles, 1 and 2:[89]

$$U = \frac{1}{4\pi\varepsilon_0}\frac{|\mu|^2}{n_m^2 R^3}\xi \quad (1)$$

where $\xi = \cos\theta_{12} - 3\cos\theta_{1R}\cos\theta_{2R}$ is the orientation factor, $n_m$ is the refractive index of the medium, $|\mu|^2$ is the squared modulus of the transition dipole moment and R is the distance between the dipole centers. Although transitions from the ground state to either excited state are possible, the number of spectral bands observed depends on the geometry of the dimer.[76,89,90] For parallel or H-type dimers (Figure 4.4a), transition to the lower energy excited state is forbidden due to the cancellation of the two dipole moments in this configuration and the spectrum consists of a single band at higher energy with

a)

$$\psi_+ = \frac{1}{\sqrt{2}}\left[\varphi_1 + \varphi_2\right]$$

EXCITED
STATE

2U

$$\psi_- = \frac{1}{\sqrt{2}}\left[\varphi_1 - \varphi_2\right]$$

GROUND
STATE

MONOMER          DIMER          MONOMER

*H* aggregate

b)

$$\psi_- = \frac{1}{\sqrt{2}}\left[\varphi_1 - \varphi_2\right]$$

EXCITED
STATE

2U

$$\psi_+ = \frac{1}{\sqrt{2}}\left[\varphi_1 + \varphi_2\right]$$

GROUND
STATE

MONOMER          DIMER          MONOMER
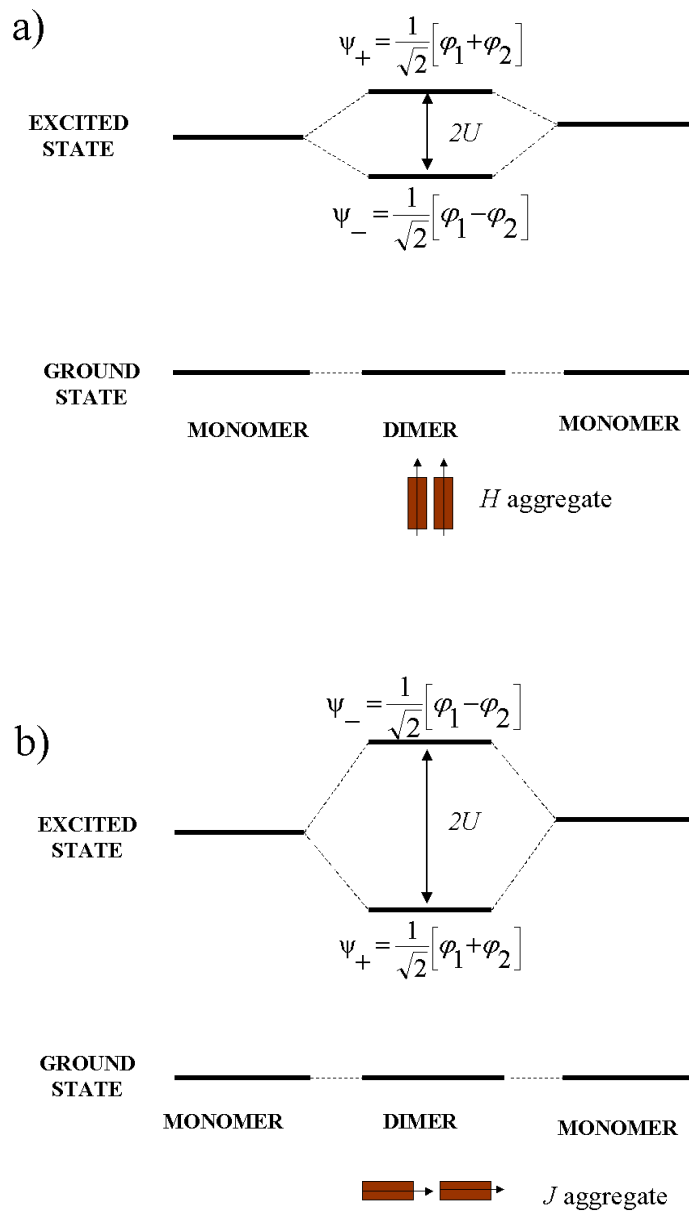
*J* aggregate

Figure 4.4: Schematic of the energy level splitting resulting from the dipolar interaction of chromophores in a dimer, showing symmetric ($\psi_+$) and anti-symmetric coupling ($\psi_-$) of excitons for (a) H aggregate geometry and (b) J aggregate geometry. (c) Exciton theory picture of the nature of the coupled longitudinal plasmon excitation in nanorod dimers: electromagnetic analogy to molecular orbital theory.

127
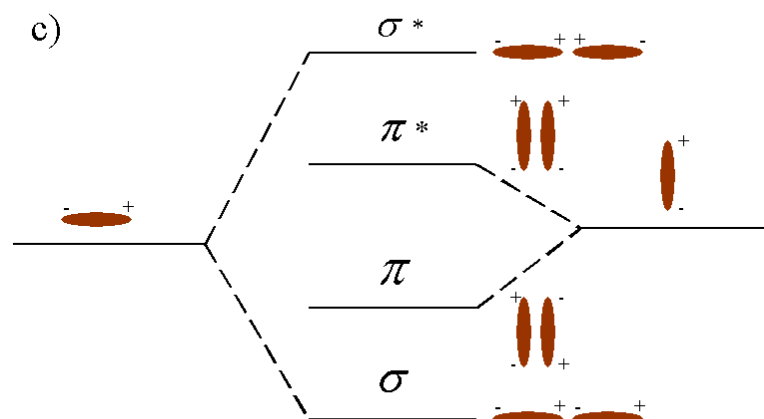
Figure 4.4 continued

respect to the monomer (because $\theta_{12}=0°$, $\theta_{1R}= \theta_{1R}= 90°$ and so $\xi_H = 1$) for which the interaction between the two transition dipoles of the dimer is repulsive. For head-to-tail or J-type dimers (Figure 4.4b), transition to the higher energy state is forbidden due to the cancellation of the two dipole moments in this configuration and the spectrum shows a single band at lower energy with respect to the monomer (because $\theta_{12}= \theta_{1R}= \theta_{1R}= 0°$ and so $\xi_J = -2$) for which the interaction between dipoles is attractive.

By considering the nanorod plasmons to be effectively excitons, the exciton coupling theory can used to explain the optical spectra of the nanorod dimers. The side-by-side nanorod dimer, for the case of longitudinal polarization, represents an H aggregate and hence we observe a blue-shifted spectrum. Conversely, the end-to-end assembly is a J aggregate, resulting in a red-shifted spectrum. For the transverse polarization, the side-by-side nanorod arrangement is a J aggregate (provided the

polarization direction is along the interparticle axis) leading to the red-shift and the end-to-end configuration is an H aggregate (however, the expected blue-shift of the transverse band may be too small to be observable because the transverse plasmon dipoles are far apart even when the rods touch each other). Thus, the optical properties of the gold nanorod assemblies and their dependence on the assembly orientation seem to be qualitatively consistent with the exciton-coupling model.

Similar reasoning also applies to the polarization dependence of the optical resonance shift in nanosphere dimers,[41] where a polarization along the interparticle axis (p-pol) results in a redshift with respect to the single nanosphere resonance whereas a perpendicular polarization (s-pol) results in a blue-shift (Figure 4.5). The near-infrared optical resonances of silica-gold core-shell particles can also be explained in terms of the
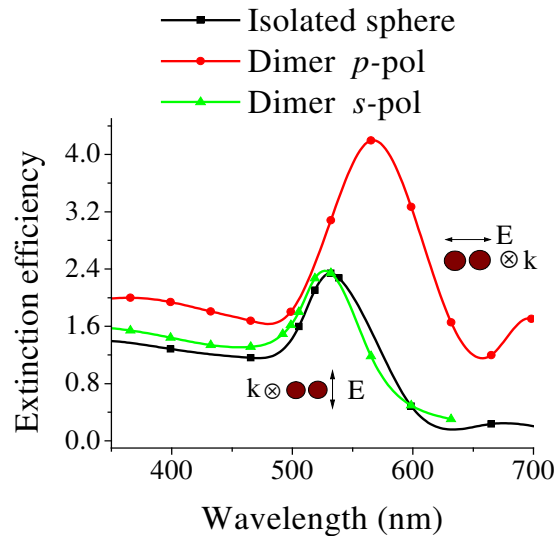


Figure 4.5: DDA-simulated extinction efficiency spectra of a dimer of gold nanospheres (radius 16 nm) for light polarization direction parallel to the inter-particle axis or p-pol (red curve) and perpendicular to the inter-particle axis or s-pol (green curve). The isolated nanosphere resonance spectrum is shown as a black curve for comparison. The center-to-center distance between the spheres was maintained at 35 nm.

exciton coupling between the plasmon supported on the outer surface of a gold sphere and that on the inner surface of a cavity.[91] In this case, the line along which the charges interact is parallel to the dipole moment vectors, corresponding to a J-type symmetry resulting in a bonding or symmetric resonance red-shifted with respect to the visible resonance of the solid gold nanosphere (around 520 nm). The anti-symmetric coupling or anti-bonding resonance is also an allowed mode since the sphere and cavity plasmon dipole moments do not cancel out but is expected to be on the UV end of the spectrum.

### 4.3.5 Trends in Assembly Induced Plasmon Shift

The assembly induced plasmon shift, in energy units, gives a measure of the strength of interparticle plasmon coupling. Figure 4.6 shows the increasing trend of the plasmon energy shift with decreasing inter-nanorod distance R for end-to-end and side-by-side nanorod dimers. There is qualitative agreement between the simulation results and exciton theory. As seen from Figure 4.6a, the magnitude of longitudinal plasmon shift for a given inter-nanorod distance is larger for the case of end-to-end dimerization, which can possibly be reconciled with the greater strength of the J-type interaction ($|\xi_J| > |\xi_H|$). Similarly, the magnitude of transverse plasmon shift (Figure 4.6b) is larger for the side-by-side dimerization case. For the same symmetry (H or J), shifts of the longitudinal plasmon band can be seen to be more prominent than those of the transverse plasmon band, which may be explained in the context of the exciton model as being due to the greater oscillator strength of the longitudinal plasmon excitation (as also seen from the higher spectral intensity of the longitudinal plasmon band as compared to transverse
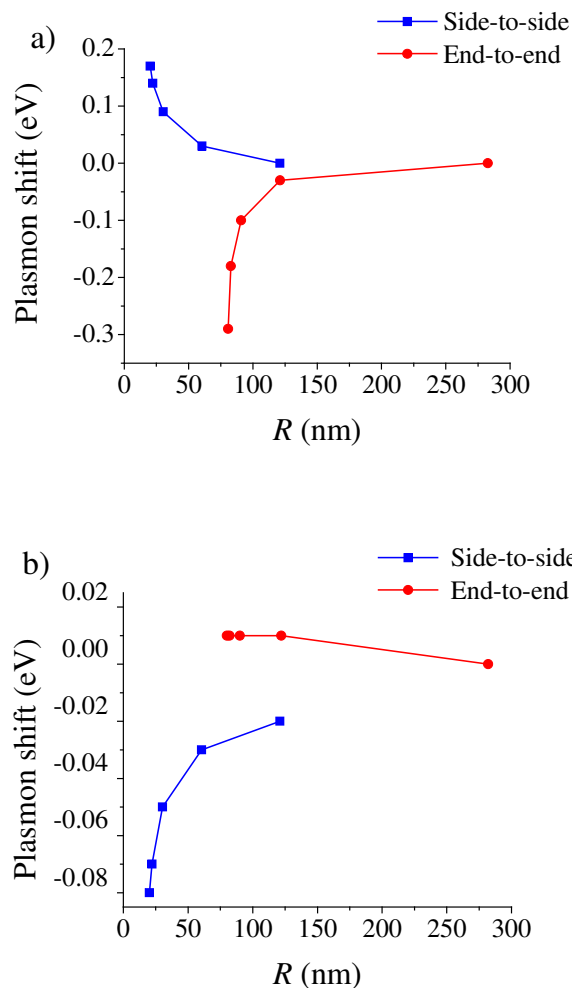
Figure 4.6: Energy shift of the surface plasmon resonance for side-by-side (blue squares) and end-to-end dimerization (red circles) of gold nanorods (a ~ 80 nm, b ~ 20 nm) as a function of the inter-nanorod center-to-center distance R for (a) longitudinal plasmon and (b) transverse plasmon oscillation.

plasmon band). This makes nanorods much more attractive as compared to nanospheres for analyte-sensing assays based on nanoparticle aggregation.[15] Note that the dependence of the plasmon energy shift with inter-nanorod distance does not however correlate with the $1/R^3$ dependence predicted by the exciton model (eq 1). This may be because the exciton-coupling model only considers interactions between point dipoles at relatively

large inter-dipole distances; higher order multipole-multipole interactions are neglected in the weak interaction limit. On the other hand, each nanorod target in our electrodynamic simulation is represented by a few thousand dipoles while accounting for the finite particle size effects (e.g., electromagnetic retardation[78,92]) and the higher order interparticle interactions[43] (which become important in the strong coupling limit and/or very small interparticle distances). Besides, due to the finite size of the particles, the center-to-center distance R does not represent the distance at which the charges induced on neighboring particles interact.

### 4.3.6 Nature of the Coupled Plasmon Excitation: Electromagnetic Analogy to Molecular Orbitals

The effect of interparticle coupling on the nature of plasmon excitation and electric-field enhancement is expected to have important consequences for the use of nanorod assemblies in near-field-coupling based applications i.e., plasmon propagation[24-29] and field-enhanced spectroscopy.[92] The exciton model, in addition to the explanation of optical band shifts, also predicts the nature of the plasmon excitation in the coupled system (see Figure 4.4c). As suggested by the exciton model, the coupled longitudinal plasmon for the end-to-end dimer is bonding in nature analogous to the formation of a $\sigma$ bond from two $p_z$ orbitals. The resulting electric field intensity is maximum in the junction between the interacting nanorods. On the other hand, the coupled longitudinal plasmon for the side-by-side dimer has an anti-bonding nature analogous to the formation of a $\pi^*$ bond from $p_{x/y}$ orbitals, with the electric field concentrated on either side of the interparticle junction. This contrast between the two modes of assembly is reinforced by the following observation. In the case of the end-to-end assembly simulation, a new band emerges at higher energies (attributable to higher-order interactions or image

132

interactions[43]) as the inter-nanorod distance becomes very small[93] (Figure 4.3a) or the number of nanorods interacting in an assembly increases (Figure 4.3c). The side-by-side assembly simulation does not show such an effect. The plasmons of closely spaced rods aligned end-to-end interact very strongly supporting an intense electric field at the interparticle junction, consistent with an earlier theoretical study on electromagnetic coupling in large gold nanorods by Aizpurua et al.[92]

**4.3.7 Dependence of Plasmon Coupling Strength on Nanorod Aspect Ratio**

The longitudinal plasmon spectra of the side-by-side and end-to-end dimers were calculated for three different aspect ratio values AR = 2.8, 3.5, and 4.0 (Figure 4.7). Note that the inter-nanorod distance R was kept at a constant value for the three cases i.e., about 25 nm for side-by-side assembly and about 91 nm for end-to-end assembly. The nanorod effective radius (and hence the total number of gold atoms) was kept constant at $r_{eff}$ = 16 nm. The plasmon energy shift is plotted against the nanorod aspect ratio in Figure 4.8a. For both side-by-side as well as end-to-end assembly, the strength of plasmon coupling as evidenced by the magnitude of the plasmon energy shift (in eV) is seen to increase with increasing nanorod aspect ratio in the selected range of investigation. In the context of exciton theory, this can be explained on the basis of an increase in the nanorod dipole polarizability $\alpha$ and hence the dipole moment $\mu$ with increasing nanorod aspect ratio.
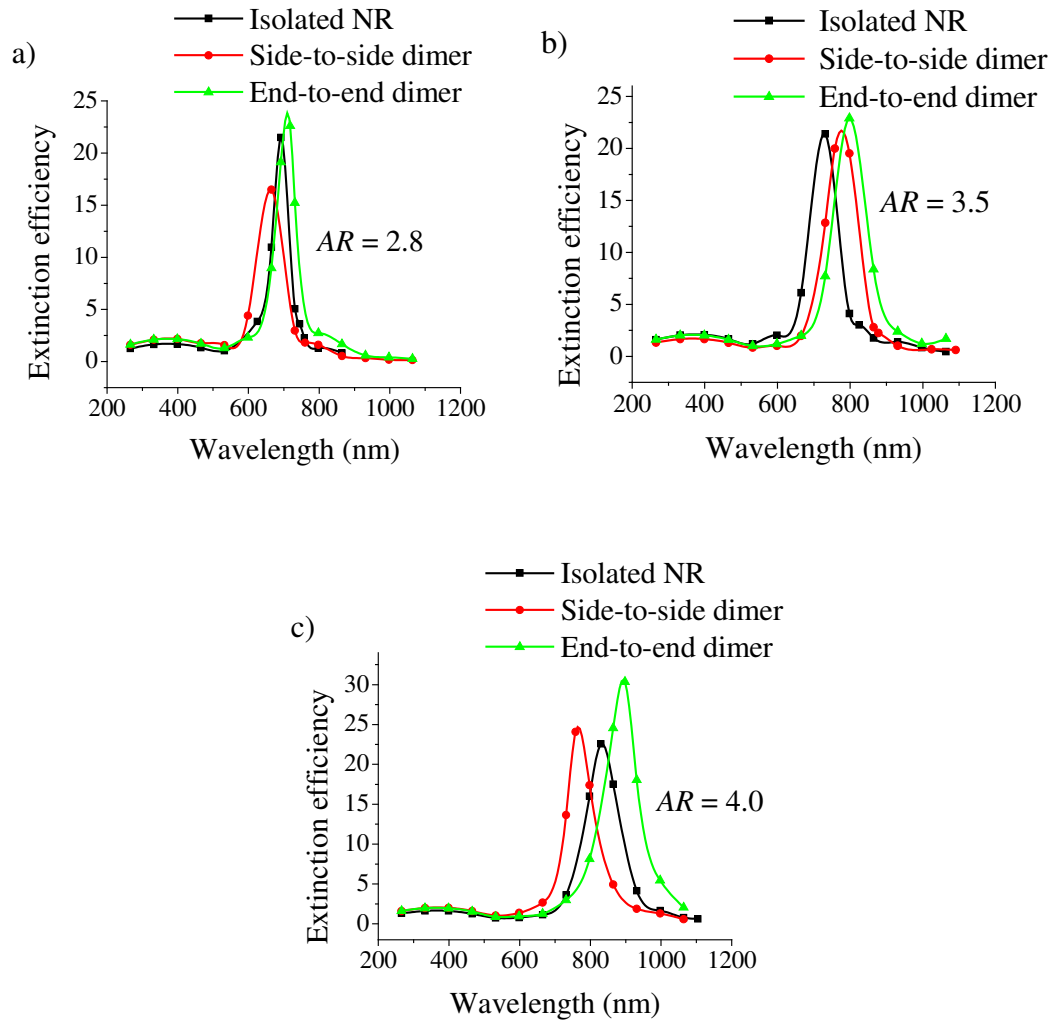
Figure 4.7: DDA-simulated extinction efficiency spectra (corresponding to the longitudinal plasmon excitation) of a dimer of gold nanorods interacting side-to-side (shown in blue) with inter-nanorod distance R about 25 nm and end-to-end (shown in red) with inter-nanorod distance R about 91 nm for three different aspect ratios: (a) 2.8, (b) 3.5 and (c) 4.0. For comparison, the spectrum of the isolated nanorod is shown as a black curve in each case. The nanorod effective radius (and hence the number of gold atoms) was kept constant at $r_{eff}$ = 16 nm across the three different cases.
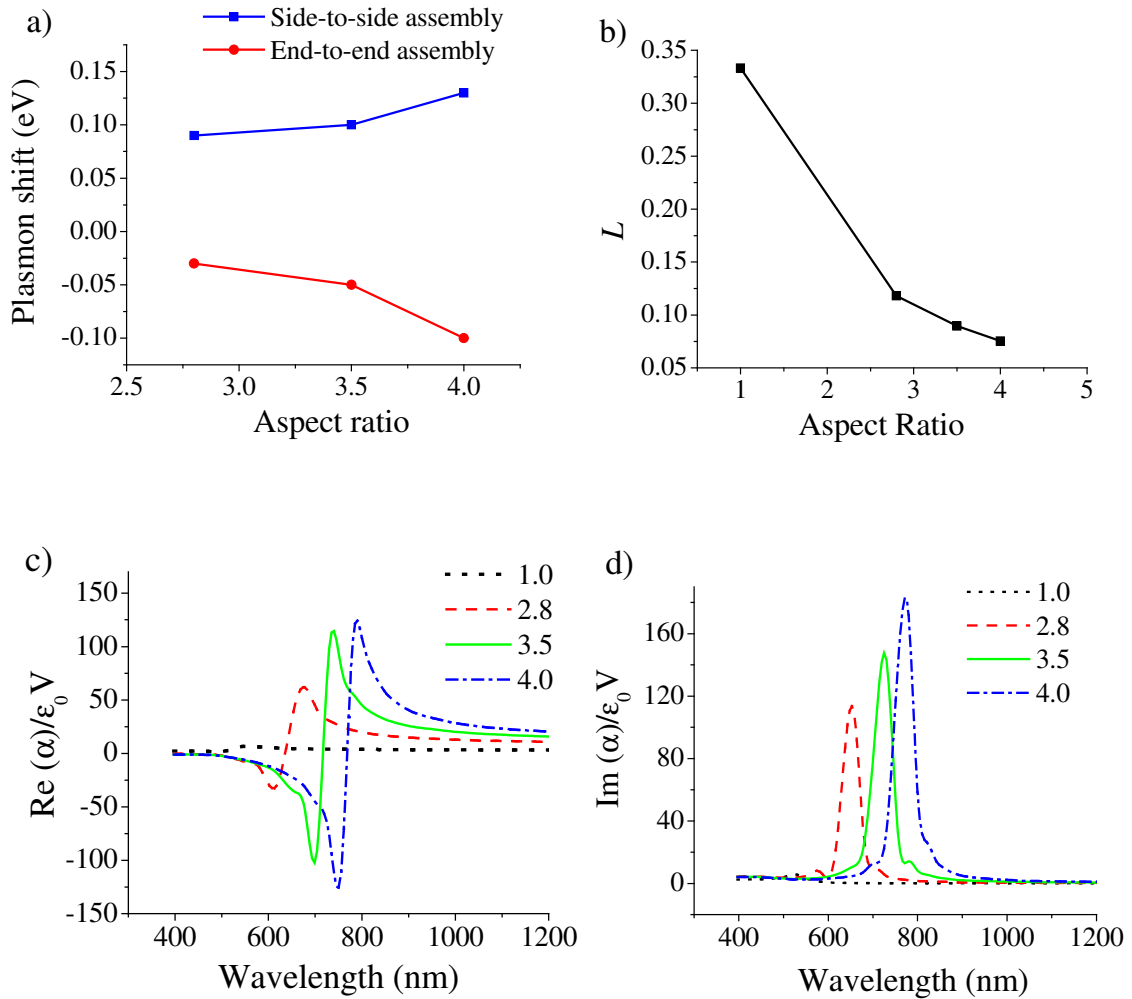
Figure 4.8: (a) Plot of the assembly-induced plasmon energy shift (in eV) versus the nanorod aspect ratio AR for side-by-side (blue squares) and end-to-end dimerization (red dots). Values of the (b) nanorod depolarization factor L, (c) real part and (d) imaginary part of the dipole polarizability, calculated for different aspect ratio values AR = 1.0 (sphere), 2.8, 3.5 and 4.0 on the basis of the Clasius-Mossotti equation. The medium refractive index $n_m$ was set equal to 1.33.

Elucidating further, the dipole moment of the nanorod plasmon in the quasi-static limit is given as:[82]

$$\mu = \varepsilon_m \alpha \hat{E} \quad (2)$$

where $\hat{E}$ is the electric field experienced by the nanorod and $\varepsilon_m = n_m^2$ is the medium dielectric constant. As per the Clausius-Mossotti relation[54] for the polarizability corresponding to the longitudinal excitation:

$$\alpha = \frac{\varepsilon_0 V}{L} \left( \frac{\varepsilon - \varepsilon_m}{\varepsilon + \left( \frac{1-L}{L} \right) \varepsilon_m} \right) \quad (3)$$

where V is the nanorod volume, $\varepsilon_0$ is the vacuum permittivity and $\varepsilon = \varepsilon_r + i\varepsilon_i$ is the complex dielectric function of gold. L is the depolarization factor corresponding to the long-axis and can be expressed as a function of the nanorod aspect ratio AR as:[56,82]

$$L = \frac{1-e^2}{e^2} \left( \frac{1}{2e} \ln \frac{1+e}{1-e} - 1 \right) \quad (4)$$

$$e = \sqrt{1-(1/AR)^2} \quad (5)$$

The value of L is 1/3 for a sphere and decreases with increasing nanorod aspect ratio (Figure 4.8b). The resonance condition from eq 3 is given by:

$$\varepsilon_r = -\left( \frac{1-L}{L} \right) \varepsilon_m \quad (6)$$

This is provided $\varepsilon_2$ is small or weakly dependent on frequency,[54] which is valid in the 600-850 nm region for gold.[83] Eq 6 explains the red-shift of the longitudinal plasmon resonance with increasing aspect ratio since the negative real part of the dielectric function $\varepsilon_r$ for gold increases with increasing wavelength.[83] At resonance, $\alpha$ is given as:

$$\mathrm{Re}\left(\alpha\right) = \frac{\varepsilon_0 V}{L} \qquad (7)$$

$$\mathrm{Im}\left(\alpha\right) = \frac{\varepsilon_0 V}{L^2}\left(\frac{\varepsilon_m}{\varepsilon_i}\right) \qquad (8)$$

The rapid decrease in L with increasing aspect ratio against a slight increase in the imaginary part of the dielectric constant with wavelength (in the region of investigation) predicts a larger polarizability for higher aspect ratios. This is depicted in the calculated plots of the real and imaginary parts of the nanorod dipole polarizability for the different aspect ratio values (Figure 4.8c,d). The explanation of increasing plasmon coupling strength with increasing nanorod aspect ratio on the basis of the quasistatic and dipole approximations serves only as a qualitative one since finite particle size (as compared to the wavelength of light) effects[78,92] and higher order interactions[43] are not included.

### 4.3.8 Symmetry-Breaking in Heterodimers

The calculated longitudinal plasmon spectrum for a dimer with two nanorods having dissimilar aspect ratios (AR = 2.8 and 4.0, respectively) but the same width (b ~ 21 nm) is shown for the side-by-side case in Figure 4.9a. As seen from Figure 4.9a, the longitudinal plasmon maximum is around 695 nm for an isolated nanorod of aspect ratio 2.8 and around 835 nm for an isolated nanorod of aspect ratio 4.0. However, plasmon coupling in the assembled dimer results in a spectrum with a blue-shifted component around 680 nm (corresponding to the symmetric plasmon coupling mode) and a red-
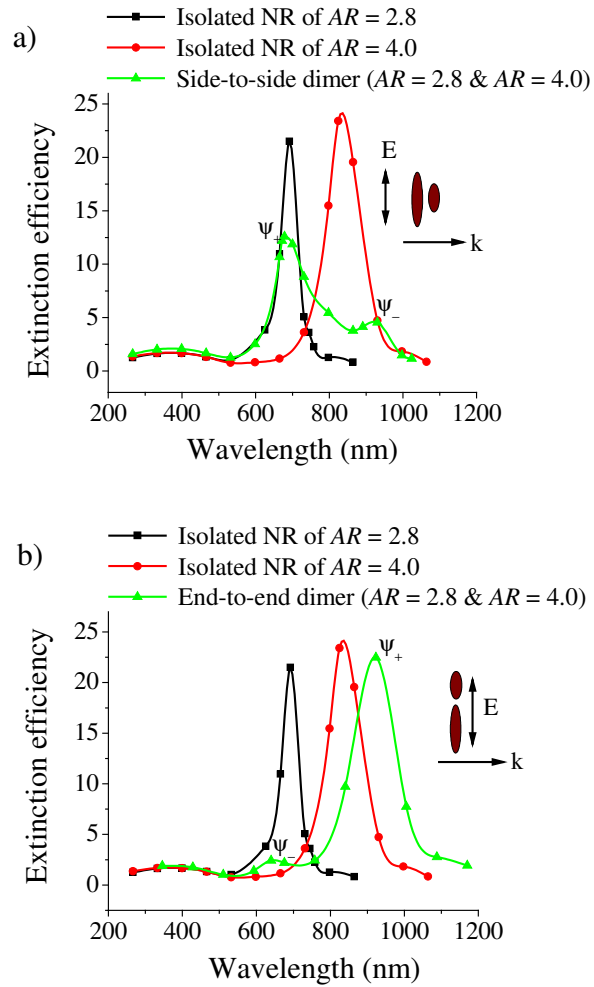
Figure 4.9: DDA-simulated extinction efficiency spectrum (corresponding to the longitudinal plasmon excitation) of a dimer of nanorods of dissimilar aspect ratios (AR = 2.8 and AR = 4.0 respectively) but the same width (b ~ 21 nm), (a) interacting side-by-side with inter-nanorod distance R = 21 nm where nanorods touch each other and (b) interacting end-to-end with inter-nanorod distance R = 70 nm where nanorods touch each other. Calculated spectra of the isolated nanorods are also shown for comparison.

shifted component around 930 nm (corresponding to the anti-symmetric coupling mode).

For a side-by-side dimer with rods of the same length, the anti-symmetric coupling mode

with lower energy would have a zero dipole moment and absorption to that level will not

be observed optically. However, when the rod lengths are dissimilar, absorption to this

red-shifted level becomes observed, although it possesses a lower spectral intensity due to the lower net dipole moment. The transverse band on assembly shows a single blue shifted band around 505 nm, which is expected since the two nanorods irrespective of their aspect ratios have the same transverse plasmon oscillation energy. Similarly as shown in Figure 4.9b, when rods of dissimilar aspect ratio are assembled end-to-end, the higher energy component corresponding to the anti-symmetric coupling becomes allowed due to symmetry breaking, although it possesses a relatively lower spectral intensity. Experimental realization of this symmetry breaking is rendered difficult due to the heterogeneous nature of the colloidal assembly process and the broad spectral bandwidths of the nanorod solutions.

The calculated spectra of rod-sphere dimers interacting side-by-side as well as end-to-end (with the light polarization along the nanorod long-axis) are seen to be red-shifted with respect to the isolated nanorod resonance (Figure 4.10). This can be explained on similar grounds as being due to the coupling of the nanorod longitudinal plasmon oscillation and the nanosphere oscillation. The magnitude of the shift for rod-sphere pairs is relatively smaller than in the case of nanorod pairs due to the energy mismatch between the longitudinal plasmon and the transverse plasmon modes and the weaker oscillator strength of the transverse plasmon mode. The blue-shifted component corresponding to the nanosphere resonance is too weak in intensity to be identified.

### 4.3.9 Dependence of Plasmon Coupling on the Angle between the Nanorod Axes

The angle between the long axes of two nanorods assembled side-by-side was varied as $\theta_{12} = 0°$, $45°$ and $90°$ with the light polarization along the long-axis of one of the

nanorods. The simulated spectra have been shown for the three cases in Figure 4.11. For the case of 0˚, i.e., with the dipoles aligned parallel to each other, the maximum blue-shift
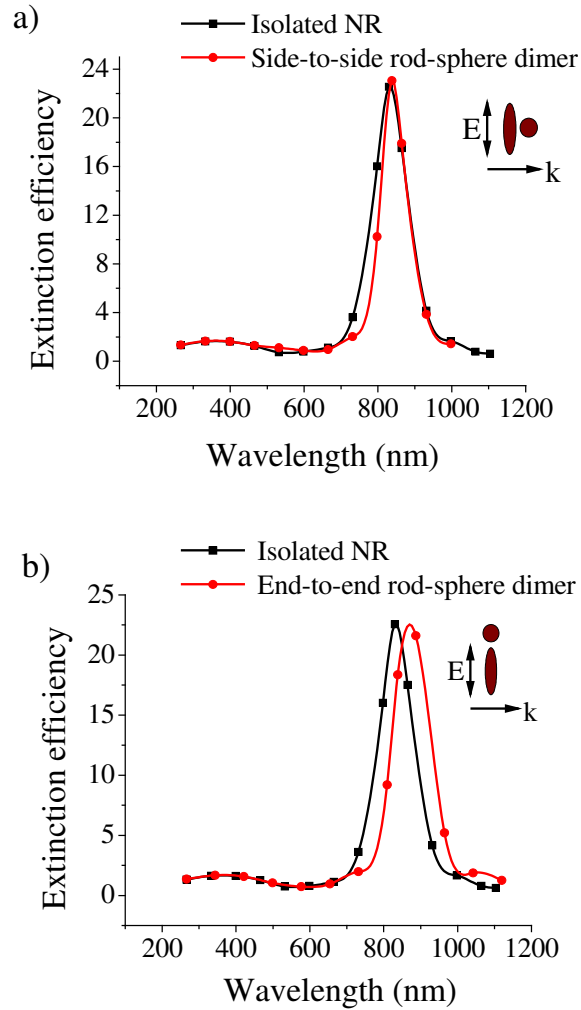


Figure 4.10: DDA-simulated extinction efficiency spectrum of a dimer of a gold nanorod (AR = 4.0, $r_{eff}$ = 16 nm) and a nanosphere (10 nm radius) (a) interacting side-by-side with an inter-particle distance R = 22 nm and (b) interacting end-to-end with an inter-particle distance R = 52 nm. The light polarization direction was along the nanorod long-axis. Calculated longitudinal plasmon spectra of the isolated nanorods are also shown for comparison (black curve).
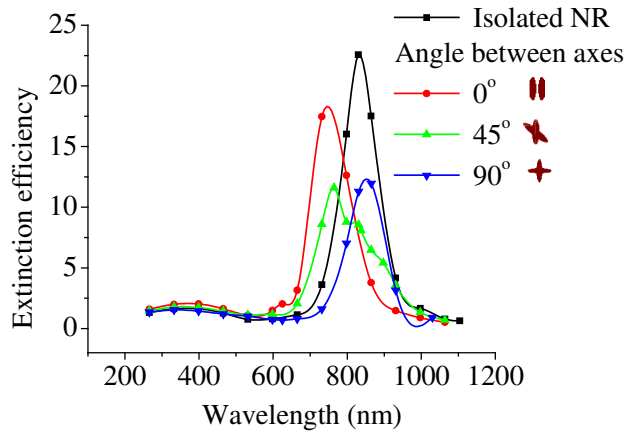
Figure 4.11: DDA-simulated extinction efficiency spectra of a dimer of gold nanorods assembled side-by-side (inter-nanorod distance R = 20 nm i.e. nanorods touching each other) as a function of the angle between the long-axes of the nanorod. The light polarization direction was maintained along one of the nanorods. The spectrum of the isolated nanorod is shown as a black curve for comparison

can be seen (corresponding to $\xi = 1$). On the other hand, at an angle of 90° between the

plasmons (corresponding to $\xi = 0$), no spectral blue-shift is seen, i.e., the longitudinal

plasmons do not couple. A slight red-shift is observed due to the coupling of the

longitudinal plasmon of one nanorod with the transverse plasmon of the other nanorod.

At an angle of 45°(corresponding to $\xi = 1/\sqrt{2}$), a plasmon blue-shift is seen, the extent of

shift slightly smaller compared to the case of $\theta_{12} = 0°$ or parallel alignment. A red-shifted

component is also seen as a combined effect of the anti-symmetric coupling of the

interacting plasmons (nonzero sum of dipole moments) in combination with the coupling

of the longitudinal plasmon of one nanorod to the transverse plasmon mode of another.

## 4.3.10 Dependence of Plasmon Coupling on the Surrounding Medium.

The $1/n_m^2$ dependence of the interaction energy in the exciton-coupling model (eq

1) predicts the interparticle plasmon interaction to be shielded by the medium dielectric.

141

Figure 4.12 shows the calculated longitudinal plasmon resonance of side-by-side and end-to-end assembled nanorod dimers with respect to the isolated single nanorod resonance, in a medium of refractive index $n_m$ = 1.7. Eq 6 explains the red-shift of the single nanorod resonance with increase in the medium refractive index $n_m$. By comparison with the case of $n_m$ = 1.33 for a similar inter-nanorod distance, it can be seen that the increase in the medium refractive index to $n_m$ = 1.7 results in a small decrease in the magnitude of the plasmon shift (0.03 eV for side-by-side dimerization and 0.01 eV for end-to-end dimerization). However, any dependence of the interparticle plasmon coupling on the medium refractive index is however complicated by the fact that increase in $n_m$ results in the red-shift of $\lambda_{max}$, increase in the nanorod polarizability (eq 8) and dipole moment (eq 2) and the variation in finite-particle size effects and multipolar contributions.
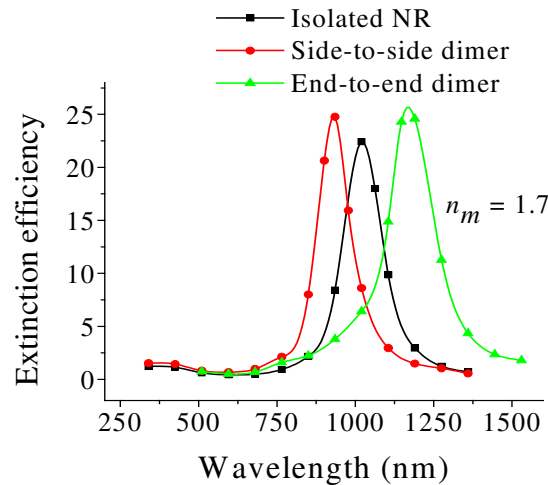


Figure 4.12: DDA-simulated extinction efficiency spectra (corresponding to the longitudinal plasmon excitation) of a dimer of gold nanorods interacting side-by-side (shown in blue) with inter-nanorod distance R = 22 nm and end-to-end (shown in red) with inter-nanorod distance R = 83 nm for medium refractive index $n_m$ = 1.7. The spectrum of the isolated nanorod (black curve) is shown for comparison.

## 4.4 Conclusion

Electrodynamic simulations of nanoparticle systems based on the DDA method provide a solid basis for the interpretation of experimental optical spectra as well as apriori prediction of the trends in optical properties. In our experiments, we observed that the solution assembly of nanorods induced by the addition of sodium citrate resulted in the blue-shift of the longitudinal nanorod plasmon bands – an observation in contrast to the red-shift observed in earlier studies[72,73] involving the end-to-end assembly of nanorods. The analysis of the assembly mechanism in our experiments pointed toward a side-by-side assembly of nanorods in solution; confirmation was obtained from the agreement of DDA simulations of dimers of nanorods with the observed plasmon shifts. Assembly induced plasmon shift results from inter-nanorod plasmon coupling, the strength of which was seen from the simulation results to increase with a decrease in the inter-nanorod distance, an increase in the number of interacting nanorods and an increase in the nanorod aspect ratio for both side-by-side as well as end-to-end assembly. Most qualitative features of the simulated trends in interparticle plasmon coupling could be explained by treating the plasmon oscillation as an exciton. On the basis of the exciton theory, an analogy could be drawn between the orientational modes of nanorod assembly and the well-known H and J aggregation of organic chromophores. However, quantitative deviations from the exciton theory arise as a result of the multipolar nature of the plasmonic interaction and the effect of finite particle size. An additional interesting theoretical observation was the symmetry breaking in dimers of nanorods either having dissimilar aspect ratios or oriented nonparallel to each other, which resulted in longitudinal plasmon resonance with both a blue-shifted and a red-shifted band. The

coupled nanorod plasmons can also thought of as electromagnetic analogues of molecular orbitals. The strong contrast between the bonding nature of the end-to-end nanorod plasmon coupling and the anti-bonding nature of the side-by-side coupling is manifested in optical spectra of the assemblies; the effect of this contrast on field enhancement-based properties needs to be exploited further.

## 4.5 References and Notes

(1)     Mann, S.; Shenton, W.; Li, M.; Connolly, S.; Fitzmaurice, D. *Adv. Mater.* **2000**, *12*, 147.

(2)     Mirkin, C. A. *Inorg. Chem.* **2000**, *39*, 2258.

(3)     Murphy, C. J.; Sau, T. K.; Gole, A. M.; Orendorff, C. J.; Gao, J.; Gou, L.; Hunyadi, S. E.; Li, T. *J. Phys. Chem. B* **2005**, *109*, 13857.

(4)     Pileni, M. P. *J. Phys. Chem. B* **2001**, *105*, 3358.

(5)     Pileni, M. P. *Appl. Surface Sci.* **2001**, *171*, 1.

(6)     Pileni, M. P. *J. Phys.: Condens. Matter* **2006**, *18*, S67.

(7)     Pileni, M. P.; Lalatonne, Y.; Ingert, D.; Lisiecki, I.; Courty, A. *Faraday Discuss.* **2003**, *125*, 251.

(8)     Storhoff, J. J.; Mirkin, C. A. *Chem. Rev.* **1999**, *99*, 1849.

(9)     Teranishi, T.; Miyake, M. *Encycl. Nanosci. Nanotechnol.* **2004**, *5*, 421.

(10)    Davis, S. A.; Breulmann, M.; Rhodes, K. H.; Zhang, B.; Mann, S. *Chem. Mater.* **2001**, *13*, 3218.

(11)  Alivisatos, A. P.; Johnsson, K. P.; Peng, X.; Wilson, T. E.; Loweth, C. J.; Bruchez, M. P., Jr.; Schultz, P. G. *Nature* **1996**, *382*, 609.

(12)  Mirkin, C. A.; Letsinger, R. L.; Mucic, R. C.; Storhoff, J. J. *Nature* **1996**, *382*, 607.

(13)  Alivisatos, P. *Nat. Biotechnol.* **2004**, *22*, 47.

(14)  Shenton, W.; Davis, S. A.; Mann, S. *Adv. Mater.* **1999**, *11*, 449.

(15)  Sudeep, P. K.; Joseph, S. T. S.; Thomas, K. G. *J. Am. Chem. Soc.* **2005**, *127*, 6516.

(16)  Elghanian, R.; Storhoff, J. J.; Mucic, R. C.; Letsinger, R. L.; Mirkin, C. A. *Science* **1997**, *277*, 1078.

(17)  Ando, M.; Kawasaki, M.; Imazeki, S.; Sasaki, H.; Kamata, T. *Appl. Phys. Lett.* **2004**, *85*, 1849.

(18)  Feldheim, D. L.; Foss, C. A., Jr. *Met. Nanopart.* **2002**, 1.

(19)  Hu, M.-S.; Chen, H.-L.; Shen, C.-H.; Hong, L.-S.; Huang, B.-R.; Chen, K.-H.; Chen, L.-C. *Nat. Mater.* **2006**, *5*, 102.

(20)  Jin, Y.; Friedman, N. *J. Am. Chem. Soc.* **2005**, *127*, 11902.

(21)  Maheshwari, V.; Saraf, R. F. *Science* **2006**, *312*, 1501.

(22)  Tan, Y.; Li, Y.; Zhu, D. *Encyclo. Nanosci. Nanotechnol.* **2004**, *8*, 9.

(23)  Pillai, S.; Catchpole, K. R.; Trupke, T.; Zhang, G.; Zhao, J.; Green, M. A. *Appl. Phys. Lett.* **2006**, *88*, 161102/1.

(24)  Krenn, J. R.; Salerno, M.; Felidj, N.; Lamprecht, B.; Schider, G.; Leitner, A.; Aussenegg, F. R.; Weeber, J. C.; Dereux, A.; Goudonnet, J. P. *J. Microsc.* **2001**, *202*, 122.

(25)    Maier, S. A.; Atwater, H. A. *J. Appl. Phys.* **2005**, *98*, 011101/1.

(26)    Maier, S. A.; Brongersma, M. L.; Kik, P. G.; Meltzer, S.; Requicha, A. A. G.; Atwater, H. A. *Adv. Mater.* **2001**, *13*, 1501.

(27)    Maier, S. A.; Friedman, M. D.; Barclay, P. E.; Painter, O. *Appl. Phys. Lett.* **2005**, *86*, 071103/1.

(28)    Maier, S. A.; Kik, P. G.; Atwater, H. A.; Meltzer, S.; Harel, E.; Koel, B. E.; Requicha, A. A. G. *Nat. Mater.* **2003**, *2*, 229.

(29)    Quinten, M.; Leitner, A.; Krenn, J. R.; Aussenegg, F. R. *Opt. Lett.* **1998**, *23*, 1331.

(30)    Barnes, W. L.; Dereux, A.; Ebbesen, T. W. *Nature* **2003**, *424*, 824.

(31)    Feldstein, M. J.; Keating, C. D.; Liau, Y.-H.; Natan, M. J.; Scherer, N. F. *J. Am. Chem. Soc.* **1997**, *119*, 6638.

(32)    Seker, F.; Malenfant, P. R. L.; Larsen, M.; Alizadeh, A.; Conway, K.; Kulkarni, A. M.; Goddard, G.; Garaas, R. *Adv. Mater.* **2005**, *17*, 1941.

(33)    Liz-Marzan, L. M. *Langmuir* **2006**, *22*, 32.

(34)    Grant, C. D.; Schwartzberg, A. M.; Norman, T. J., Jr.; Zhang, J. Z. *J. Am. Chem. Soc.* **2003**, *125*, 549.

(35)    Lazarides, A. A.; Schatz, G. C. *J. Phys. Chem. B* **2000**, *104*, 460.

(36)    Lin, S.; Li, M.; Dujardin, E.; Girard, C.; Mann, S. *Adv. Mater.* **2005**, *17*, 2553.

(37)    Jain, P. K.; Qian, W.; El-Sayed, M. A. *J. Phys. Chem. B* **2006**, *110*, 136.

(38)    Storhoff, J. J.; Lazarides, A. A.; Mucic, R. C.; Mirkin, C. A.; Letsinger, R. L.; Schatz, G. C. *J. Am. Chem. Soc.* **2000**, *122*, 4640.

(39)    Su, K. H.; Wei, Q. H.; Zhang, X.; Mock, J. J.; Smith, D. R.; Schultz, S. *Nano Lett.* **2003**, *3*, 1087.

(40)    Sönnichsen, C.; Reinhard, B. M.; Liphardt, J.; Alivisatos, A. P. *Nat. Biotechnol.* **2005**, *23*, 741.

(41)    Rechberger, W.; Hohenau, A.; Leitner, A.; Krenn, J. R.; Lamprecht, B.; Aussenegg, F. R. *Opt. Commun.* **2003**, *220*, 137.

(42)    Nordlander, P.; Oubre, C.; Prodan, E.; Li, K.; Stockman, M. I. *Nano Lett.* **2004**, *4*, 899.

(43)    Xiao, J. J.; Huang, J. P.; Yu, K. W. *Phys. Rev. B.* **2005**, *71*, 045404/1.

(44)    Haynes, C. L.; McFarland, A. D.; Zhao, L.; Van Duyne, R. P.; Schatz, G. C.; Gunnarsson, L.; Prikulis, J.; Kasemo, B.; Käll, M. *J. Phys.Chem. B* **2003**, *107*, 7337.

(45)    Sweatlock, L. A.; Maier, S. A.; Atwater, H. A.; Penninkhof, J. J.; Polman, A. *Phys. Rev. B.* **2005**, *71*, 235408/1.

(46)    Hao, E.; Schatz George, C. *J. Chem. Phys.* **2004**, *120*, 357.

(47)    Jiang, J.; Bosnick, K.; Maillard, M.; Brus, L. *J. Phys. Chem. B* **2003**, *107*, 9964.

(48)    Michaels, A. M.; Jiang, J.; Brus, L. *J. Phys. Chem. B* **2000**, *104*, 11965.

(49)    Ritchie, G.; Burstein, E. *Phys. Rev. B* **1981**, *24*, 4843.

(50)    Maillard, M.; Monchicourt, P.; Pileni, M. P. *Chem. Phys. Lett.* **2003**, *380*, 704.

(51)    Shalaev, V. M.; Poliakov, E. Y.; Markel, V. A. *Phys. Rev. B* **1996**, *53*, 2437.

(52)    Markel, V. A.; Shalaev, V. M.; Zhang, P.; Huynh, W.; Tay, L.; Haslett, T. L.; Moskovits, M. *Phys. Rev. B* **1999**, *59*, 10903.

(53)     Link, S.; El-Sayed, M. A. *J. Phys. Chem. B* **1999**, *103*, 8410.

(54)     Kreibig, U.; Vollmer, M. *Optical Properties of Metal Clusters*, Series in Materials Science 25; Springer: New York, 1995.

(55)     Gans, R. *Ann. Phys.* **1915**, *47*, 270.

(56)     Link, S.; Mohamed, M. B.; El-Sayed, M. A. *J. Phys. Chem. B* **1999**, *103*, 3073.

(57)     Link, S.; El-Sayed, M. A.; Mohamed, M. B. *J. Phys. Chem. B* **2005**, *109*, 10531.

(58)     Jain, P. K.; Lee, K. S.; El-Sayed, I. H.; El-Sayed, M. A. *J. Phys. Chem. B* **2006**, *110*, 7238.

(59)     Gans, R. *Ann. Phys.* **1912**, *37*, 881.

(60)     Mohamed, M. B.; Volkov, V.; Link, S.; El-Sayed, M. A. *Chem. Phys. Lett.* **2000**, *317*, 517.

(61)     Eustis, S.; El-Sayed, M. *J. Phys. Chem. B* **2005**, *109*, 16350.

(62)     Nikoobakht, B.; El-Sayed, M. A. *J. Phys. Chem. A* **2003**, *107*, 3372.

(63)     Nikoobakht, B.; Wang, J. P.; El-Sayed, M. A. *Chem. Phys. Lett.* **2002**, *366*, 17.

(64)     Dickson, R. M.; Lyon, L. A. *J. Phys. Chem. B* **2000**, *104*, 6095.

(65)     Murphy, C. J.; Jana, N. R.; Gearheart, L. A.; Obare, S. O.; Caswell, K. K.; Mann, S.; Johnson, C. J.; Davis, S. A.; Dujardin, E.; Edler, K. J. *Chem. Nanomater.* **2004**, *1*, 285.

(66)     Orendorff, C. J.; Hankins, P. L.; Murphy, C. J. *Langmuir* **2005**, *21*, 2022.

(67)     Jana, N. R.; Gearheart, L. A.; Obare, S. O.; Johnson, C. J.; Edler, K. J.; Mann, S.; Murphy, C. J. *J. Mater. Chem.* **2002**, *12*, 2909.

(68)    Nikoobakht, B.; Wang, Z. L.; El-Sayed, M. A. *J. Phys. Chem. B* **2000**, *104*, 8635.

(69)    Gole, A.; Murphy, C. J. *Langmuir* **2005**, *21*, 10756.

(70)    Caswell, K. K.; Wilson, J. N.; Bunz, U. H. F.; Murphy, C. J. *J. Am. Chem. Soc.* **2003**, *125*, 13914.

(71)    Dujardin, E.; Mann, S.; Hsin, L.-B.; Wang, C. R. C. *Chem. Commun.* **2001**, 1264.

(72)    Thomas, K. G.; Barazzouk, S.; Ipe, B. I.; Joseph, S. T. S.; Kamat, P. V. *J. Phys. Chem. B* **2004**, *108*, 13066.

(73)    Joseph, S. T. S.; Ipe, B. I.; Pramod, P.; Thomas, K. G. *J. Phys. Chem. B* **2006**, *110*, 150.

(74)    Kasha, M. *Radiat. Res.* **1963**, *20*, 55.

(75)    Kasha, M.; Rawls, H. R.; El-Bayoumi, M. A. *Pure Appl. Chem.* **1965**, *11*, 371.

(76)    Valdes-Aguilera, O.; Neckers, D. C. *Acc. Chem. Res.* **1989**, *22*, 171.

(77)    Draine, B. T.; Flatau, P. J. *J. Opt. Soc. Am. A* **1994**, *11*, 1491.

(78)    Kelly, K. L.; Coronado, E.; Zhao, L. L.; Schatz, G. C. *J. Phys. Chem. B* **2003**, *107*, 668.

(79)    Schatz, G. C. *Theochem* **2001**, *573*, 73.

(80)    Brioude, A.; Jiang, X. C.; Pileni, M. P. *J. Phys. Chem. B* **2005**, *109*, 13138.

(81)    Lee, K.-S.; El-Sayed, M. A. *J. Phys. Chem. B* **2005**, *109*, 20331.

(82)    Gluodenis, M.; Foss, C. A., Jr. *J. Phys. Chem. B* **2002**, *106*, 9484.

(83)    Johnson, P. B.; Christy, R. W. *Phys. Rev. B* **1972**, *6*, 4370.

(84)    Draine, B. T.; Goodman, J. *Astrophys. J.* **1993**, *405*, 685.

(85)    Eustis, S.; El-Sayed, M. A. *J. Appl. Phys.* **2006**, *100,* 044324/1.

(86)    Taleb, A.; Petit, C.; Pileni, M. P. *Chem. Mater.* **1997**, *9*, 950.

(87)    Motte, L.; Billoudet, F.; Lacaze, E.; Douin, J.; Pileni, M. P. *J. Phys. Chem. B* **1997**, *101*, 138.

(88)    Cortie, M. B.; Xu, X.; Ford, M. J. *Phys. Chem. Chem. Phys.* **2006**, *8*, 3520.

(89)    Packard, B. Z.; Toptygin, D. D.; Komoriya, A.; Brand, L. *J. Phys.Chem. B* **1998**, *102*, 752.

(90)    Kasha, M. *Phys. Process. Radiation Biol., Proc. Intern. Symp., Mich. State Univ.* **1964**, 17.

(91)    Prodan, E.; Radloff, C.; Halas, N. J.; Nordlander, P. *Science* **2003**, *302*, 419.

(92)    Aizpurua, J.; Bryant, G. W.; Richter, L. J.; Garcia de Abajo, F. J.; Kelley, B. K.; Mallouk, T. *Phys. Rev. B* **2005**, *71*, 235420/1.

(93)    The spectral band structure is significantly altered when the two nanorods are touching each other end-to-end (Figure 4.3a, *R* = 81 nm). Interesting spectral characteristics of particles touching each other have already been investigated by Atwater and co-workers (ref 45). At the same time, exceptions to the applicability of electrodynamic simulations to particles touching each other have also been cited (ref 46).

# CHAPTER 5

# UNIVERSAL SCALING BEHAVIOR OF THE DISTANCE DECAY

# OF PLASMON COUPLING IN METAL NANOPARTICLE PAIRS

## Abstract

Localized surface plasmon resonances (LSPR) in lithographically fabricated gold nanodisc pairs are investigated using microabsorption spectroscopy and electrodynamic simulations. In agreement with previous work, we find that the fractional plasmon wavelength shift for polarization along the interparticle axis decays nearly exponentially with the interparticle gap. In addition, we find that the decay length is roughly 0.2 in units of the particle size for different nanoparticle size, shape, metal type, or medium dielectric constant. The near-exponential distance decay and the interesting "universal" scaling behavior of interparticle plasmon coupling can be qualitatively explained on the basis of a dipolar-coupling model as being due to the interplay of two factors: the direct dependence of the single-particle polarizability on the cubic power of the particle dimension and the decay of the plasmonic near-field as the cubic power of the inverse distance. Using this universal scaling behavior, we are able to derive a "plasmon ruler equation" that estimates the interparticle separation between Au nanospheres in a biological system from the observed fractional shift of the plasmon band. We find good agreement of the interparticle separations estimated using this equation with the experimental observations of Reinhard et al from Nano Lett. 2005, 5, 2246-2252.

## 5.1 Introduction

The unique interaction of metal nanoparticles with electromagnetic radiation is constituted by localized surface plasmons, which are coherent oscillations of the metal electrons in resonance with light of a certain frequency, i.e., the localized surface plasmon resonance (LSPR) frequency.[1-6] The LSPR results in a strongly enhanced electric near-field localized at the particle surface, which forms the basis of surface-enhanced spectroscopy using metal nanoparticles.[7,8] The plasmon oscillations also decay radiatively or nonradiatively, respectively, giving rise to strongly enhanced scattering (in the far-field) and absorption at the LSPR frequency.[2,9,10] These optical properties have been utilized in optical technologies for chemical and biological imaging,[11,12] sensing,[13-15] and therapeutics.[16-19] Many of the applications of metal nanoparticles are being realized from their assemblies and hence, recent studies have been focused on the assemblies/arrays of metal nanoparticles.[20] These studies have established that the plasmonic properties are strongly dependent on interparticle interactions.[21-29] The near-field on one particle has the ability to interact with that on an adjacent particle in close proximity, coupling the plasmon oscillations together.[1,23,28,30,31] This interparticle plasmon coupling forms the basis of the intense enhancement of spectroscopic signals (e.g., SERS) from molecules adsorbed at nanoparticle junctions, providing the capability for single-molecule sensing and detection.[32,33] Near-field coupling in ordered nanoparticle assemblies has also been exploited for electromagnetic energy transport and sub-wavelength photonic waveguiding.[34-37]

The coupled-particle LSPR occurs at a frequency that is shifted from the single-particle LSPR frequency. The assembly or aggregation of gold nanoparticles in solution

results in a red-shift of the plasmon extinction wavelength maximum from that of isolated gold nanoparticle solution at ~520 nm, as also evidenced by a visual color change from red to purple.[22,38,39] As shown by the Alivisatos and Mirkin groups,[40,41] by employing a biomolecular recognition event (e.g., DNA hybridization) to trigger the assembly of nanoparticles in solution, the spectral shift in the plasmon resonance can be employed to detect specific biomolecules including DNA and protein biomarkers for cancer and other diseases.[13] The magnitude of the assembly-induced plasmon shift depends on the strength of the interparticle coupling, which, in turn, depends on the proximity of the individual nanoparticles. The plasmon shift thus gives a measure of the distance between the particles.[39,42,43] Sonnichsen et al. and Reinhard et al. utilized this recently to design a "plasmon ruler" to measure nanoscale distances in biological systems on the basis of the spectral shift resulting from the coupling of two gold nanoparticles by a defined biomolecular binding scheme.[42,44] The plasmon ruler has some distinct advantages over the fluorescence resonance energy transfer (FRET) technique traditionally used for distance measurement, viz. a longer distance range and better photostability of the optical probes.[42,43] However, a major prerequisite for the application of the plasmonic ruler is the systematic calibration and standardization of the spectral shift as a function of the interparticle separation.[43] While the distance dependence of FRET is well established,[45] there have been few quantitative studies on the distance dependence of plasmon coupling.[21,23,27,43] The decay of electromagnetic fields in nanostructures is also fundamentally interesting from the point of view of plasmonics.[30,34]

The electron beam lithography technique, which provides the ability to produce metal nanoparticle structures with controlled dimensions and spacing, has already been

shown by Aussenegg and Krenn to be extremely powerful for such studies.[23,46-48] Recently, Su et al. studied plasmon coupling in lithographically produced elliptical gold nanoparticle pairs and observed that the plasmon shift decays almost exponentially as a function of the interparticle separation.[21] Gunnarsson et al.[27] further verified this near-exponential behavior in a system of Ag nanodisc pairs. A fundamental model explaining the distance dependence of plasmon coupling is lacking, however, which is the goal of the present work.

In this chapter, we describe the study of the plasmon resonances of lithographically fabricated pairs of Au nanodiscs for different interparticle separations. The polarization dependence of the plasmon coupling is clearly evident, in line with an earlier study by Rechberger et al.[23] The exponential-like decay of the plasmonic shift with interparticle gap for polarization along the interparticle axis is also observed. Discrete dipole approximation simulations of the nanodisc pairs verify the observation of Su et al. that the near-exponential trend of the plasmon shift with respect to the interparticle gap becomes independent of the nanodisc diameter when the shift and separation gap are scaled respectively by the single-particle plasmon wavelength and the nanodisc diameter.[21] We further find that the decay constant measured for our Au-based system matches very well with that of the Ag system studied earlier.[27] The decay constant is calculated also to be similar for nanoparticles of different shape as well as for different dielectric media. Thus, the distance decay of interparticle plasmon coupling manifests a universal scaling behavior, the origin of which we explain on the basis of a simple dipolar-coupling model.

## 5.2. Experimental Methods

### 5.2.1 Lithographic Fabrication of Nanodisc Pair Arrays

Au nanodisc pairs were fabricated by electron beam lithography (EBL) and characterized by Wenyu Huang, another group member. Quartz slides (Technical Glass Products, Inc.) cleaned in piranha solution (1 part 30% $H_2O_2$ and 3 parts $H_2SO_4$) for 1.5 h at 80 °C and dried in air were spin-coated with 65 nm PMMA 950k electron-sensitive resist followed by curing at 180 °C for 3 min. In order to render the substrate conductive, it was coated with a 10 nm gold layer in a thermal evaporator. The pattern for the nanodisc array was written on the substrate using the JEOL JBX-9300FS EBL system. The gold layer was then etched with an aqueous solution of KI and $I_2$ followed by development in 1:3 methyl isobutyl ketone/isopropyl alcohol for 180 s. The patterned substrate was then washed in isopropyl alcohol for 30 s and dried in pure $N_2$. A thin 0.4 nm Cr layer was deposited on the substrate in an electron beam evaporator in order to improve the adhesion of the subsequent Au layer deposited to a 25 nm thickness at a rate of 0.5 Å/s. Finally, the PMMA resist and the overlaying Au layer is removed by lift-off in hot acetone (~63 °C). Following this procedure, we fabricated two-dimensional 80 μm x 80 μm arrays of 88 nm diameter Au nanodiscs with an interparticle center-to-center spacing of 300 nm between the particle rows and a center-to-center spacing of 600 nm between particles within each row. In each subsequent sample, every second particle row is shifted closer to the previous row to give different arrays of particle pairs with interparticle edge-to-edge separation gap varying as 212, 27, 17, 12, 7, and 2 nm. The patterns were imaged by scanning electron microscopy (SEM) on a LEO 1530 thermally-

assisted field emission SEM, Zeiss/LEO. A representative image of the array with an

interparticle gap of 12 nm is shown in Figure 5.1.
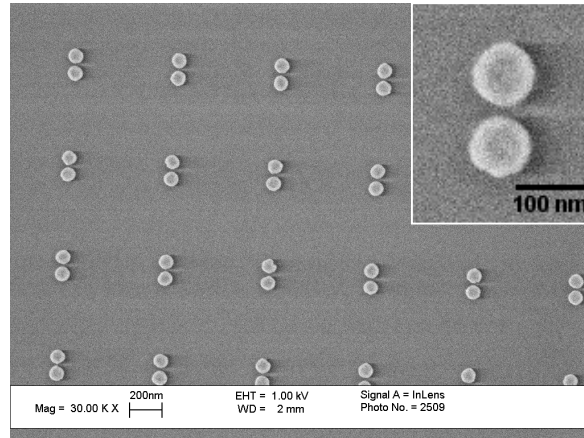


Figure 5.1: A representative SEM image of the array of nanodisc pairs used in the present study, having an inter-particle edge-to-edge separation gap of 12 nm, showing the homogeneity of the sample. The inset shows a magnified image of a single nanodisc pair clearly showing the inter-particle gap. Each nanodisc has a diameter of 88 nm and thickness of 25 nm. Images of arrays with other inter-particle gaps are not shown.

Optical spectra of the nanodisc pairs were obtained on the substrate using a SEE

1100 microabsorption spectrophotometer in the transmission mode under polarized light

excitation using a 20x objective. The area examined was 8 x 8 $\mu m^2$.

**5.2.2 Electrodynamic Simulations of Nanodisc Pair**

The plasmon resonance spectra of the nanodisc pairs were simulated by the

Discrete dipole approximation (DDA) method by using the DDSCAT 6.1 code developed

by Draine and Flatau. Dipole polarizabilities were assigned by the lattice dispersion

relation (LDR) by Draine and Goodman, which includes a radiative reaction correction

term required for finite dipole arrays. The target nanostructure was approximated as a

pair of cylinders, each represented by a cubic array of point dipoles with an inter-dipole spacing ~ 2 nm. The diameter of the cylinder D was 86.5 nm while the height h was 25.5 nm. The edge-to-edge separation between the nanodiscs was varied as 2, 8, 12, 18, 28, and 208 nm. Two other disc diameters, 54.0 nm and 68.0 nm, were also investigated while keeping the aspect ratio h/D ≈ 0.3 as well as the inter-dipole spacing constant. The dielectric properties of the nanostructure were simulated by the bulk dielectric function for Au, which as per the DDSCAT procedure was scaled by the dielectric constant $\varepsilon_m$ of the surrounding environment/medium. Calculations were performed for different values of $\varepsilon_m$ = 1.00, 1.38, and 2.25. The plane wave propagation direction was normal to the plane of the cylinder pair. Calculations of the extinction efficiency were performed for two separate polarization directions, i.e. one along the inter-particle axis, and the other perpendicular to it. Spectra were formed from the calculated extinction efficiency at discrete wavelengths by cubic interpolation of the data points.

## 5.2 Results and Discussion

### 5.2.1 Experimental Plasmon Resonance Spectra

LSPR spectra of lithographically fabricated Au nanodisc pair arrays with different inter-nanodisc separation gap s = 212, 27, 17, 12, 7, and 2 nm were obtained by microabsorption spectroscopy (Figure 5.2a,c). Two different polarization directions of the incident light were chosen, i.e., one parallel to the interparticle axis (Figure 5.2a) and the other perpendicular (Figure 5.2c) to the axis. The spectral behavior is in sharp contrast for the two polarization directions, as already observed by Tamaru et al.,[49] Rechberger et al.,[23] and Maier et al.[30] Under parallel polarization, the plasmon resonance strongly red-

shifts as the interparticle gap is reduced. Conversely, there is a very weak blue-shift with decreasing gap for orthogonal polarization. The resonance shift results from the electromagnetic coupling of the single-particle plasmons, the polarization dependence of which can be explained on the basis of a simple dipole-dipole coupling model. The dipole-dipole interaction is attractive for parallel polarization, which results in the reduction of the plasmon frequency (red-shift of the plasmon band), while that for the orthogonal polarization is repulsive, resulting in the increase in the plasmon frequency (blue-shift).[23,50] The interparticle interactions are clearly stronger for parallel polarization, as seen from the larger wavelength shifts. In fact, under parallel polarization, at extremely small interparticle gaps, i.e., s = 2 nm, a new shoulder appears at shorter wavelengths, similar to earlier studies on pairs of Ag nanodisc[27] and Au nanorods[50] with nearly touching particles. It must be noted that this new band is attributed to higher-order interactions, possibly the quadrupole mode,[27,51] and cannot be explained by the dipolar interaction model.

The shift in the plasmon extinction maximum is plotted against the interparticle edge-to-edge separation gap for the parallel polarization in Figure 5.3a. Note that the plasmon maximum for s = 212 nm (particles spaced enough to assume minimal coupling) has been used as the reference for calculation of the shift. Because these spectra are from an ensemble of particle pairs rather than single particle pairs, the data point for s = 2 nm was not included due to the significant dispersion in the lithographic fabrication of such a small gap. The plot of the plasmon shift versus the interparticle gap follows nearly an exponential decay with a decay length of 15.5 nm $\pm$ 3.0 nm.

(a)



(b)
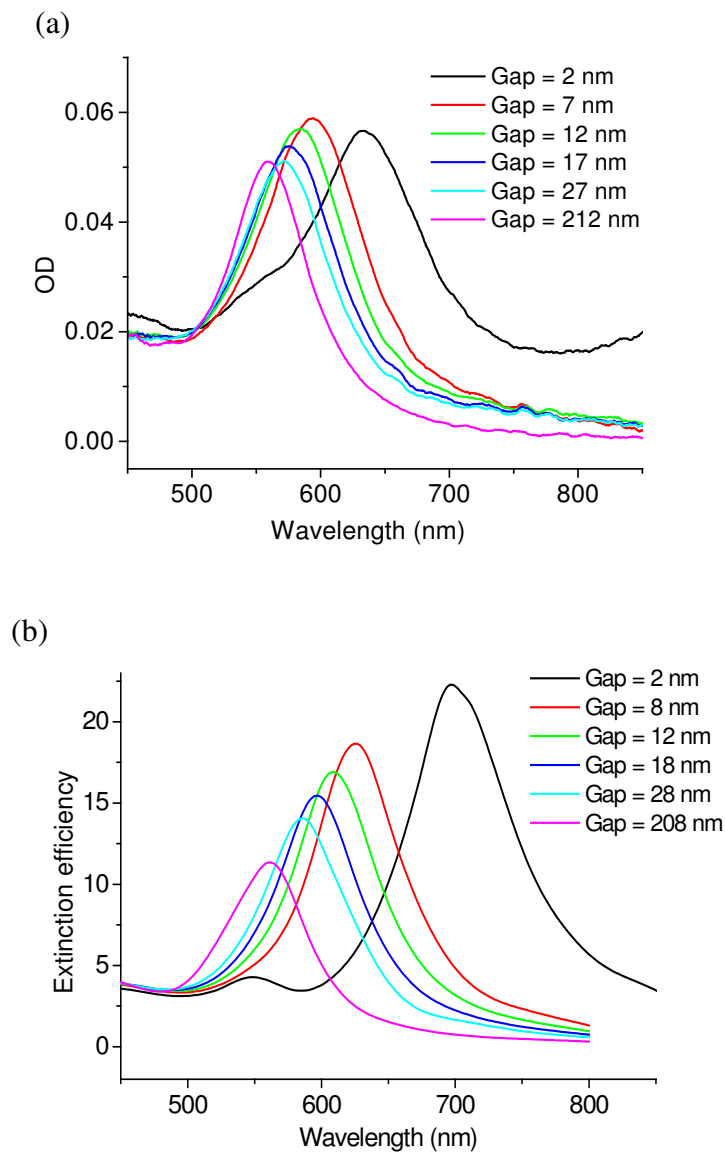


Figure 5.2: (a&c) Micro-absorption and (b&d) DDA-simulated extinction efficiency spectra of Au nanodisc pairs for varying inter-particle separation gap for incident light polarization direction (a&b) parallel and (c&d) perpendicular to the inter-particle axis.

(c)



(d)
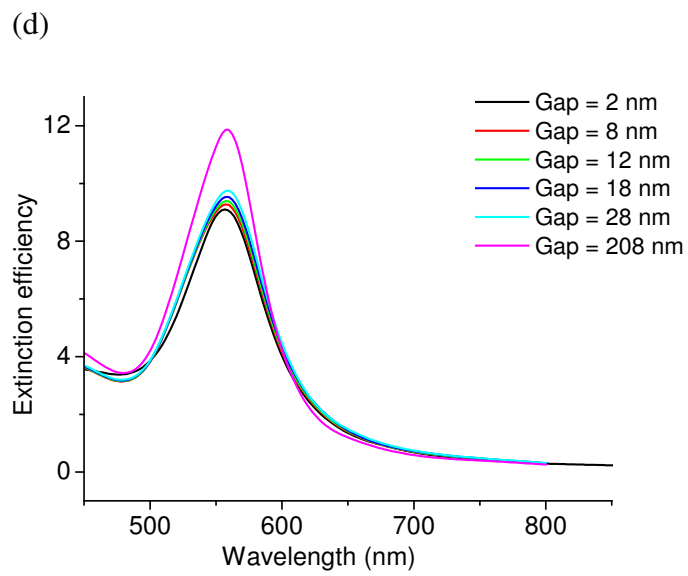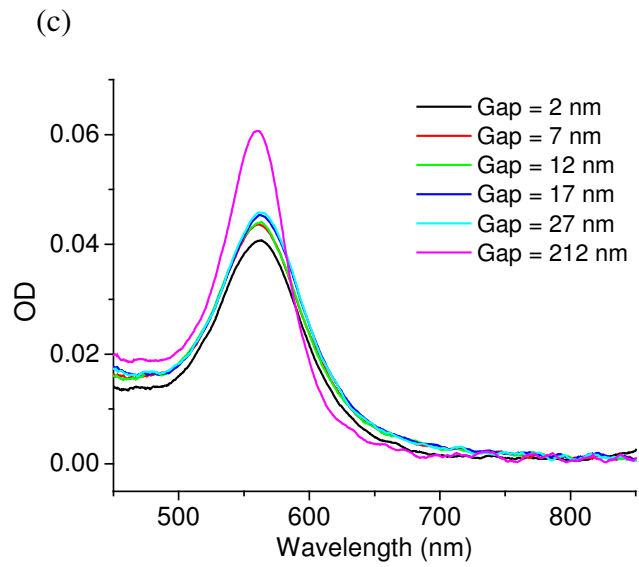


Figure 5.2 continued

**5.2.2 DDA Simulations**

The discrete dipole approximation (DDA) method[52] was used to simulate the LSPR spectra of the Au nanodisc pairs. The DDA method has been demonstrated by the Schatz group to be suitable for optical calculations of the extinction spectrum and the local electric field distribution in metal particles with different geometries and environments.[2,53] While DDA has limitations in calculating electromagnetic fields around particles, [54,55] we are interested in the extinction properties of the particle pairs, which are simulated quite well by DDA, as established by the work of the Schatz group, including recent calculations of lithographically prepared silver nanodisc pairs.[27] As argued earlier by Rechberger et al.,[23] it is reasonable to consider in the calculations a single particle pair instead of the entire 2-D array. This is because the individual particle pairs in the experiment, especially for the smaller gap samples, are separated from each other well enough (much larger than 2.5 particle diameters)[21] to have any significant near-field coupling between different pairs. This ensures that only the interaction with the pair partner is important.[23]

The results of discrete dipole approximation simulations of a pair of Au nanodiscs are shown for the light polarization direction parallel to the interparticle axis (Figure 5.2b) and that perpendicular to the axis (Figure 5.2d). In our calculations, each nanodisc was approximated by a cylinder of diameter 86.5 nm and height 25.5 nm, with the cylinder axis normal to the substrate. The dielectric constant of the surrounding medium $\varepsilon_m$ used was 1.0 for air, however, the most accurate treatment would require the consideration of the dielectric properties of the substrate, which consists of a quartz slide covered by a very thin chromium layer. The simulation assumes idealized isotropic

cylinders with homogeneous sizes and interparticle gaps, which deviates from the true experimental situation. Our calculations also do not include a parameter to account for experimental inhomogeneities. All these factors contribute to the deviations of the DDA results from the experimental spectra. Nevertheless, the features of the experimental data are clearly reproduced in our simulation. The plasmon band for the disc pair with the maximum separation, i.e., s = 208 nm (which is close to 2.5 particle diameters),[21,30] closely matches the isolated nanodisc plasmon maximum at ~561 nm. With decreasing interparticle gap, a strong red-shift is seen for parallel polarization, along with increase in the extinction efficiency similar to the experimental observation. When the gap reaches around 2 nm, a small shoulder emerges around 550 nm similar to the experimental case. For perpendicular polarization, only a weak blue-shift of the plasmon band with decreasing gap is seen along with a decrease in the extinction efficiency.

In the case of lithographic arrays, in addition to the near-field coupling between the particles in a pair, there also exists a far-field radiative coupling between particles at large feature separations (or grating constant) on the order of the wavelength of light. This has been studied in detail by Lamprecht et al. in 150 nm diameter gold nanodisc arrays, who showed that a change in the grating constant of the array has a significant effect on the single-particle plasmon resonance wavelength and the plasmon resonance line width.[46] In our experimental samples with small interparticle gaps (2-27 nm), the near-field coupling can be expected to be much stronger than any grating effects, while in the sample with interparticle gap of 212 nm, the grating constant is 300 nm (distance between rows), which may be lower than that required for significant far-field coupling.[23]

(a)                                    (b)
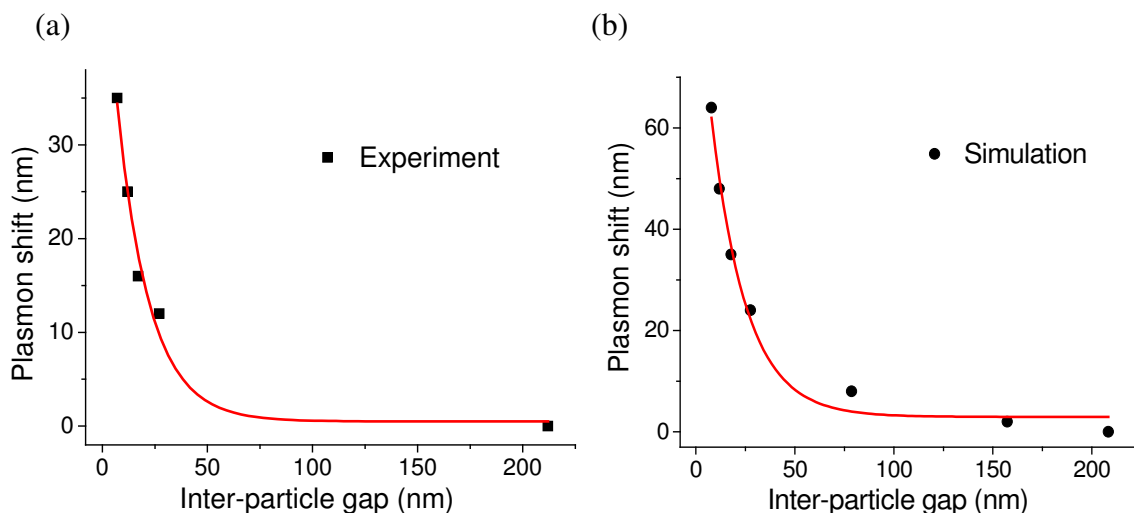
Figure 5.3: Shift in the plasmon wavelength maximum of a pair of Au nanodiscs as a function of the inter-particle edge-to-edge separation gap for (a) experiment and (b) DDA simulation. The red curves are least-squares fits to an exponential decay $y = y_0 + a.e^{-x/l}$, yielding a decay length l of $15.5 \pm 3.0$ nm ($R^2 = 0.985$) for experiment and $17.6 \pm 2.5$ nm ($R^2 = 0.989$) for simulations.

In any case, by means of the DDA simulation of single particle pairs, we can study the near-field plasmon coupling, which is the aim of the present study, without including the complicating effect of the far-field radiative coupling or grating effects. Figure 5.3b shows a plot of the DDA-simulated plasmon shift versus the interparticle separation gap for the parallel polarization. The shift can be fit very nearly to an exponential decay with a decay length of $17.6 \pm 2.5$ nm, close to the experimental value (Figure 5.3a). Note that this plot does not include the data points where the discs are nearly touching, which results in the emergence of higher-order resonances.

163

### 5.2.3 Scaling Behavior

Su et al. have shown that the plot of the experimentally observed plasmon shift versus interparticle separation gap follows the same trend for particles of different dimensions when the shift and separation are scaled respectively by the single-particle plasmon wavelength maximum $\lambda_0$ and the particle size.[21] Accordingly, using the DDA method, we calculated the plasmon shift as a function of the interparticle separation for discs of different diameters at a constant aspect ratio h/D $\approx$ 0.3 and medium dielectric constant $\varepsilon_m$ = 1.0. Figure 5.4a shows the plasmon shift versus the interparticle center-to-center distance for three different particle diameters, D = 54, 68, and 86 nm. With increasing particle size, the magnitude of the plasmon shift at a given interparticle distance increases (Figure 5.4a). In addition, the plasmon coupling exhibits a decay length, which increases with increasing nanodisc size (13.7, 15.5, and 17.5 nm, respectively). Figure 5.4b shows a plot of the fractional plasmon shift versus the ratio of the interparticle separation scaled by the nanodisc diameter for the three different particle sizes. It is seen that the decay trend becomes independent of the nanoparticle size on account of this scaling. On fitting with an exponential decay of the form $y = a.e^{-x/\tau}$ (where x = s/D), the decay constant $\tau$ for this universal trend is estimated to be 0.23 $\pm$ 0.03, close to the experimental value $\tau$ = 0.18 $\pm$ 0.02 (Figure 5.4c). In essence, the plasmon coupling decays over a length that is roughly 0.2 times the nanodisc diameter. It is interesting to find that the decay constant estimated here closely matches the one observed by Gunnarsson et al. ($\tau$ = 0.22) in a system of nanodisc pairs of a different plasmonic metal, i.e., Ag.[27] The Ag system, however, exhibits larger magnitude of the plasmon shift

(a)

(b)
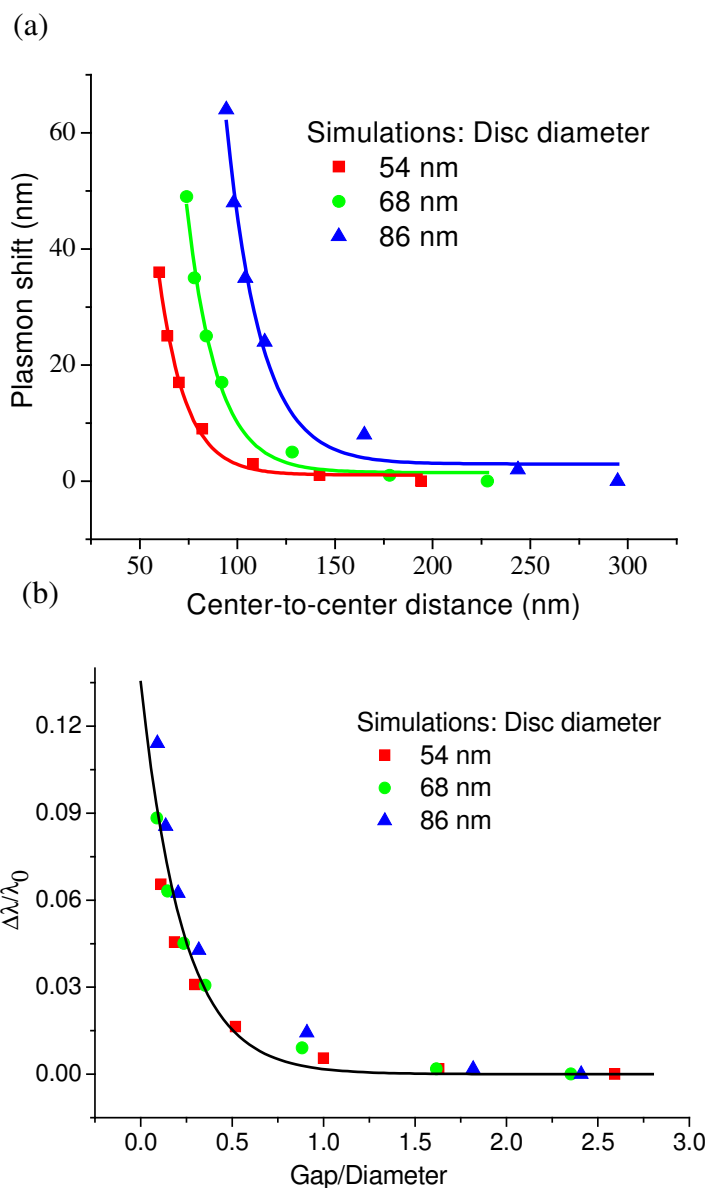
Figure 5.4: (a) Calculated plasmon shift versus the center-to-center distance in Au nanodisc pairs for different disc diameters. The solid curves represent least-squares fits to single exponential decay function $y = y_0 + a.e^{-x/l}$. The decay lengths $l$ obtained from the fit are 13.7, 15.5 and 17.7 nm for nanodisc diameter D = 54, 68 and 86 nm respectively. (b) Calculated fractional plasmon shift versus the ratio of inter-particle gap to nanodisc diameter, showing that the scaled data points for the different disc sizes follow a common trend, which can be fit together to the single exponential decay (solid curves) $y = a.e^{-x/\tau}$ with a= 0.14 $\pm$ 0.01 and $\tau = 0.23 \pm 0.03$. (c) Experimental fractional plasmon shift versus ratio of gap to diameter and exponential fit (solid curve) with a= 0.10 $\pm$ 0.01 and $\tau = 0.18 \pm 0.02$.

(c)
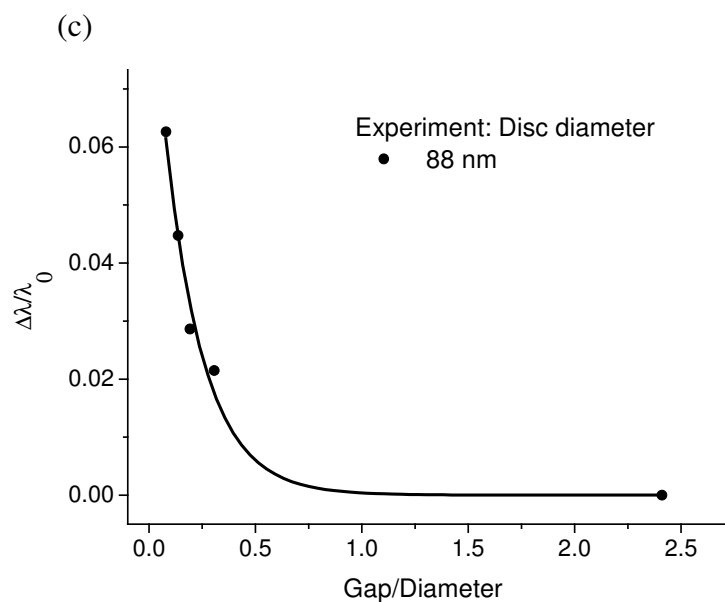


Figure 5.4 continued

(indicated by the parameter a of the fit), which can be attributed for by the well-known

fact that the electromagnetic fields are stronger in the Ag system. In Au, the proximity of

the plasmon resonance and the interband transition energies results in the damping of the

plasmon resonance by interband electron excitations and hence in a reduction of the

strength of the plasmonic field in comparison to the Ag system.[56] Regardless of this

difference, the distance decay of the plasmon field itself appears to be independent of the

nature of the metal.

We further investigate the simulated dependence of the distance decay of the

plasmon shift on the medium dielectric constant. Figure 5.5a shows the calculated

plasmon wavelength maximum versus the interparticle gap for three different values of
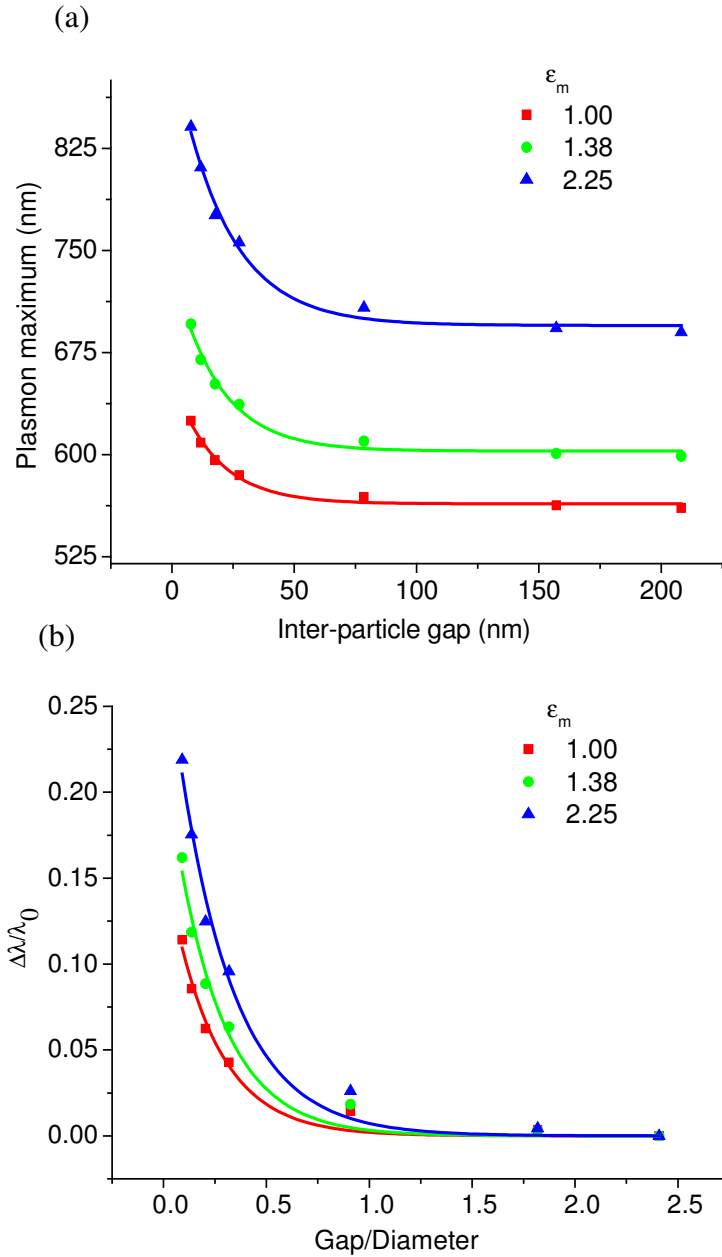
Figure. 5.5: (a) Plot of the calculated plasmon maximum of the Au nanodisc pair system as a function of the inter-particle distance for different values of the medium dielectric constant $\varepsilon_m$. The plot shows that the magnitude of the plasmon shift is higher for higher values of $\varepsilon_m$. (b) Plot of the calculated fractional shift versus the gap/diameter ratio for different $\varepsilon_m$. The data plots for different $\varepsilon_m$ are fit to single exponential decay $y = a.e^{-x/\tau}$ (solid curves) with similar decay constant $\tau = 0.23 \pm 0.04$, $0.24 \pm 0.03$ and $0.27 \pm 0.03$ but increasing amplitude $a = 0.16 \pm 0.02$, $0.23 \pm 0.02$ and $0.29 \pm 0.02$ for $\varepsilon_m = 1.00$, $1.38$ and $2.25$ respectively.

the medium dielectric constant $\varepsilon_m$ = 1.00, 1.38, and 2.25, for constant nanodisc dimensions (D = 86.5 nm and h = 25.5 nm). It is well-established that the single-particle LSPR red-shifts with increasing medium dielectric constant, which we observe. However, we also observe that the extent of the plasmon shift (and hence the strength of the plasmon coupling) increases with an increase in the medium dielectric constant. This is counterintuitive to the well-known screening of electrostatic interactions in a higher dielectric constant medium. The plot of the fractional shift versus the gap/diameter ratio (Figure 5.5b) shows a decay rate, which is similar for the different values of $\varepsilon_m$ while the amplitude increases with increasing dielectric constant ($\tau$ = 0.23, 0.24, and 0.27; a = 0.16, 0.23, and 0.29 for $\varepsilon_m$ = 1.00, 1.38, and 2.25, respectively).

The nanoparticle shape also does not seem to have much influence on the decay behavior. We performed DDA calculations of the plasmon extinction efficiency of a pair of diameter 10 nm Au nanospheres, each represented by a 30 x 30 x 30 cubic array of dipoles, corresponding to an interdipole spacing of 0.33 nm. The medium refractive index was 1.33 for water. The calculated spectra for the incident light polarization direction parallel to the interparticle axis (Figure 5.6a) show that the plasmon band red-shifts with decreasing interparticle separation gap, similar to the case of the nanodisc pairs. The magnitude of the plasmon shift is much smaller in this case, as likely due to the smaller volume of these spheres as compared to the nanodiscs. However, the fractional plasmon shift versus the gap/diameter ratio (Figure 5.6b) follows a trend with a decay constant ($\tau$ = 0.21 $\pm$ 0.02) similar to that in the nanodisc system. At extremely small gap (i.e., 0.67 nm), where the particles are almost touching each other, a new band (possibly due to the quadrupolar mode) can be seen to emerge at shorter wavelengths. This data point is not

included in the plot in Figure 5.6b. Experimentally, Reinhard et al.[43] have calibrated the

distance dependence of the plasmon shift in a pair of 42 nm Au nanospheres, and from
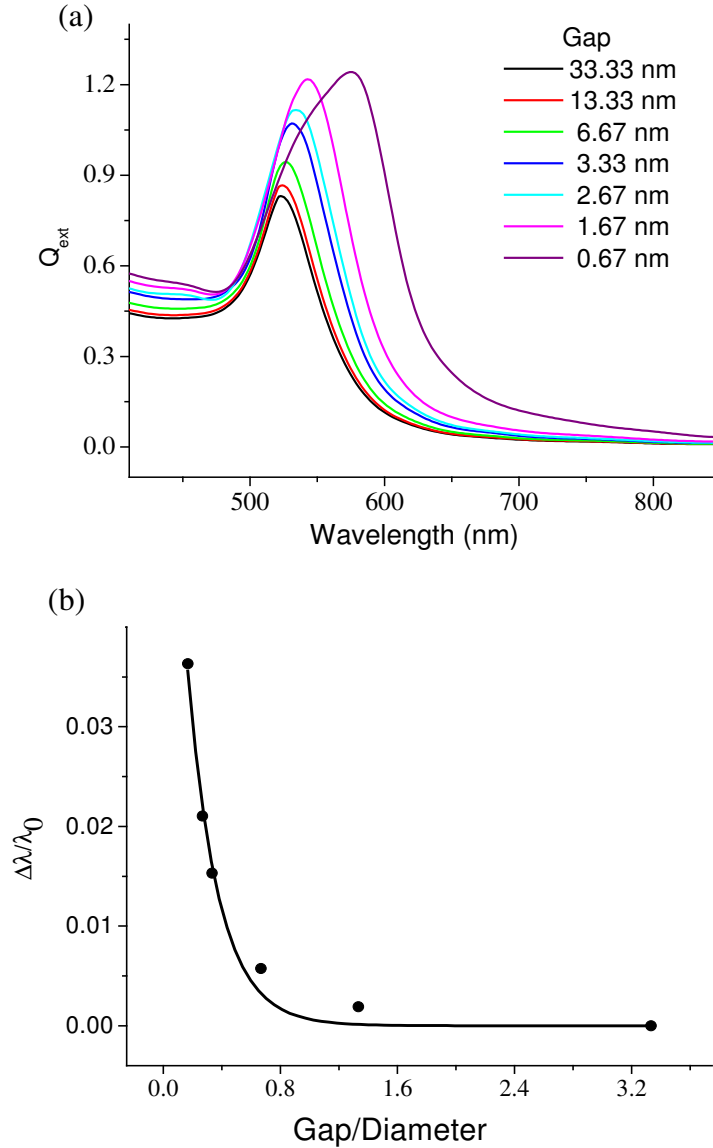


Figure 5.6: (a) DDA-simulated extinction efficiency spectra of 10 nm diameter Au nanosphere pair in water ($\varepsilon_m = 1.77$) for varying inter-particle separation gap, for incident light polarization direction parallel to the inter-particle axis. (b) Plot of fractional plasmon shift in Au nanosphere pair as a function of the gap/diameter ratio. The solid curve is a least-squares fit to an exponential decay function of the form $y = a.e^{-x/\tau}$ where $a = 0.08 \pm 0.01$ and $\tau = 0.21 \pm 0.02$.

the fit to their data, we estimate their decay constant to be about 0.24. Simulations by Wei et al.[57] based on the T-matrix method and by Reinhard et al.[43] based on DDA also agree with these results, excluding particles that are nearly touching each other. The universal scaling of the distance decay of plasmon coupling, demonstrated above, is also the likely reason for the good agreement of our experimental and calculated decay constants despite the difference between the experimental parameters and those idealized in the simulations.

### 5.2.4 Plasmon Ruler Equation

We can take advantage of the universal scaling behavior to derive an empirical equation, which can be used to estimate the interparticle separation from an experimentally observed plasmon shift. This can serve as a useful calibration guide for the plasmon ruler designed to measure distances in biological systems.[42-44] The refractive index for proteins is estimated to be about 1.6.[43] We derive the "plasmon ruler equation"[58] for a Au particle pair in such a protein medium to be:

$$\frac{\Delta\lambda}{\lambda_0} \approx 0.18 \exp\left(\frac{-(s/D)}{0.23}\right) \quad (1)$$

where $\Delta\lambda/\lambda_0$ is the fractional plasmon shift, s is the interparticle edge-to-edge separation, and D is the particle diameter. Reinhard et al.[43] recently obtained plasmon resonance spectra of pairs of 42 nm Au nanoparticles bound by ds-DNA spacers of known base pair lengths and therefore having defined interparticle separations (see Table 5.1). In their experiments, the dark-field microscopy technique was employed for obtaining plasmon spectra to ensure high spectral sensitivity and hence the observed $\Delta\lambda/\lambda_0$ is for the plasmon

Table 5.1: Experimental Interparticle Separation of Au Nanoparticle Pair Linked by DNA Spacers (Data from Reinhard et al.) as Compared to the Interparticle Separation Calculated from the Observed Percentage Plasmon Shift (from the Experiment of Reinhard et al.) Using Our Plasmon Ruler Equation (eq 1)

| DNA spacer length (base pairs) | Observed $\Delta\lambda/\lambda_0$ (%) | Experimental Separation (nm) | Calculated separation from equation (nm) |
|---|---|---|---|
| 250 | 0.0015 | 93 | 91 |
| 110 | 0.16 | 45 | 46 |
| 67 | 0.66 | 31 | 32 |
| 40 | 1.62 | 22 | 23 |
| 20 | 3.14 | 15 | 17 |
| 10 | 4.38 | 11 | 14 |

resonance scattering band. As shown in Table 5.1, we used the plasmon ruler equation (eq 1) to calculate the interparticle separation s of a nanoparticle pair from the corresponding $\Delta\lambda/\lambda_0$ observed by Reinhard et al, which we obtained from the published fit to their data.[43]

Note that we have excluded from this analysis the data of Reinhard et al. for "pairs with zero separation". The experimental values of the pair separation in the third column were obtained as per the procedure of Reinhard et al., i.e., assuming a contour length of 0.34 nm per base pair and an additional distance of 8 nm to account for the thickness of the protein layer on the nanoparticles.[43] Indeed, we get good agreement between our calculated values and the experimental interparticle separation, with reasonable deviations only at the smallest separations. It should also be noted that our calculated expression is for the light polarization direction along the interparticle axis,

unlike the experiments in solution. But Reinhard et al. have already pointed out that experimental polarization effects have low significance for smaller nanoparticles (up to 40 nm size range); they become important for larger (87 nm) nanoparticles.[43]

### 5.2.5 Dipolar-Coupling Model

A simple model based on dipole-dipole interactions can provide us an intuitive picture of the distance decay of plasmon coupling in metal nanostructures. The dipolar coupling model, described by Kreibig and Vollmer,[1] has been found in the past to explain interparticle plasmon coupling effects with good qualitative agreement.[23,59] The electric dipole moment μ of the single particle in an electric field E is given as

$$\mu = \alpha \varepsilon_m E \qquad (2)$$

where α is the Clausius-Mossotti dipole polarizability for an isolated metal nanoparticle in the quasistatic approximation, which is proportional to the particle volume V as:

$$\alpha = \varepsilon_0 V (1 + \kappa) \left( \frac{\varepsilon - \varepsilon_m}{\varepsilon + \kappa \varepsilon_m} \right) \qquad (3)$$

where $\varepsilon = \varepsilon_r + i\varepsilon_i$ is the wavelength dependent dielectric function of bulk gold, $\varepsilon_m$ is the medium dielectric constant, $\varepsilon_0$ is the vacuum permittivity and κ is a factor which depends on the nanoparticle shape, e.g. κ = 2 for spheres. In the presence of a neighboring particle, the electric field felt by each particle is the sum of the incident light field E and the near-field of the electric dipole on the neighboring particle, which decays as the cube of the distance d from the particle:

$$E' = E + \frac{\xi \mu'}{4\pi \varepsilon_m \varepsilon_0 d^3} \qquad (4)$$

172

$\xi$ is an orientation factor, which depends on the alignment of the two single-particle dipoles. $\xi = 2$ for dipoles arranged head-to-tail corresponding to parallel polarization in our experiments, while $\xi = -1$ for dipoles aligned side-by-side corresponding to perpendicular polarization. The SPR shift in opposite directions for these two polarizations originates from the opposite sign of $\xi$ for the two cases. Also since $|\xi|_{parallel} > |\xi|_{perp}$ the shift magnitude is larger for the parallel polarization case (Figure 5.7). From eq 2 and eq 4, the net polarizability $\alpha'$ of the two-particle system is given as

$$\alpha' = \frac{\alpha}{\left(1 - \frac{\xi\alpha}{4\pi\varepsilon_0 d^3}\right)} \qquad (5)$$

Further we use eq 3 and $V = \pi D^3/6\Lambda$, where D is the particle dimension along the axis of inter-particle interaction and $\Lambda$ depends on the other particle dimensions, e.g. $\Lambda = 1$ for spheres and $\Lambda = (1/\text{Aspect ratio})$ for oblate spheroids interacting along the long-axis.

$$\alpha' = \frac{4\pi\varepsilon_0 D^3(\varepsilon - \varepsilon_m)(1+\kappa)}{\varepsilon\left(24\Lambda - \frac{\xi(1+\kappa)D^3}{d^3}\right) + \varepsilon_m\left(24\Lambda\kappa + \frac{\xi(1+\kappa)D^3}{d^3}\right)} \qquad (6)$$

The SPR condition is thus specified by the maximum of the polarizability as:

$$\varepsilon_r\big|_{SP\max} = -\varepsilon_m\left(\frac{\kappa(s/D+1)^3 + \xi(1+\kappa)/24\Lambda}{(s/D+1)^3 - \xi(1+\kappa)/24\Lambda}\right) \qquad (7)$$

since $s = d+D$. We can now utilize the near-linear dependence of $\varepsilon_r$ on wavelength in the visible (500-700 nm) region for Au, $\lambda = 464.6 - 14.3\varepsilon_r$, and get:

$$\lambda\big|_{SP\max} = 464.6 + 14.3\varepsilon_m\left(\frac{\kappa(s/D+1)^3 + \xi(1+\kappa)/24\Lambda}{(s/D+1)^3 - \xi(1+\kappa)/24\Lambda}\right) \qquad (8)$$

Denoting the single-particle resonance wavelength maximum as $\lambda_0$ (for $s/D \to \infty$) we get for the parallel polarization, i.e. $\xi = 2$:

$$\Delta\lambda / \lambda_0 = \frac{14.3\varepsilon_m(1+\kappa)^2}{\left(12\Lambda(s/D+1)^3 - (1+\kappa)\right)\left(464.6 + 14.3\varepsilon_m\kappa\right)} \quad (9)$$

From eq 9, we see that $\Delta\lambda/\lambda_0$ is a rational function of s/D, which can be approximated very nearly to an exponential decay (Figure 5.7). This function has a somewhat smoother curvature than the exponential function – a behavior, which is also reflected in the exponential fits to our experimental and DDA simulation plots. While the function predicted by the dipolar model explains the near-exponential decay, the estimated $\tau$ value of 0.40 is much higher than that observed in the experiments and DDA simulations, suggesting that the dipolar model underestimates the coupling strength at smaller inter-particle gaps. Nevertheless, the dipolar model can be used for qualitative elucidation of the decay of the plasmon coupling. The part of the rational function in eq 9:

$f(s/D) = \dfrac{1}{\left(12\Lambda(s/D+1)^3 - (1+\kappa)\right)}$, which governs the decay rate of $\Delta\lambda/\lambda_0$ with respect

to s/D, has no functional dependence on the medium dielectric constant or the metal type. The effect of shape on the decay rate is also weak as shown in Figure 5.8. The other parameters in the function only influence the amplitude of the decay and this includes the effect of the medium dielectric constant ($\varepsilon_m$), the metal type (through the relationship between $\lambda$ and $\varepsilon_r$) and the nanoparticle shape (through $\Lambda$ and $\kappa$). As an example, the dependence of the amplitude on $\varepsilon_m$ is shown in Figure 5.9.
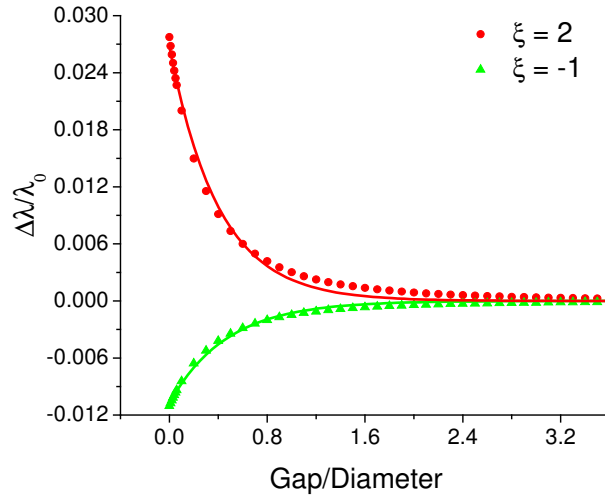
Figure 5.7: Plot of the fractional shift as a function of gap/diameter calculated using the dipolar-coupling model (eq 9) for our Au nanodisc pair system, modeled by a pair of oblate spheroids of aspect ratio 0.28, interacting along their long axis for parallel polarization, i.e. $\xi = 2$, and perpendicular polarization, i.e. $\xi = -1$, in a medium of dielectric constant = 1.0. Solid curves are fits to the single exponential decay $y = a.e^{-x/\tau}$ where $\tau = 0.40 \pm 0.01$, $a = 0.03$ for parallel polarization whereas $\tau = 0.47 \pm 0.01$, $a = -0.01$ for perpendicular polarization.
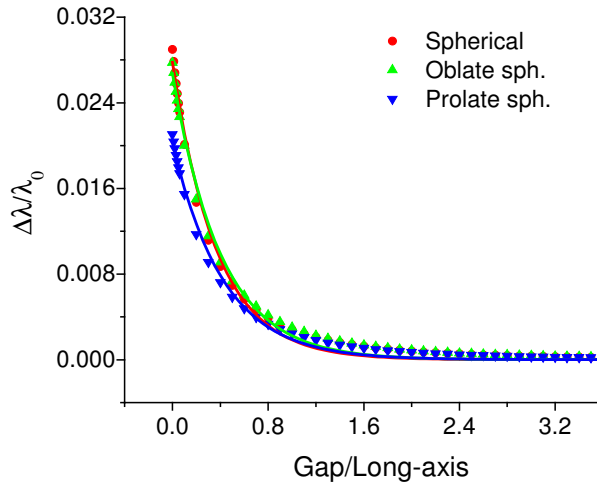


Figure 5.8. Plot of the fractional shift versus the ratio of gap to long-axis dimension for Au nanoparticle pairs for different shapes: spherical, oblate spheroids of aspect ratio 0.28 and prolate spheroids of aspect ratio 3.0, calculated using the dipolar-coupling model (eq 9) for parallel polarization and medium dielectric constant = 1.0. The interaction of the spheroids was considered along their long axis. The solid curves represent least-square fits to the exponential decay $y = a.e^{-x/\tau}$ where $\tau = 0.37 \pm 0.01$, $0.40 + 0.01$ and $0.42 + 0.01$ and amplitude $a = 0.028$, $0.027$ and $0.020$ for spherical, oblate and prolate shapes respectively.

175
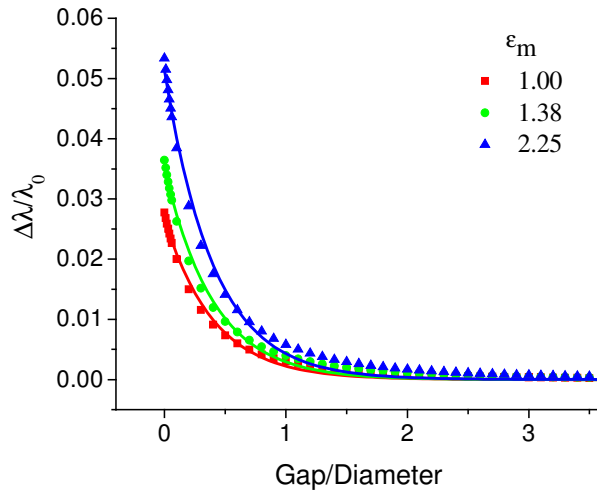
Figure 5.9. Plot of the fractional shift versus gap/diameter for Au nanodisc pair under parallel polarization for different medium dielectric constants, calculated using the dipolar-coupling model (eq 9). The solid curves are least-squares fits to the single exponential decay $y = a.e^{-x/\tau}$ showing similar decay constant $\tau = 0.40$ for the different medium dielectric constants but increasing amplitude a = 0.027, 0.035 and 0.051 for $\varepsilon_m$ = 1.00, 1.38 and 2.25 respectively.

In summary as per the dipolar coupling model, the interesting size-scaling relationship can be understood as follows. The fractional plasmon shift $(\Delta\lambda/\lambda_0)$ can be thought to reflect the strength of the interparticle electromagnetic coupling relative to the intraparticle plasmonic restoring potential.[24] While the interparticle dipolar coupling potential is known to decay with center-to-center distance as $d^{-3}$,[30] the intraparticle restoring potential (reflected by the inverse of the dipole polarizability) is inversely proportional to the volume or $D^3$. As a result, $\Delta\lambda/\lambda_0$ becomes a function of $(d/D)^{-3}$ or $(s/D+1)^{-3}$. Thus the dependence of the plasmon coupling strength on similar powers of separation s and diameter D allows the dimensional scaling of the function and hence the universality over particle pairs of varied dimensions. This functional dependence of fractional shift on $(s/D+1)^{-3}$ as shown above involves no contribution from the

surrounding medium dielectric constant and the metal type. Moreover, the effect of shape is weak (Figure 5.8). Thus, the scaling behavior (indicated by the decay constant $\tau$) is similar for different nanoparticle size, shape, metal type, or medium dielectric constant; these parameters only govern the magnitude of the fractional shift in the system (indicated by the amplitude a). For instance, the simple dipolar picture predicts that when the medium dielectric constant is changed from 1.00 to 2.25, the value of the amplitude nearly doubles without any significant effect on the decay constant (Figure 5.9). This is similar to the observation from the DDA simulations (Figure 5.5b). The predicted effect of the medium dielectric constant on the plasmon shift deserves further experimental investigation. This can potentially be useful for the estimation of the local medium dielectric constant by plasmon resonance spectroscopy.

The quasistatic dipolar-coupling model, however, is qualitative because it does not take into account electromagnetic retardation effects as well as higher-order/multipolar interactions unlike the DDA method, where each particle is simulated by several thousand dipoles and retardation correction is included. As finite particle size and multipolar effects become increasingly important, deviations from the predictions of the dipolar model can be seen. Our observation is that the dipolar model underestimates the plasmon coupling strength at small interparticle gaps, in line with earlier analyses.[27,60] The dipolar model is clearly not valid for interactions between particles, which are nearly touching each other.[27] In such a case, a complete treatment[60,61] involving all modes of interaction (dipolar, quadrupolar, ...) needs to be employed. We conjecture that the scaling may still be valid (only with a decay rate faster than that predicted by the purely dipolar model) when higher-order terms (e.g., quadrupoles) enter into the interaction at

small interparticle separation. For instance, the quadrupolar interaction energy is proportional to the fifth power of the inverse distance, while the quadrupole polarizability is proportional to the fifth power of the particle dimensions.

## 5.4 Conclusion

In summary, our investigation of the plasmon resonances in Au nanodisc pairs shows that interparticle plasmon coupling strength for polarization along interparticle axis decays nearly exponentially with a decay length, which is roughly about 0.2 in units of the particle size for different nanoparticle size, shape, metal type, and medium dielectric constant. A dipolar-coupling model qualitatively explains that this behavior results from the interplay of two factors: the dependence of the single-particle polarizability on the cubic power of the particle dimension and the decay of the particle plasmon near-field as the cubic power of the inverse distance. The universal plasmon scaling behavior deduced in our work can be a useful guide for the design of nanostructured devices, which are based on interparticle plasmon coupling, especially the plasmon ruler.[43] As compared to FRET, which has a range of less than 10 nm due to a steep $1/R^6$ dependence of the interaction between molecular species,[45] plasmon coupling provides a much longer distance range, due to its softer distance-dependence ($1/R^3$ within dipole approximation) and also since the interaction range can be increased directly by increasing the nanoparticle dimension D, as per the size scaling model. The quantification of the plasmon coupling decay behavior also allows us to derive a "plasmon ruler equation" that gives an estimate of the interparticle separation between spherical Au

nanoparticles in a biological system from the fractional plasmon shift observed spectroscopically.

## 5.5 References and Notes

(1)     Kreibig, U.; Vollmer, M. *Optical Properties of Metal Clusters*; Springer: Berlin, 1995; Vol. 25.

(2)     Kelly, K. L.; Coronado, E.; Zhao, L. L.; Schatz, G. C. *J. Phys. Chem. B* **2003**, *107*, 668.

(3)     El-Sayed, M. A. *Acc. Chem. Res.* **2001**, *34*, 257.

(4)     Link, S.; El-Sayed, M. A. *J. Phys. Chem. B* **1999**, *103*, 8410.

(5)     Bohren, C. F.; Huffman, D. R. *Absorption and Scattering of Light by Small Particles*; Wiley: New York, 1983.

(6)     Hutter, E.; Fendler, J. H. *Adv. Mater.* **2004**, *16*, 1685.

(7)     Chen, C. K.; Heinz, T. F.; Ricard, D.; Shen, Y. R. *Phys. Rev. B* **1983**, *27*, 1965.

(8)     Schatz, G. C. *Acc. Chem. Res.* **1984**, *17*, 370.

(9)     Jain, P. K.; Lee, K. S.; El-Sayed; I. H.; El-Sayed, M. A. *J. Phys. Chem. B* **2006**, *110*, 7238.

(10)    Sönnichsen, C.; Franzl, T.; Wilk, T.; von Plessen, G.; Feldmann, J.; Wilson, O.; Mulvaney, P. *Phys. Rev. Lett.* **2002**, *88*, 077402.

(11)    Sokolov, K.; Follen, M.; Aaron, J.; Pavlova, I.; Malpica, A.; Lotan, R.; Richards-Kortum, R. *Cancer Res.* **2003**, *63*, 1999.

(12)    El-Sayed, I. H.; Huang, X.; El-Sayed, M. A. *Nano Lett.* **2005**, *5*, 829.

(13)     Rosi, N. L.; Mirkin, C. A. *Chem. Rev.* **2005**, *105*, 1547.

(14)     Alivisatos, A. P. *Nature Biotechnol.* **2004**, *22*, 47.

(15)     Haes, A. J.; Hall, W. P.; Chang, L.; Klein, W. L.; Van Duyne, R. P. *Nano Lett.* **2004**, *4*, 1029.

(16)     Huang, X.; El-Sayed, I. H.; Qian, W.; El-Sayed, M. A. *J. Am. Chem. Soc.* **2006**, *128*, 2115.

(17)     Hirsch, L. R.; Stafford, R. J.; Bankson, J. A.; Sershen, S. R.; Rivera, B.; Price, R. E.; Hazle, J. D.; Halas, N. J.; West, J. L. *Proc. Natl. Acad. Sci. U.S.A.* **2003**, *100*, 13549.

(18)     Huang, X.; Jain, P. K.; El-Sayed, I. H.; El-Sayed, M. A. *Photochem. Photobiol.* **2006**, *82*, 412.

(19)     Jain, P. K.; El-Sayed, I. H.; El-Sayed, M. A. *Nano Today* **2007**, *2*, 18.

(20)     Pileni, M. P. *J. Phys. Chem. B* **2001**, *105*, 3358.

(21)     Su, K. H.; Wei, Q.-H.; Zhang, X.; Mock, J. J.; Smith, D. R.; Schultz, S. *Nano Lett.* **2003**, *3*, 1087.

(22)     Jain, P. K.; Qian, W.; El-Sayed, M. A. *J. Phys. Chem. B* **2006**, *110*, 136.

(23)     Rechberger, W.; Hohenau, A.; Leitner, A.; Krenn, J. R.; Lamprecht, B.; Aussenegg, F. R. *Opt. Commun.* **2003**, *220*, 137.

(24)     Aizpurua, J.; Bryant, G. W.; Richter, L. J.; García de Abajo, F. J.; Kelley, B. K.; Mallouk, T. *Phys. Rev. B* **2005**, *71*, 235420/1.

(25)     Seker, F.; Malenfant, P. R. L.; Larsen, M.; Alizadeh, A.; Conway, K.; Kulkarni, A. M.; Goddard, G.; Garaas, R. *Adv. Mater.* **2005**, *17*, 941.

(26)     Lin, S.; Li, M.; Dujardin, E.; Girard, C.; Mann, S. *Adv. Mater.* **2005**, *17*, 2553.

(27)    Gunnarsson, L.; Rindzevicius, T.; Prikulis, J.; Kasemo, B.; Käll, M.; Zou, S.; Schatz, G. C. *J. Phys. Chem. B* **2005**, *109*, 1079.

(28)    Sweatlock, L. A.; Maier, S. A.; Atwater, H. A.; Penninkhof, J. J.; Polman, A. *Phys. Rev. B* **2005**, *71*, 235408/1.

(29)    Xiao, J. J.; Huang, J. P.; Yu, K. W. *Phys. Rev. B* **2005**, *71*, 045404/1.

(30)    Maier, S. A.; Brongersma, M. L.; Kik, P. G.; Atwater, H. A. *Phys. Rev. B* **2002**, *65*, 193408/1.

(31)    Kottmann, J. P.; Martin, O. J. F. *Opt. Express* **2001**, *8*, 655.

(32)    Nie, S.; Emory, S. R. **1997**, *275*, 1102.

(33)    Michaels, A. M.; Jiang, J.; Brus, L. *J. Phys. Chem. B* **2000**, *104*, 11965.

(34)    Brongersma, M. L.; Hartman, J. W.; Atwater, H. A. *Phys. Rev. B* **2000**, *62*, R16356.

(35)    Maier, S. A.; Brongersma, M. L.; Kik, P. G.; Meltzer, S.; Requicha, A. A. G.; Atwater, H. A. *Adv. Mater.* **2001**, *13*, 1501.

(36)    Maier, S. A.; Kik, P. G.; Atwater, H. A.; Meltzer, S.; Harel, E.; Koel, B. E.; Requicha, A. A. G. *Nat. Mater.* **2003**, *2*, 229.

(37)    Krenn, J. R.; Salerno, M.; Felidj, N.; Lamprecht, B.; Schider, G.; Leitner, A.; Aussenegg, F. R.; Weeber, J. C.; Dereux, A.; Goudonnet, J. P. *J. Microsc.* **2001**, *202*, 122.

(38)    Storhoff, J. J.; Elghanian, R.; Mucic, R. C.; Mirkin, C. A.; Letsinger, R. L. *J. Am. Chem. Soc.* **1998**, *120*, 1959.

(39)    Storhoff, J. J.; Lazarides, A. A.; Mucic, R. C.; Mirkin, C. A.; Letsinger, R. L.; Schatz, G. C. *J. Am. Chem. Soc.* **2000**, *122*, 4640.

(40)     Alivisatos, A. P.; Johnsson, K. P.; Peng, X.; Wilson, T. E.; Loweth, C. J.; Bruchez, M. P., Jr.; Schultz, P. G. *Nature* **1996**, *382*, 609.

(41)     Storhoff, J. J.; Mirkin, C. A. *Chem. Rev.* **1999**, *99*, 1849.

(42)     Sönnichsen, C.; Reinhard, B. M.; Liphardt, J.; Alivisatos, A. P. *Nat. Biotechnol.* **2005**, *23*, 741.

(43)     Reinhard, B. M.; Siu, M.; Agarwal, H.; Alivisatos, A. P.; Liphardt, J. *Nano Lett.* **2005**, *5*, 2246.

(44)     Reinhard, B.; Sheikholeslami, S.; Mastroianni, A.; Alivisatos, A. P.; Liphardt, J. *Proc. Natl. Acad. Sci. U.S.A.* **2007**, *104*, 2667.

(45)     Deniz, A. A.; Dahan, M.; Grunwell, J. R.; Ha, T.; Faulhaber, A. E.; Chemla, D. S.; Weiss, S.; Schultz, P. G. *Proc. Natl. Acad. Sci. U.S.A.* **2007**, *96*, 3670.

(46)     Lamprecht, B.; Schider, G.; Lechner, R. T.; Ditlbacher, H.; Krenn, J. R.; Leitner, A.; Aussenegg, F. R. *Phys. Rev. Lett.* **2000**, *84*, 4721.

(47)     Salerno, M.; Félidj, N.; Krenn, J. R.; Leitner, A.; Aussenegg, F. R.; Weeber, J. C. *Phys. Rev. B* **2001**, *63*, 165422/1.

(48)     Krenn, J. R.; Dereux, A.; Weeber, J. C.; Bourillot, E.; Lacroute, Y.; Goudonnet, J. P.; Schider, G.; Gotschy, W.; Leitner, A.; Aussenegg, F. R.; Girard, C. *Phys. Rev. Lett.* **1999**, *82*, 2590.

(49)     Tamaru, H.; Kuwata, H.; Miyazaki, H. T.; Miyano, K. *Appl. Phys. Lett.* **2002**, *80*, 1826.

(50)     Jain, P. K.; Eustis, S.; El-Sayed, M. A. *J. Phys. Chem. B* **2006**, *110*, 18243.

(51)     Krenn, J. R.; Schider, G.; Rechberger, W.; Lamprecht, B.; Leitner, A.; Aussenegg, F. R.; Weeber, J. C. *Appl. Phys. Lett.* **2000**, *77*, 3379.

(52)     Draine, B. T.; Flatau, P. J. *J. Opt. Soc. Am. A* **1994**, *11*, 1491.

(53)     Schatz, G. C. *Theochem* **2001**, *573*, 73.

(54)     Brioude, A.; Jiang, X. C.; Pileni, M. P. *J. Phys. Chem. B* **2005**, *109*, 13138.

(55)     Kelly, K. L.; Lazarides, A. A.; Schatz, G. C. *Comput. Scie. Eng.* **2001**, *3*, 67.

(56)     Pustovit, V. N.; Shahbazyan, T. V. *J. Opt. Soc. Am. A* **2006**, *23*, 1369.

(57)     Wei, Q.-H.; Su, K.-H.; Durant, S.; Zhang, X. *Nano. Lett.* **2004**, *4*, 1067.

(58)     This equation was estimated by the DDA simulation method with discrete dipole spacing of 1 nm and a nanosphere diameter of 40 nm. Similar to other analyses in this work, data points where the two particles nearly touch each other (indicated by emergence of an additional extinction band at shorter wavelengths) were excluded.

(59)     Gluodenis, M.; Foss, C. A., Jr. *J. Phys. Chem. B* **2002**, *106*, 9484.

(60)     Nordlander, P.; Oubre, C.; Prodan, E.; Li, K.; Stockman, M. I. *Nano Lett.* **2004**, *4*, 899.

(61)     Ruppin, R. *Phys. Rev. B* **1982**, *26*, 3440.

# CHAPTER 6

# UNIVERSAL SCALING OF PLASMON COUPLING IN METAL NANOSTRUCTURES: EXTENSION FROM PARTICLE PAIRS TO NANOSHELLS

**Abstract**

It has been recently shown that the strength of plasmon coupling between a pair of plasmonic metal nanoparticles falls as a function of the interparticle gap scaled by the particle size with a near-exponential decay trend that is universally independent of nanoparticle size, shape, metal type, or medium dielectric constant. In this letter, we extend this universal scaling behavior to the dielectric core-metal shell nanostructure. By using extended Mie theory simulations of silica core-metal nanoshells, we show that when the shift of the nanoshell plasmon resonance wavelength scaled by the solid nanosphere resonance wavelength is plotted against the shell thickness scaled by the core radius, nanoshells with different dimensions (radii) exhibit the same near-exponential decay. Thus, the nanoshell system becomes physically analogous to the particle-pair system, i.e., the nanoshell plasmon resonance results from the coupling of the inner shell surface (cavity) and the outer shell surface (sphere) plasmons over a separation distance essentially given by the metal shell thickness, which is consistent with the plasmon hybridization model of Prodan, Halas, and Nordlander. By using the universal scaling

behavior in the nanoshell system, we propose a simple expression for predicting the dipolar plasmon resonance of a silica-gold nanoshell of given dimensions.

## 6.1 Introduction

Plasmonic nanostructures have attracted great interest in recent years due to their potential applications in molecular-specific imaging and spectroscopy,[1-3] chemical and biological sensing,[4-7] biomedicine,[8-11] and nano-optical devices.[12] At the same time, a lot of fundamental interest has been focused on the interesting size, shape, composition, and medium dependence of the plasmon resonance in noble metal nanostructures.[13-17] A classic example of this unique optical tunability is the dielectric core-metal shell nanostructure, especially the gold nanoshell studied in detail by the Halas and Nordlander groups,[18-20] which consists of a silica core covered with a few nanometer thin gold layer. Other similar nanostructures include the gold sulfide core-gold shell,[21-23] hollow metal shell,[24] and polystyrene core-metal shell nanostructures.[25,26] The plasmon resonance of the metal shell nanostructure has been found to be strongly dependent on the relative dimensions of the metal shell and the dielectric core.[18] By decreasing the thickness of the gold shell, the plasmon band of the nanoshell red-shifts from the visible region resonance (~520 nm) of the solid gold nanosphere toward the near-infrared region. Tunability of the plasmon resonance in the near-infrared region makes the nanoshell structure very useful for in vivo biomedical imaging and therapy applications[8,9,27,28] because biological tissue shows maximum optical transmissivity in the 650-900 nm region. Nanoshells also show promise for applications in nanooptical devices,[29] sensing,[30,31] and surface-enhanced spectroscopy[32,33] due to their strong and tunable plasmon resonance. A nanostructure that

shows optical tunability similar to metal nanoshell is the hitherto unrelated metal nanoparticlepair system.[34-40] The plasmon resonance of the gold nanoparticle pair can be red-shifted from the visible region resonance (ca. 520 nm) for an isolated gold nanosphere toward the near-infrared region by reducing the interparticle gap between the interacting particles for incident light polarized along the interparticle axis.[37,39] The magnitude of this red-shift increases almost exponentially with decreasing interparticle gap.[34,35,39] The plasmon shift scaled by the isolated-particle plasmon resonance plotted against the interparticle gap scaled by the particle dimension shows a near-exponential decay trend that is universally independent of nanoparticle size, shape, metal type, or surrounding dielectric medium.[39]

In this chapter, we present an interesting extension of this universal scaling behavior to the metal nanoshell structure. Extended Mie theory calculations show that as we move from a solid gold nanosphere to a nanoshell with decreasing shell thickness, there is an almost exponential red-shift in the plasmon resonance wavelength maximum. At the same time, the resonance wavelength shift is also dependent on the nanoshell size, i.e., the rise in the plasmon resonance red-shift with decreasing shell thickness is less steep for nanoshells with a larger size. However, when the shift of the nanoshell plasmon resonance wavelength scaled by the solid nanosphere resonance wavelength is plotted against the shell thickness scaled by the core radius, nanoshells with different dimensions show the same near-exponential decay trend. On the basis of this scaling behavior, we demonstrate the nanoshell system to be physically analogous to the particle-pair system. Our observation corroborates the "plasmon hybridization" model developed by Prodan et al.[19] for explanation of the plasmon resonances in the nanoshell structure. In addition, our

approach provides a simple expression to predict the dipolar plasmon resonance of a nanoshell with given core and shell dimensions.

## 6.2 Calculation Method

The extinction efficiency ($Q_{ext}$) spectrum of a metal shell of thickness t surrounding a dielectric core of radius R was calculated in the visible-near-infrared region by using an extended Mie theory simulation scheme developed by Charamisinau et al.[41] We used a refractive index of 1.45 for the core material corresponding to silica. For the gold shell, we used the wavelength-dependent complex refractive index of bulk gold.[42] The surrounding medium was assumed to have a refractive index of 1.33 for liquid water.

In the case where the shell thickness is reasonably smaller than the electronic mean free path of gold, the dielectric function needs to be corrected for increased electron scattering at the shell boundaries.[21] The exact form of the correction is debated; however, it is known that the interface electron scattering results in increased damping of the resonance (i.e., lower extinction and increased linewidths); however, there is little effect on the plasmon resonance maximum position.[43] Because we are interested in the plasmon resonance positions, we have not included the correction. Nehl et al. have already demonstrated the ability of Mie theory, without inclusion of surface-scattering corrections, to simulate nanoshell plasmon resonances in good agreement with those determined from single-particle and solution-phase experiments.[44] We have ensured that the extended Mie theory calculation algorithm used in this work for core-shell particles shows excellent agreement with the results of Mie theory for homogeneous spheres for

the three limiting cases: vanishing shell, vanishing core, and vanishing refractive index difference between core and shell materials.

## 6.3 Results and Discussion

### 6.3.1 Nanoshell Resonances and Universal Size Scaling

Figure 6.1 shows the calculated extinction efficiency spectra for 80 nm diameter silica-gold nanoshells with varying gold shell thickness. The calculated spectrum for the 80 nm diameter solid nanosphere has a wavelength maximum $\lambda_0$ at 549 nm corresponding to its dipolar plasmon resonance. As the shell thickness t decreases from 40 nm (solid sphere) to 4 nm, the dipolar plasmon resonance progressively red-shifts. In addition, with decreasing shell thickness, the plasmon band extinction increases. At the smallest shell thickness, t = 4 nm, a small shoulder is observed around 690 nm, which
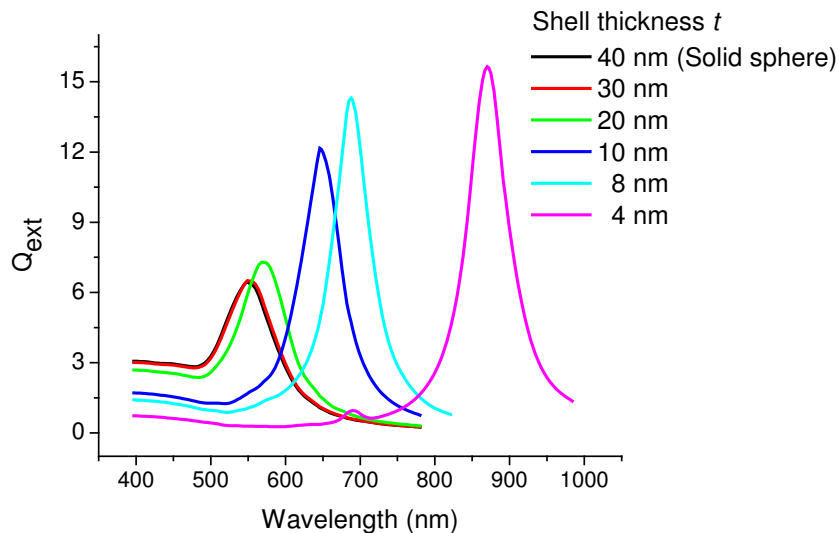


Figure 6.1: Extended-Mie-theory calculations of the extinction efficiency spectra of 80-nm diameter silica core-gold nanoshell in water for different shell thickness: t = 40 nm (solid sphere), 30 nm, 20 nm, 10 nm, 8 nm, and 4 nm.

corresponds to the quadrupolar/higher-order resonance mode.[20]

These observed trends are very similar to those observed in a system of two interacting particles excited by light polarized along their interparticle axis.[38,39] In the two-particle system, as the interparticle gap decreases, there is a red-shift in the dipolar plasmon resonance along with an increase in the plasmon band extinction, and an emergence of the quadrupolar or higher-order modes at very small gap.[39] In fact, similar to the nanoparticle-pair system, there is a near-exponential red-shift in the dipolar plasmon resonance wavelength maximum with decreasing shell thickness (Figure 6.2). Figure 6.2 gives a comparison of this trend for four different nanoshell sizes, where it is evident that the rise in the plasmon red-shift with decreasing shell thickness is less steep for nanoshells with a larger size.

It must be noted that Oldenburg et al. have already elucidated by experiment and simulation the dependence of the silica core-gold nanoshell plasmon resonance on the shell thickness.[18] They have also acknowledged the role of the total nanoshell size in determining the plasmon resonance. However, for the first time, we demonstrate a unique size scaling that exists in the nanoshell system analogous to that demonstrated in the particle-pair system. In Figure 6.3, we have plotted the fractional shift ($\Delta\lambda/\lambda_0$) of the nanoshell plasmon resonance wavelength with respect to the solid nanosphere resonance wavelength versus the shell thickness scaled by the core radius (t/R).[45] By applying this scaling, the trend becomes independent of the nanoshell dimensions. The exponential decay constant of this universal trend is $0.18 \pm 0.02$. The decay constant does not seem to be affected much by a change in the material of the core or shell or the surrounding medium. For instance, the decay constants for 60 nm diameter hollow core-gold nanoshell in water, 60 nm diameter silica core-silver nanoshell in water, and 60 nm diameter silica-gold nanoshell in air are close (Figures 6.4, 6.5 and 6.6). The amplitude of
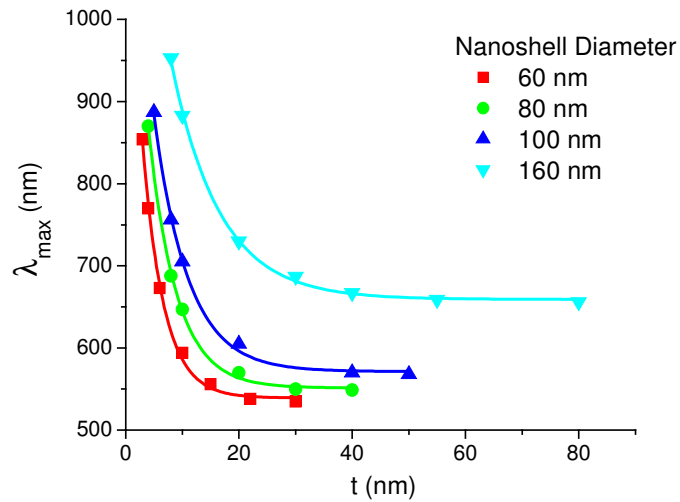
Figure 6.2: Calculated dipolar plasmon resonance wavelength maximum ($\lambda_{max}$) of silica core-gold nanoshell in water as a function of shell thickness (t) for four different nanoshell diameters. The solid lines represent least-squares fits of the data to the single exponential decay $y = y_0 + a.\exp(-x/l)$, yielding $l = 3.71, 4.91, 5.93$ and $8.55$ nm for nanoshell diameter $= 60, 80, 100$ and $160$ nm respectively.
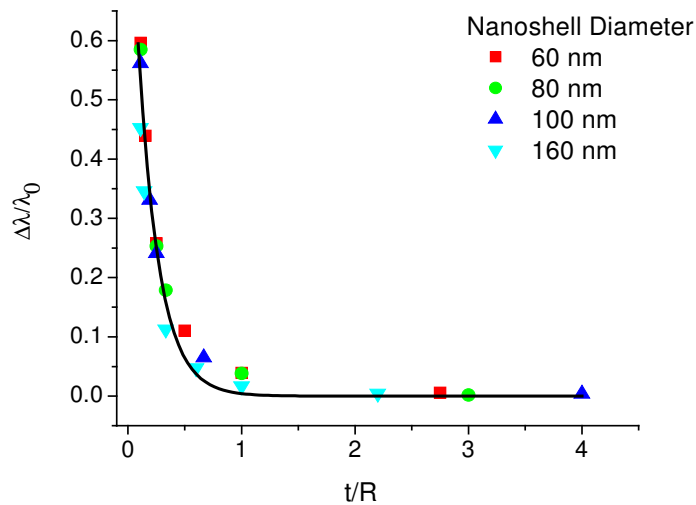


Figure 6.3: The fractional shift ($\Delta\lambda/\lambda_0$) of the dipolar plasmon resonance wavelength maximum of the silica core-gold nanoshell in water with respect to the solid gold nanosphere plasmon resonance maximum plotted against the ratio of the shell thickness to the core radius (t/R) for four different nanoshell diameters. The data-points for the different nanoshell diameters fall on the same curve, given by the solid line, which is a least-squares fit ($R^2 = 0.962$) of the data to the single exponential decay $y = a.\exp(-x/\tau)$ with $\tau = 0.18 \pm 0.02$ and $a = 0.97 \pm 0.08$.

190
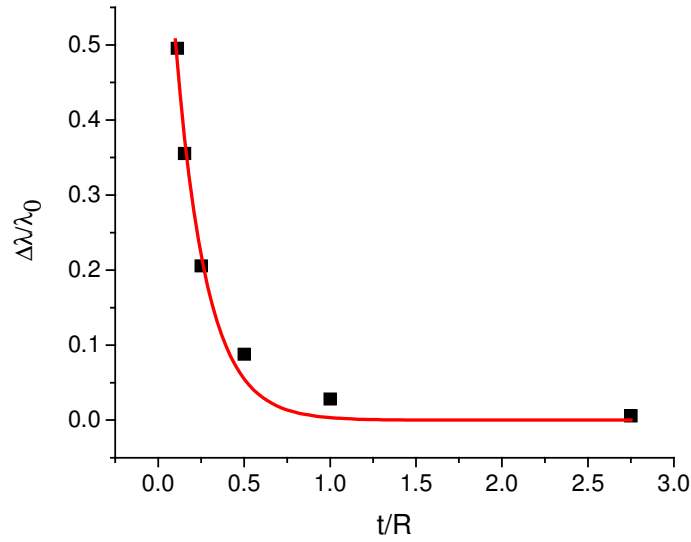
Figure 6.4: The fractional shift ($\Delta\lambda/\lambda_0$) of the dipolar plasmon resonance wavelength maximum of 60-nm diameter hollow core-gold nanoshell in water with respect to solid gold nanosphere plasmon resonance maximum plotted against the ratio of the shell thickness to the core radius (t/R). The solid line is a least-squares fit ($R^2 = 0.986$) of the data to the single exponential decay $y = a.\exp(-x/\tau)$ with $\tau = 0.18 \pm 0.02$ and $a = 0.88 \pm 0.10$.
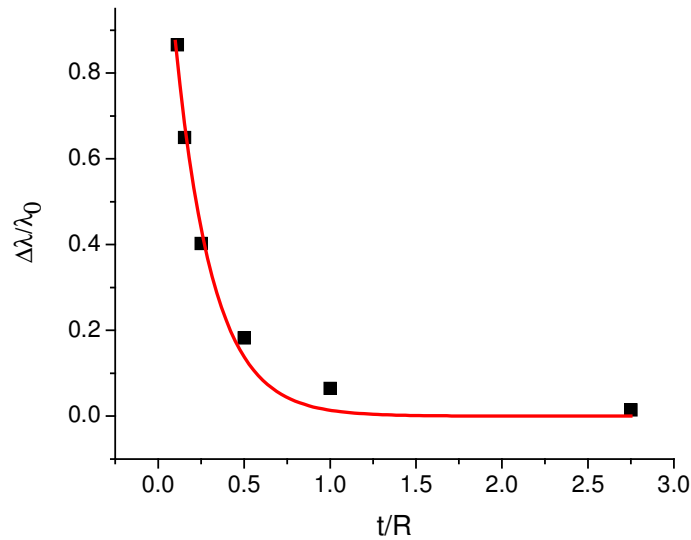


Figure 6.5: The fractional shift ($\Delta\lambda/\lambda_0$) of the dipolar plasmon resonance wavelength maximum of 60-nm diameter silica core-silver nanoshell in water with respect to solid silver nanosphere plasmon resonance maximum plotted against the ratio of the shell thickness to the core radius (t/R). The solid line is a least-squares fit ($R^2 = 0.986$) of the data to the single exponential decay $y = a.\exp(-x/\tau)$ with $\tau = 0.22 \pm 0.03$ and $a = 1.39 \pm 0.14$.
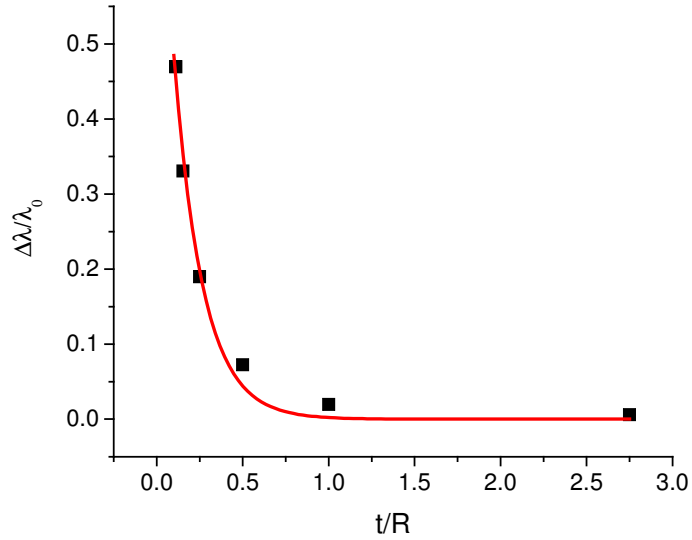
Figure 6.6: The fractional shift ($\Delta\lambda/\lambda_0$) of the dipolar plasmon resonance wavelength maximum of 60-nm diameter silica core-gold nanoshell in air with respect to solid gold nanosphere plasmon resonance maximum plotted against the ratio of the shell thickness to the core radius (t/R). The solid line is a least-squares fit ($R^2 = 0.989$) of the data to the single exponential decay $y = a.exp(-x/\tau)$ with $\tau = 0.17 \pm 0.02$ and $a = 0.88 \pm 0.09$.

the fractional shift, however, does depend on the dielectric properties of the core, shell, and environment. In general, we find that higher dielectric constant of the core or that of the surrounding medium leads to a larger fractional shift,[46] which is similar to the observation in the particle-pair system.[39] As also proposed for the particle-pair system,[7,34,39] using silver as the material of the plasmonic shell also leads to a larger resonance shift (Figure 6.5) as compared to that of gold due to the stronger electromagnetic fields in silver. The line widths for silver are also much narrower.

## 6.3.2 Quasistatic Dipolar-Coupling Model

This interesting parallel between the particle-pair system and the nanoshell structure is very well reconciled with the plasmon hybridization model, which was

developed by Prodan et al.[19] for explanation of the physical origin of the tunable plasmon resonance in metal nanoshells. As per this model, the metal nanoshell is a two-interface system, which supports two distinct plasmon modes: an outer shell-surface sphere mode and an inner shell-surface cavity mode, which couple/hybridize with each other, leading to a splitting into two new modes. The anti-symmetric combination of these modes results in a higher-energy (blue-shifted) plasmon mode, while the symmetric combination results in a lower energy (red-shifted) plasmon mode, which lies in the visible-near-infrared region. The position of the visible-near-infrared resonance is thus determined by the extent of the splitting, in other words, the strength of the plasmon interaction. The metal shell thickness represents the distance over which this interaction takes place. The plasmon coupling strength between the cavity and sphere modes vanishes over the shell thickness t similar to the decay of the plasmonic field in the interparticle gap of the particle-pair system. The plasmon coupling strength in the nanoparticle-pair system is determined by the strength of the near-field, which for dipolar interaction falls as the inverse cube of distance.[38,39] At the same time, a higher value of the particle polarizability (which for the dipolar mode is proportional to the cube of the particle size) ensures stronger coupling. As a consequence, the fractional shift $\Delta\lambda/\lambda_0$ for the dipolar resonance of the nanoparticle-pair system has a functional dependence on $(s/D + 1)^{-3}$ (where s is the interparticle separation and D is the particle diameter) that can be approximated to an exponential decay.[39] Likewise, in the nanoshell system, we can expect the fractional shift of the dipolar resonance to be a function of $(t/R + 1)^{-3}$, where t is the shell thickness and R is the core radius. In other words, a larger core has a larger polarizability and a thinner shell ensures stronger near-field coupling, thus leading to a larger fractional plasmon

shift. In fact, the dipolar resonance condition for a core-shell structure in the quasistatic limit is specified by: [17,23]

$$\varepsilon_c = -2\varepsilon_s \frac{\varepsilon_s(1-f)+\varepsilon_m(2+f)}{\varepsilon_s(1+2f)+2\varepsilon_m(1-f)} \quad (1)$$

where $\varepsilon_c$, $\varepsilon_s$ and $\varepsilon_m$ are the dielectric constants of the core, shell and medium respectively and f is the fraction of the volume of the core in the composite structure. It is interesting to note that f is essentially $(t/R+1)^{-3}$. This analogy serves to qualitatively explain the similarity of the distance dependence and scaling behavior of plasmon coupling in the nanoshell structure to that in the particle-pair structure. Further analysis (Figure 6.7) shows that the fractional dipolar resonance shift for a silica core-gold nanoshell calculated from eq 1 when plotted against t/R shows a near-exponential decay with a decay constant of 0.19 $\pm$ 0.01. The plasmon hybridization model by Prodan et al. also results in an expression where the nanoshell resonance frequency is a function of the core radius to shell radius ratio raised to the power (2l + 1) where l = 1, 2, ..., corresponding to the dipole, quadrupole, ..., etc.[22] The plasmon hybridization model has also been shown to be valid for describing plasmonic coupling in nanoparticle dimers.[40]

In addition to the plasmon resonance maximum position, we can also expect the extinction efficiency,[16] ratio of scattering to absorption,[16] resonance line width,[43] and refractive index sensitivity[31] of the nanoshell system to have some defined functional dependence on f, at least within the limit of the quasistatic and dipole approximations. In
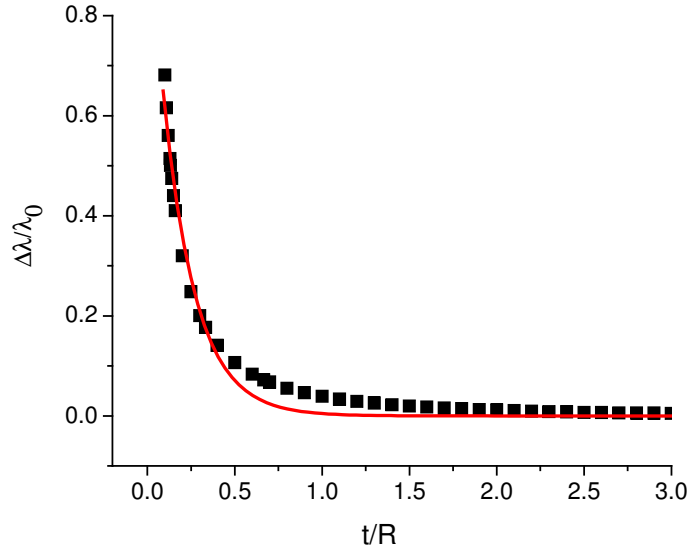
Figure 6.7: The fractional plasmon shift ($\Delta\lambda/\lambda_0$) for a gold nanoshell calculated from the quasistatic dipolar resonance condition (eq 1) plotted against the ratio of the shell thickness to the core radius (t/R). The solid line is a least-squares fit ($R^2 = 0.985$) of the data to the single exponential decay $y = a.\exp(-x/\tau)$ with $\tau = 0.19 \pm 0.01$ and $a = 1.06 \pm 0.04$. For this calculation, we used $\varepsilon_c = 2.10$ (silica) and $\varepsilon_m = 1.77$ (water). A near-linear relationship between the wavelength and the real part of the dielectric constant ($\lambda = 473.11-13.39\varepsilon_s$) in the wavelength range 500-900 nm was assumed for gold.

the case of larger sizes, the complicating effect of electromagnetic retardation[43] and higher-order interactions[20] may result in some deviations from the universality.

While we have approximated the plasmon coupling in the core-shell structure as well as the particle-pair by a dipole-dipole type interaction, which falls with distance d as $1/d^3$; in a more complete treatment, one should consider that the dipolar resonance mode of each pair-partner interacts with the higher-energy multipolar plasmon modes of the other partner, thus resulting in the formation of a hybridized "dipolar" plasmon mode with a mixed multipolar composition. In general, the interaction between a plasmon mode of order l and that of order l′ falls with distance as $1/d^{(l+l'+1)}$. Thus, the complete multipolar interaction can be represented as a geometric series in 1/d, which effectively

reflects an exponential decay. While the approximation of dipole-dipole interaction works very well at relatively larger interaction distances, at smaller distances, the multipolar contribution to the interaction becomes increasingly important, thus leading to a "non-dipolar" shift in the dipolar plasmon resonance.[39] While this is true for the particle-pair system, the spherical symmetry in the nanoshell system[47] allows only modes of the same angular momentum to interact (i.e., $l' - l = 0$). This is probably why a purely dipolar interaction (for example, eq 1) can be used to explain the dipolar nanoshell resonance with good quantitative agreement, unlike the particle-pair system.[39]

### 6.3.2 Estimation of Nanoshell Resonances

In addition to providing fundamental insight into the nature of the plasmon coupling in the nanoshell structure, our extension of the scaling behavior of the plasmon coupling to the nanoshell system allows us to present a simple empirical expression to estimate the plasmon resonance extinction wavelength maximum $\lambda_{max}$ for a nanoshell of given dimensions. From the fit to the universal trend exhibited by silica-gold nanoshells in water (Figure 6.3), we get:

$$\frac{\Delta\lambda}{\lambda_0} = 0.97 \exp\left(\frac{-t/R}{0.18}\right) \quad (2)$$

where t is the gold shell thickness, R is the core radius, $\lambda_0$ is the plasmon extinction wavelength maximum of a solid sphere of the same size as the nanoshell, and $\Delta\lambda = \lambda_{max} - \lambda_0$ is the shift of the nanoshell extinction wavelength maximum from the resonance maximum of this solid sphere. Hirsch et al. employed a nanoshell with a silica core of 110 nm diameter and a 10 nm gold shell thickness for in vivo cancer therapy.[9] For this

case, $\lambda_0 = 606$ nm from Mie theory for a 65 nm radius gold nanosphere. Thus, from eq 2 we get $\lambda_{max} = 820$ nm, which agrees with the experimental extinction maximum of 820 nm. Eq 2 thus provides a simple design guideline (in lieu of detailed electrodynamic calculations) for tuning the nanoshell optical resonance in aqueous media, which would be useful for biomedicinal imaging and therapy applications in vivo.

## 6.4 Conclusion

Thus, we have extended the universal scaling behavior of plasmon coupling from the particle-pair system to the metal shell nanostructure, thus drawing a clear analogy between these two systems in corroboration of the plasmon hybridization model. Note that our scaling model of the nanoshell incorporates the dependence of the nanoshell plasmon resonance wavelength maximum on both the shell-to-core ratio and the total nanoshell volume, unlike earlier models.[18,19] In addition, our analysis is based on a fully retarded Mie theory, which includes size-dependent electromagnetic retardation effects. We also obtain a simple expression based on the scaling model (eq 2) that calculates the plasmon resonance wavelength maximum of a silica core-gold nanoshell of given dimensions, which is useful for tuning the nanoshell structure for desired biomedical and optical applications.

## 6.5 References and Notes

(1)      El-Sayed, I. H.; Huang, X.; El-Sayed, M. A. *Nano Lett.* **2005**, *5*, 829.

(2)      Sokolov, K.; Follen, M.; Aaron, J.; Pavlova, I.; Malpica, A.; Lotan, R.; Richards-Kortum, R. *Cancer Res.* **2003**, *63*, 1999.

(3)      Loo, C.; Hirsch, L. R.; Lee, M. H.; Chang, E.; West, J.; Halas, N.; Drezek, R. *Opt. Lett.* **2005**, *30*, 1012.

(4)      Alivisatos, A. P. *Nat. Biotechnol.* **2004**, *22*, 47.

(5)      Rosi, N. L.; Mirkin, C. A. *Chem. Rev.* **2005**, *105*, 1547.

(6)      Haes, A. J.; Zou, S.; Schatz, G. C.; Van Duyne, R. P. *J. Phys. Chem. B* **2004**, *108*, 6961.

(7)      Sönnichsen, C.; Reinhard, B. M.; Liphardt, J.; Alivisatos, A. P. *Nat. Biotechnol.* **2005**, *23*, 741.

(8)      Loo, C. A.; Lowery, A.; Halas, N.; West, J.; Drezek, R. *Nano Lett.* **2005**, *5*, 709.

(9)      Hirsch, L. R.; Stafford, R. J.; Bankson, J. A.; Sershen, S. R.; Rivera, B.; Price, R. E.; Hazle, J. D.; Halas, N. J.; West, J. L. *Proc. Natl. Acad. Sci. U.S.A* **2003**, *100*, 13549.

(10)     Huang, X.; El-Sayed, I. H.; Qian, W.; El-Sayed, M. A. *J. Am. Chem. Soc.* **2006**, *128*, 2115.

(11)     Jain, P. K.; El-Sayed, I. H.; El-Sayed, M. A. *Nano Today* **2007**, *2*, 18.

(12)     Maier, S. A.; Brongersma, M. L.; Kik, P. G.; Meltzer, S.; Requicha, A. A. G.; Atwater, H. A. *Adv. Mater.* **2001**, *13*, 1501.

(13)     Kelly, K. L.; Coronado, E.; Zhao, L. L.; Schatz, G. C. *J. Phys. Chem. B* **2003**, *107*, 668.

(14)    El-Sayed, M. A. *Acc. Chem. Res.* **2001**, *34*, 257.

(15)    Link, S.; El-Sayed, M. A. *Int. Rev. Phys. Chem.* **2000**, *19*, 409.

(16)    Jain, P. K.; Lee, K. S.; El-Sayed, I. H.; El-Sayed, M. A. *J. Phys. Chem. B* **2006**, *110*, 7238.

(17)    Bohren, C. F.; Huffman, D. R. *Absorption and Scattering of Light by Small Particles*; Wiley: New York, 1983.

(18)    Oldenburg, S. J.; Averitt, R. D.; Westcott, S. L.; Halas, N. J. *Chem. Phys. Lett.* **1998**, *28*, 243.

(19)    Prodan, E.; Radloff, C.; Halas, N. J.; Nordlander, P. *Science* **2003**, *302*, 419.

(20)    Oldenburg, S. J.; Jackson, J. B.; Westcott, S. L.; Halas, N. J. *Appl. Phys. Lett.* **1999**, *75*, 2897.

(21)    Averitt, R. D.; Sarkar, D.; Halas, N. J. *Phys. Rev. Lett.* **1997**, *78*, 4217.

(22)    Prodan, E.; Nordlander, P.; Halas, N. J. *Nano Lett.* **2003**, *3*, 1411.

(23)    Zhou, H. S.; Honma, I.; Komiyama, H.; Haus, J. W. *Phys. Rev. B* **1994**, *50*, 12052.

(24)    Sun, Y.; Mayers, B.; Xia, Y. *Adv. Mater.* **2003**, *15*, 641.

(25)    Shi, W.; Sahoo, Y.; Swihart, M. T.; Prasad, P. N. *Langmuir* **2005**, *21*, 1610.

(26)    Liang, Z.; Susha, A.; Caruso, F. *Chem. Mater.* **2003**, *15*, 3176.

(27)    Loo, C.; Lin, A.; Hirsch, L.; Lee, M.-H.; Barton, J.; Halas, N.; West, J.; Drezek, R. *Technol. Cancer Res. Treat.* **2004**, *3*, 33.

(28)    O'Neal, D. P.; Hirsch, L. R.; Halas, N. J.; Payne, J. D.; West, J. L. *Cancer Lett.* **2004**, *209*, 171.

(29)    Sershen, S. R.; Mensing, G. A.; Ng, M.; Halas, N. J.; Beebe, D. J.; West, J. L. *Adv. Mater.* **2005**, *17*, 1366.

(30)    Sun, Y.; Xia, Y. *Anal. Chem.* **2002**, *74*, 5297.

(31)    Tam, F.; Moran, C.; Halas, N. *J. Phys. Chem. B* **2004**, *108*, 17290.

(32)    Jackson, J. B.; Halas, N. J. *Proc. Natl. Acad. Sci. U.S.A.* **2004**, *101*, 17930.

(33)    Tam, F.; Goodrich, G. P.; Johnson, B. R.; Halas, N. J. *Nano Lett.* **2007**, *7*, 496.

(34)    Gunnarsson, L.; Rindzevicius, T.; Prikulis, J.; Kasemo, B.; Käll, M.; Zou, S.; Schatz, G. C. *J. Phys. Chem. B* **2005**, *109*, 1079.

(35)    Su, K. H.; Wei, Q.-H.; Zhang, X.; Mock, J. J.; Smith, D. R.; Schultz, S. *Nano Lett.* **2003**, *3*, 1087.

(36)    Rechberger, W.; Hohenau, A.; Leitner, A.; Krenn, J. R.; Lamprecht, B.; Aussenegg, F. R. *Opt. Commun.* **2003**, *220*, 137.

(37)    Reinhard, B. M.; Siu, M.; Agarwal, H.; Alivisatos, A. P.; Liphardt, J. *Nano Lett.* **2005**, *5*, 2246.

(38)    Jain, P. K.; Eustis, S.; El-Sayed, M. A. *J. Phys. Chem. B* **2006**, *110*, 18243.

(39)    Jain, P. K.; Huang, W.; El-Sayed, M. A. *Nano Lett.* **2007**, *7*, 2080.

(40)    Nordlander, P.; Oubre, C.; Prodan, E.; Li, K.; Stockman, M. I. *Nano Lett.* **2004**, *4*, 899.

(41)    Charamisinau, I.; Happawana, G.; Evans, G.; Rosen, A.; Hsi, R. A.; Bour, D. *Appl. Opt.* **2005**, *44*, 5055.

(42)    Johnson, P. B.; Christy, R. W. *Phys. Rev. B* **1972**, *6*, 4370.

(43)    Grady, N. K.; Halas, N. J.; Nordlander, P. *Chem. Phys. Lett.* **2004**, *399*, 167.

(44)    Nehl, C. L.; Grady, N. K.; Goodrich, G. P.; Tam, F.; Halas, N. J.; Hafner, J. H.
        *Nano Lett.* **2004**, *4*, 2355.


(45)    Note that, in the present analysis, we have consistently used a lower bound on the
        t/R value of about 0.1 for the different nanoshell diameters.


(46)    Prodan, E.; Nordlander, P.; Halas, N. J. *Chem. Phys. Lett.* **2003**, *368*, 94.


(47)    Wang, H.; Wu, Y.; Lassiter, B.; Nehl, C. L.; Hafner, J. H.; Nordlander, P.; Halas,
        N. J. *Proc. Natl. Acad. Sci. U.S.A.* **2006**, *103*, 10856.

# CHAPTER 7

# SURFACE PLASMON RESONANCE SENSITIVITY OF METAL

# NANOSTRUCTURES: PHYSICAL BASIS AND UNIVERSAL

# SCALING IN METAL NANOSHELLS AND PARTICLE PAIRS

## Abstract

In this chapter, we show using extended Mie theory simulations that the sensitivity of the surface plasmon resonance (SPR) of a dielectric core-metal nanoshell increases near-exponentially as the ratio of the shell thickness-to-core radius is decreased. The plasmon sensitivity thus shows the same universal scaling behavior established recently for plasmon coupling in metal nanoshells and that in metal nanoparticle pairs. Following from the analogy between the nanoshell structure and the particle-pair, we also suggest similar enhancements in the plasmon sensitivity of a particle pair with decreasing inter-particle separation gap. From these observations, we propose a general physical principle that the sensitivity is determined by the ease of surface polarization of the electrons in the nanostructure by the light. This can be used as a generalized physical principle for designing plasmonic nanostructures for effective SPR chemical and biological sensing.

## 7.1 Introduction

Plasmonic nanostructures have found a wide range of nanotechnological applications on account of their intense surface plasmon resonance (SPR) and the ability to tune this resonance by changing the size, shape, composition, and surrounding medium of the nanostructure.[1-4] The strong plasmon-enhanced light scattering of plasmonic metal nanoparticles has been utilized recently for biological imaging and labeling.[5,6] Complementarily, the strong plasmon absorption has been employed in the photothermal therapy of cancer and other disorders.[7-10] The relative contribution of scattering and absorption is controlled by changing the nanoparticle size,[4] while the plasmon resonance band can be tuned from the visible to near-infrared region (biological window useful for in vivo applications) in nanostructures such as metal nanorods and metal nanoshells by variation of their geometrical parameters.[4,11] These nanostructures also offer a strongly enhanced near field for enhancement of spectroscopic signals of adsorbed molecules, for example, SERS[12,13] and plasmon-enhanced fluorescence.[14]

Plasmonic nanostructures have also been receiving increasing attention for the optical sensing of chemical and biological analytes. While one class of metal nanoparticle sensors is based on the analyte-induced assembly of metal nanoparticles,[15,16] another well-developed strategy of sensing is based on SPR wavelength shifts.[17] It is well known that the SPR wavelength maximum is strongly dependent on the dielectric properties of the local environment of the nanoparticles including substrate, solvent, and adsorbates. Thus, by following the shift in the SPR wavelength $\lambda_{sp}$ in response to adsorbate-induced changes in the local dielectric environment of the nanoparticle, nanoscale chemical and biological sensors have been developed.[17,18] In order to ensure high analyte sensitivity, as

required in the case of sensing of trace pollutants or biological agents as DNA, one would require large changes in the SPR wavelength in response to relatively small changes in the medium refractive index, that is, a high value of $d\lambda_{sp}/dn_m$ (nm/refractive index unit or RIU). It is interesting that those nanostructure shapes, especially nanotriangles,[17] nanorods,[19] and nanoshells,[20] which offer good resonance tunability and strong field enhancement, offer high SPR sensitivity as well. Van Duyne and workers have already established that Ag nanoparticles fabricated in a triangular shape are extremely sensitive to the presence of alkanethiol adsorbates, shown by a linear wavelength red-shift of about 3.0 nm for every carbon atom in the alkane chain.[21] Lee and El-Sayed have already elucidated by means of electrodynamic simulations that moving from nanospheres to nanorods of increasing aspect ratio offers an increased sensitivity of the long-wavelength plasmon resonance band.[19] In fact, the high refractive index sensitivity of the longitudinal band of gold nanorods has been utilized for effective multiplexed detection of antibodies via their binding to recognition molecules (IgG Fab) conjugated to the ends of the nanorod.[22] Another interesting configuration from the point of view of sensing is the metal nanoshell structure.[11,23] Sun and Xia found that 50-nm-diameter hollow gold nanoshells (thickness ~ 4.5 nm) are over 6 times more sensitive to solvent changes and thiol modification of their surfaces as compared to solid gold nanospheres of the same size.[20] In a later work, Tam et al. elucidated for the silica-gold core-shell nanoparticles that increasing the total nanoparticle size is a key handle for improving the plasmon sensitivity.[24]

In this chapter, we discuss our investigation of the geometrical parameters and the physical basis of surface plasmon resonance sensitivity to the surrounding dielectric

using the metal nanoshell as our model nanostructure. We find that starting from a solid metal nanosphere and moving toward a metal nanoshell with decreasing shell thickness there is a near-exponential increase in the SPR sensitivity. The sensitivity falls near-exponentially with an increase in the shell thickness-to-core radius ratio with a decay constant of ~0.2 that is universal for different nanoshell size, inner core dielectric material, or type of plasmonic metal (Au or Ag). It is very interesting that the same universal scaling behavior has been observed for the nanoshell plasmon resonance frequency.[25] The similar scaling behavior of the nanostructure plasmon sensitivity and the plasmon resonance frequency is explained by the model of dipolar polarizability, which shows that the sensitivity of a nanostructure is determined by the ease of polarization of the electrons by the light to the interface of the metal and the medium. Based on the analogy between the nanoshell structure and the particle-pair, we also suggest similar enhancements in the plasmon sensitivity of a particle pair with decreasing inter-particle separation gap.

## 7.2 Calculation Methods

### 7.2.1 Metal Nanoshell

The plasmon spectra of nanoshells can be calculated accurately using the extended Mie theory for core-shell nanoparticles described by Bohren and Huffman.[3] We calculated the extinction efficiency ($Q_{ext}$) spectrum in the visible-near-infrared region for a metal shell of thickness t surrounding a dielectric core (radius R). For the metal (gold or silver) shell, we used the wavelength-dependent complex refractive index data from Johnson and Christy.[26] These bulk refractive index values were not corrected for surface

scattering at the shell boundaries because it does not affect the predicted plasmon resonance positions. For a silica core, a refractive index of 1.45 was used. The refractive index of the surrounding medium, $n_m$, was varied from 1.0 (air) to 1.6 (typical biological media)[27] in steps of 0.1, and the corresponding plasmon resonance wavelength maximum ($\lambda_{sp}$) was obtained from the calculated spectrum. The sensitivity was defined as the change in $\lambda_{sp}$ per unit refractive index (RIU) change, that is, $d\lambda_{sp}/dn_m$. Note that although this definition captures the physical origin of the plasmon resonance sensitivity effectively other factors such as spectral line width (homogeneous and inhomogeneous) and effects due to the chemical interaction of adsorbates with the metal surface are not included in this definition. Although practical sensitivity estimates can be obtained by including these parameters, the goal of this work is to provide a simple physical model for plasmon sensitivity, which can be realized by analyzing purely the shift/RIU.

### 7.2.2 Metal Nanoparticle Pair

Discrete dipole approximation (DDA)-simulated plasmon resonance spectra of pairs of gold nanodiscs (86.5 nm diameter, 25.5 thickness) with varying inter-particle separation from 208 nm to 8 nm, as described in Chapter 5, were analyzed as a function of varying medium refractive index $n_m = 1.0$, 1.175, 1.203, and 1.5.

### 7.3 Results and Discussion

### 7.3.1 Metal Nanoshell

Figure 7.1 shows the typical response of the plasmon resonance of a silica core-gold nanoshell of diameter 80 nm and 10-nm shell thickness to a change in the

surrounding medium refractive index from 1.0 to 1.6. With increasing refractive index, there is a strong red-shift in the dipolar plasmon resonance of the nanoshell along with an increase in the plasmon extinction.[28] Although extinction or intensity changes can be difficult to follow reliably in complex experimental media, the change in the plasmon resonance wavelength maximum with refractive index change is a good measure of the nanostructure sensitivity. For the 80-nm-diameter and 10-nm-thick gold nanoshell, the sensitivity is calculated to be 215 nm/RIU, as given by the slope ($\Delta\lambda_{sp}/\Delta n_m$) of the linear fit of the plasmon resonance maximum shift versus medium refractive index (Figure 7.1 inset). The sensitivity for a solid gold nanosphere of the same size is much lower, i.e., 129 nm/RIU. In fact, as we systematically vary the shell thickness from 40 nm (solid nanosphere) down to 4 nm while keeping the total nanoshell diameter constant, we
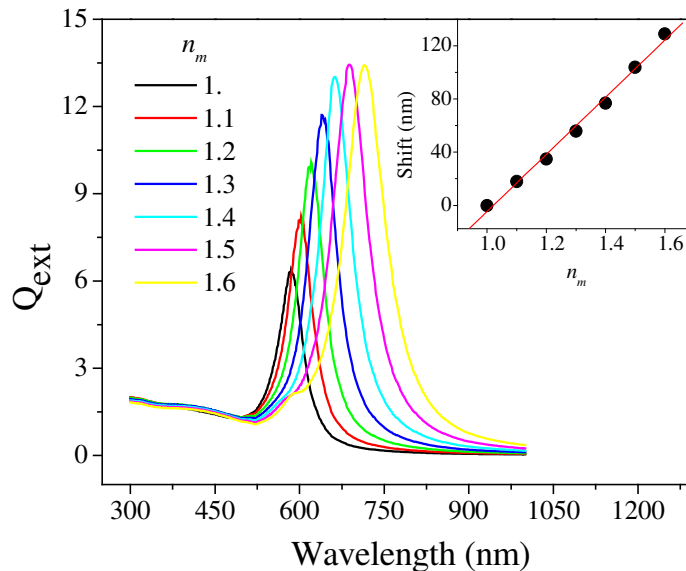


Figure 7.1: Calculated extinction efficiency ($Q_{ext}$) spectrum of a silica core-gold nanoshell with total diameter 80 nm and 10-nm shell thickness for different values of the medium refractive index $n_m$. Inset shows the plasmon shift as a function of the medium refractive index and a straight line fit.

a)



b)
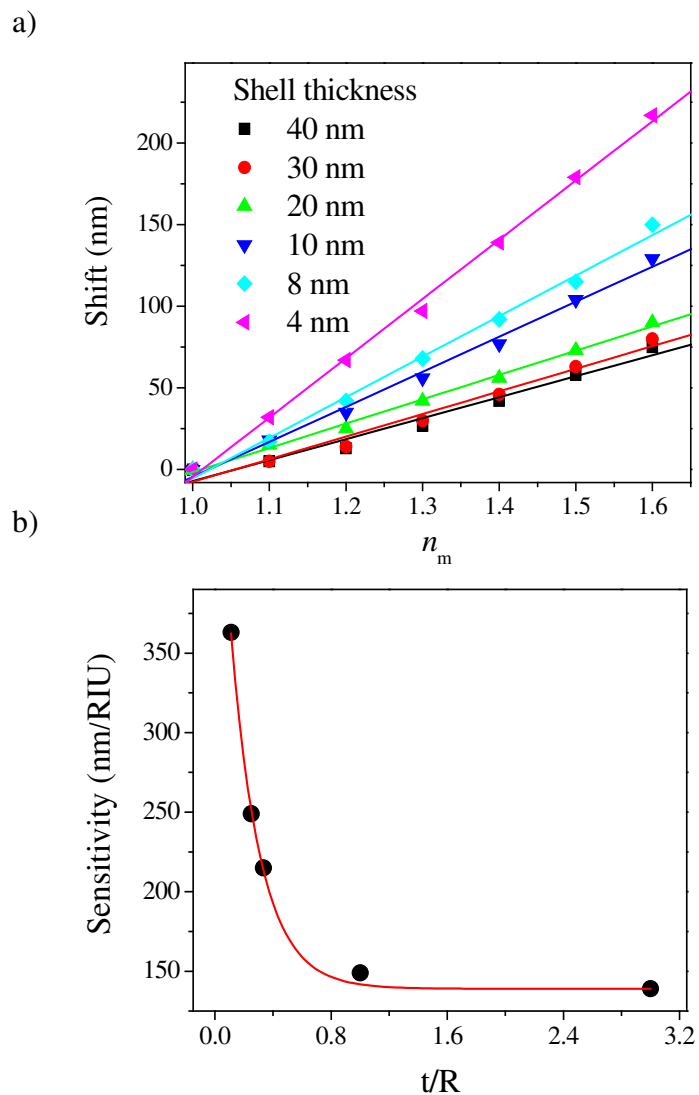


Figure 7.2: (a) The plasmon resonance shift of the silica core-gold nanoshell versus increasing medium refractive index for different shell thickness but the same total size of 80 nm. The solid lines are straight-line fits. (b) Sensitivity ($\Delta\lambda_{sp}/\Delta n_m$) plotted as a function of the shell thickness-to-core radius ratio (t/R). The sensitivity falls near-exponentially with increasing t/R as seen from the fit (solid line) to the single-exponential decay $y = y_0 + a.\exp(-x/\tau)$ with $\tau = 0.20 \pm 0.01$, $a = 386 \pm 15$ and $y_0 = 139$ nm/RIU.

observe (Figure 7.2) that the sensitivity is enhanced from 129 nm/RIU to 363 nm/RIU, at an almost exponential rate. Figure 7.2b shows the dependence of the plasmon sensitivity $(\Delta\lambda_{sp}/\Delta n_m)$ on the shell thickness-to-core radius ratio (t/R). The sensitivity falls near-exponentially with increasing t/R with a decay constant of 0.20. The sensitivity versus t/R decays near-exponentially with the same rate ($\tau \sim 0.2$) even for other nanoshell sizes, 60 and 100 nm, as well in the case of the quasistatic dipolar approximation (Figures 7.3, 7.4 and 7.5).

Thus, the nanoshell plasmon sensitivity shows essentially the same size scaling behavior that we described recently for the plasmon resonance of the metal nanoshell. The plasmon resonance wavelength of the nanoshell also falls near-exponentially as a function of the shell thickness-to-core shell ratio with $\tau \sim 0.2$.[25] What is the origin of the similar scaling behavior of the frequency of the plasmon resonance and its medium sensitivity? In the dipolar quasistatic approximation, the polarizability of a metal nanoparticle is given as:[1]

$$\alpha = \varepsilon_0 V (1 + \kappa) \frac{(\varepsilon - \varepsilon_m)}{(\varepsilon + \kappa \varepsilon_m)} \quad (1)$$

where $\varepsilon_0$ is the vacuum permittivity, $\varepsilon(\omega) = \varepsilon_r + i\varepsilon_i$ is the complex dielectric constant of the metal as a function of the light frequency $\omega$, $\varepsilon_m$ is the dielectric constant of the surrounding medium, V is the nanoparticle volume, and $\kappa$ is a shape factor. The dipolar plasmon resonance is given by the maximum of the polarizability:

$$\varepsilon_r = -\kappa \varepsilon_m \quad (2)$$

assuming $\varepsilon_i$ is relatively constant with frequency. The real part of the metal dielectric constant $\varepsilon_r$ is negative and has a near-linear dependence on wavelength in the 500-900

Figure 7.3: Sensitivity ($\Delta\lambda_{sp}/\Delta n_m$) plotted as a function of the shell thickness-to-core radius ratio (t/R) for 60-nm silica core-gold nanoshell. The sensitivity falls near-exponentially with increasing t/R as seen from the fit (solid line) to the single-exponential decay $y = y_0 + a.\exp(-x/\tau)$ with $\tau=0.23 \pm 0.02$, $a = 378 \pm 25$ and $y_0 = 102$ nm/RIU.
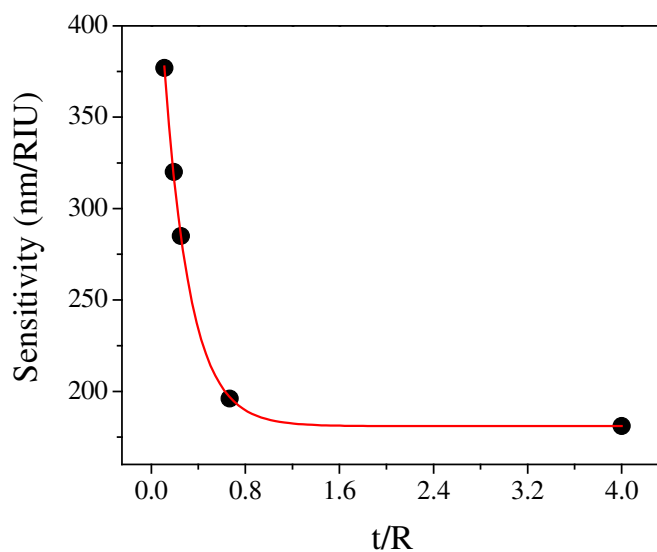


Figure 7.4: Sensitivity ($\Delta\lambda_{sp}/\Delta n_m$) plotted as a function of the shell thickness-to-core radius ratio (t/R) for 100-nm silica core-gold nanoshell. The sensitivity falls near-exponentially with increasing t/R as seen from the fit (solid line) to the single-exponential decay $y = y_0 + a.\exp(-x/\tau)$ with $\tau=0.22 \pm 0.00$, $a = 326 \pm 4$ and $y_0 = 181$ nm/RIU.
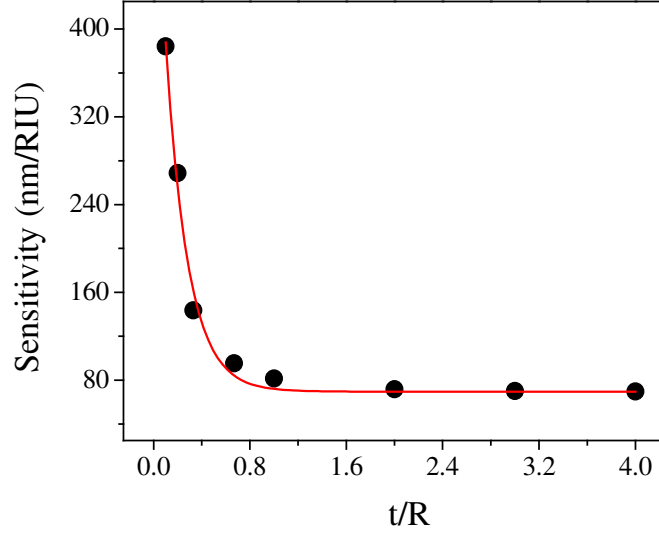
Figure 7.5: Sensitivity ($\Delta\lambda_{sp}/\Delta n_m$) plotted as a function of the shell thickness-to-core radius ratio (t/R) calculated from dipolar quasistatic approximation for a silica core-gold nanoshell. The sensitivity falls near-exponentially with increasing t/R as seen from the fit (solid line) to the single-exponential decay $y = y_0 + a.exp(-x/\tau)$ with $\tau=0.18 \pm 0.01$, a = $547 \pm 37$ and $y_0 = 70$ nm/RIU.

nm range. The shape factor $\kappa$ represents the ease with which the electrons can be polarized for a particular geometry. For instance, for a nanorod, $\kappa$ increases with increasing aspect ratio making it progressively easier to excite a plasmon against the lower restoring force by the positive metallic background.[29] Hence, the plasmon energy progressively red-shifts as the nanorod aspect ratio is increased.

At the same time, it is well known that the presence of a dielectric medium results in the screening of the Coulomb forces between the oscillating electrons and the positive lattice.[30] Thus, with increasing medium dielectric constant $\varepsilon_m$ the plasmon energy red-shifts. This is reflected in the direct proportionality between the negative real part of the metal dielectric constant and the medium dielectric constant given in the resonance

condition (eq 2). It must be noted that the slope of $\varepsilon_r$ (and hence $\lambda_{sp}$) with respect to $\varepsilon_m$ is governed by $\kappa$. Thus, $\kappa$ directly determines the sensitivity of the plasmon resonance to the medium dielectric. This explains the increase in sensitivity as we move from a spherical shape to a rod of increasing aspect ratio.[19] Physically, it can be said that a higher value of $\kappa$ implies a greater ease of the polarization of the electrons to the interface of the nanoparticle and the medium. In such a case, the plasmon can be expected to be more sensitive to the dielectric changes in the medium or environment.

In the case of the nanoshell, the plasmon resonance is the result of the electromagnetic coupling between the inner surface cavity plasmon and the outer surface sphere plasmon.[25,31] In such a case, $\kappa$ is determined by the strength of this coupling. The stronger the coupling, the higher the $\kappa$ and consequently the lower the plasmon resonance frequency. In fact, we have shown already for a pair of interacting particle plasmons that $\kappa$ is a function of the interparticle separation (s) scaled by the size of the single particle (D), such that with decreasing s/D there is a near-exponential increase in $\kappa$ and hence also in the plasmon resonance wavelength maximum.[32] Because of the direct dependence of the plasmon sensitivity on $\kappa$, the sensitivity also follows the same near-exponential scaling behavior. In the case of the nanoshell, in analogy to the particle pair system, the corresponding geometrical factor is given by t/R, that is, the shell thickness scaled by the core radius.[25] In the case of the plasmon pair system, it is quite intuitive to visualize that a higher $\kappa$ or stronger interparticle coupling implies a greater ease with which the electrons can be polarized to the interface/junction between the two particles. This is, in fact, the characteristic of a "bonding" plasmon as well as the origin of the strong near-field enhancement at the junction of a pair of interacting metal particles.[33] In the case of the

nanoshell too, a thin shell geometry relative to the core dimensions is associated, in principle, with a strong resonant electric field at the outer surface of the nanoshell,[34] corresponding to the bonding plasmon mode of the nanoshell.

Similar to the case of the nanoshell plasmon resonance, the plasmon sensitivity also shows universality in its scaling behavior. That is, we still observe a $\tau \sim 0.2$ decay when we change the shell metal to silver or when we replace the silica core by a hollow one (Figures 7.6 and 7.7). Although the decay behavior is universal, it may be noted that the hollow gold nanoshell shows much larger enhancement in the sensitivity as compared to the silica core-gold nanoshell of the same total size, in agreement with the findings of Sun and Xia.[20] For instance, the amplitude of the exponential decay fit is 603 nm/RIU for a 60-nm hollow gold nanoshell as compared to 378 nm/RIU for a 60-nm silica-core gold nanoshell (Figure 7.7). In the case of the hollow nanoshell, the surrounding solvent or medium is allowed to fill the hollow core space.[20] Thus, more surface area (up to a maximum of 2 times) of the hollow nanoshell is exposed to the medium dielectric as compared to the silica core-gold nanoshell of the same size. Alternatively, it can be said in the case of the hollow nanoshell that both cavity and sphere plasmons are exposed to the dielectric environment, thus resulting in a larger effect of the medium dielectric on the plasmon resonance and consequently a much more enhanced sensitivity.

It must be pointed out that we also find that the sensitivity is dependent on the total nanoparticle size, as also described by Tam et al.[24] It is conceivable that for a given shell thickness an increase in the size results in a smaller t/R value, thus providing a strongly polarizable particle with a higher sensitivity. However, the particle size plays an additional role. For instance, in the case of the solid nanosphere, in the quasistatic dipolar
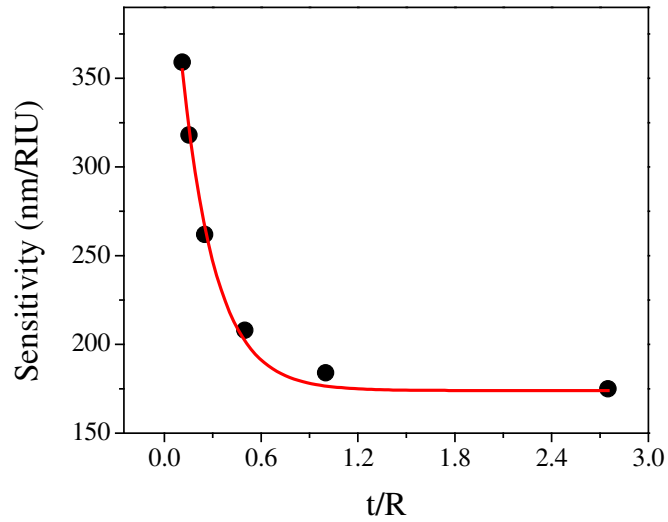
Figure 7.6: Sensitivity ($\Delta\lambda_{sp}/\Delta n_m$) plotted as a function of the shell thickness-to-core radius ratio (t/R) for 60-nm silica-core silver nanoshell. The sensitivity falls near-exponentially with increasing t/R as seen from the fit (solid line) to the single-exponential decay $y = y_0 + a.\exp(-x/\tau)$ with $\tau = 0.21 \pm 0.02$, $a = 308 \pm 19$ and $y_0 = 174$ nm/RIU.
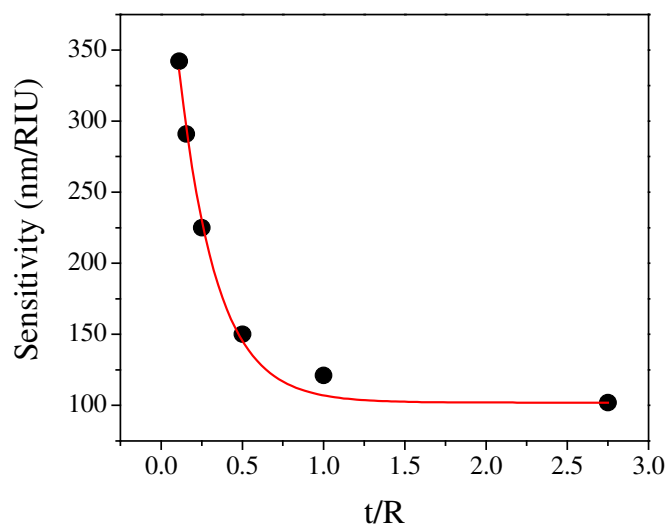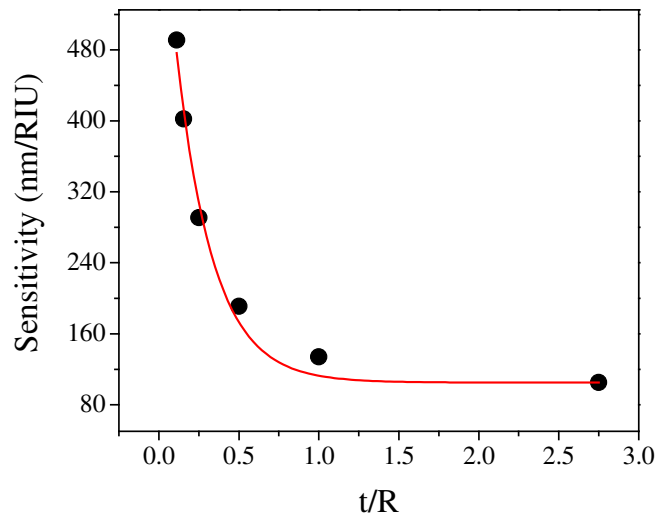


Figure 7.7: Sensitivity ($\Delta\lambda_{sp}/\Delta n_m$) plotted as a function of the shell thickness-to-core radius ratio (t/R) for 60-nm hollow core-gold nanoshell. The sensitivity falls near-exponentially with increasing t/R as seen from the fit (solid line) to the single-exponential decay $y = y_0 + a.\exp(-x/\tau)$ with $\tau = 0.23 \pm 0.03$, $a = 603 \pm 53$ and $y_0 = 105$ nm/RIU.

limit, the plasmon sensitivity is estimated to be roughly 70 nm/RIU; however, as the nanosphere diameter is increased beyond 60 nm up to 100 nm, the sensitivity increases from 99 nm/RIU to 181 nm/RIU. This can be attributed to the effect of electromagnetic retardation. An increase in the medium dielectric leads to a red-shift in the plasmon band as per eq 2. In addition, a higher medium dielectric results in a reduced wavelength of the light in the medium. For larger nanoparticles, this results in an additional red-shift due to the phase retardation of the light as it interacts with a particle of size comparable to its wavelength. Indeed, these finite-size effects also play a part in determining the nanoshell sensitivities; however, they do not affect the trend in the sensitivity as a function of t/R analyzed at a fixed particle size. It must be noted also that increase in particle size results in broader bandwidths (again due to retardation effects), rendering the detection of wavelength changes experimentally difficult. Moreover, a larger surface area has to be covered by analyte molecules to effectively change the medium refractive index. It can thus be recommended that a variation in the geometrical parameters while keeping total size constant is a better handle to enhance sensitivity. Such easy handles for enhancing the plasmon sensitivity are available in two common nanostructures, that is, nanorods (aspect ratio)[19] and nanoshells (shell thickness-to-core radius ratio).[25] However, one must also be aware of the practical limitations that exist in realizing this geometric tunability. For instance, making extremely thin metal shells with low sample heterogeneity is synthetically challenging and, at the same time, it results in increased plasmon broadening due to the greater contribution of electron-surface scattering.

**7.3.2 Metal Nanoparticle Pair**

In Chapter 6, we demonstrated that the plasmon coupling in the nanoshell system is analogous to that in the particle pair system, as evidenced by their similar universal size-scaling behavior. Does the plasmon sensitivity of a nanoparticle pair also get enhanced with decreasing inter-particle separation (or increasing coupling) in analogy to what we have seen for the nanoshell sensitivity? As per the quasistatic dipolar model in Chapter 5, the shape factor (proportionality constant between the negative real part of the metal dielectric constant and the medium dielectric constant) of the particle-pair, which determines the surface plasmon resonance maximum, increases with decreasing separation s in units of the particle size D as a function of $(s/D+1)^{-3}$. Since the shape factor determines the plasmonic sensitivity, the sensitivity of the particle pair is also expected to increase with decreasing inter-particle gap (in units of particle diameter) as per the universal scaling behavior. In other words, the sensitivity is expected to be enhanced in direct correlation with the increase in the inter-particle plasmon coupling.

Figure 7.8 shows the DDA-simulated plasmon resonance wavelength maxima of gold nanodisc pairs with varying separation from 208 nm to 8 nm, as a function of the medium refractive index. It can be seen that with increasing medium refractive index, there is a linear increase in the plasmon resonance wavelength maximum for each of the nanodisc pairs. The slope ($\Delta\lambda_{sp}/\Delta n_m$) of this plot, which is the plasmon sensitivity, is higher for the smaller inter-particle separations. In fact, the plasmon sensitivity increases near exponentially with the inter-particle separation expressed in units of the particle diameter with a trend ($\tau = 0.29$) similar to the universal scaling behavior observed for the plasmon shift in the particle pairs. The considerable deviation of this value from the
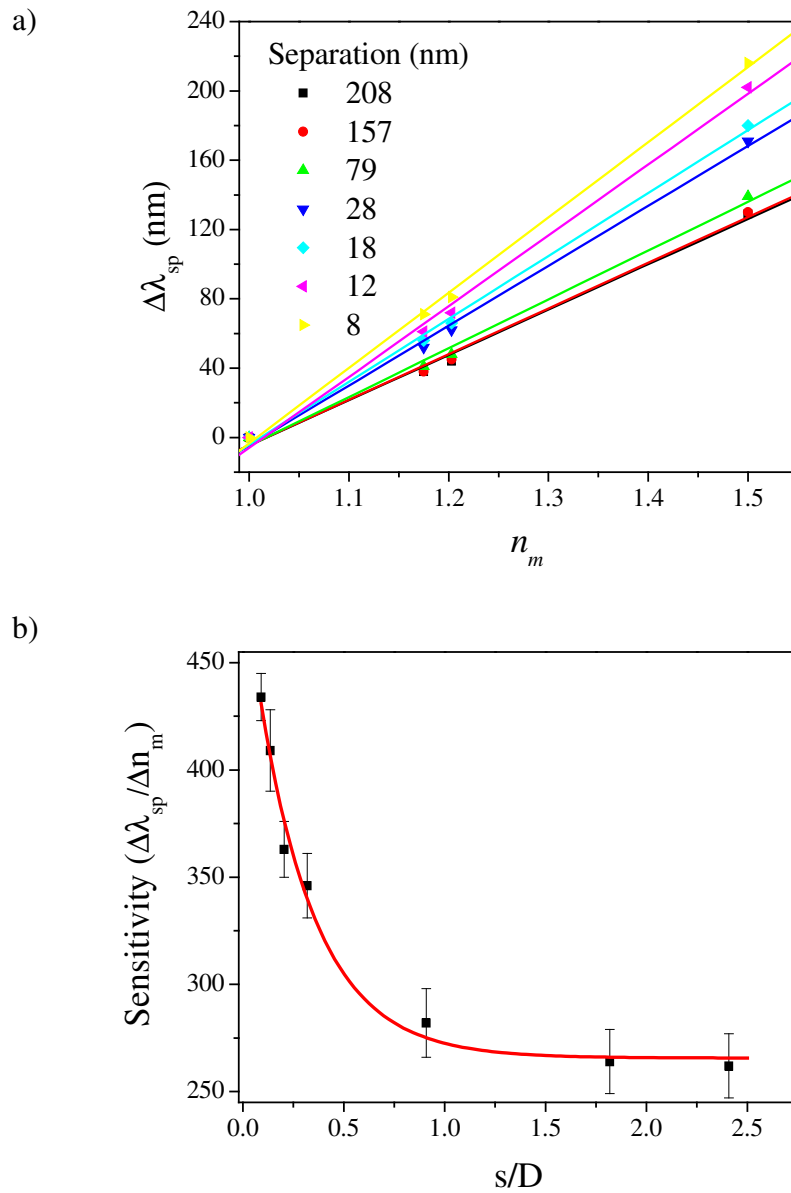
Figure 7.8: (a) The plasmon resonance shift of a pair of gold nanodiscs (86.5 nm diameter, 25.5 nm thickness) with increasing medium refractive index for different inter-particle separations. The solid lines are straight-line fits. (b) Sensitivity ($\Delta\lambda_{sp}/\Delta n_m$) plotted as a function of the separation-to-particle diameter ratio (s/D). The sensitivity falls near-exponentially with increasing s/D as seen from the fit (solid red line) to the single-exponential decay $y = y_0 + a.exp(-x/\tau)$ where $\tau=0.29 \pm 0.04$. The error bars are obtained from the error in the straight line fits in a.

universal scaling decay rate may be due to the complicating effect of electromagnetic retardation, which becomes important as the medium dielectric constant is increased. It is expected that electromagnetic retardation effects would also complicate the experimental observation of this predicted sensitivity enhancement unless particle pairs of size much smaller than the wavelength of light are employed.

This sensitivity enhancement with increasing plasmon coupling is conceptually related to the counter-intuitive increase in the coupling-induced fractional plasmon shift with increase in medium dielectric seen for particle pairs in Chapter 5 and for nanoshells in Chapter 6. The increase in medium dielectric is expected to decrease the coupling strength between the plasmons. However, at the same time, the oscillator strength of the individual plasmons (which decrease in frequency in a higher dielectric constant medium) increases. As a result, the coupling between the plasmons is strengthened. In other words, the fractional plasmon shift is a measure of inter-particle interactions relative to intra-particle interactions. The increase in medium dielectric shields the inter-particle Coulombic attraction, but at the same time, it also decreases the intra-particle Coulombic restoring force on the electrons by the positive metal nanoparticle lattice, possibly more than countering the former shielding effect.

### 7.4 Conclusion

In conclusion, we have shown using the metal nanoshell as a model nanostructure that the sensitivity of the plasmon resonance to the medium dielectric follows a universal scaling behavior similar to the frequency of the nanoshell plasmon resonance.[25] Similar sensitivity enhancement is also predicted in the nanoparticle pair with decreasing inter-

particle separation. Based on these results we present a fundamental physical basis for plasmon sensitivity. A nanostructure geometry, in which the electrons can be polarized by the light to the interface of the metal and medium with greater ease, provides much highly enhanced plasmon sensitivity. Shapes with sharp surface curvatures (e.g., tips of nanotriangles[17] and long axis of nanorods[19] ) or those with junctions (e.g., closely spaced particle pairs[32] or thin nanoshells[25]) satisfy this criterion, making them suited for enhanced plasmon sensing and possibly even single-molecule detection.

## 7.5 References and Notes

(1)     Kreibig, U.; Vollmer, M. Optical Properties of Metal Clusters; Springer: Berlin, 1995; Vol. 25.

(2)     Kelly, K. L.; Coronado, E.; Zhao, L. L.; Schatz, G. C. *J. Phys. Chem. B* **2003**, 107, 668.

(3)     Bohren, C. F.; Huffman, D. R. *Absorption and Scattering of Light by Small Particles*; Wiley: New York, 1983.

(4)     Jain, P. K.; Lee, K. S.; El-Sayed, I. H.; El-Sayed, M. A. *J. Phys. Chem. B* **2006**, 110, 7238.

(5)     Sokolov, K.; Follen, M.; Aaron, J.; Pavlova, I.; Malpica, A.; Lotan, R.; Richards-Kortum, R. *Cancer Res.* **2003**, 63, 1999.

(6)     El-Sayed, I. H.; Huang, X.; El-Sayed, M. A. *Nano Lett.* **2005**, 5, 829.

(7)     El-Sayed, I. H.; Huang, X.; El-Sayed, M. A. *Cancer Lett.* **2006**, 239, 129.

(8)     Huang, X.; Jain, P. K.; El-Sayed, I. H.; El-Sayed, M. A. *Photochem. Photobiol.* **2006**, 82, 412.

(9)     Loo, C. A.; Lowery, A.; Halas, N.; West, J.; Drezek, R. *Nano Lett.* **2005**, 5, 709.

(10)    Jain, P. K.; El-Sayed, I. H.; El-Sayed, M. A. *Nano Today* **2007**, 2, 18.

(11)    Oldenburg, S. J.; Averitt, R. D.; Westcott, S. L.; Halas, N. J. *Chem. Phys. Lett.* **1998**, 28, 243.

(12)    Nikoobakht, B.; Wang, J.; El-Sayed, M. A. *Chem. Phys. Lett.* **2002**, 366, 17.

(13)    Jackson, J. B.; Halas, N. J. *Proc. Natl. Acad. Sci. U.S.A.* **2004**, 101, 17930.

(14)    Tam, F.; Goodrich, G. P.; Johnson, B. R.; Halas, N. J. *Nano Lett.* **2007**, 7, 496.

(15)    Rosi, N. L.; Mirkin, C. A. *Chem. Rev.* **2005**, 105, 1547.

(16)    Sonnichsen, C.; Reinhard, B. M.; Liphardt, J.; Alivisatos, A. P. *Nature Biotechnol.* **2005**, 23, 741.

(17)    Haes, A. J.; Van Duyne, R. P. *J. Am. Chem. Soc.* **2002**, 124, 10596.

(18)    Haes, A. J.; Hall, W. P.; Chang, L.; Klein, W. L.; Van Duyne, R. P. *Nano Lett.* **2004**, 4, 1029.

(19)    Lee, K.-S.; El-Sayed, M. A. *J. Phys. Chem. B* **2006**, 110, 19220.

(20)    Sun, Y.; Xia, Y. *Anal. Chem.* **2002**, 74, 5297.

(21)    Malinsky, M. D.; Kelly, K. L.; Schatz, G. C.; Van Duyne, R. P. *J. Am. Chem. Soc.* **2001**, 123, 1471.

(22)    Yu, C.; Irudayaraj, J. *Anal. Chem.* **2007**, 79, 572.

(23)    Sun, Y.; Mayers, B.; Xia, Y. *Adv. Mater.* **2003**, 15, 641.

(24)    Tam, F.; Moran, C.; Halas, N. *J. Phys. Chem. B* **2004**, 108, 17290.

(25)    Jain, P. K.; El-Sayed, M. A. *Nano Lett.* **2007**, 7, 2854.

(26)    Johnson, P. B.; Christy, R. W. *Phys. Rev. B* **1972**, 6, 4370.

(27)    Reinhard, B. M.; Siu, M.; Agarwal, H.; Alivisatos, A. P.; Liphardt, J. *Nano Lett.* **2005**, 5, 2246.

(28)    It must be noted that the rise in extinction efficiency with increasing medium refractive index is eventually countered by the effect of electromagnetic retardation resulting from the shorter wavelength of light in a medium of higher refractive index. The retardation effect is an additional complication in the dependence of the plasmon resonance wavelength position on the medium refractive index.

(29)    Aizpurua, J.; Bryant, G. W.; Richter, L. J.; Garcia de Abajo, F. J.; Kelley, B. K.; Mallouk, T. *Phys. Rev. B* **2005**, 71, 235420/1.

(30)    Prodan, E.; Nordlander, P.; Halas, N. J. *Chem. Phys. Lett.* **2003**, 368, 94.

(31)    Prodan, E.; Radloff, C.; Halas, N. J.; Nordlander, P. *Science* **2003**, 302, 419.

(32)    Jain, P. K.; Huang, W.; El-Sayed, M. A. *Nano Lett.* **2007**, 7, 2080.

(33)    Jain, P. K.; Eustis, S.; El-Sayed, M. A. *J. Phys. Chem. B* **2006**, 110, 18243.

(34)    Jackson, J. B.; Westcott, S. L.; Hirsch, L. R.; West, J. L.; Halas, N. J. *Appl. Phys. Lett.* **2003**, 82, 257.

# CHAPTER 8

# SURFACE PLASMON COUPLING AND ITS UNIVERSAL SIZE SCALING IN METAL NANOSTRUCTURES OF COMPLEX GEOMETRY: ELONGATED PARTICLE PAIRS AND NANOSPHERE TRIMERS

## Abstract

Recently we showed that the plasmon resonance coupling between two interacting metal nanoparticles decays with the inter-particle separation (in units of particle size) with the same universal trend independent of particle size, shape, metal type, or medium. This universal scaling behavior has been shown to apply to lithographically fabricated nanoparticle pairs, the metal nanoshell, plasmonic sensing, and the plasmon ruler useful in determining inter-site distances in biological systems. In this work, using electrodynamic simulations we examine the general applicability of this universal scaling behavior to more complex nanostructure geometries, for example head-to-tail dimers of elongated particles of varying aspect ratios and curvatures and a trimer of nanospheres. We find that the plasmon coupling between two elongated nanoparticles assembled head-to-tail decays according to the same universal law if the inter-particle gap is scaled by the particle long-axis dimension. The absolute plasmon coupling strength, however, depends on the particle shape (i.e. aspect ratio and curvature), without affecting the universal

scaling behavior. The universal scaling is also valid in a system of three interacting nanospheres, a first step towards extending this model to chains/arrays/assemblies of metal nanoparticles.

## 8.1 Introduction

The surface plasmon resonance oscillation of electrons in noble metal nanostructures[1-3] imparts them with large field enhancements resulting in strong light scattering and absorption, [4-6] which has been utilized in a range of applications ranging from nanophotonics[7] to biomedicine.[8-11] In recent years, there has been increasing interest in the coupling of these surface plasmon fields in assembled metal nanostructures.[12-20] For instance, when gold nanospheres assemble, the surface plasmon resonance frequency shifts to lower energies with respect to the single particle resonance because of the favorable coupling of the electronic oscillations of the interacting particles.[21-23] This assembly-induced plasmon resonance shift has become an effective optical/spectroscopic tool for biological sensing by utilizing gold nanoparticles (conjugated with specific recognition ligands), which assemble only in the presence of the target analyte.[21,24] The near-field coupling between the nanoparticles also results in a large field enhancement at the inter-particle junctions,[25] which amplifies the Raman scattering from adsorbed molecules by up to 14-15 orders of magnitude.[26-28]

There has been an increasing interest in the distance dependence of plasmon coupling.[13,29-32] Studies on metal nanoparticle pairs fabricated with systematically varying inter-particle separations using electron-beam lithography have shown that the plasmon resonance of a pair of interacting particles (of size much smaller than the wavelength of

light such that there are no drastic retardation effects) red-shifts exponentially with decrease in the inter-particle gap.[13,14,30] Su et al. showed that when the inter-particle gap is normalized by the particle size, this exponential trend becomes independent of the particle size.[13] We found experimentally that the fractional shift ($\Delta\lambda/\lambda_0$) of the plasmon resonance wavelength decays over an inter-particle separation gap s, which is roughly 0.2 in units of the particle dimension D for nanodisc pairs of both gold[30] and silver,[14] and in simulations for gold nanosphere pairs.[30] We found that the scaling behavior expressed as: $\Delta\lambda/\lambda_0 \sim a.\exp^{-s/0.2D}$ is universal independent of the particle size, shape, the type of metal, or the medium.[30] We also found[30] that the universal scaling model gave a "plasmon ruler equation"[30] that was able to calculate, in good agreement with the known experimental values, the inter-particle separation in pairs of gold nanospheres assembled by DNA linkers of varying number of base pairs[32] from their observed plasmon shifts, thus making it helpful in determining inter-site distances in biological systems using the plasmon ruler.[29,32,33] The universal scaling model, which gives a simple intuitive picture of plasmon coupling in metal nanostructures, is also very general. The plasmon resonance of a metal nanoshell,[34] which results from the coupling between the inner and outer shell surface plasmons,[35] also follows a similar universal size-scaling behavior with respect to the metal shell thickness normalized by the core size.[36] Even the dielectric sensitivity of assembled nanostructures, e.g., the metal nanoshell gets enhanced with increasing plasmon coupling, as per the universal scaling model.[37]

The size scaling behavior and its universality has been deduced from studies on nanodisc and nanosphere pairs in which case the choice of the particle dimension D to be used for the scaling is trivial. However, what is the geometric dimension that should be

used for the size-scaling of the plasmon coupling in complex assemblies, e.g., a pair of elongated particles? In this work, using electrodynamic simulations we study the plasmon coupling in pairs of elongated particles assembled head-to-tail. We find that the distance dependence of the plasmon coupling follows the universal scaling trend when the inter-particle distance is scaled by the long-axis dimension. The universal scaling behavior is not affected by variations in the particle curvature and aspect ratio, however these factors determine the absolute plasmon shift resulting from the inter-particle coupling. We also find that the plasmon shift in a system of three interacting gold nanospheres (arranged in a chain) also decays as a function of the inter-particle separation-to-particle size ratio with the same universal scaling behavior as that observed for particle pairs.

## 8.2 Calculation Methods

We used the Discrete Dipole Approximation (DDA) method[38] to simulate the extinction efficiency ($Q_{ext}$) spectra of nanoparticle pairs as a function of the inter-particle separation. In principle, as per the DDA procedure the target geometry is discretized into several virtual dipoles. The interaction of the light with each dipole is solved taking into account the inter-dipole interactions. This simple procedure makes DDA a powerful method for simulating the electrodynamics of nanostructures of any arbitrary geometry.[4,39] Besides, by defining each nanoparticle by several thousand dipoles, finite size effects including retardation and higher-order oscillation modes are accounted for, unlike a purely dipolar model where each particle is represented by a single dipole.[14,30] The number of dipoles in DDA is ensured to be large enough such that the discrete-dipole

spacing is much smaller than the wavelength of light and the nanostructure size to achieve reliable results.
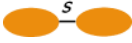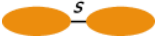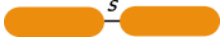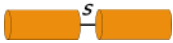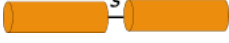
The different nanostructures geometries we simulated included a dimer of spheroids for two different aspect ratios, a dimer of cylinders for two different aspect ratios, a dimer of hemisphere-end capped rods, and a trimer of nanospheres. For each case, the extinction efficiency spectrum was obtained as a function of the inter-particle separation s. The details of each target geometry along with the nanostructure dimensions and the number of dipoles used for the target definition in the simulation are presented in Table 8.1. While electron-beam lithography (EBL) is a powerful technique for experimentally realizing such a systematic study,[30,40] analysis of such a wide range of structures would be impractical. Besides extremely small separations and sharp curvatures are difficult to obtain even with the high resolution of EBL and it is also difficult to separate out the effect of complex substrates (e.g. a quartz slide coated with chromium).[30] Nevertheless, EBL-fabricated nanostructures can be effectively used to verify some of the results obtained in this simulation study.

In all structures, the dielectric function of the target material was assumed to be that of bulk gold. The medium was assumed to have a refractive index of 1.33 + 0i for water. The DDSCAT 6.1 code was employed for the electrodynamic solution. The light polarization direction in each case was assumed to be parallel the axis of inter-particle interaction.

### 8.3 Results and Discussion

The study of elongated or rod-shaped particles is interesting since these particles

Table 8.1: Different Nanostructure Geometries Simulated Using DDA

| Nanostructure Geometry | Particle Dimensions | Number of Discrete Dipoles/Particle |
|---|---|---|
| Dimer of spheroids | Short-axis = 10 nm<br>Long-axis = 20 nm | 8320 |
| Dimer of spheroids | Short-axis = 10 nm<br>Long-axis = 30 nm | 12632 |
| Dimer of rods | Width ~ 18 nm<br>Length ~ 72 nm | 2952 |
| Dimer of cylinders | Diameter ~ 17 nm<br>Length ~ 52 nm | 2400 |
| Dimer of cylinders | Diameter ~ 17 nm<br>Length ~ 70 nm | 3200 |
| Trimer of spheres | Diameter = 10 nm | 4224 |

possess two modes of plasmon resonance: one due to electronic oscillation along the short- axis and the other due to oscillation along the long-axis.[41-43] The long-axis mode is tunable in both its resonance frequency and its oscillator strength or polarizability by simply adjusting the aspect ratio or the surface curvature of the particle.[25,39,42,44] The high oscillator strength of the plasmons of elongated/sharp tipped-particles can be expected to

227

give rise to very strong inter-particle plasmon coupling.[15,45] The strength of the plasmon coupling can be systematically tuned by changing the elongation and/or curvature of the particles.[45,46] However, the role of these factors needs to be understood in addition to the distance dependence of the plasmon coupling between elongated particles. Systematic understanding of the particle elongation, curvature, and inter-particle gap required to get optimum plasmon coupling can be very useful for developing substrates with super enhancements in Raman cross-sections[47] along with control over the resonance frequency of the Raman enhancement. Similarly, the optimization of the coupling can be used to enhance the high dielectric sensitivity for biosensing applications.[37]

The second interesting aspect is that depending on the relative orientation of two elongated particles, their long-axis plasmon modes can either bond favorably with each other (when aligned head-to-tail) or anti-bond with each other (aligned side-by-side).[15] We are mainly interested in the strongly coupled bonding mode. Figure 8.1a shows the DDA-simulated plasmon resonances in a pair of gold spheroids interacting along their long axes (head-to-tail configuration). The light polarization direction is maintained parallel to the inter-particle axis so that we can follow the bonding of the long-axis modes as a function of the inter-particle separation gap[48] between the two particles.

## 8.3.1 Distance Dependence and Universal Scaling

With decreasing inter-particle gap, we see that the longitudinal plasmon resonance of the pair red-shifts and increases in strength. The red-shift in the plasmon resonance is almost exponential with decreasing inter-particle separation (Figure 8.1b). This is very similar to the observation in dimers of circular particles, either nanodiscs[30] or nanospheres.[30,32] In nanodisc or nanosphere pairs, when the inter-particle

Figure 8.1: (a) Longitudinal plasmon resonance spectrum of a pair of gold spheroids of aspect ratio 2 interacting head-to-tail, as a function of the inter-particle separation. The spectrum of a single isolated gold spheroid (short axis = 10 nm and long-axis = 20 nm) is shown in black for comparison. The spectra were generated by fitting calculated data points by cubic interpolation. (b) The plasmon resonance wavelength red-shifts exponentially with decreasing inter-particle gap in the spheroid pair. The red line is a single exponential decay with $R^2$ = 0.98063. In the exponential-decay fit, the offset $y_o$ was set to 595 nm, which is the single particle resonance wavelength.
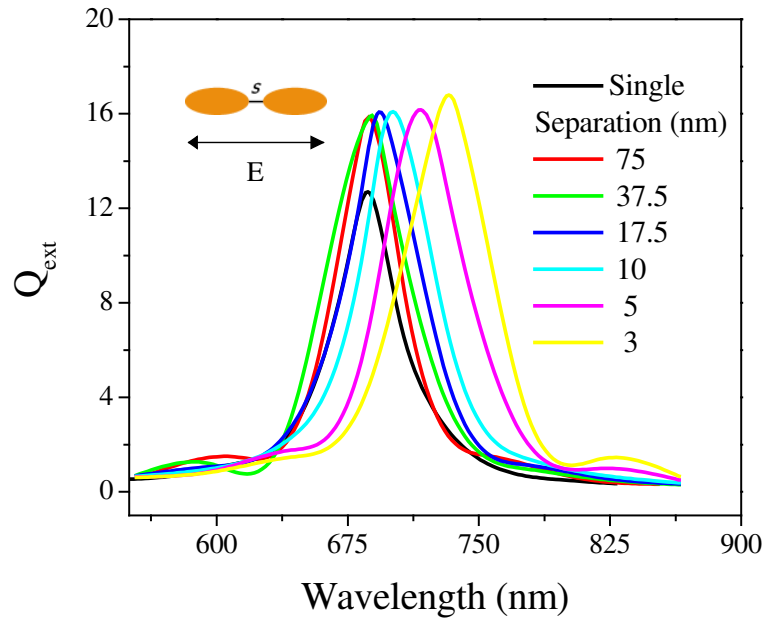
Figure 8.2: Longitudinal plasmon resonance spectrum of a pair of gold spheroids of aspect ratio 3 interacting head-to-tail, as a function of the inter-particle separation. The spectrum of a single isolated gold spheroid (short axis = 10 nm and long-axis = 30 nm) is shown in black for comparison.

separation is expressed in units of particle diameter, the fractional plasmon shift decays near-exponentially with a universal trend with $\tau \sim 0.2$.[30] In other words, the plasmon coupling strength decays over a distance, which is roughly 0.2 times the particle dimension. In the case of elongated particles, what is the geometric dimension that should be used for such scaling of the plasmon coupling? Figure 8.3a shows that when the fractional plasmon shift ($\Delta\lambda/\lambda_0$) in the spheroid pair is plotted against the inter-particle separation in units of the long-axis dimension, we obtain a decay constant ($\tau = 0.2$) which is similar to that seen in the nanosphere or nanodisc pairs universally independent of their size, metal, or medium.[30] At the farthest inter-particle separation i.e. 50 nm, which is 2.5 times the long-axis dimension, the plasmon resonance wavelength is the same (595 nm)

a)

Pair of spheroids of aspect ratio 2

$\tau = 0.2$

b)

Pair of spheroids of aspect ratio 3

$\tau = 0.2$
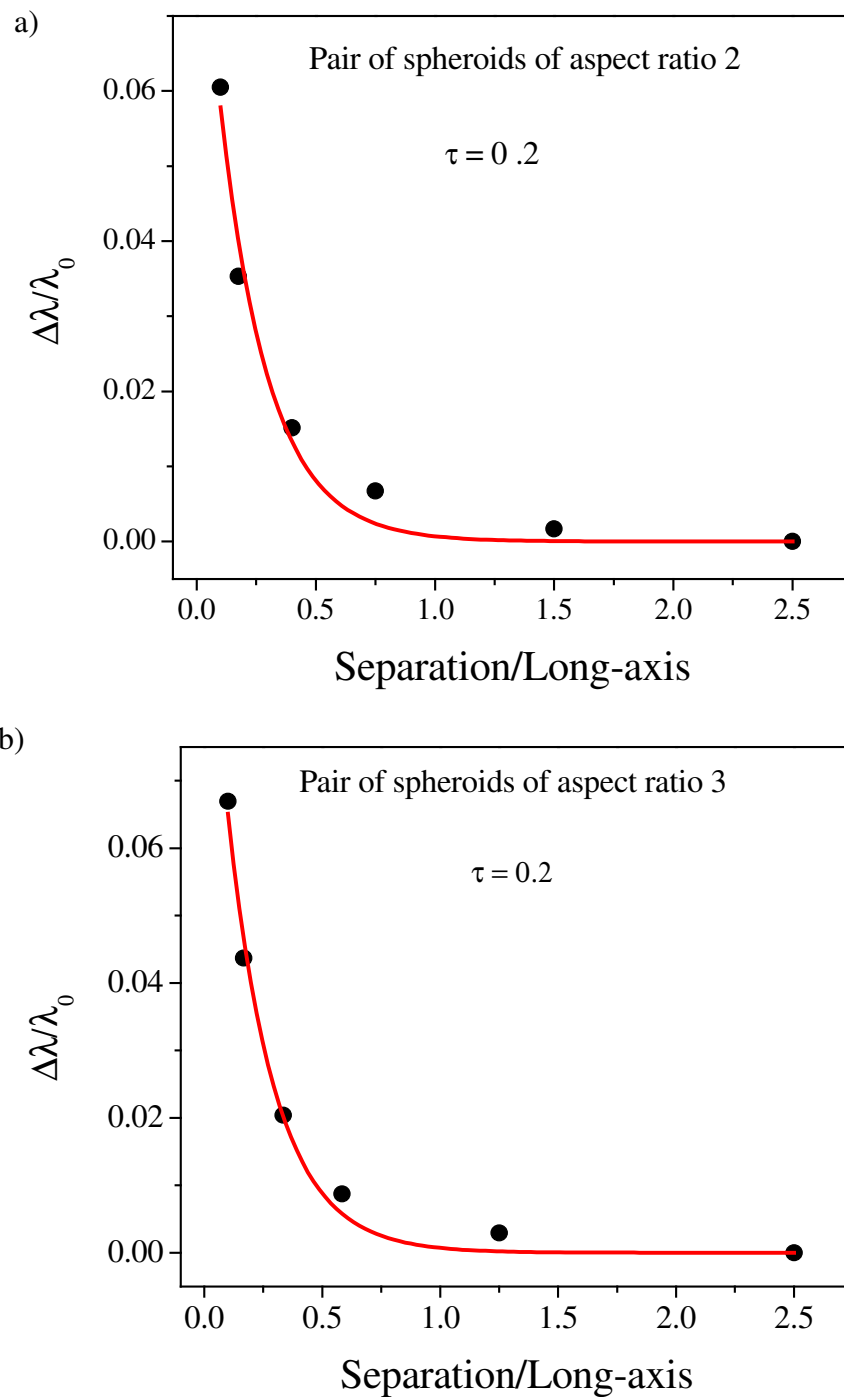
Figure 8.3: Fractional plasmon shift plotted as a function of the inter-particle separation in units of long-axis dimension for a pair of gold spheroids of (a) aspect ratio 2 and (b) aspect ratio 3. In each case the trend was fit by a single exponential decay of the form $y = a.\exp(-x/\tau)$ where $\tau = 0.20 \pm 0.03$, $a = 0.09 \pm 0.01$ for aspect ratio 2 and $\tau = 0.20 \pm 0.02$, $a = 0.11 \pm 0.01$ for aspect ratio 3.

as that for a single spheroid. We use the plasmon resonance at the farthest separation as $\lambda_0$ in each of the cases analyzed.

### 8.3.2 Effect of Particle Aspect Ratio

Even in a pair of spheroids with a higher aspect ratio of 3, we see a similar decay constant ($\tau = 0.2$) when the inter-particle gap is expressed in units of the long-axis dimension, which is 30 nm in this case (Figure 8.3b). In this case too, the plasmon resonance wavelength (687 nm) at an inter-particle gap of 150 nm, which is 2.5 times the long-axis dimension, is nearly equal to that of the single spheroid (686 nm). This verifies that the long-axis dimension is the appropriate dimension for the scaling of the distance dependence of the plasmon coupling.

It is also interesting to note that the fractional shift ($\Delta\lambda/\lambda_0$) for a given separation/long-axis value is quite close for the two different aspect ratios, as denoted by their similar amplitude (a) values obtained from their single exponential decay fits. This implies that the absolute shift ($\Delta\lambda$) is almost proportional to the single particle resonance wavelength $\lambda_0$. The single particle resonance wavelength for a spheroid varies directly with the aspect ratio.[41,42] The single spheroid of aspect ratio 2 shows a plasmon resonance wavelength maximum of 595 nm whereas for the aspect ratio 3 particle the maximum is at 686 nm. Thus, the absolute plasmon shift increases with increasing aspect ratio of the particle.

### 8.3.3 Cylindrical Particle Pairs

We have similarly analyzed the plasmon coupling in a pair of gold cylinders of aspect ratio 3 and 4 (Figure 8.4a and 8.4b respectively). Here, aspect ratio is defined as the length to the diameter of the cylinder. We see that the fractional plasmon shift decays
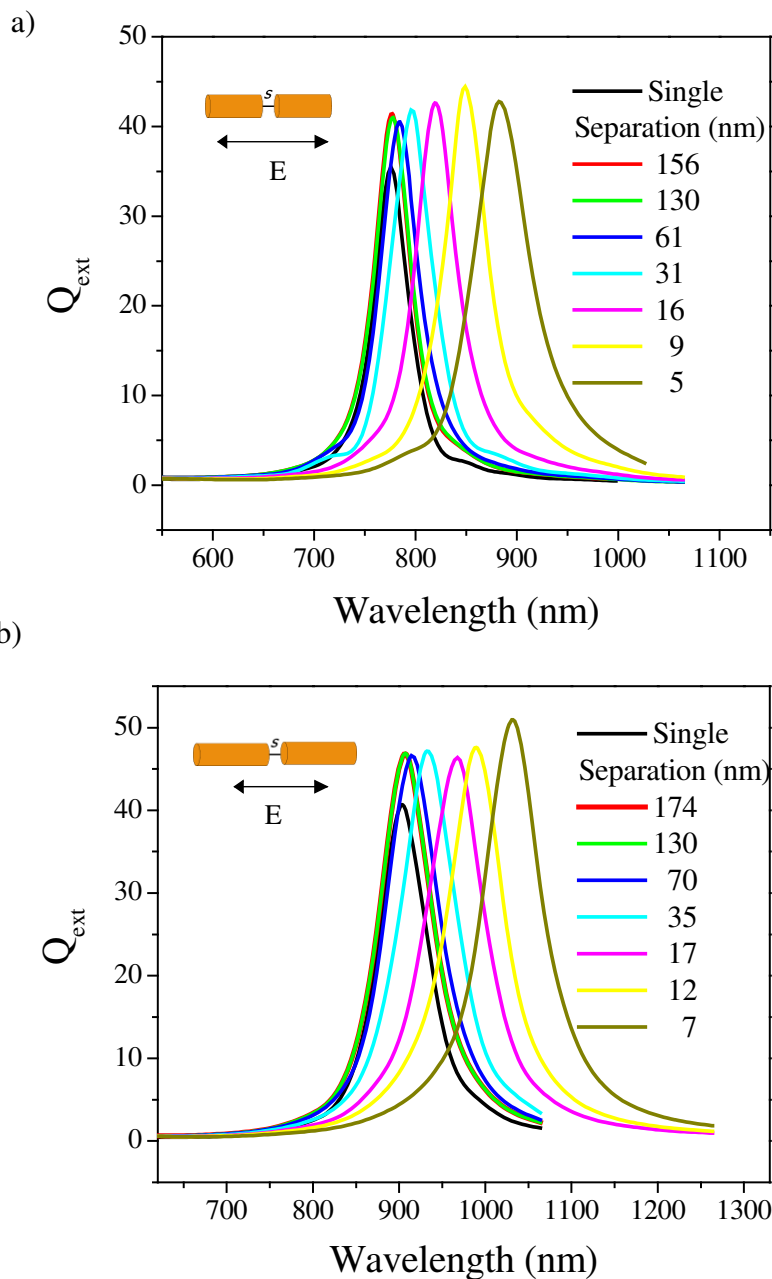
Figure 8.4: (a) Longitudinal plasmon resonance spectrum of a pair of gold cylinders of aspect ratio 3 interacting head-to-tail, as a function of the inter-particle separation. The spectrum of a single isolated gold cylinder (diameter = 17 nm and length = 52 nm) is shown in black for comparison. (b) Longitudinal plasmon resonance spectrum of a pair of gold cylinders of aspect ratio 4 interacting head-to-tail, as a function of the inter-particle separation. The spectrum of a single isolated gold cylinder (diameter = 17 nm and length = 70 nm) is shown in black for comparison.

over a distance roughly 0.2 times the length of the cylinder, which is the particle dimension in the direction of the coupling. Thus, the change in the particle shape from spheroidal to cylindrical does not affect the universal size-scaling behavior.

Similar to the case of the spheroids, it can be seen for the cylinders also that the amplitude of the fit (a) is very similar for the two different aspect ratios 3 and 4 (Figure 8.5). While the single-cylinder resonance is at 776 nm for aspect ratio 3, it is at 904 nm for aspect ratio 4. Thus, the plasmon shift at a given separation-to-length ratio in the cylinder pair is larger for the higher aspect ratio. From the observations on the spheroids and cylinders, the absolute shift appears to be directly related to the elongation of the particle. On the other hand, the fractional shift is not affected by the aspect ratio for a given shape.

### 8.3.4 Effect of Curvature

However, the fractional plasmon shift at a given separation/particle size is higher for the cylinder pair (a = 0.20) as compared to the spheroid pair (a = 0.11) for the same aspect ratio of 3. This can be attributed to the abrupt end-curvature of the cylinder as compared to the much smoother surface curvature of the spheroid ends. Thus, we propose that the ends of the cylinders support much stronger near-fields, resulting in much stronger plasmon coupling in the cylinder pair as compared to the spheroid pair.

This is further supported when we smooth the ends of the cylinders such that they end in hemispherical caps (third row, Table 8.1), while keeping the aspect ratio constant at 4 and the dimensions similar (Figure 8.6).
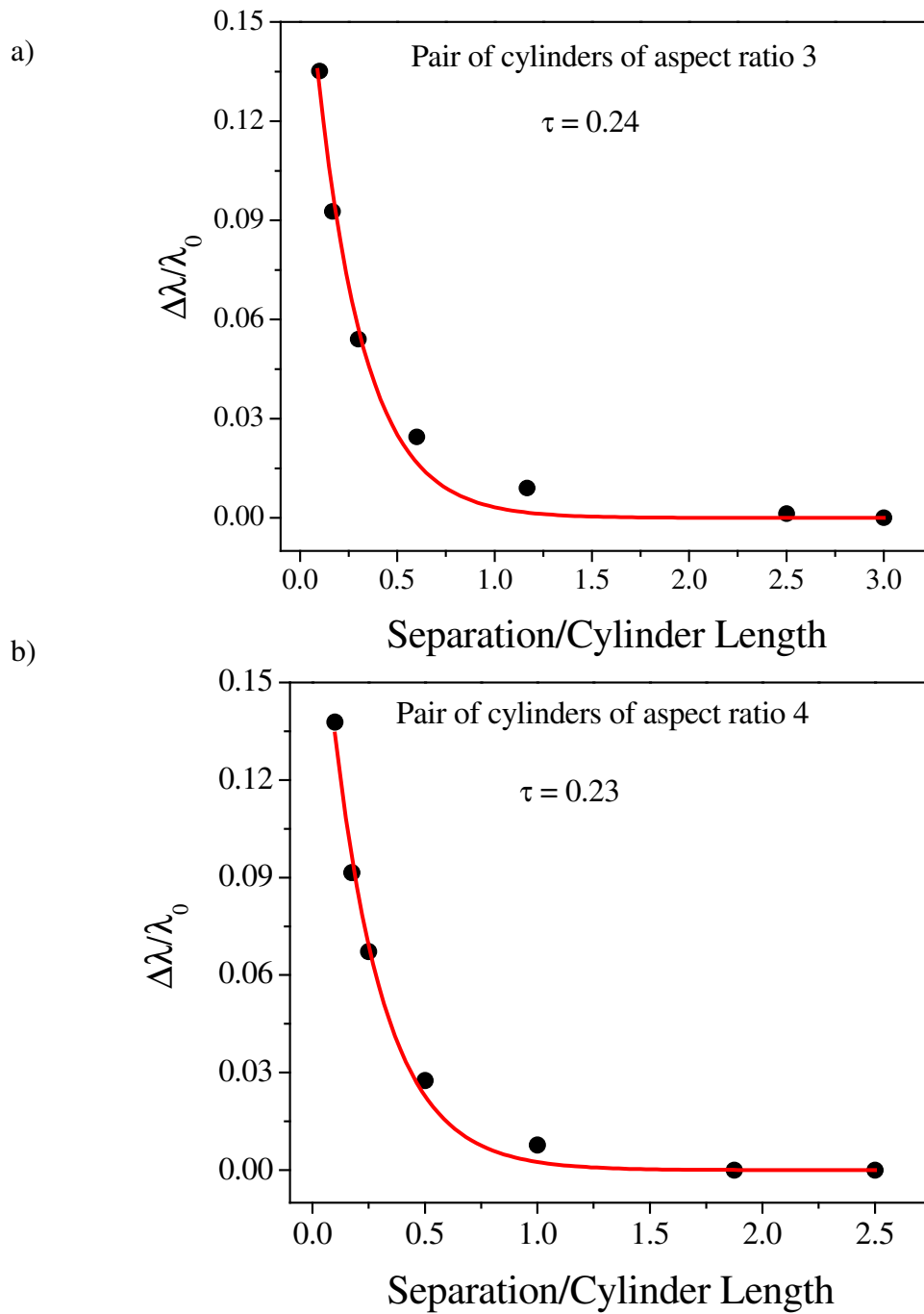
Figure 8.5: Fractional plasmon shift for a pair of gold cylinders of (a) aspect ratio 3 and (b) aspect ratio 4, plotted as a function of the inter-particle separation in units of the cylinder length. In each case the trend can be fit by a single exponential decay of the form $y = a.\exp(-x/\tau)$ with $\tau = 0.24 \pm 0.03$, $a = 0.20 \pm 0.02$ for aspect ratio 3 and $\tau = 0.23 \pm 0.02$, $a = 0.21 \pm 0.01$ for aspect ratio 4.
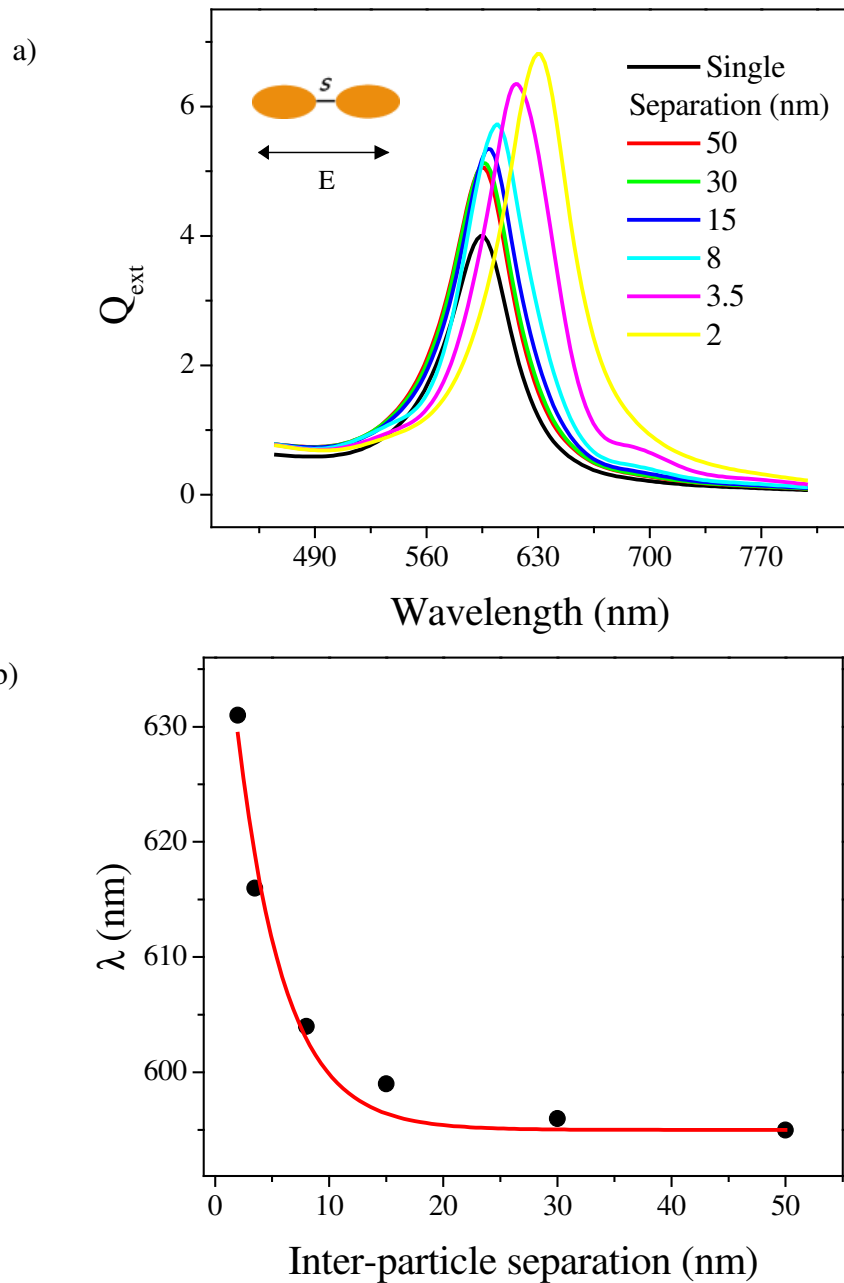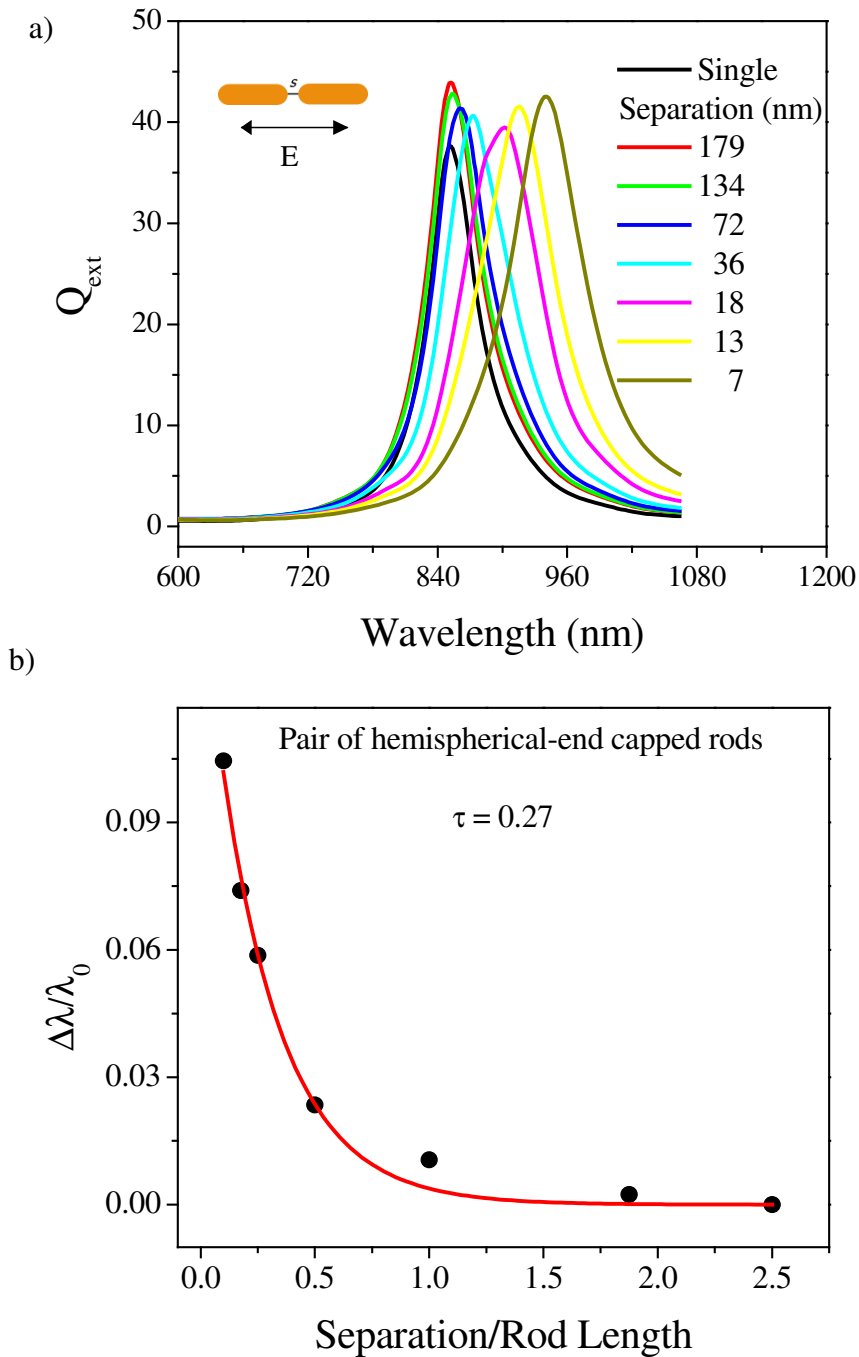
Figure 8.6: (a) Longitudinal plasmon resonance spectrum of a pair of gold hemispherical-end capped rods of aspect ratio 4 interacting head-to-tail, as a function of the inter-particle separation. The spectrum of a single isolated gold rod (width = 18 nm and length = 72 nm) is shown in black for comparison. (b) Fractional plasmon shift in a pair of gold hemispherical-end capped rods of aspect ratio 4 plotted as a function of the inter-particle separation in units of the length. The red line denotes a single exponential decay $y = a.exp(-x/\tau)$ with $\tau = 0.27 \pm 0.02$, $a = 0.15 \pm 0.01$.

The hemisphere-end capped rod has a shorter single-particle plasmon resonance wavelength (852 nm) as compared to the single-cylinder resonance wavelength (904 nm). At the same time, the fractional shift (and the absolute shift) in the pair of hemispherical-end capped rods (a = 0.15) is considerably smaller than that in the cylinder pair (a = 0.21) for the same separation-to-length ratio. Thus, the smoother curvature of the rods as compared to the cylinders gives less strong field coupling.

### 8.3.5 Extension to More than Two Particles

Figure 8.7 shows the simulated plasmon resonance in a trimer of gold nanospheres as a function of the inter-particle separation between the spheres. The trimer shows a single resonance peak that red-shifts with decreasing inter-particle separation. While the plasmon shift in the trimer is larger compared to that in the dimer,[15,30] the fractional plasmon shift shows the same universal decay trend ($\tau = 0.21$) when the inter-particle separation is scaled by the nanosphere diameter.

### 8.4 Conclusion

In summary, we show that the universal size-scaling behavior of plasmon coupling also extends to complex assembled nanostructures. In the case of a pair of elongated particles assembled head-to-tail, plasmon coupling decays with inter-particle separation as per the universal law when the particle dimension in the direction of the coupling is used for scaling the inter-particle separation. The concept of the scaling dimension has important implications for nanophotonics. In analogy to the concept of the diffraction limit, as per which two components cannot be completely resolved when they
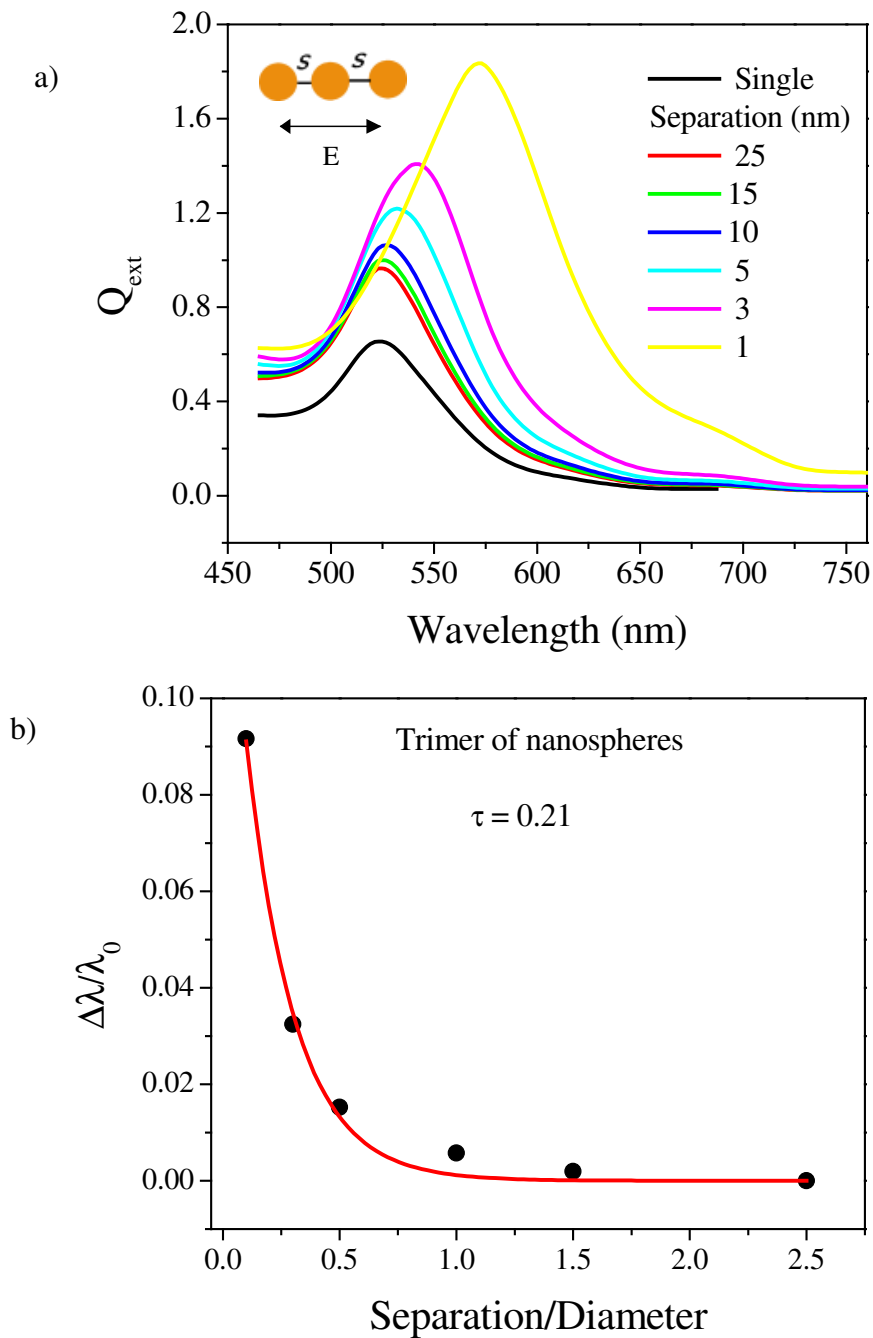
Figure 8.7: (a) Plasmon resonance spectrum of a "linear" trimer of gold nanospheres as a function of the inter-particle separation. The spectrum of a single gold nanosphere (10-nm diameter) is shown in black for reference. (b) The fractional plasmon shift in the nanosphere trimer as a function of the inter-particle separation in units of the particle diameter. The red line is a single exponential decay fit $y = a.exp(-x/\tau)$ with $\tau = 0.15 \pm 0.01$, $a = 0.21 \pm 0.02$.

are separated by less than a distance on the order of the wavelength of light; on the nanoscale, two plasmons cannot be independent (i.e. they couple) when they are separated by less than a distance on the order of the wavelength of the plasmon mode. It is interesting to note that the particle dimension in the light polarization direction is roughly half the wavelength of the plasmon (dipolar) mode. Therefore, plasmon coupling decays on the order of this particle dimension universally independent of particle size, shape, metal type, or medium.[30]

We have shown how the particle shape, elongation and curvature influence the coupling-induced plasmon shift, without affecting the universal size scaling behavior. We also show that the universal scaling model is valid in a system of three interacting particles, which is a first step in the extension of this model to larger chains/assemblies/arrays of particles.[22,49] In 3-D assemblies, the volume fraction (or its cube-root) of the nanoparticles could be the scaling variable corresponding to the separation-to-size ratio used in the psuedo-1-D cases presented here. It must be noted however that as the net size of the assembled nanostructure approaches the wavelength of light, electromagnetic retardation becomes increasingly important,[50] the effect of which is yet to be characterized on the plasmon coupling distance dependence and its universal scaling. We have not considered far-field diffractive coupling effects,[20,51,52] that become important at separations on the order of the light wavelength, since for the separations we have studied, near-field coupling is dominant. Our work is a step towards the detailed characterization of the distance-dependent plasmon resonances in complex assemblies, which can be very useful in the plasmon ruler application as well as in optimizing nanoparticle assembly-based biosensing.[53]

## 8.5 References and Notes

(1)     Kreibig, U.; Vollmer, M. *Optical Properties of Metal Clusters*; Springer: Berlin, 1995; Vol. 25.

(2)     El-Sayed, M. A. *Acc. Chem. Res.* **2001**, *34*, 257.

(3)     Bohren, C. F.; Huffman, D. R. *Absorption and Scattering of Light by Small Particles*; Wiley: New York, 1983.

(4)     Kelly, K. L.; Coronado, E.; Zhao, L. L.; Schatz, G. C. *J. Phys. Chem. B* **2003**, *107*, 668.

(5)     Jain, P. K.; Lee, K. S.; El-Sayed, I. H.; El-Sayed, M. A. *J. Phys. Chem. B* **2006**, *110*, 7238.

(6)     Jain, P. K.; Huang, X.; El-Sayed, I. H.; El-Sayed, M. A. *Plasmonics* **2007**, *2*, 107.

(7)     Maier, S. A.; Brongersma, M. L.; Kik, P. G.; Meltzer, S.; Requicha, A. A. G.; Atwater, H. A. *Adv. Mater.* **2001**, *13*, 1501.

(8)     Huang, X.; El-Sayed, I. H.; Qian, W.; El-Sayed, M. A. *J. Am. Chem. Soc.* **2006**, *128*, 2115.

(9)     Huang, X.; Jain, P. K.; El-Sayed, I. H.; El-Sayed, M. A. *Photochem. Photobiol.* **2006**, *82*, 412.

(10)    Jain, P. K.; El-Sayed, I. H.; El-Sayed, M. A. *Nano Today* **2007**, *2*, 18.

(11)    Loo, C., A.; Lowery, A.; Halas, N.; West, J.; Drezek, R. *Nano Lett.* **2005**, *5*, 709.

(12)    Maier, S. A.; Brongersma, M. L.; Kik, P. G.; Atwater, H. A. *Phys. Rev. B* **2002**, *65*, 193408/1.

(13)    Su, K. H.; Wei, Q.-H.; Zhang, X.; Mock, J. J.; Smith, D. R.; Schultz, S. *Nano Lett.* **2003**, *3*, 1087.

(14)    Gunnarsson, L.; Rindzevicius, T.; Prikulis, J.; Kasemo, B.; Käll, M.; Zou, S.;
         Schatz, G. C. *J. Phys. Chem. B* **2005**, *109*, 1079

(15)    Jain, P. K.; Eustis, S.; El-Sayed, M. A. *J. Phys. Chem. B* **2006**, *110*, 18243.

(16)    Sundaramurthy, A.; Crozier, K. B.; Kino, G. S.; Fromm, D. P.; Schuck, P. J.;
         Moerner, W. E. *Phys. Rev. B* **2005**, *72*, 165409/1.

(17)    Sweatlock, L. A.; Maier, S. A.; Atwater, H. A.; Penninkhof, J. J.; Polman, A.
         *Phys. Rev. B* **2005**, *71*, 235408/1.

(18)    Thomas, K. G.; Barazzouk, S.; Ipe, B. I.; Joseph, S. T. S.; Kamat, P. V. *J. Phys.
         Chem. B* **2004**, *108*, 13066.

(19)    Nordlander, P.; Oubre, C.; Prodan, E.; Li, K.; Stockman, M. I. *Nano Lett.* **2004**, *4*,
         899.

(20)    Fromm, D. P.; Sundaramurthy, A.; Schuck, P. J.; Kino, G.; Moerner, W. E. *Nano
         Lett.* **2004**, *4*, 957.

(21)    Elghanian, R.; Storhoff, J. J.; Mucic, R. C.; Letsinger, R. L.; Mirkin, C. A.
         *Science* **1997**, *277*, 1078.

(22)    Storhoff, J. J.; Lazarides, A. A.; Mucic, R. C.; Mirkin, C. A.; Letsinger, R. L.;
         Schatz, G. C. *J. Am. Chem. Soc.* **2000**, *122*, 4640.

(23)    Jain, P. K.; Qian, W.; El-Sayed, M. A. *J. Phys. Chem. B* **2006**, *110*, 136.

(24)    Mirkin, C. A. *Inorg. Chem.* **2000**, *39*, 2258.

(25)    Hao, E.; Schatz George, C. *J. Chem. Phys.* **2004**, *120*, 357.

(26)    Nie, S.; Emory, S. R. *Science* **1997**, *275*, 1102.

(27)    Kneipp, K.; Wang, Y.; Kneipp, H.; Itzkan, I.; Dasari, R. R.; Feld, M. S. *Phys.
         Rev. Lett.* **1996**, *76*, 2444.

(28)    Michaels, A. M.; Jiang, J.; Brus, L. *J. Phys. Chem. B* **2000**, *104*, 11965.

(29)    Sonnichsen, C.; Reinhard, B. M.; Liphardt, J.; Alivisatos, A. P. *Nat. Biotechnol.* **2005**, *23*, 741.

(30)    Jain, P. K.; Huang, W.; El-Sayed, M. A. *Nano Lett.* **2007**, *7*, 2080.

(31)    Rechberger, W.; Hohenau, A.; Leitner, A.; Krenn, J. R.; Lamprecht, B.; Aussenegg, F. R. *Opt. Commun.* **2003**, *220*, 137.

(32)    Reinhard, B. M.; M. Siu; Agarwal, H.; Alivisatos, A. P.; Liphardt, J. *Nano Lett.* **2005**, *5*, 2246.

(33)    Reinhard, B.; Sheikholeslami, S.; Mastroianni, A.; Alivisatos, A. P.; Liphardt, J. *Proc. Natl. Acad. Sci., USA* **2007**, *104*, 2667.

(34)    Oldenburg, S. J.; Averitt, R. D.; Westcott, S. L.; Halas, N. J. *Chem. Phys. Lett.* **1998**, *28*, 243.

(35)    Prodan, E.; Radloff, C.; Halas, N. J.; Nordlander, P. *Science* **2003**, *302*, 419.

(36)    Jain, P. K.; El-Sayed, M. A. *Nano Lett.* **2007**, *7*, 2854.

(37)    Jain, P. K.; El-Sayed, M. A. *J. Phys. Chem. C* **2007**, *111*, 17451.

(38)    Draine, B. T.; Flatau, P. J. *J. Opt. Soc. Am. A* **1994**, *11*, 1491.

(39)    Lee, K.-S.; El-Sayed, M. A. *J. Phys. Chem. B* **2005**, *109*, 20331.

(40)    Huang, W.; Qian, W.; Jain, P. K.; El-Sayed, M. A. *Nano Lett.* **2007**, *7*, 3227.

(41)    Gans, R. *Ann. Phys.* **1915**, *47*, 270.

(42)    Link, S.; Mohamed, M. B.; El-Sayed, M. A. *J. Phys. Chem. B* **1999**, *103*, 3073 and Erratum: *J. Phys. Chem. B* **2003**, *109*, 10531.

(43)    Murphy, C. J.; Sau, T. K.; Gole, A. M.; Orendorff, C. J.; Gao, J.; Gou, L.; Hunyadi, S. E.; Li, T. *J. Phys. Chem. B* **2005**, *109*, 13857.

(44)    Wiley, B. J.; Chen, Y.; McLellan, J. M.; Xiong, Y.; Li, Z.-Y.; Ginger, D.; Xia, Y. *Nano Lett.* **2007**, *7*, 1032.

(45)    Aizpurua, J.; Bryant, G. W.; Richter, L. J.; Garcia de Abajo, F. J.; Kelley, B. K.; Mallouk, T. *Phys. Rev. B* **2005**, *71*, 235420/1.

(46)    Onuta, T.-D.; Waegele, M.; DuFort, C. C.; Schaich, W. L.; Dragnea, B. *Nano Lett.* **2007**, *3*, 557.

(47)    Nikoobakht, B.; El-Sayed, M. A. *J. Phys. Chem. A* **2003**, *107*, 3372.

(48)    Note that we have used in all our analyses a lower bound of 0.1 on the separation-to-size ratio for consistency with current and previous studies.

(49)    Wei, Q.-H.; Su, K.-H.; Durant, S.; Zhang, X. *Nano Lett.* **2004**, *4*, 1067.

(50)    Dahmen, C.; Schmidt, B.; von Plessen, G. *Nano Lett.* **2007**, *7*, 318.

(51)    Lamprecht, B.; Schider, G.; Lechner, R. T.; Ditlbacher, H.; Krenn, J. R.; Leitner, A.; Aussenegg, F. R. *Phys. Rev. Lett.* **2000**, *84*, 4721.

(52)    Haynes, C. L.; McFarland, A. D.; Zhao, L.; Van Duyne, R. P.; Schatz, G. C.; Gunnarsson, L.; Prikulis, J.; Kasemo, B.; Käll, M. *J. Phys. Chem. B* **2003**, *107*, 7337.

(53)    Sudeep, P. K.; Joseph, S. T. S.; Thomas, K. G. *J. Am. Chem. Soc.* **2005**, *127*, 6516.

# CHAPTER 9

# ULTRAFAST COOLING OF PHOTOEXCITED ELECTRONS IN GOLD-NANOPARTICLE-THIOLATED DNA CONJUGATES INVOLVES THE DISSOCIATION OF THE GOLD-THIOL BOND

## Abstract

Using UV-visible extinction spectroscopy and femtosecond pump-probe transient absorption spectroscopy, we have studied the effect of femtosecond laser heating on gold nanoparticles attached to DNA ligands via thiol groups. It is found that femtosecond pulse excitation of the thiolated DNA-modified nanoparticles at a wavelength of 400 nm leads to desorption of the thiol ligands from the nanoparticle surface by the dissociation of the gold-sulfur bond. The laser-initiated gold-sulfur bond-breaking process is a new pathway for nonradiative relaxation of the optically excited electrons within the thiol-modified gold nanoparticles, as manifested by a faster decay rate of the excited electronic distribution at progressively higher laser pulse energies. Based on the experimental observations, we suggest a bond dissociation mechanism involving the coupling between the photoexcited electrons of the nanoparticles and the gold-sulfur bond vibrations over one involving the conventional phonon-phonon thermal heating processes.

## 9.1 Introduction

Noble metal nanoparticles are fascinating materials with great nanotechnological potential due to their unique and strongly size-dependent electronic, optical, physical, and chemical properties.[1,2] Additionally, the surfaces of nanoparticles can be easily functionalized with various organic and biomolecular ligands, among which the molecules with a sulfur head-group are attracting considerable interest.[3] The strong affinity of sulfur to gold has been exploited to form molecular contacts, to link other species to the gold surface, or to form well-ordered self-assembled monolayers (SAMs)[4] for applications like surface patterning[5] and molecular electronics.[6] In the case of biomolecules, sulfur-containing cysteine and cystine amino acids, often found on the border of large proteins, have been employed to anchor proteins to gold nanoparticles, thus imparting the nanoparticles with essential biochemical functions like targeting, biocompatibility, etc.[7] Recent strategies[8,9] have employed alkanethiol-capped DNA oligonucleotides to link gold nanoparticle building blocks to form periodic functional assemblies, in addition to serving as efficient DNA detection schemes.

Recently, an interesting application of gold nanoparticles has emerged − as antennae for remote control of the activity of biomolecules bound to their surface. For instance, radio wave field-based induction heating of gold nanocrystals linked to DNA oligonucleotides in solution has recently been shown to dehybridize the DNA in a manner that is both reversible and specific.[10] More recently, research from our group has demonstrated the promising use of gold nanoparticles in spectroscopic and optical imaging-based cancer diagnostics,[11] as well as in immunotargeted laser photothermal cancer therapy.[12] This work was based on the surface plasmon enhancement of both

absorption and scattering of gold nanoparticles. The observed tumor therapy is a result of the fact that the strongly enhanced absorption of light by immunotargeted gold nanoparticles is rapidly converted to heat on the picosecond time domain,[13] resulting in the heating of the neighboring cell surface, ultimately leading to cell death. It is thus obvious that the light absorbed by the gold nanoparticles is transferred to the antibody molecules and the cell environment by rapid electron-phonon relaxation in the nanoparticle followed by phonon-phonon relaxation,[13] resulting in an increase in the temperature of the cells.[14]

In the present study, we aim to examine the rate, efficiency, and mechanism by which the light energy absorbed by gold nanoparticles is transferred to thiolated DNA ligands conjugated to the surface of the nanoparticle. Due to their very high surface-to-volume ratios, nanoparticles are expected to show unique surface or interface effects[15] in their interaction with light and their photothermal properties. In correlation with surface or interfacial phenomena, the predominant role of non-equilibrium electrons in driving the most basic reactions, such as desorption, dissociation, or motion of molecules on metal surfaces, has been recently established.[16,17] To study similar phenomena in metal nanoparticles, the demonstrated ability of femtosecond pulse excitation to create non-equilibrium conditions[18] can be employed, and thus the mechanism of nonradiative dynamical processes occurring on the nanoparticle surface can be determined.

We employ UV-visible extinction spectroscopy and femtosecond pump-probe transient absorption spectroscopy to study the effect of photothermal heating of gold nanoparticles with surfaces modified by thiolated DNA. It is found that femtosecond pulse excitation of the nanoparticle-thiol conjugates initiated the cleavage of the surface

246

gold-sulfur bond. Femtosecond transient absorption spectroscopy further revealed that bond-breaking serves as an additional mechanism for the relaxation of the optically excited electrons in the nanoparticle. The evolution of the bond-breaking can thus be indirectly followed in time by using ultrafast pump-probe transient absorption spectroscopy of the nanoparticles. The experimental results suggest that the surface bond dissociation does not result from a pure thermal heating of the irradiated nanoparticles resulting from phonon-phonon relaxation processes, but rather results from an ultrafast process driven by hot electrons of the nanoparticles.

## 9.2 Experimental Methods

### 9.2.1 Synthesis of Thiolated DNA-Modified Gold Nanoparticles

Gold nanoparticles (av diameter 13.1 nm) were prepared by the citrate reduction of chloroauric acid.[19] A self-assembled monolayer (SAM) of thiolated ss-DNA was formed on the surface of the gold nanoparticles by well-established procedures.[20] Typically, 2.4 nmol of purified 5′-SH-CH2-CH2-CH2-CGC-ATT-CAG-GAT-3′ (Integrated DNA Technologies Inc.) was added to 1 mL of ~11 nM gold nanoparticle solution. After 24 h, the solution was brought to 0.1 M NaCl concentration and allowed to stand at room temperature for a further 40 h. The solution was then centrifuged at 12 400 rpm for 30 min. The supernatant was removed, and the reddish pellets at the bottom of the tube were dispersed in 1 mL of 0.1 M NaCl, 10 mM sodium phosphate buffer (pH 7) solution. This procedure was repeated, and the pellets at the bottom of the centrifuge tube were dispersed in 0.3 M NaCl, 10 mM sodium phosphate buffer (pH 7). The

247

synthesized nanoparticle conjugates were characterized by UV-visible extinction (300-800 nm) on a Shimadzu UV-3101-PC spectrophotometer in transmission mode.

## 9.2.2 Femtosecond Pulse Heating of Thiolated DNA-Modified Gold Nanoparticles

A frequency-doubled Nd:vanadate laser (Coherent Verdi) was used as the pump for the Ti:sapphire laser system (Clark MXR CPA 1000), which generated laser pulses of 100 fs duration (fwhm) with energy of 1 mJ at 800 nm at a repetition rate of 1 kHz. The pump beam was mechanically chopped with a light beam chopper (HMS 221). The second harmonic of the 800 nm fundamental at 400 nm was used for the optical heating of the DNA-modified gold nanoparticle solution placed in an optical cell (path length = 2 mm), kept under constant stirring. The diameter of the laser focus spot on the sample was 100 μm. The laser pump pulse energy used in the experiments was reduced to less than 250 nJ with neutral density filters. The solution was irradiated with various pulse energies ranging from 150 nJ/pulse to 24 μJ/pulse, for successive periods of 5 min each. The effect of optical heating on the sample was monitored by obtaining the UV-visible extinction at each pulse energy.

## 9.2.3 Femtosecond Electron Relaxation Dynamics of Thiolated DNA-Modified Gold Nanoparticles

Bigot et al.[21] and Melinger et al.[22] have already shown, using femtosecond pump-probe spectroscopy, the effect of the surrounding/embedding medium on the ultrafast electron relaxation dynamics in noble metal nanoparticles. To study the effect of the thiol modification of the gold nanoparticle surface on the electron relaxation dynamics, we employed femtosecond transient absorption spectroscopy.[23] In our work, 100 fs pulses (fwhm) at 400 nm (which were used for the optical heating) were used as the excitation

source (pump). A white-light continuum, generated by focusing a small portion (4%) of the 800 nm fundamental beam of the Ti:sapphire laser onto a 1 mm sapphire plate, was used to probe the transient absorption of the sample at various delay times (t). The differential transmission signal S(t) was recorded with a pair of silicon photodiodes (Thorlab) and a lock-in amplifier (Stanford Research Systems). The recorded signal S(t) can be expressed as:

$$S(\lambda, t) = \Delta T/T = (I_{\lambda, t} - I_{\lambda, 0})/I_{\lambda, 0} \quad (1)$$

where $\Delta T/T$ is the % change in the transmission of probe light, $I_{\lambda, t}$ is the intensity of the probe light at wavelength $\lambda$ after a delay time t from the pump laser heating pulse, and $I_{\lambda, 0}$ is the intensity of the probe light at $\lambda$ without the pump. As a result, the recorded signal $S(\lambda, t)$ represents a transient bleach, which results from the optical excitation of the free electron distribution within the nanoparticles. Following this procedure, the electron relaxation dynamics of thiolated DNA-modified gold nanoparticles was measured for different pump pulse energies ranging from 30 to 900 nJ/pulse (low fluence regime) and compared with the dynamics in unmodified gold nanoparticles under similar aqueous solution conditions. The probe wavelength was set at the absorption maximum for both samples. The concentrations of the thiol modified and unmodified nanoparticle solutions were adjusted such that both solutions had a similar absorbance at the pump wavelength, i.e., 400 nm, in order to ensure similar hot electron excitation in both samples and thus enable comparison of their electron relaxation dynamics.

## 9.3 Results and Discussion

### 9.3.1 UV-vis Extinction of Thiolated DNA-Modified Gold Nanoparticles

The UV-vis extinction spectra (300-800 nm) of thiolated DNA-modified gold nanoparticles and unmodified gold nanoparticles are shown in Figure 9.1. As evidenced

Figure 9.1: UV-Visible extinction spectrum of DNA-modified ~13 nm Au NPs (red) and
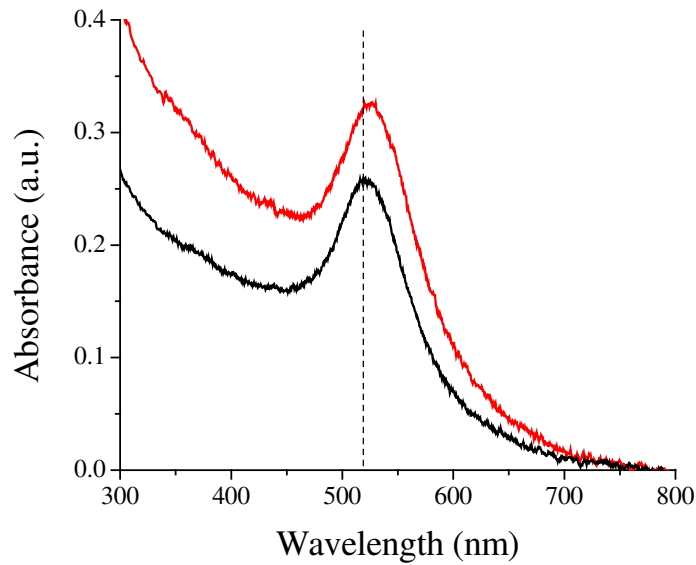


unmodified ~13 nm gold nanoparticles (black) in the wavelength range 300-800 nm. The optical path length was 2 mm. The dashed black line is a guide to the eye, representing the extinction maximum at 519 nm for the unmodified gold nanoparticles.

by the spectra, the formation of a SAM of thiolated DNA on the gold nanoparticle surface

by gold-sulfur bonding caused a shift in the surface plasmon absorption peak from 519 to

525 nm. Surface plasmon absorption properties are generally discussed within the

framework of the Drude model,[24] according to which the plasmon peak position ($\lambda_{sp}$)

depends on the dielectric constant of the surrounding medium ($\varepsilon_m$), as governed by:

$$\lambda_{sp}^{2} = \lambda_{p}^{2}(\varepsilon_\infty + 2\varepsilon_m) \quad (2)$$

where $\varepsilon_\infty$ is the high frequency dielectric constant of gold due to interband and core transitions. $\lambda_p$ is the bulk plasmon frequency of gold given by the following relation:

$$\lambda_p = 2\pi c/(Ne^2/m_e\varepsilon_0)^{1/2} \quad (3)$$

where $\varepsilon_0$ is the permittivity in vacuum, c is the speed of light in vacuum, e is the electronic charge, N is the density of free electrons in the nanoparticle and $m_e$ is the effective mass of the electron. The red-shift in the plasmon wavelength resulting from the formation of the SAM can thus be attributed to a local increase in the medium refractive index as a result of the thiols[25] or to a change in the free electron density of the gold nanoparticle due to the strong surface coupling with sulfur.[26] Such shifts in the plasmon absorption maximum have been commonly employed in surface plasmon resonance (SPR)-based sensing of analytes.[27]

## 9.3.2 Femtosecond Pulse Heating of Thiolated DNA-Modified Gold Nanoparticles

Figure 9.2 shows the UV-visible extinction of the femtosecond pulse irradiated DNA-modified gold nanoparticle solution after 5 min heating periods at different pulse energies ranging from 150 nJ/pulse to 24 µJ/pulse. The figure shows that excitation of the thiolated DNA-modified gold nanoparticles with femtosecond pulses of increasing energy up to 2.74 µJ/pulse results in a gradual blue-shift in their plasmon extinction maximum from 525 to 519 nm, which is the plasmon maximum for unmodified gold nanoparticles (indicated by the dashed black line). This suggests that laser photothermal heating of the thiolated DNA-modified gold nanoparticles results in the dissociation of the gold-sulfur bond between the thiolated DNA strand and the nanoparticle surface. As shown in Figure 9.2 and the inset, the extent of the blue-shift (and thus the suggested
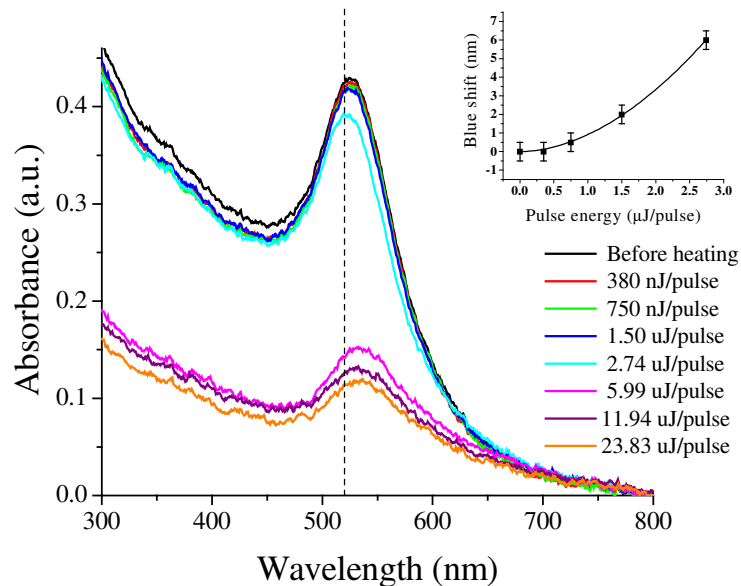
Figure 9.2: UV-Visible extinction (300-800 nm) of thiolated DNA-modified gold nanoparticles after heating with 100 fs 400 nm pulses for successive 5 minute periods at pulse energy of 380 nJ/pulse, 750 nJ/pulse, 1.50 μJ/pulse, 2.74 μJ/pulse, 5.99 μJ/pulse, 11.94 μJ/pulse and 23.83 μJ/pulse. The optical path length was 2 mm. The dashed black line is a guide to the eye, representing the extinction maximum at 519 nm for unmodified gold nanoparticles. The inset shows the blue shift of the absorption maximum from an initial wavelength of 525 nm, versus the excitation pulse energy up to 2.74 μJ/pulse. The solid black curve in the inset is a power law fit (R = 0.9995) to the data points, given by y $\alpha$ $x^{1.87 \pm 0.08}$. Error in estimating the blue shift is 0.5 nm based on the step size in the absorbance scan.

bond dissociation) increases super-linearly with increasing excitation pulse energy. Higher optical pumping powers finally gave rise to a red-shifted, broadened, and diminished absorption. In other words, the nanoparticles finally aggregate when there are not enough surface ligands to stabilize/passivate the nanoparticles in solution, thus resulting in the broadened and diminished absorption and bluish-purple precipitation of gold metal observed on the sides of the optical cell. The observed blue-shift on femtosecond excitation was fairly reproducible for three separate experimental batches (having similar absorbance at the excitation wavelength of 400 nm). The pulse energies at

which the maximum blue-shift was observed were similar, ~3 µJ/pulse for the different

batches. Figure 9.3 shows a plot of the observed blue-shift in the plasmon maximum with

the absorbed laser energy, based on data obtained from the different batches.

Figure 9.4 shows similar blue-shift of the surface plasmon maximum of ~13 nm

gold nanoparticles capped with mercaptoacetic acid (HS-CH$_2$COOH) on laser irradiation

using 100 fs pulses. Note that the formation of the SAM of mercaptoacetic acid on the

gold nanoparticle surface via gold-sulfur bonds shifts the extinction maximum from 519
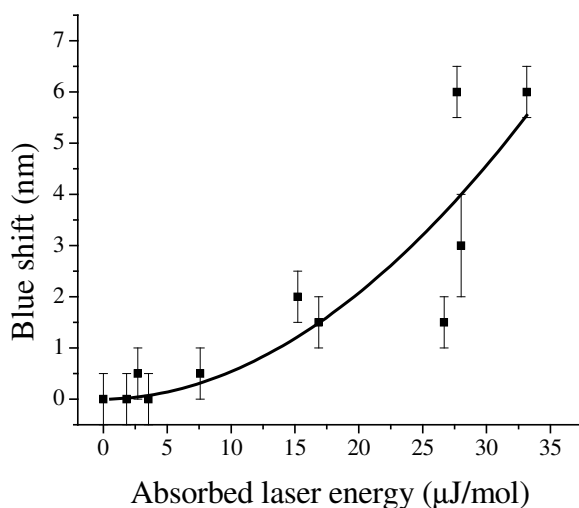


Figure 9.3: The observed blue shift (nm) of the plasmon maximum versus the absorbed laser energy (µJ/mole). The data was obtained from three different batches of thiolated DNA-modified gold nanoparticles. The absorbed laser energy was calculated per mole of the nanoparticles in solution using the incident pulse energy in µJ/pulse, the solution absorbance at the excitation wavelength of 400 nm, the irradiation time of 5 min at each pulse energy and the nanoparticle concentration in solution. The solid black curve is a power law fit (R = 0.8718) to the data points, given by y $\alpha$ x$^{1.95 \pm 0.80}$. Error in estimating the blue shift is based on the step size in the absorbance scan.
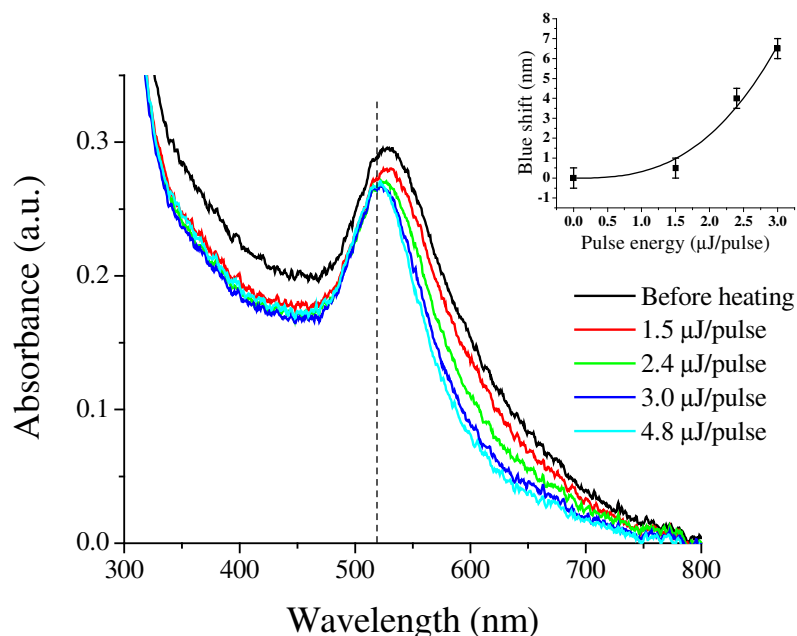
Figure 9.4: UV-Visible extinction (300-800 nm) of mercaptoacetic acid-modified gold nanoparticles after heating with 100 fs 400 nm pulses for successive 5 minute periods at pulse energy of 1.5 μJ/pulse, 2.4 μJ/pulse nJ/pulse, 3.0 μJ/pulse and 4.8 μJ/pulse. The optical path length was 2 mm. The dashed black line is a guide to the eye, representing the extinction maximum at 519 nm for unmodified gold nanoparticles. The inset shows the blue shift of the absorption maximum from an initial wavelength of 528 nm, versus the excitation pulse energy up to 3 μJ/pulse. The solid black curve in the inset is a power law fit (R = 0.9883) to the data points, given by y α $x^{2.76 \pm 0.69}$. Error in estimating the blue shift is 0.5 nm based on the step size in the absorbance scan.

nm for unmodified nanoparticles to 528 nm for the thiol-modified nanoparticles, the shift thus being larger than that in case of the thiolated DNA modification, possibly due to a tighter SAM for mercaptoacetic acid molecules. The SAM formation also leads to an observable broadening of the plasmon band of the nanoparticles, as attributed commonly to chemical interface damping.[2,28-30] Thus, on femtosecond pulse irradiation up to 3 μJ/pulse (Figure 9.4 and inset), the resulting blue-shift of the plasmon maximum from 528 to 521.5 nm, as well as the decrease in the plasmon band fwhm from ~140 to ~100

nm, is clearly attributable to the gold-sulfur bond dissociation on the nanoparticle surface. Similar gold-sulfur bond dissociation in alkanethiolate SAMs on gold surfaces by STM-induced excitation and electron beam irradiation has been reported by Avouris et al.[31] and Chen et al.,[32] respectively.

### 9.3.3 Femtosecond Electron Relaxation Dynamics in DNA-Modified Gold Nanoparticles

Figure 9.5 shows a comparison of the transient bleaching dynamics of DNA-modified gold nanoparticles with unmodified gold nanoparticles for pump pulse energy ranging from 30 to 900 nJ/pulse. It is well known that the rise of the transient bleach signal is a result of electron-electron scattering within the nanoparticles, while the decay can be directly related to the dynamics of relaxation of excited/hot electrons by the process of electron-phonon coupling on the time scale of ~1 ps and phonon-phonon coupling on longer time scales of ~100 ps.[13] The rise and decay were fit to an exponential function[33] of the form $(1-\exp(-t/\tau_r)).\exp(-t/\tau_d)$, so as to obtain the rise $\tau_r$ (ps) and decay time or the hot electron lifetime $\tau_d$ (ps).

It can be seen from Figure 9.5 that, at a lower value of the pulse energy (38 nJ/pulse), the hot electron lifetimes of the DNA-modified gold nanoparticles ($\tau_d'' = 1.04 \pm 0.04$ ps) and the unmodified gold nanoparticles ($\tau_d' = 1.10 \pm 0.04$ ps) are similar. At progressively higher pulse energies, the electron relaxation in both DNA-modified and unmodified nanoparticles becomes slower as a result of the linear increase of the electronic heat capacity with the hot electron temperature.[34] However, with higher pulse

a)                                      b)

Pulse energy = 38 nj/pulse



$\tau'_d = $ 1.10 +/- 0.04 ps

$\tau''_d = $ 1.04 +/- 0.04 ps

Pulse energy = 119 nj/pulse



$\tau'_d = $ 1.98 +/- 0.08 ps

$\tau''_d = $ 1.73 +/- 0.07 ps

Pulse energy = 378 nj/pulse



$\tau'_d = $ 4.30 +/- 0.22 ps

$\tau''_d = $ 3.44 +/- 0.16 ps

Pulse energy = 864 nj/pulse



$\tau'_d = $ 9.16 +/- 1.13 ps

$\tau''_d = $ 7.39 +/- 0.84 ps
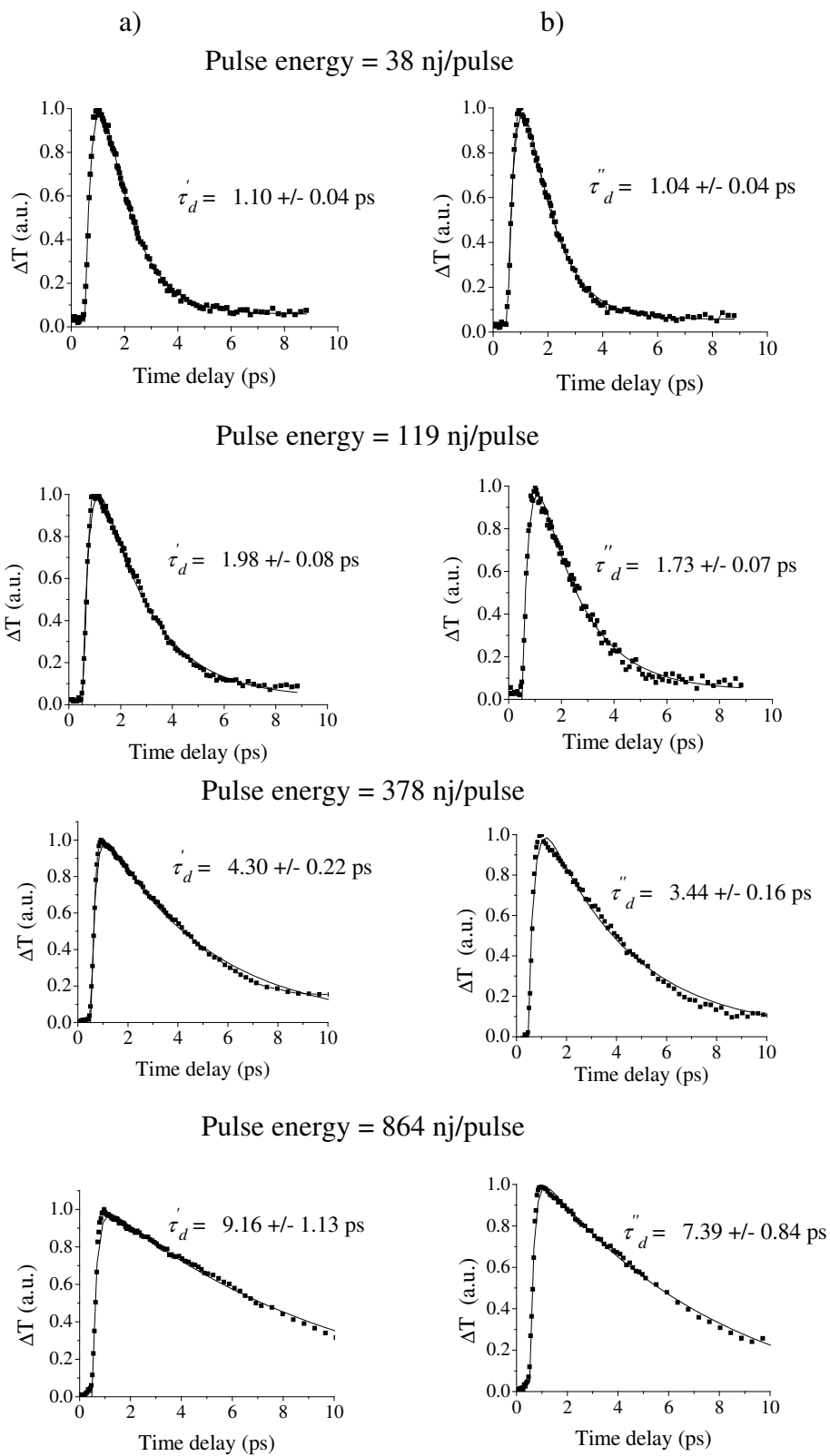
Figure 9.5: Femtosecond transient bleaching in (a) unmodified gold nanoparticles and (b) thiolated DNA-modified gold nanoparticles, pumped with 100 fs 400 nm pulses at an energy of 38 nJ/pulse, 119 nJ/pulse, 378 nJ/pulse and 864 nJ/pulse, and probed at their respective absorption maximum. The rise and decay of the transient bleaching are fit to the exponential function $(1-\exp(-t/\tau_r)).\exp(-t/\tau_d)$ to obtain the hot electron relaxation time $\tau_d{}'$ in unmodified gold nanoparticles and $\tau_d{}''$ in DNA-modified gold nanoparticles. The error bars in the hot electron relaxation times are obtained from the fitting.

energy, the electron relaxation rate in DNA-modified nanoparticles gets progressively faster than that in unmodified nanoparticles. As can be seen from the previous section, the femtosecond pulse excitation of the nanoparticle electrons initiates cleavage of the gold-sulfur bond; the extent of this bond-breaking process increases with increasing pump energy. Since a part of the energy of the hot electrons is utilized in the bond-breaking, an additional pathway is opened up for the electron energy relaxation in the DNA-modified nanoparticles. The electron relaxation in DNA-modified nanoparticles as compared to that in the unmodified nanoparticles is therefore progressively faster at progressively higher input pulse energies.

It is conceivable that the presence of the thiolated DNA ligands around the gold nanoparticle enhances the electronic relaxation of the latter. In other words, energy can be transferred to the DNA ligands, leading to an increase in the nanoparticle relaxation rate, and this energy can be used for the dissociation of the gold-sulfur bond on a later time scale. However, due to the large density of vibrational states in the DNA ligands, it would be unlikely for this transferred energy to be later localized in the gold-sulfur bond, leading to the dissociation. Hence, we believe that direct coupling between the hot electrons and the gold-sulfur bond is responsible for the bond-breaking process. Besides, the pulse energy dependence of the hot electron relaxation dynamics can be best

explained by the femtosecond pulse-initiated dissociation of the gold-sulfur bond. The bond dissociation process could be indirectly followed in time by monitoring the ultrafast electron dynamics by using the femtosecond transient absorption spectroscopy. The gold-sulfur bond-breaking cannot be attributed to a conventional thermal heating of the irradiated nanoparticles. Conventional heating takes place by phonon-phonon relaxation which occurs on a much longer time scale, typically ~100 ps.[13] The occurrence of bond-breaking on the electron-phonon coupling time scale (typically within ~1 ps for gold) suggests a hot-electron-initiated process rather than one that involves a phonon heat bath as the energy source. It has also been established recently that the non-equilibrium between electrons and phonons created by ultra-short pulse excitation generally favors non-conventional electron-mediated reaction pathways.[35]

## 9.3.4 Temporal Dynamics of the Bond-Breaking Process

A mechanism of desorption of ligands from a metal substrate, driven by highly excited local surface vibrational modes (surface phonons or metal-adsorbate bond vibrations) thermally equilibrated with hot electrons, has been proposed in surface science.[36] The rate of desorption by such a mechanism is expected to go as $\exp(-E_d/k_bT_e)$,[37] where $E_d$ is the activation barrier for the metal-adsorbate bond dissociation and $T_e$ is the temperature of the hot electron bath. To verify the presence of such a mechanism, we modeled the time evolution of the laser-initiated bond-breaking in terms of the electron relaxation dynamics in the nanoparticles. The dynamics of the electron relaxation process in gold nanoparticles is generally described by the two-temperature model (TTM)[38] as:

$$c_e \frac{dT_e}{dt} = -G(T_e - T_l) \quad (4)$$

where $c_e$ is the electronic heat capacity ($c_e = 66T_e$ $Jm^{-3}K^{-1}$),[27] $T_e$ is the electronic temperature (K), $T_l$ is the lattice temperature (K), t represents the time (s), G is the electron-phonon coupling constant ($Wm^{-3}K^{-1}$), and the temporal profile of the pulse and the thermal conduction term[39] have been neglected in the equation. We further modified the TTM model for the DNA-modified particles by incorporating the additional relaxation pathway due to the bond-breaking process (assumed first-order) as:

$$c_e \frac{dT_e}{dt} = -G(T_e - T_l) - R(T_e)\Delta H \quad (5)$$

$$R(T_e) = k(T_e)[Au - S] \quad (6)$$

where $\Delta H$ is the enthalpy for the gold-sulfur bond dissociation (155 kJ.mol^{-1}),[40] R is the rate of gold-sulfur bond dissociation ($mol.m^{-3}s^{-1}$), k is the first-order rate constant of gold-sulfur bond-breaking ($s^{-1}$), and [Au-S] is the gold-sulfur bond concentration (~300 $mol.m^{-3}$). Thus, this simple model based on eqs 4-6 incorporates two experimental trends: first, the electron-phonon relaxation dynamics getting slower in both DNA-modified and unmodified nanoparticles at higher powers due to the dependence of the electronic heat capacity on the pulse power ($c_e = 66T_e$), and second, the additional energy relaxation channel due to the bond-breaking in DNA-modified nanoparticles increasing in contribution with higher pulse energies ($k = f(T_e)$). The first-order decay dynamics in the unmodified nanoparticles can be described as $T_e = T_{e,0}\exp(-t/\tau_d')$ and hence:

$$\frac{dT_e}{dt} = -\frac{T_e}{\tau_d'} \quad (7)$$

where $T_{e,0}$ is the peak electronic temperature. Similarly for DNA-modified nanoparticles,

$$\frac{dT_e}{dt} = -\frac{T_e}{\tau_d''} \quad (8)$$

Substituting eqs 7 and 8 in eqs 4 and 5 respectively, subtracting eq 5 from eq 4, and using eq 6,

$$k(T_e) = \frac{c_e T_e}{[Au - S]\Delta H}\left(\frac{1}{\tau_d''} - \frac{1}{\tau_d'}\right) \quad (9)$$

Using the dependence of the electronic heat capacity on the electronic temperature for gold ($c_e = 66T_e$ $Jm^{-3}K^{-1}$), substituting the values of $\Delta H$ and [Au-S], the bond dissociation rate constant k at the peak electronic temperature can be obtained as:

$$k = \frac{1.47\times10^{-6}T_{e,0}^2}{\tau_{bb}} \quad (10)$$

$$\text{where} \qquad \tau_{bb} = \left(\frac{1}{\tau_d''} - \frac{1}{\tau_d'}\right)^{-1} \quad (11)$$

can be viewed as the time constant for the bond dissociation process and can be calculated from the experimental hot electron lifetimes for the two different samples obtained from Figure 9.5. The peak electronic temperatures were calculated for different pulse energies as per the method in an earlier reference.[41] The calculated rate constants k have been plotted against the pulse energy in Figure 9.6a. The plot of the calculated bond-breaking rate constant k with the pulse energy shows a super-linear trend, similar to the plot of the blue-shift of the surface plasmon absorption versus the laser pulse energy. The super-linear dependence ($y \propto x^{1.43}$) of the bond dissociation rate constant on the pulse energy eliminates the possibility of direct one-photon electronic excitation of the thiol adsorbate. Figure 9.6b shows a plot of $\ln(hk/k_bT_e)$ versus $1/T_e$, which demonstrates

a)                                         b)
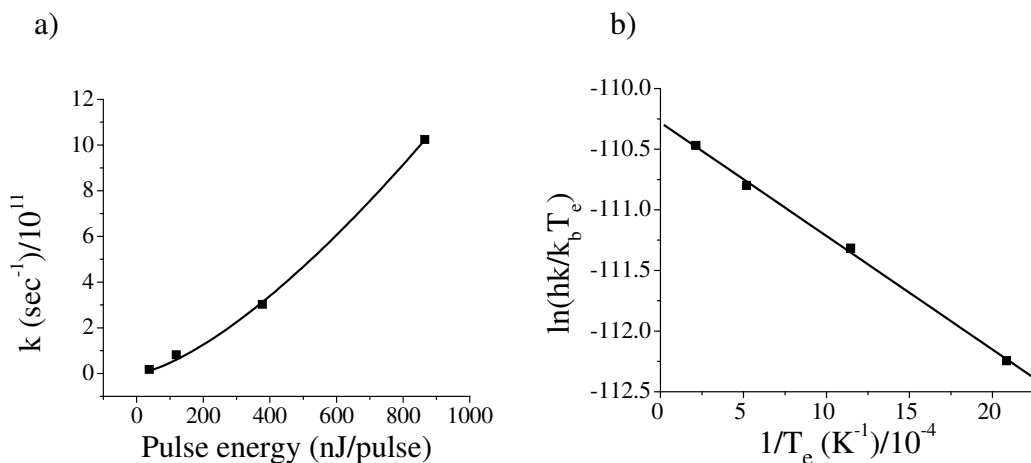


Figure 9.6: (a) Plot of the calculated gold-sulfur bond-breaking rate constant k $(\text{sec}^{-1})/10^{11}$ against the excitation pulse energy (nJ/pulse). The curve is a power law fit (R = 0.9995) to the experimental data having a form y $\alpha$ $x^{1.43\,\pm\,0.06}$. (b) Eyring plot of $\ln(hk/k_b T_e)$ versus $1/T_e$ $(\text{K}^{-1})/10^{-4}$. The solid line is a straight line fit (R = - 0.9992) to the data given by y = -936.5x –110.3 yielding $\Delta H_d/R$ = 0.9365 K and $\Delta S_d/R$ = -0.1103

that the estimated kinetics of the bond-breaking satisfies the activated Eyring rate process with respect to the electronic temperature $T_e$. In other words, k $\propto$ exp($-E_d/k_b T_e$). This strongly supports hot-electron-initiated cleavage of the gold-sulfur bonds. The activation energy $E_d$ for the dissociation (with respect to an electronic temperature) is calculated to be 10.3 $\text{kJ.mol}^{-1}$ (0.1 eV) from the Eyring plot. A previous measurement by Ramachandran et al.,[40] based on conductivity switching in thiol SAMs on a gold surface, yielded a similar value. The low activation barrier of 0.1 eV (as compared to the gold-sulfur bond dissociation energy of 1.6 eV) has been suggested to be a consequence of weakened bonds between gold atoms attached to the sulfur and neighboring gold atoms.[42]

A hot-electron-initiated bond dissociation mechanism involving the population of anti-bonding states of metal-adsorbate bonds lying above the metal Fermi level by

excited conduction electrons is well known in the literature[43] and may explain the trend of k with the excitation pulse energy. However, the anti-bonding orbital of the gold-sulfur bond has been calculated to be 0.64 eV below the Fermi level of gold.[44] Nevertheless, the orbital energy distribution for the gold-sulfur bond may not be known well enough to eliminate such a mechanism. Alternatively, surface phonons of the nanoparticle initiated by the hot electrons may also drive dissociation by weakening the surface-ligand bonds through vibrations.[45,46]

### 9.3.5 Efficiency of the Laser-Initiated Bond-Breaking Process

The thermodynamic efficiency of the laser-initiated bond-breaking process ($\eta$) can be calculated as

$$\eta = W/Q \quad (12)$$

where Q is the absorbed laser energy and W is the amount of energy required to break all the gold-sulfur bonds within the optical cell of volume 0.63 $cm^3$. On the basis of an optical density of 0.42 for the sample (i.e., a gold nanoparticle concentration of 7.8 nM) and a bond dissociation energy of 155 x $10^3$ J $mol^{-1}$ for the gold-sulfur bond, and assuming 220 DNA strands per ~13 nm nanoparticle,[47] W is estimated to be 0.17 mJ. Figure 9.2 indicates that the maximum blue-shift (and thus the maximum gold-sulfur bond dissociation) occurs at a pulse energy of ~3 $\mu$J/pulse, or an absorbed energy of 1.46 $\mu$J/pulse based on an absorbance of 0.29 at 400 nm. For this pulse energy and a pulse repetition rate of 1 kHz, the laser energy Q absorbed by the solution in the 5 min irradiation time was estimated to be 0.44 J. Consequently, an upper limit on the efficiency $\eta$ at this pulse energy is calculated to be ~4 x $10^{-4}$. Insight into the low value of

this efficiency can be obtained by analyzing the mechanism of the hot electron relaxation, the source of bond-breaking.

Relaxation of the hot electron gas in nanoparticles is believed to occur through two different channels: bulk electron-phonon interactions and electron-surface interactions.[48] The latter process occurs by coupling between the electrons and two kinds of surface phonon modes, namely acoustic and capillary surface modes. Thus, the effective electron-phonon coupling constant is determined by summing the different contributions:

$$G_{eff} = G_{bulk} + G_a + G_c \quad (13)$$

where $G_{bulk}$ is the bulk contribution, measured to be ~2.95 x $10^{16}$ W m$^{-3}$K$^{-1}$ by Groenveld et al.[49] $G_a$ and $G_c$ stand for the acoustic and capillary surface mode coupling terms, respectively, given by Belotskii et al.[48] as:

$$G_c = \left(\frac{3}{16\pi}\right) k_B \left(\frac{\upsilon_f}{R}\right) n \left(\frac{m_e \omega_l^2}{\sigma}\right) \left(\frac{V_0}{\varphi_0}\right)^2 \quad (14)$$

$$G_a = \left(\frac{1}{16\pi}\right) k_B \left(\frac{\upsilon_f}{R^2}\right) n \left(\frac{m_e}{\rho}\right) \left(\frac{\omega_D}{c_l}\right)^2 \left(\frac{V_0}{\varphi_0}\right)^2 \quad (15)$$

where $k_b$ is Boltzmann's constant (1.38 x $10^{-23}$ J K$^{-1}$), n is the free electron density for gold (5.9 x $10^{28}$ m$^{-3}$), $m_e$ is the electron mass (9.1 x $10^{-31}$ kg), $\sigma$ is the surface tension of solid gold (2 x $10^{-3}$ N/m), $\varphi_0$ is the work function of gold (4.7 eV), $V_0$ is the Fermi energy (5.5 eV), $\upsilon_f$ is the Fermi velocity (1.4 x $10^6$ ms$^{-1}$), R is the nanoparticle radius (6.5 nm), $\omega_D$ is the Debye frequency (2.2 x $10^{13}$ s$^{-1}$), $\rho$ is the density of gold (19 300 kg m$^{-3}$), and $c_l$ is the longitudinal speed of sound in gold (3240 ms$^{-1}$). $\omega_l$ is the maximum frequency of the capillary modes,

$$\omega_l = \sqrt{\frac{\sigma}{\rho R^3} l(l-1)(l+2)} \quad (16)$$

where l is the angular momentum number corresponding to the shortest possible surface wave, which is given by the integer part of $\pi R/d$, where d is the lattice parameter for gold, i.e., 4 Å. Accordingly, the contribution of the surface modes ($G_a + G_c$) to the electronic relaxation of the ~13 nm gold nanoparticles is estimated to be 3.34 x $10^{14}$ W m$^{-3}$ K$^{-1}$, i.e., ~$10^{-2}$ times the net electron-phonon coupling constant $G_{eff}$.

The low energy efficiency of the bond-breaking process may thus be accounted for by the small contribution of the gold nanoparticle surface to the hot electron relaxation, in the case of a mechanism where surface phonon modes initiated by the photoexcited excited electrons of the nanoparticle drive the cleavage of the surface gold-sulfur bonds. There have been several studies in the past by our group[25] and others[50] to measure the contribution of surface phonon scattering in gold nanoparticles to the electron-phonon relaxation. It was found that the relaxation rate was independent of shape or size down to a nanoparticle diameter as small as 3 nm (electronic mean free path in gold is ca. 40 nm). Hartland and co-workers have shown that the contribution of electron-surface phonon scattering to the overall electron-phonon scattering cross section is very small due to the small number of valence electrons in gold (only one electron) combined with a large atomic mass.[50] However, in the present study, the hot electron energy lost to the surface modes, although small in contribution, might be detected by the dissociation of the gold-sulfur bonds on the nanoparticle surface. The resulting bond dissociation is concluded experimentally from the observed changes in the plasmon absorption as well as the increase in the transient bleach decay rate.

### 9.3.6 Comparison with Photothermal Heating of Gold Nanoparticle-Protein Conjugates

The effect of femtosecond excitation on thiolated DNA-modified gold nanoparticles is in sharp contrast to the photothermal laser heating of gold nanoparticle-protein conjugates using a simple continuous wave (cw) laser as encountered in photothermal therapy using gold nanostructures.[12,14] In case of the thiolated DNA ligands, bound covalently to the gold surface, the energy of the non-equilibrium hot electrons (generated by ultrafast excitation) is coupled into the surface gold-sulfur bonds. However, in case of the much slower cw laser heating of the protein-conjugated gold nanoparticles, energy relaxation is attained by conventional phonon-phonon cooling within the gold nanoparticles and the surrounding medium, leading to a temperature rise in the surrounding medium in proportion to the laser energy.[12,14] Moreover, the protein molecules that are held to the gold surface only by a number of non-covalent interactions[52] may not provide an adequate channel for energy dissipation of excited electrons unlike the surface-bound thiols.

## 9.4 Conclusion

We found that exposure of thiolated DNA-modified gold nanoparticles to femtosecond laser pulses led to the desorption of the thiolated DNA strands from the nanoparticle surface by breaking the gold-sulfur bond, as evidenced by the changes in the nanoparticle surface plasmon absorption band. The bond-breaking process led to an observed increase in the rate of the excited electron relaxation in the DNA-modified nanoparticles. Thus, we were able to follow the time evolution of gold-sulfur bond

dissociation by femtosecond transient absorption spectroscopy of the thiolated DNA-modified gold nanoparticles. The experimental results suggest that the rapid surface bond dissociation does not result from a pure thermal heating of the irradiated nanoparticles, but rather is initiated by the photoexcited electrons of the nanoparticle, possibly via electronic coupling to the surface gold-sulfur bond vibrations or the nanoparticle surface phonons. This additional pathway for electron relaxation in the gold nanoparticle conjugates may be related to the concept of chemical interface damping,[28-30] which results in broadening of the plasmon resonance band due to increased dephasing/damping of electrons by interaction with interface molecules. Hot-electron-mediated chemistry on metal surfaces is well established in surface science; our experimental findings extend these ideas to the realm of nanoparticles, where the surface is of the utmost importance.[11] The behavior of the covalently bound thiolated DNA ligands on exposure to femtosecond pulses is in sharp contrasted with the cw laser photothermal heating of gold nanoparticle/protein conjugates, where a local temperature rise results from the conversion of light to heat by phonon-phonon relaxation processes in the nanoparticle.

## 9.5 References

(1)    Kelly, K. L.; Coronado, E.; Zhao, L. L.; Schatz, G. C. *J. Phys. Chem. B* **2003**, *107*, 668.

(2)    Kreibig, U.; Vollmer, M. *Optical Properties of Metal Clusters*; Springer: New York, 1995.

(3)    Nuzzo, R. G.; Allara, D. L. *J. Am. Chem. Soc.* **1983**, *105*, 4481.

(4)    Ulman, A. *Chem. Rev*. **1996**, *96*, 1533.

(5)     Xia, Y.; Rogers, J. A.; Paul, K. E.; Whitesides, G. M. *Chem. Rev.* **1999**, *99*, 1823.

(6)     Joachim, C.; Gimzewski, J. K.; Aviram, A. *Nature* **2000**, *408*, 541.

(7)     Katz, E.; Willner, I. *Angew. Chem., Int. Ed.* **2004**, *43*, 6042.

(8)     Mirkin, C. A.; Letsinger, R. L.; Mucic, R. C.; Storhoff, J. J. *Nature* **1996**, *382*, 607.

(9)     Nam, J.-M.; Stoeva, S. I.; Mirkin, C. A. *J. Am. Chem. Soc.* **2004**, *126*, 5932.

(10)    Hamad-Schifferli, K.; Schwartz, J. J.; Santos, A. T.; Zhang, S.; Jacobson, J. M. *Nature* **2002**, *415*, 152.

(11)    El-Sayed, I. H.; Huang, X.; El-Sayed, M. A. *Nano Lett.* **2005**, *5*, 829.

(12)    El-Sayed, I. H.; Huang, X.; El-Sayed, M. A. *Cancer Lett.* **2006**, *239*, 129.

(13)    Link, S.; El-Sayed, M. A. *Annu. Rev. Phys. Chem.* **2003**, *54*, 331.

(14)    Huang, X.; Jain, P. K.; El-Sayed, I. H.; El-Sayed, M. A. *Photochem. Photobiol.* **2006**, *82*, 412.

(15)    Del Fatti, N.; Flytzanis, C.; Vallée, F. *Appl. Phys. B* **1999**, *68*, 433.

(16)    Petek, H.; Weida, M. J.; Nagano, H.; Ogawa, S. *Science* **2000**, *288*, 1402.

(17)    Wolf, M.; Ertl, G. *Science* **2000**, *288*, 1352.

(18)    Hodak, J. H.; Henglein, A.; Hartland, G. V. *J. Phys. Chem. B* **2000**, *104*, 9954.

(19)    Turkevich, J.; Stevenson, P. C.; Hillier, J. *Discuss. Faraday Soc.* **1951**, *11*, 55.

(20)    Mirkin, C. A.; Letsinger, R. L.; Mucic, R. C.; Storhoff, J. J. *Nature* **1996**, *382*, 607.

(21)    Bigot, J.-Y.; Halte, V.; Merle, J.-C.; Daunois, A. *Chem. Phys*. **2000**, *251*, 181.

(22)    Melinger, J. S.; Kleiman, V. D.; McMorrow, D.; Grohn, F.; Bauer, B. J.; Amis, E. *J. Phys. Chem. A*. **2003**, *107*, 3424.

(23)    Logunov, S. L.; Volkov, V. V.; Braun, M.; El-Sayed, M. A. *Proc. Natl. Acad. Sci. U.S.A*. **2001**, *98*, 8475.

(24)    Mulvaney, P. *Langmuir* **1996**, *12*, 788.

(25)    Ghosh, S. K.; Nath, S.; Kundu, S.; Esumi, K.; Pal, T. *J. Phys. Chem. B* **2004**, *108*, 13963.

(26)    Zhang, P.; Sham, T. K. *Phys. Rev. Lett*. **2003**, *90*, 245502.

(27)    Van Duyne, R. P.; Hulteen, J. C.; Treichel, D. A. *J. Chem. Phys*. **1993**, *99*, 2101.

(28)    Persson, B. N. J. *Surf. Sci*. **1993**, *283*, 1993, 153.

(29)    Hövel, H.; Fritz, S.; Hilger, A.; Kreibig, U. *Phys. Rev. B* **1993**, *48*, 18178.

(30)    Bosbach, J.; Hendrich, C.; Stietz, F.; Vartanyan, T.; Trager, F. *Phys. Rev. Lett*. **2002**, *89*, 257404.

(35)    Hamers, R. J. *Surf. Sci*. **2005**, *583*, 1.

(36)    Budde, F.; Heinz, T. F.; Kalamarides, A.; Loy, M. M. T.; Misewich, J. A. *Surf. Sci*. **1993**, *283*, 143.

(37)    Prybyla, J. A.; Tom, H. W. K.; Aumiller, G. D. *Phys. Rev. Lett*. **1992**, *68*, 503.

(38)    Sun, C. K.; Vallee, F.; Acioli, L. H.; Ippen, E. P.; Fujimoto, J. G. *Phys. Rev. B* **1994**, *50*, 15337.

(39)    Bauer, C.; Abid, J.-P.; Fermin, D.; Girault, H. H. *J. Chem. Phys*. **2004**, *19*, 15.

(40)    Ramachandran, G. K.; Hopson, T. J.; Rawlett, A. M.; Nagahara, L. A.; Primak, A.; Lindsay, S. M. *Science* **2003**, *300*, 1413.

(41)    Averitt, R. D.; Westcott, S. L.; Halas, N. J. *J. Opt. Soc. Am. B* **1999**, *16*, 1814.

(42)    Beardmore, K. M.; Kress, J. D.; Gronbech-Jensen, N.; Bishop, A. R. *Chem. Phys. Lett.* **1998**, *286*, 40.

(43)    Bonn, M.; Funk, S.; Hess, C.; Denzler, D. N.; Stampf, C.; Scheffler, M.; Wolf, M.; Ertl, G. *Science* **1999**, *285*, 1042.

(44)    Felice, R. D.; Selloni, A.; Molinari, E. *J. Phys. Chem. B* **2003**, *107*, 1151.

(45)    Trenhaile, B. R.; Antonov, V. N.; Xu, G. J.; Nakayana, K. S.; Weaver, J. H. *Surf. Sci.* **2005**, *583*, L135.

(46)    Watanabe, K.; Kato, H.; Matsumoto, Y. *Surf. Sci. Lett.* **2000**, *446*, L134.

(47)    Demers, L. M.; Mirkin, C. A.; Mucic, R. C.; Reynolds, R. A.; Letsinger, R. L.; Elghanian, R.; Viswanadham, G. *Anal. Chem.* **2000**, *72*, 5535.

(48)    Belotskii, E. D.; Tomchuk, P. M. *Int. J. Electron.* **1992**, *73*, 955.

(49)    Groenveld, R. H. M.; Sprik, R.; Lagendijk, A. *Phys. Rev. Lett.* **1990**, *64*, 784.

(50)    Hodak, J. H.; Henglein, A.; Hartland, G. V. *J. Chem. Phys.* **2000**, *112*, 5942.

(51)    Hirsch, L. R.; Stafford, R. J.; Bankson, J. A.; Sershen, S. R.; Rivera, B.; Price, R. E.; Hazle, J. D.; Halas, N. J.; West, J. L. *Proc. Natl. Acad. Sci. U.S.A.* **2003**, *100*, 13549.

(52)    Sokolov, K.; Follen, M.; Aaron, J.; Pavlova, I.; Malpica, A.; Lotan, R.; Richards-Kortum, R. *Cancer Res.* **2003**, *63*, 1999.

# CHAPTER 10

# FUTURE OUTLOOK

In this thesis, we described how the coupling between plasmonic nanoparticles in assembled nanostructures could be used to tune their plasmon resonance frequency, the plasmonic enhancement, as well as the non-radiative electron dynamics. There is great potential for future researchers to use the simple fundamental guidelines (e.g. polarization "selection" rules and the universal scaling of plasmon coupling) developed in this thesis for designing and optimizing the inter-particle coupling in assembled nanostructures for:

i) Tuning the plasmon resonances of assembled nanostructures to specific nanophotonic and nanomedicinal applications by systematic variation in geometrical parameters.

ii) Enhancing surface-enhanced Raman scattering and similar optical enhancements, possibly down to the single-molecule level.

iii) Maximizing the plasmonic sensitivity of nanostructures for molecular and biological sensing.

iv) Maximizing coupling-induced plasmon shifts for assembly-based analyte sensing.

v) Designing plasmon rulers for nanoscale distance measurement with defined distance calibration, longer distance range, and increased complexity and therefore improved measurement capabilities.

vi) Tuning the ultrafast bleach recovery/switching times of nanoparticle assemblies for nano-optic device applications.

Considering, the range of applications that could be impacted by this work, some future work is suggested to enhance the general applicability of our results.

i) It will be interesting to study the plasmon coupling in 1-D, 2-D and 3-D assemblies with multiple particles, which we initiated in Chapter 8. How are plasmon coupling and its size scaling behavior influenced by an increase in the number of particles in the assembly? A quasistatic model may be helpful but due to the approach of the nanostructure size to the light wavelength, it will be also necessary to understand the effect of electromagnetic retardation and incorporate it into the plasmon-coupling model. The experimental study and verification of these effects can be carried out on lithographic arrays and colloidal assemblies designed with defined inter-particle distances.

ii) Chapter 3 and 8 suggest the role of particle shape, curvature, and inter-particle orientation in tuning and enhancing the near-field coupling. The experimental realization and application of these ideas for developing highly enhanced Raman substrates and dielectric sensors will constitute an important advance.

iii) Non-radiative electron-phonon dynamics may also be studied as a function of the inter-particle interaction distances in controlled colloidal assemblies.


We hope that future studies such as those suggested above will be able to expand the models for plasmon coupling presented here to more complex nanostructures/assemblies that are encountered in real nanosystems/nanodevices.

# APPENDIX A

# DESCRIPTION OF DDSCAT PROCEDURE

## A.1 Concept of Discrete Dipole Approximation (DDA) Method

The discrete dipole approximation (DDA) is a method for solving the Maxwell's equations for particles of arbitrary size and shape and thus computing their absorption and scattering cross-sections. Details about the DDA method, its historical development, implementation, and capabilities can be found in Draine, B. T.; Flatau, P. J. *J. Opt. Soc. Am. A* **1994**, *11*, 1491 and references therein. The DDA method was originally developed by Purcell and Pennypacker and advanced by Draine, Goodman, and Flatau. Briefly, in the DDA method, the target structure is discretized into a cubic array of N virtual point dipoles with polarizabilities $\alpha_i$ located at positions $\mathbf{r}_i$. In the presence of an incident electric field $\mathbf{E}_o$, the polarization of each dipole $\mathbf{P}_i$ is given as:

$$\mathbf{P}_i = \alpha_i \, \mathbf{E}_{loc}(\mathbf{r}_i) \qquad (1)$$

where $\mathbf{E}_{loc}$ is the local electric field felt by the dipole, which is the sum of the incident electric field and the contribution from the other N - 1 dipoles:

$$\mathbf{E}_{loc}(\mathbf{r}_i) = \mathbf{E}_{inc,i} + \mathbf{E}_{other,i} = \mathbf{E}_o \exp(i\,\mathbf{k}.\mathbf{r}_i - i\omega t) - \sum_{j \neq i} \mathbf{A}_{i,j}.\mathbf{P}_j \qquad (2)$$

where $\mathbf{k}$ is the wave vector of the incident plane wave. $\mathbf{A}_{i,j}$ is a matrix that represents the interaction between all dipoles as follows:

$$\mathbf{A}_{i,j}.\mathbf{P}_j = \frac{\exp(i k \, \mathbf{r}_{ij})}{\mathbf{r}_{ij}^3} \left\{ k^2 \, \mathbf{r}_{ij} \, x(\mathbf{r}_{ij} \, x \, \mathbf{P}_j) + \frac{(1 - i k \, \mathbf{r}_{ij})}{\mathbf{r}_{ij}^2} x \left[ \mathbf{r}_{ij}^2 \mathbf{P}_j - 3 \mathbf{r}_{ij}(\mathbf{r}_{ij}.\mathbf{P}_j) \right] \right\} \quad \text{for } j \neq i \quad (3)$$

where $\mathbf{r}_{ij} = \mathbf{r}_i - \mathbf{r}_j$. Starting with an initial guess for the polarizations $\mathbf{P}_j$, the system of equations represented by eq 2 is solved iteratively for $\mathbf{P}_j$. The extinction, absorption and scattering cross-section can be then calculated as follows:

$$C_{ext} = \frac{4\pi k}{|\mathbf{E}_o|^2} \sum_{j=1}^{N} \text{Im}\left(\mathbf{E}_{inc, j}^* . \mathbf{P}_j\right) \tag{4}$$

$$C_{abs} = \frac{4\pi k}{|\mathbf{E}_o|^2} \sum_{j=1}^{N} \left\{ \text{Im}\left[\mathbf{P}_j \left(\alpha_j^{-1}\right)^* \mathbf{P}_j^*\right] - \frac{2}{3}k^3 |\mathbf{P}_j|^2 \right\} \tag{5}$$

$$C_{sca} = C_{ext} - C_{abs} \tag{6}$$

where Im implies the imaginary part.

According to Draine and Flatau, the DDA method is analogous to the continuum representation of the dielectric properties of a solid by the polarizabilities of its constituent atoms (Clausius-Mossotti relation). Such an approximation is valid at length scales that are large compared to the interatomic spacing. Similarly, the discrete dipole array can accurately reproduce the target properties on length scales much larger than the interdipole separation.

## A.2 DDSCAT

DDSCAT is the most popular code available for the implementation of the DDA method. The code has been developed by astrophysicist B. T. Draine (Princeton University) and P. J. Flatau (UCSD) and is freely available along with a comprehensive user guide. Here I have described some important steps and considerations that were involved in my experience with DDSCAT.

The DDSCAT 6.1 code that I used in my studies is available in Fortran and therefore standard compilers were used to build the DDSCAT executable for

1. Windows-based PC

2. UNIX/LINUX system for running simulations on our supercomputer

The procedure for running the DDSCAT executable differed slightly depending on the system used.

### A.2.1 Input

In addition to the executable, two additional files serve as the input for the program. The first one is the diel.tab (a sample available with the DDSCAT package), which contains the information of the dielectric function of the target material. In this file, real and imaginary parts of the material refractive index, n and k are listed sequentially for the different wavelengths in the spectral range in which the calculations are to be run. Note that values of the wavelength, n and k have to be normalized by the medium refractive index. Thus, the wavelength of light used in the calculation is that in the medium. In the case of structures with multiple components, a separate dielectric file corresponding to each component has to be used.

The second file is the parameter file ddscat.par (a sample available with the DDSCAT package), which specifies all other input parameters for the DDA simulation. Important parameters include

1. The shape definition: The shape is defined by the variable CSHAPE. A number of standard definitions are available within DDSCAT including ellipsoids (ELLIPS), cylinders (CYLNDR) and triangular prisms (PRISM3), which I have used commonly. The relative dimensions of the target are specified by the shape parameters PAR1 PAR2 PAR3, which are the number of dipoles along each

dimension of the shape. For example, a spheroid of aspect ratio 4 can be represented as 40 10 10 or 80 20 20.

2. Number of dipoles: The difference between the above two cases is that the latter case simulates the structure with 8x greater number of dipoles. The greater the number of dipoles, the better is the accuracy of the calculations, but the higher is the computational cost. I have used on a case-to-case basis between 0.5 to 2 dipoles per nm dimension of the nanostructure with good results. The general rule is that the inter-dipole lattice spacing should be much smaller than the wavelength of the light and the size of the nanostructure to get reliable results. For instance, it would not be reasonable for a spheroid of 10 nm width and 40 nm length to be defined by (PAR1, PAR2, PAR3) = (4, 1, 1).

3. Size: The number of dipoles along each dimension does not specify the real size of the structure. The actual size of the target structure is defined by its effective radius, which is equal to $(3V/4\pi)^{1/3}$ where V is the total volume occupied by the target.

4. Wavelength: The range of wavelengths has to be specified (same units, i.e. microns, as the effective radius) along with the number of intervals at which the calculations are to be run.

5. The polarization of the light can be chosen to be along the x, y, or z directions by defining e01 vector. E.g., e01 = (0.,0.) (1.,0.) (0.,0.) implies polarization along the y-axis. However, it must be noted that the target orientation with respect to light can also be changed by specifying the angles *beta*, *thetha*, and *phi*.

6. The number of components can be specified by NCOMP along with the identification of each of their dielectric files.

## A.2.2 Non-standard Shapes or Structures

For defining target shapes or structures, which are not standard to DDSCAT, a third file shape.dat has to be used as the input for the shape definition. CSHAPE is set to FRMFIL in this case and the name of the file is passed instead of the shape parameters. The shape.dat file specifies the number of dipoles and the (x,y,z) lattice positions of all the dipoles. While any suitable method can be used to generate a dipolar array that defines a custom shape, I have frequently used the graphing software Origin to combine standard shapes to give the custom shape. DDSCAT provides a separate routine that generates a target.out file for a specified standard shape. The target.out file has a format very similar to shape.dat. It specifies the total number of dipoles in the specified shape and (x,y,z) positions of each one of them. All the standard shape definition (target.out) files that need to be combined are imported into an Origin worksheet. The different shapes can be moved, rotated, or truncated along any of the dimensions by use of standard Origin add, multiply or subtract operations on the X, Y, Z columns. Very basic knowledge of vectors helps to determine the operation to be used. Once the custom shape is built, it can be plotted in 3-D to verify accuracy, following which the worksheet can be exported into a shape.dat file.  A couple of examples of custom-built shapes are given below.

1. A colloidal nanorod shape can be generated by combining in Origin a cylinder with a hemisphere (diameter = cylinder width) capping each end of the cylinder. The hemispheres can be obtained by splitting a sphere into half.

2. For defining dimers, trimers, or larger assemblies of particles of given shape, the shape definition file of the single particle can be duplicated the desired number of times in Origin. In order to change the inter-particle spacing, the different particles can be moved with respect to one another by Origin column operations.

### A.2.3. Program Execution

Once all the input parameters and files have been set, the executable is run. The executable terminates immediately if there is an error in any of the parameter definitions or in the file formats of ddscat.par or diel.tab. In addition, if the number of dipoles exceeds that allowed by the memory allocation of the DDSCAT program, it will terminate.

In order to run DDSCAT on the supercomputer (to take advantage of fast parallel computations), all the files including the UNIX/LINUX-compiled executable, the parameter file, the dielectric files, and shape.dat files, if any, have to be transferred by an ssh utility to the user folder, which in my case was located on Egate (egate.chemistry.gatech.edu). The executable cannot be run directly on the supercomputer. Instead, an additional "job" file (with .cmd extension) is required to be submitted, which contains the details of the program/job to be run.

### A.2.4 Output

In the case of a successful run, an output file is created for each of the wavelengths, e.g. w000r00ori.avg, w001r00ori.avg, w000r00ori.avg, and so on. Note that multiple effective radii can also be specified in ddscat.par in which case a file will be generated for each combination of wavelength and effective radius. The important quantities calculated are $Q_{ext}$, $Q_{abs}$, and $Q_{sca}$ which can be found in the output file (for

each wavelength) along with several other quantities, that may or may not be needed depending on the user or the end-utility.

# APPENDIX B

# LIST OF DOCTORAL PUBLICATIONS

1. <u>Prashant K. Jain</u>, Mostafa A. El-Sayed, "Surface plasmon coupling and its universal size scaling in metal nanostructures of complex geometry: Elongated particle pairs and nanosphere trimers," *Journal of Physical Chemistry C*. **2007,** submitted.

2. <u>Prashant K. Jain</u>, Xiaohua Huang, Ivan H. El-Sayed, Mostafa A. El-Sayed, "Noble metals at the nanoscale: Optical and photothermal properties and applications in imaging, sensing, biology, and medicine," *Accounts of Chemical Research*, **2007,** submitted.

3. <u>Prashant K. Jain</u>, Mostafa A. El-Sayed, "Surface plasmon resonance sensitivity of metal nanostructures: Physical basis and universal scaling in metal nanoshells," *Journal of Physical Chemistry C*, **2007**, 111(47), 17451-17454.

4. Wenyu Huang, Wei Qian, <u>Prashant K. Jain</u>, Mostafa A. El-Sayed, "The effect of plasmon field on the coherent lattice phonon oscillation in electron-beam nanofabricated gold particle pairs," *Nano Letters*, **2007**, 7(10), 3227-3234.

5. <u>Prashant K. Jain</u>, Mostafa A. El-Sayed, "Universal scaling of plasmon coupling in metal nanostructures: Extension from particle pairs to nanoshells," *Nano Letters*, **2007**, 7(9), 2854-2858.

6. <u>Prashant K. Jain</u>, Wenyu Huang, Mostafa A. El-Sayed, "On the universal scaling behavior of the distance decay of plasmon coupling in metal nanoparticle pairs," *Nano Letters*, 7(7), **2007**, 2080-2088.

7. Xiaohua Huang, <u>Prashant K. Jain</u>, Ivan H. El-Sayed, Mostafa A. El-Sayed, "Gold nanoparticles and nanorods in medicine: From cancer diagnostics to photothermal therapy," Invited Review, *Nanomedicine*, **2007**, 2(5), 681-693.

8. Xiaohua Huang, <u>Prashant K. Jain</u>, Ivan H. El-Sayed, Mostafa A. El-Sayed, "Plasmonic photothermal therapy (PPTT) using gold nanoparticles," Invited Review, *Lasers in Medical Science*, **2007**, published online 3rd Aug.

9. <u>Prashant K. Jain</u>, Xiaohua Huang, Ivan H. El-Sayed, Mostafa A. El-Sayed, "Review of some surface plasmon resonance-enhanced properties of noble metal nanoparticles and their applications to biosystems," Invited review, *Plasmonics Special Issue on Advances in Metal-Molecular interactions*, **2007**, 2(3), 107-118.

10. <u>Prashant K. Jain</u>, Ivan H. El-Sayed, Mostafa A. El-Sayed, "Au nanoparticles target cancer," Invited review, *Nano Today (Elsevier, UK)*, **2007**, 2(1), 18-29.

11. <u>Prashant K. Jain</u>, Susie Eustis, Mostafa A. El-Sayed, "Plasmon coupling in gold nanorod assemblies: Optical absorption, Discrete Dipole Approximation simulation and exciton coupling model," *Journal of Physical Chemistry B*, **2006**, 110(37), 18243-18253.

12. <u>Prashant K. Jain</u>, Kyeong Seok Lee, Ivan H. El-Sayed, Mostafa A. El-Sayed, "Calculated absorption and scattering properties of gold nanoparticles of different shape and composition: Applications in biological imaging and biomedicine," *Journal of Physical Chemistry B*, **2006**, 110(14), 7238-7248. (Top 10 most accessed articles for 2006)

13. Xiaohua Huang, <u>Prashant K. Jain</u>, Ivan H. El-Sayed, Mostafa A. El-Sayed, "Determination of the minimum temperature required for selective photothermal destruction of cancer cells with the use of immunotargeted gold nanoparticles," *Photochemistry and Photobiology*, **2006**, 82(2), 412-417.

14. <u>Prashant K. Jain</u>, Wei Qian, Mostafa A. El-Sayed, "Ultrafast cooling of photoexcited electrons in gold nanoparticle-thiolated DNA conjugates involves the dissociation of the gold-thiol bond," *Journal of the American Chemical Society*, **2006**, 128(7), 2426-2433.

15. <u>Prashant K. Jain</u>, Wei Qian, Mostafa A. El-Sayed, "Ultrafast electron relaxation dynamics in coupled metal nanoparticles in aggregates," *Journal of Physical Chemistry B*, **2006**, 110(1), 136-142.

# VITA

## PRASHANT K. JAIN

PRASHANT was born in Bijowa, Rajasthan, India. He grew up in Mumbai, where he attended St Anne's High School and D. G. Ruparel College. He completed his B. Tech with Honors from the University Institute of Chemical Technology ranking at the top, cumulative over the four-year program. While at UICT, he received a number of awards including the L.V. Pitre prize (2001), the Sohrab & Coomi Mistry Foundation Prize (2002), and the UICT Merit Prizes (2001 and 2002). He was also a Homi Bhabha Bal Vaigyanik in his younger days. Prashant proceeded to graduate school at Georgia Tech with study-abroad doctoral scholarships from the Lotus Trust, the American Alumni Association (India), and the University of Mumbai. Since the past four years, he has been carrying out doctoral studies at Georgia Tech with Prof. Mostafa A. El-Sayed on the optical properties of noble metal nanostructures. He has published 15 peer-reviewed papers in this area and has given a number of research talks and conference presentations. Prashant has been the recipient of the Graduate Student Gold Award of the Materials Research Society (2007), the best graduate research poster award from the American Chemical Society PHYS division (2006), the best graduate student award from Georgia Tech's School of Chemistry and Biochemistry (2006), recognition from the College of Sciences (2007), and the Atlanta Area Chemical Physics Award (2008). He was elected to full membership of the Sigma Xi Scientific Research Society in 2005. Prashant has been offered the Miller Fellowship of the University of California at Berkeley for 2008-2011, which he is set to begin after post-doctoral work at Harvard University.